3D Field Ion Microscopy and Atom Probe Tomography Techniques for the Atomic Scale Characterisation of Radiation Damage in Tungsten

Michal Dagan

St Edmund Hall

University of Oxford

A thesis submitted for the degree of

Doctor of Philosophy

Michaelmas term, 2016

Abstract

In this work, new reconstruction and analysis methods were developed for 3D field ion microscopy (FIM) data, motivated by the goal of atomic scale characterisation of radiation damage for fusion applications.

A comparative FIM/ atom probe tomography (APT) study of radiation damage in self-implanted tungsten revealed FIM advantages in atomistic crystallographic characterisation, able to identify dislocations, large vacancy clusters, and single vacancies. While the latter is beyond the detection capabilities of APT, larger damage features were observed indirectly in APT data via trajectory aberrations and solute segregation.

An automated 3DFIM reconstruction approach was developed to maintain reliable, atomistic, 3D insights into the atomic arrangements and vacancies distribution in ion-implanted tungsten. The new method was utilized for the automated 'atom-by-atom' reconstruction of thousands of tungsten atoms yielding highly accurate reconstructions of atomically resolved poles but also applied to larger microstructural features such as carbides and a grain boundary, extending across larger portions of the sample. Additional tools were developed to overcome reconstruction challenges arising from the presence of crystal defects and the intrinsic distortion of FIM data. Those were employed for the automated 3D mapping of vacancies in ion-implanted tungsten, analysing their distribution in a volume extending across 50nm into the depth of the sample.

The new FIM reconstruction also opened the door for more advanced analyses on FIM data. It was applied to the preliminary studies of the distortion of the reconstructed planes, found to depend on crystallographic orientation, with an increased variance in atomic positions measured in a radial direction to the centre of the poles. Additional analyses followed the subtle displacements in atomic coordinates on consecutive FIM images, to find them affected by the evaporation of atoms from the same plane. The displacements were found to increase with size as the distance to the evaporated atom decreased, and are likely to be the result of a convolution between image gas effects, surface atoms relaxation, and charge re-distribution. These measurements show potential to probe the dynamic nature of the FIM experiment and possibly resolve contributions from the different processes effecting the final image.

Finally, APT characterisation was performed on bulk and pre-sharpened needles to determine the effect of sample's geometry on the resulting implantation profiles, and the extent to which pre-sharpened needles could be employed in radiation damage studies. While the ions depth profiles in needles were not found within a good match to SRIM simulations, the damage profiles exhibited closer agreement. Further, the concentration of implanted ions in bulk samples was found significantly higher than in the respective needle implanted samples, with excessive loss found for the light ion implantation.

Preface

Parts of this thesis have been included in the following publications:

1. Dagan M, Hanna LR, Xu A, Roberts SG, Smith GDW, Gault B, Edmondson PD, Bagot PAJ, Moody MP "Imaging of radiation damage using complementary field ion microscopy and atom probe tomography" Ultramicroscopy 159 (2015): 387-394.

2. Dagan M, Gault B, Smith GDW, Bagot PAJ, Moody MP “Automated atom-by-atom three-dimensional reconstruction of field ion microscopy data" Microscopy and Microanalysis 23 (2017): 255-268.

3. Vurpillot F, Danoix F, Gilbert M, Koelling S, Dagan M, Seidman DN “True Atomic-Scale Imaging in Three Dimensions: A Review of the Rebirth of Field-Ion Microscopy” Microscopy and Microanalysis 23 (2017): 210-220.

The reconstruction code developed in this work along with some demonstration videos are available in: https://oxfile.ox.ac.uk/oxfile/work/extBox?id=3898370562509BCD63

Acknowledgements

The research described in this thesis would not be possible without the help and support of the following people: My supervisors: Prof Michael Moody and Dr Paul Bagot, have provided constant support, both professional and moral, encouragement and ideas and I thank them greatly. Dr Baptiste Gault has been an inexhaustible source of knowledge, ideas and inspiration and I'm thankful for the opportunity to collaborate with him. I would also like to thank Prof George Smith, and Prof Steve Roberts for their guidance, and Mr Terry Godfrey who has saved the field ion microscope at Oxford, and me by extension, more than once.

All members of the Oxford atom probe group have been wonderful colleagues and friends, and discussions with them are greatly appreciated, in particular Dr Daniel Haley and Dr Andrew London - both always generous with their advice and time, and Mr James Douglas to whom I thank for his help and time on the FIB.

Finally, I thank my husband Amir, for his support, partnership and help during these years, while pursuing his own doctorate.

Contents

1 Introduction

Materials performance is intimately linked to microstructural architecture at the atomic-scale. The continued development of models to explain mechanical properties, and ultimately design new and improved materials is therefore critical for an increasing number of applications. However, directly imaging in 3D not only all constituent atoms within a material, but also vacancies and other types of defects, has proven to be beyond the resolution limit of most current conventional microscopy techniques, and remains a formidable challenge.

Such atomic-scale characterisation capabilities are essential in radiation damage studies. A remaining hurdle in the development of nuclear fusion power generation is the lack of materials that can withstand the extreme operating conditions inside the reactor [1]. A thorough understanding of radiation-induced degradation mechanisms of the internal microstructure under such conditions is therefore of paramount importance. Bombardment by neutrons initializes atomic scale changes in the microstructures of materials inside the reactor in the form of displaced lattice atoms, along with chemical products of transmutation reactions. These initial atomic scale changes further develop into a variety of chemical and structural features [2], [3] which can ultimately undermine critical mechanical properties through phenomena such as radiation induced embrittlement [4], radiation hardening [5] and radiation induced clustering [6]. It is therefore crucial to fully understand mechanisms that are in operation from even the earliest stages of atomic scale damage. Such knowledge will allow the accurate evaluation of operational

lifetime of the different components and the development of new, sustainable materials towards internal components of nuclear reactors.

Recent efforts in electron microscopy have proposed complex solutions to atomic-scale tomographic imaging of materials [7], [8]. Field ion microscopy (FIM) however was the first microscopy technique to image individual atoms, lattice defects in metals including single vacancies[9], interstitials and extended dislocations [10], [11]. In contrast to other high-resolution microscopy techniques, FIM relies on the ionization of inert gas atoms from prominent positions on the specimen surface exploiting an intense electric field. Although each FIM image is intrinsically 2D, pulsed evaporation of surface atoms results in a series of images, each representing a 'snapshot' of the surface during the field evaporation process. As the depth of the specimen is probed by the removal of the constituent atoms, the images progressively provide 3D atomic information on the specimen. FIM's experimental procedures as well as data analysis are currently manual, laborious tasks.

In recent years FIM has been somewhat overshadowed by the emergence of Atom Probe Tomography (APT). APT is similarly based on the concept of field evaporation of specimen atoms from the surface [12]. The evaporated ions strike a position-sensitive detector and their time-of-flight is measured, informing as to their chemical identity. Ultimately, using the digitally-recorded detector coordinates and a reverse-projection model, a 3D atomistic reconstruction of the tip is obtained [13].

With the rise to prominence of APT, the potential of its forerunner, field ion microscopy (FIM), has largely been overlooked. While APT has proven capabilities for the study of small scale

radiation induced chemical changes [14], it lacks the necessary spatial resolution and detection efficiency to image individual sites on the crystal lattice and therefore struggles in the direct imaging of atomic scale crystal damage [15]. FIM, on the other hand, is comparatively more limited in terms of analytical capabilities, however it enables direct imaging of complete crystallographic arrangements of atoms on the surface of the sample, and can therefore constitute as a highly beneficial complementary technique to APT.

This thesis aims to further establish FIM as a leading instrument to atomic scale crystallographic characterisation specifically focusing on applying FIM to radiation damage studies. In terms of materials tungsten is at the experimental focus of this work, as it is a leading candidate for future fusion reactors components, along with being a well-studied material in FIM.

The background chapter will explore important terms in the fields of radiation damage and field emission microscopy (the term is used in this thesis to describe APT, FIM and similar techniques based on field induced processes). The role of tungsten in new fusion reactors is discussed as well as radiation damage mechanisms, and current practices in radiation damage experimental studies. Further, the operational mechanisms of FIM and APT will be explained. Since the FIM technique is at the centre of this thesis, a special emphasis is placed on the review of data analysis techniques for FIM. Finally, FIM and APT studies of radiation damage in tungsten are reviewed, highlighting their past and potential contributions to the field. All experimental methods employed in this thesis are described in chapter 2.

In chapter 3 a combined APT/FIM study of radiation-induced crystal damage in tungsten samples is demonstrated. The strengths and weaknesses of each technique are discussed and compared, and the complementary value of FIM to APT is proven.

Chapters 4-8 are focused on expanding FIM capabilities in 3D and developing new tools to analyse and reconstruct 3DFIM data. In order to fully utilize the unique imaging capabilities of FIM and explore larger volumes accurately and consistently, chapter 4 introduces the first automated 'atom-by-atom' approach to 3D FIM data reconstruction. Chapter 5 demonstrates advanced information extractable from the FIM experiment, as sub-angstrom displacements of atomic positions on FIM images are measured with the new technique. Chapter 6 utilizes the new method to analyse the reconstructed structure, quantifying its divergence from the expected crystallographic structure in cases of both damaged and un-damaged reconstructed volumes. Chapter 7 applies the technique to the reconstruction of microstructural features across a wider area of the sample than the previously analysed atomically-resolved poles, demonstrating how larger volumes can be reconstructed. Chapter 8 expands the reconstruction method to handle volumes of the lattice that contain defects. The vacancy distribution along the depth of an ion-implanted tungsten sample is extracted with the new technique. Finally, chapter 9 addresses the unique sample geometry required to perform FIM/APT experiments, exploring its influence on the resulting radiation damage profiles.

1.1 Tungsten in nuclear fusion - Introduction

The continued rise of global population and living standards is creating a massive increase in energy consumption [16]. This has driven research into new energy production technologies with

an added emphasis on clean and safe energy production. Fossil fuels, nuclear fission, renewables will all contribute to fulfil some of the world's energy requirements in the foreseeable years to come [16], [17] . Fusion based energy is being increasingly recognized as a potential alternative that could offer a secure source of energy with no production of greenhouse gases, no long-lived radioactive waste and almost unlimited fuel supplies.

The fuels used in fusion reactors are deuterium and tritium mixes, found to produce the highest energetic gain at the lowest temperatures. In a chemical reaction, the D-T or D-D particles are fused together to create heavier elements. The easiest reaction to initiate is given by:

$$\mathrm{D} + \mathrm{T} \rightarrow {}^{4}\mathrm{He}\ (3.5\ \mathrm{MeV}) + \mathrm{n}\ (14.1\ \mathrm{MeV})$$

For the fusion reaction to occur, extreme temperatures (millions of Celsius) have to be achieved for the nuclei to overcome the repulsive coulomb barrier between them, therefore they are heated to a plasma state [18]. The DT fusion reaction releases a large amount of energy, mostly in the form of high energy (14 MeV) neutrons that can be harvested, nearly 4 million times more energy than the equivalent burning of coal, oil or gas [19].

The unlimited supply of fuels is another advantage to fusion energy. Deuterium can be extracted from sea water and tritium is produced inside the fusion reactor as free neutrons interact with lithium (which in turn exists in the earth crust and sea reserves in quantities sufficient to last millions of years) [19].

The sustainability of the fusion reactor has been instigated in the Joint European Torus (JET) project [18], soon to be followed by the 'International Thermonuclear Experimental Reactor' (ITER) [19], [20] and the 'Demonstration' power plant (DEMO) [21], the next significant stages

towards a self-sustaining, energetically profitable fusion reactor [22], [23]. While the goal of ITER is to demonstrate a large scale operable fusion reactor, DEMO will be the first demonstration of a fusion reactor power plant.

JET, ITER and DEMO are all designed to operate a Tokamak based fusion reactor. In this approach, the heated plasma required to sustain the fusion reaction is confined magnetically within a Tokamak – a torus shaped device that is used to confine the plasma by creating magnetic fields travelling both around the torus, and in circles orthogonal to it [24]. However, materials selection for the plasma facing components of the Tokamak is a great challenge due to the extreme conditions they are expected to withstand.

This section reviews tungsten's potential role in new fusion reactors, the different damage mechanisms operating under irradiation conditions, and the methods currently used to simulate and study radiation damage.

1.1.1 Tungsten for use in Tokamak

The extreme conditions of high temperatures and highly energetic neutrons inside a fusion reactor make materials selection for construction of the Tokamak a true challenge. Candidate materials must have low activation energies to minimize radioactive waste production, high melting temperature, thermal fatigue resistance, strength, ductility in the range of working conditions and resistance to a range of different types of degradation damage [1], [25], [26].

Since both face the plasma, the blanket and divertor are considered the most challenging components to design in ITER. Carbon fibre composites meet many of the requirements for plasma facing components (PFCs) and were studied intensively as an initial leading option [27].

However, their extremely rapid erosion rate under neutron bombardment makes them unsuitable for use as long-term components in a fusion reactor [28]. Beryllium and tungsten are alternative candidate materials and their behaviour under suitable conditions is now the focus of significant research [29]–[31].

The divertor plays an important role in securing the steady operation of the fusion reactor by controlling the concentration of impurities and helium ash in the plasma. Impurities of first wall materials, as well as helium and hydrogen created from the fusion reaction along with excess heat, must be removed from the plasma in order to sustain the fusion reaction [19]. These impurity ions are magnetically directed towards the divertor plates, located at the bottom of the Tokamak, as can be seen in Figure 1.1a. As they strike, their kinetic energy turns to heat which is then removed by cooling water. As about 15% of the fusion generated heat as well as highly energetic plasma impurities are to be removed through the divertor [4], it stands to be the highest thermally loaded component in the reactor, with a peak load of $20\ \mathrm{MW/m^2}$ in the ITER design [19] ($10\ \mathrm{MW/m^2}$ under normal operation conditions). Tungsten is currently the leading choice for the ITER divertor armour material.

The blanket in ITER is designed to protect the inner walls of the vacuum vessels in which the fusion reaction takes place, and the magnet system from the heat and high energy neutrons. The plasma facing surface of these blankets is called the first wall and is illustrated in Figure 1.1b. The first wall is expected to experience heat flux of 0.5 MW/m^2 under standard operation conditions, peaking at 1.2 MW/m^2 [21]. While tungsten was considered for the first wall, and is still being investigated for the first wall in future designs, the current selection for ITER is beryllium [19].

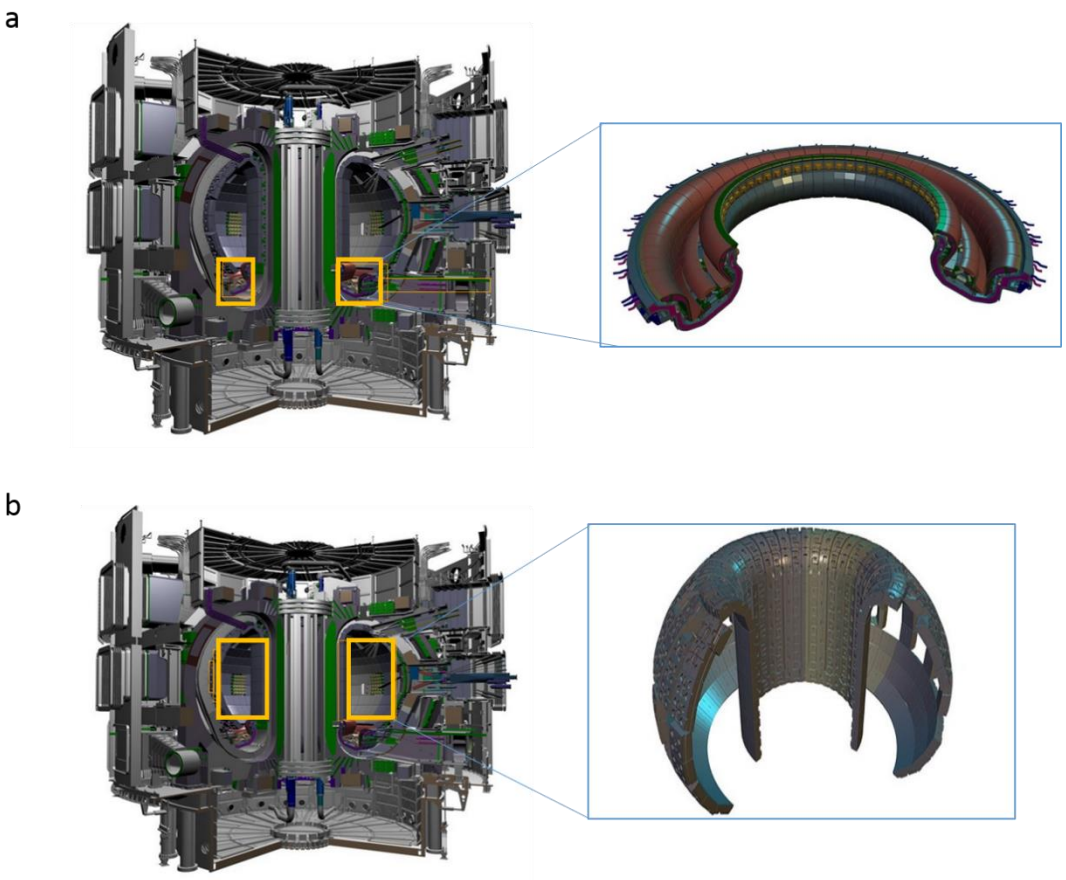

Figure 1.1 (adapted from [19]): Plasma facing components of the Tokamak for which tungsten is being considered (a) Divertor : extracts heat and ash to reduce plasma contamination. (b) The first wall/blanket: protects the vacuum vessels and magnets from heat and neutrons.

Tungsten is the element with the highest melting temperature of 3422℃. It has high thermal conductivity, a low expansion coefficient and low erosion rate [32]. However, under irradiation conditions these qualities may change, and these changes are at the heart of extensive current investigations [4], [33]. The brittle-ductile transition temperature (BDTT) in tungsten lies in the range of 150-500℃ (depending on microstructure, loading method, strain rate) and can be shifted up by hundreds of degrees due to neutron damage [34],[4]. Tungsten's embrittlement and high BDTT are a major limitation for tungsten use. The upper temperature limit for tungsten

use was shown to be restricted by thermal creep, helium embrittlement and corrosion, narrowing the operation temperature window further to 800-1300℃ [34].

1.1.2 Radiation damage mechanisms

Radiation damage in fusion reactors is the result of the different elastic and in-elastic interaction routes component materials have with the free neutrons produced in the fusion reaction. The different interaction types are schematically described in Figure 1.2, and are detailed in the next sections.

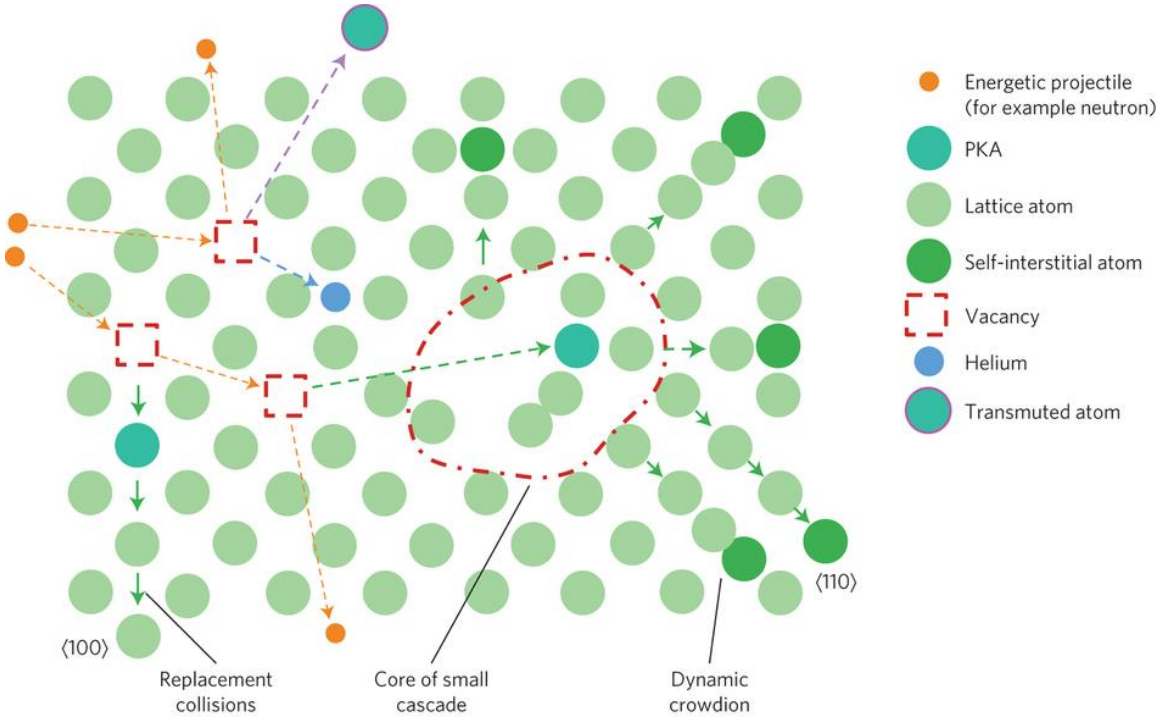

Figure 1.2 [1]: Schematic illustration of the different interaction types between the hitting neutrons and lattice atoms. The impacting particle (in orange) can cause primary displacements of lattice atoms (PKA) resulting in vacancies and self-interstitials. Neutrons can also cause transmutation of lattice atoms resulting the creation of helium atoms.

1.1.2.1 Displacement damage

For an atom to be displaced from its lattice position, a minimum value of energy needs to be transferred to the atom in the collision. This energy is termed the displacement energy, E_d, and

is a function of the crystallographic direction. It is found to be 42eV / 70eV for [001] / [011] directions respectively in tungsten [35]. The first atom displaced by the interaction with the colliding neutron is called the primary knock on atom (PKA). PKAs with an energy larger than E_d go on to deflect other atoms in the lattice, causing a cascade of displacements in the atomic structure, resulting in Frenkel pairs of self-interstitial atoms and vacancies [36]. Defects in the cascade, and from different cascades will tend to agglomerate to form larger type defects that are more thermodynamically stable, where the agglomeration behaviour tightly depends on the temperature and defect concentration. Voids are found to be the more stable configuration in comparison to vacancy loops as their formation energy is smaller [37]. Vacancies are more facilitated in fusion environments as helium and hydrogen (by-products of the fusion reaction) form stable complexes with vacancies [38], [39]. Due to the large difference in migration energy of vacancies and self-interstitials (SIAs), 1.78eV for vacancies, vs 0.088-0.102eV for SIAs in tungsten [40], [41], SIA's are much harder to image, and require very low irradiation and observation temperatures to be detected in the field ion microscope (which is at the experimental focus of this research) [42].

1.1.2.1.1 Quantification of damage

Several models exist to quantify the number of displaced atoms by one PKA. The most commonly used is the Kinchin and Pease (K-P) model [43], also employed by the SRIM software used in this thesis. The model assumes head-on elastic collisions, a threshold value E_d for the energy required to displace a lattice atom, and an energy cutoff value E_c, for the energy transferred to an atom in a collision. According to the model, below E_d no displacements will be added, and any energy access above E_c would be entirely dissipated in electronic excitation and ionization. Between E_c

and E_d a linear relation between the number of displaced atoms and the energy of the PKA is assumed. It is important to note that the model does not take into account any relaxation and recombination processes that occur after the initial creation of defects and is effectively representative of the defects distribution at 0K. Figure 1.3 plots the predictions of the model for the number of displaced atoms as a function of the energy of the colliding ion. As can be seen, at an energy above the cutoff, E_c, the number of displaced atoms reaches saturation, while below E_d no displacement occurs.

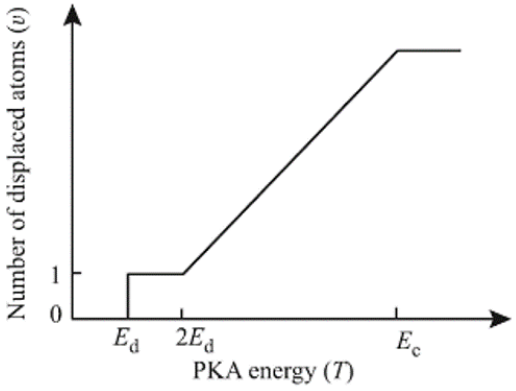

Figure 1.3 [44]: Predictions of the K-P model for the number of displaced atom in a single PKA event as a function of the impacting ion. Threshold energies are set such that below E_d no displacemens occur and above E_c the number of displaced atoms saturates.

The NRT model [45] which is based on the K-P method incorporates a more detailed approach to the quantification of the dissipated energy in collisions and electronic loses. The NRT model assumes that only a fraction of the original PKA energy is available for elastic scattering, and that the number of displaced atoms is dependent on this fraction of PKA energy. According to the NRT model, which was adopted by the international community as the standard method for damage calculations, the number of stable Frenkel-pairs produced by a PKA is given by:

$$\nu_{NRT} = 0.8T_{dam}(E_{PKA})/2E_d$$

Where E_{PKA} is the energy of the PKA and T_{dam} is the energy portion dissipated in elastic collisions. Note that the factor '0.8' was experimentally found to be a function E_{PKA} [46]. Both low temperature measurements in metals [47] and elevated temperature segregation measurements in alloys [48], [49] showed a decrease in this factor associated with ' the damage efficiency', with increasing PKA energy. This dependence is often disregarded by common radiation damage calculations, and should be remembered when comparing different energy implantation results.

For the purpose of comparative discussion between different irradiation parameters, the notion of 'dpa' – displacements per atom, was introduced into the field, and is currently being used to replace the total number of displaced atoms. 'dpa' can be thought of as normalized displacements number, describing the number of displacements for a given volume, divided by the theoretical number of atoms expected within the material. Irradiations of particles with different energies, or at different doses, can potentially generate similar 'dpa' values, demonstrating that the 'dpa' measure is not representative of those, and allow comparison between experiments across a wide range of parameters. 'dpa' can be calculated from the SRIM software output for a set of ion/target and energy, as will be explained in chapter 2. While there is an ongoing discussion about the validity of the SRIM output, and its alignment with the NRT model, and in turn, the real number of created defects [50], [51] the true value of the 'dpa' quantity is the comparative approach to other systems, and even across radiation sources. It is therefore important, for the validity of the comparisons to use the standard ASTM guide for SRIM selection parameters [52].

It is important to note that the final defect distribution inside tungsten samples will greatly depend on the operating temperature, which is completely omitted from the calculations described above. Recovery stages can occur in tungsten, resulting in recombination of defects and clustering of defects at temperatures where they are mobile. Such recovery processes have mostly been measured by electrical resistivity changes [53], [54], FIM [55], [56], and TEM [57]. Five stages were identified in accordance with the recovery mechanism active in each stage, each operating within a different temperature range. The species migrating at each stage are still under debate, however three prominent stages are agreed upon, with stage 1 corresponding to the movement of free interstitials at temperatures below -170℃, Stage 3 at 350℃ corresponding with mono-vacancy mobility, and stage 5 at 1000℃ corresponding to the dissolution of small vacancy clusters.

1.1.2.2 Transmutation damage

Transmutation occurs as a result of slow neutrons being absorbed by the target material, changing its mass or atomic number (or both). As can be expected such reactions over time can lead to significant changes in the materials composition, microstructure, and in turn, mechanical properties. Transmutation also results in the formation of helium and hydrogen. These dissolved gases often cause considerable volume changes in the crystal lattice via swelling and blisters [58],[59]. They were also recently found to have a significant impact on tungsten's hardness, as it was found to increase post helium implantation [5].

According to simulations, the expected transmutation composition in the first wall of ITER after 1 year is [98 at% W, 0.91 at% Re, 0.06 at% Os] , after 3 years: [96.3 at% W, 2.59 at% Re, 0.53 at% Os] and [94 at% W, 3.8 at% Re, 1.38 at% Os], after five years, along with helium and hydrogen

that make up the rest of the composition [2]. These new metal elements can lead to the formation of intermetallic phases, which will have an effect on the component's mechanical properties. Tungsten transmutation into rhenium, combined with displacement damage was seen to result in the formation of WRe clusters and irradiation hardening that increased linearly with rhenium content when exposed to displacement damage above 1.5 dpa [6]. Further transmutation to osmium was found to suppress the clustering but significantly harden the material [60].

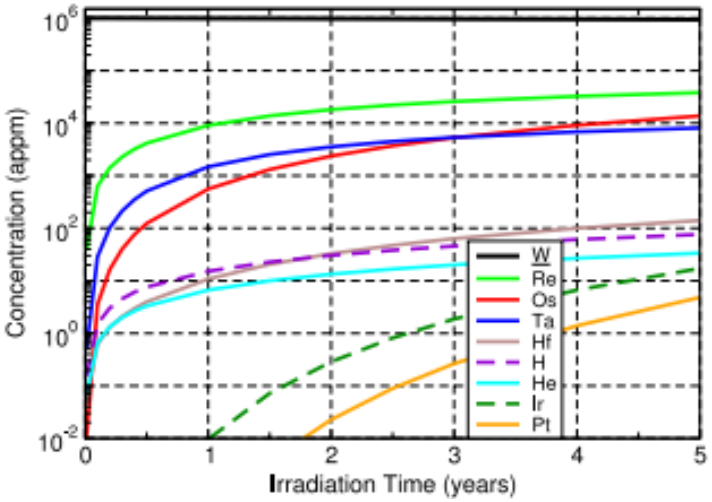

Figure 1.4: [2] Predictions for transmutation products of tungsten after 5 years of operation under first wall conditions.

1.1.3 Ion implantations

Radiation damage studies require a controlled environment of experimental conditions characteristic of different stages in the life time of a fusion reactor. Current lab-scale fusion reactors do not operate in a continues mode as future fusion reactors are expected to, and control of irradiation dose, rate and temperature is very difficult to achieve. Accelerator based facilities can generate the necessary 14.1 MeV neutrons characteristic of fusion reaction [61],

however these operate at an order of magnitude lower flux than real time fusion reactors, and are expected to generate helium and hydrogen at levels 5-10 times above the fusion reactor predictions per dpa, as well as a variety of transmutation products not expected in a fusion reactor. Fission reactors have also been utilized to study radiation damage. However, as the characteristic neutron energy is lower (<2MeV), the damage cascades caused by fission neutrons are smaller. Further, their operating temperatures are significantly lower than those expected for a fusion reactor, and less hydrogen and helium will be generated in a fission reactor [62].

To this end the 'international fusion materials irradiation facility' (IFMIF) is in design stages and is expected to provide continuous high neutron flux tailored for future nuclear plants materials selection [63],[64],[1]. This project is based on two parallel deuteron accelerators and a Li screen and is expected to be operational by the middle of the next decade.

Figure 1.5 compares the neutron spectrum and helium/dpa production in a number of different irradiation facilities.

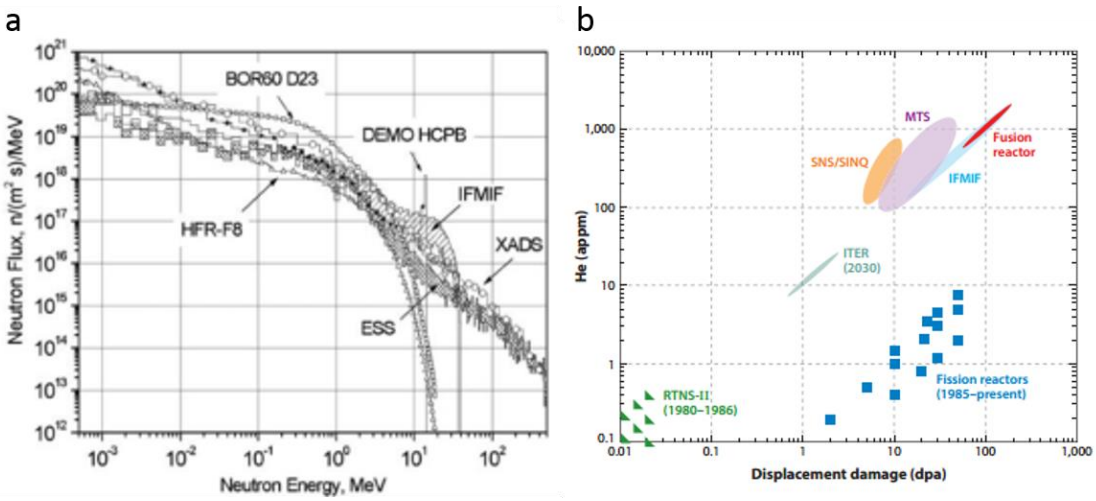

Figure 1.5: (a) Neutron Spectrum of different irradiation facilities [64] (b) Helium/dpa expected in different irradiation facilities[65]. HFR,BOR-60 are fission reactors. ESS,XADS,MTS,SNS,SINQ are spallation sources.

Ion implantations are currently the most utilized technique to simulate radiation damage. These are readily available worldwide and can produce lattice displacements in much shorter time scales than fission reactors (several dpa per day, about 5 times faster than a fission facility). Ion implantations do not induce transmutation therefore their products are not radioactive and are easier to handle. The dose, temperature and energy spectrum are easy to control. However, the analogy to neutron radiation is not complete for these reasons precisely. The expedited dose rate of damage is a cause for concern to the validity of the simulation. Moreover, ion implantation damage is confined nearer to the surface in ion irradiations, while neutrons can penetrate much deeper into the lattice before they interact with an atom in a head-on collision. Transmutation effect will not occur in ion implantation and so a variety of W-Re-Os compositions will have to be produced and tested to simulate transmutation in tungsten. Finally, while reactor neutron radiation is characterised by a spectrum of energies, ion implantations are of a constant energy, and can only be combined sequentially to simulate a wide spectrum. Several works have investigated the damage profiles in tungsten implanted with tungsten ions in comparison to neutrons and were able to find combinations of implantation conditions where a good match was achieved [66], [67]. In spite of its shortcomings, self-ion implantations are commonly employed in tungsten to simulate displacement damage. These implantations can also be performed sequentially with helium and hydrogen implantation to closely simulate the situation in a fusion reactor [5].

1.2 Field emission microscopy - Introduction

Field emission microscopy is a term referring to several microscopy techniques that employ the phenomena of field ionization or field evaporation. By applying high voltage, thus generating high

electric fields in the direct vicinity of the needle-shaped specimen, atoms are removed from its surface to form an atomically-resolved image [12]. Two of the most prominent field emission techniques that are the focus of this thesis are field ion microscopy (FIM) and atom probe tomography (APT).

With growing demand for the development of new nanostructured materials, APT has become an important, mainstream technique to characterise both structural and chemical nano-scale phenomena.

Since the invention of the FIM in 1951 by E.W.Muller [68] , FIM has been employed to a variety of metallurgical systems [69], including GP zones in steels [70], nitrides in Fe-Cr alloys [71] and fine scale precipitates in CuFeNi [72], as well as nickel and titanium aluminides [73]. It was also used to study the structure of grain boundaries [74], along with diffusion and adsorption behaviour in metal surfaces [75]. More recently, FIM has been uniquely employed to study real-time chemical reaction behaviours of catalytic hydrogenation of NO and NO_2 on platinum-group metals [76], and dopant clustering behaviour in ion-implanted silicon [77].

Ground-breaking research in the 1960's and 1970's demonstrated the unique insights FIM can bring into the study of radiation damage, in particular to primary stages of damage [56], [78]–[80]. In this irradiation regime the dose of implantations is low such that damage cascades corresponding to different colliding ions are not interacting with each other. In particular, they are characterised by very small, sometimes atomic-sized defects, which remain unresolved by traditional microscopy techniques. In a series of experiments, Seidman *et al.* directly imaged the early stages of radiation damage, manifesting as very small, atomic-scale defects in the crystal

lattice by developing a novel 3D FIM approach, characterising spatial distributions and densities of vacancies [79]–[81].

Subsequent instrumental advances [82] such as the incorporation of laser pulsing [83] and the position sensitive detector [84] have led to the development of the atom probe in which chemical analysis and 3D reconstruction were also made possible. Atom probe has provided new insights into the microstructure of materials, and has been used in materials science to study crystal defects, phase compositions, solute/dopant clustering, precipitation and more. It has been extended to study electronic materials [85], thin films and multilayers [86], amorphous materials [87], geological samples [88] and has also been greatly employed for the study of nuclear materials [14]. Among these, case studies include radiation-induced clustering in tungsten alloys [60], precipitation in thermally aged reactor pressure vessels (RPV) steels [89]–[92], particle stability and distribution of oxide particles in oxide dispersion strengthened steels (ODS) [93]–[95], and surface oxidation processes of stainless steels [96] and zirconium alloys [97] in corrosive environment.

In this chapter, the operational mechanisms of the two most prominent instruments of field emission microscopy, the field ion microscope and its successor the atom probe, will be discussed in detail. Special emphasis is given to FIM reconstruction methods, as these are a main objective of this thesis.

1.2.1 Field ion microscopy

Field Ion Microscopy (FIM) is a 2-dimensional imaging technique based on the process of field ionization, which has the capacity to map the configuration of atoms on the surface of the specimen with atomic resolution.

In this technique, the specimen takes the form of a very sharp needle, with a tip diameter size of several tens of nms. The sample is placed inside a vacuum chamber cooled to a cryogenic temperature, into which a small amount ($\sim 3\times10^{-5} mbar$) of inert imaging gas such as neon or helium is admitted. A high voltage (several kV) is then applied to the specimen. Due to the sharp geometry of the specimen this voltage generates an intense electric field at the apex of the tip, according to the field-radius relation:

$$E = \frac{V}{k_f R}$$

where R is the radius of the tip (approximated to be a perfect sphere), k_f is the field factor accounting for the geometry deviation from the perfect sphere (evaluated in [98], [99] to be 2.5-8 for tungsten) and V is the applied voltage. It is also according to this field-radius relation that regions of protruding atoms on the surface will generate higher fields, as those can be regarded as local regions of even smaller radius and larger charge density [12].

The small radius of the tip is therefore necessary to generate an intense electric field, causing polarized atoms of imaging gas to be attracted and absorbed to its surface in a process called field adsorption. Given a sufficiently high field, the gas atoms are subsequently ionized in a process termed field ionization, before being accelerated by the electric field away from the tip

towards a micro channel plate/ phosphor screen, creating a highly magnified image of its surface, as seen in Figure 1.7.

Several models exist to describe the field adsorption and ionization mechanism of the gas and define the potential barrier for the process [100]–[104]. Gas atoms that reach the surface are thought to collide with the surface, and gradually lose their energy in a decaying series of jumps across the surface of the sample [102], [101]. As their velocity is reduced, the time spent on high field atomic sites is increased, increasing the probability for ionization. In the field ionization process an electron from the outer shell of a gas atom will tunnel through its field-distorted potential barrier to an empty energy level at the metallic surface of the sample [100]. On the one hand, the probability for tunnelling increases as the field is higher, therefore the probability is increased in the vicinity of high-field atomic positions. On the other hand, tunnelling requires the electron to have an energy higher than the lowest conduction band of the metal, therefore the probability for ionization is lowered right at the surface where gas atoms are slowed to an energy too low [103]. A critical distance can therefore be defined, X_c, for the optimal distance for ionization of gas atoms from the surface:

$$X_c = \frac{I_0 - \emptyset_e}{eE}$$

Where I_0 is the first ionization energy, $\emptyset_e$ is the work function of the surface, E is the electric field. X_c is estimated at 0.4nm above the surface for FIM of a tungsten sample imaged with helium, with a very narrow $0.1X_c$ variation [105],[106]. Figure 1.6 demonstrates the dependence of X_c on I_0, $\emptyset_e$ and E. The figure plots the potential energy curve of an electron of a gas atom in the vicinity of the tip in the absence (a) and presence (b) of an electric field. The potential is

plotted as a function of the distance from the tip's surface. As can be seen in (b), the electric field distorts the potential curve, such as to determine X_c, the closest distance from the surface where the electron's energy is comparable with E_F in the field distorted potential.

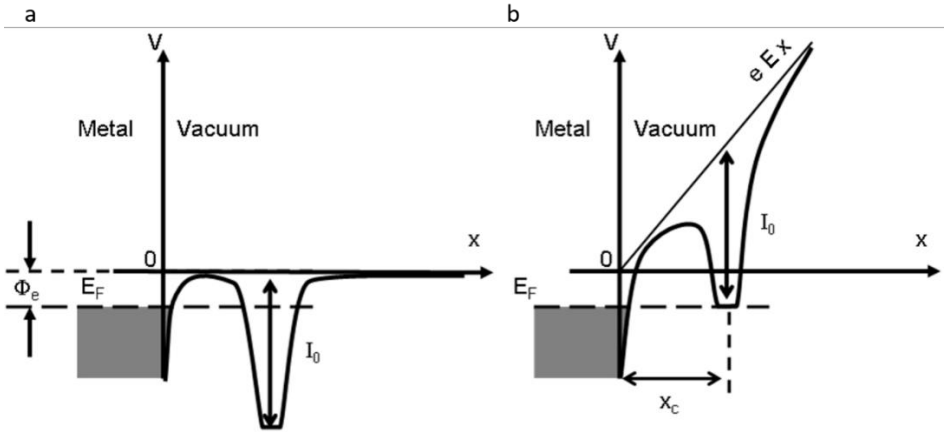

Figure 1.6[12] : Potential energy diagram of an electron from a gas atom, as a function of distance, x, from the surface of the tip (a) in the absence of an electric field, (b) in the presence of an electric field, E. I_0 is the first ionization energy, E_F fermi energy, ϕ_e work function of the surface, and X_c the critical distance for ionization.

Once ionized, the charged image ion will move under the influence of the field away from the sample, to hit the FIM detector. The FIM image is constructed of bright points, each representing an atom on the surface of the tip. The intensity of the spots is influenced directly by the topography of the surface of the tip, as more protruding atoms will generate a higher field around them, causing more gas atoms to be absorbed in their proximity. Bearing in mind the highly curved surface of the specimen, the resulting image is in fact a stereographic projection of the crystal, resolving the atomic topography of the surface.

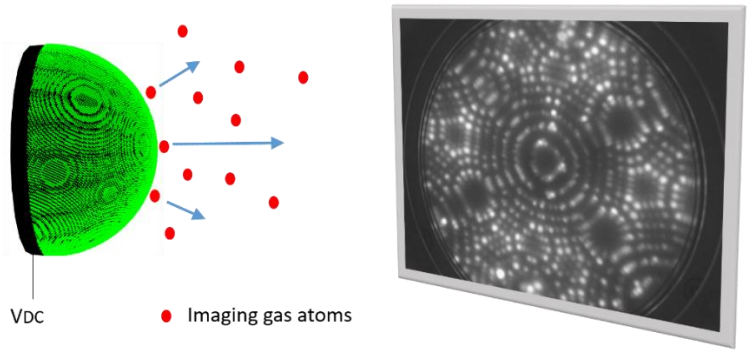

Figure 1.7 : FIM set up. Imaging gas atoms are absorbed on atomic sites on the sample's surface, and get ionized by the strong electric field. They hit a phosphor screen, and create the FIM image where every bright spot represents an atom on the surface of the specimen.

The magnification of the FIM image by the adaptation of a point projection model is given by:

$$M = \frac{L}{\varepsilon R}$$

where L is the distance of the tip from the screen, R is its radius, and ε is the image compression factor (ICF). For typical values of the above, a magnification factor of 10^6 is achieved, sufficient to resolve individual atoms. The ICF compensates for the known phenomena of field line deflections towards the main axis of the sample, more prominent for atoms ionizing from the edges of the sample. Figure 1.8 demonstrates the geometrical definition of the ICF according to the point projection model: As field lines are distorted (due to the imperfect spherical nature of the tip as well as its electrostatic environment), the evaporated ions deviate from their straight radial trajectories, and hit the screen to create the angle θ_{obs} on the FIM image. A new centre to the tip can then be determined at point P along the main tip axis and behind the true centre, such that ions hitting the screen at the same points as before could be considered as evaporated from a theoretical sphere centred at P, resulting in the expected crystallographic angle, θ_{crys}. The ICF can therefore be defined as $\varepsilon = \frac{\theta_{obs}}{\theta_{crys}}$.

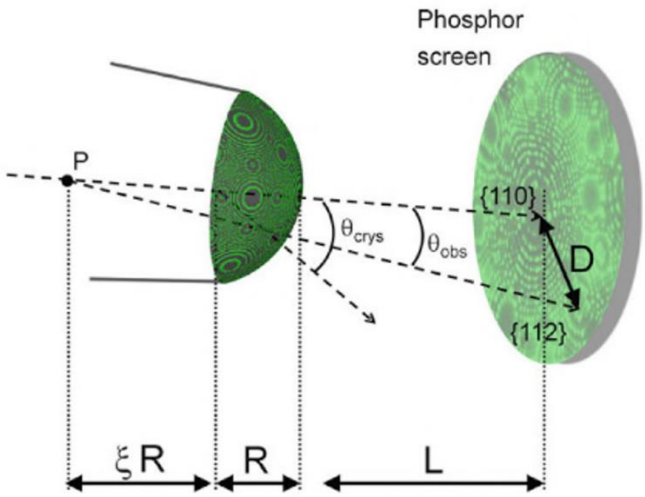

Figure 1.8 [12]: Image compression factor as defined by the point projection model: a new centre is defined at point P for the tip such that evaporated ions trajectories are radial, and create the expected crystallographic angle, θ_{crys}, on the final FIM image, as opposed to the observed angle, θ_{obs}.

The point projection model is widely utilized in the field of atom probe and field ion microscopy reconstruction however several studies reviewed different projections [107]–[109]. Other projections considered include the stereographic projection , and the $D = k\theta$ projection assuming a constant relation between the distance of a pole on the projected image from the centre of the image , D, and its angle from the tip axis , θ [110] .The ICF is estimated to be between 1 (radial projection) and 2 (stereographic projection).

1.2.1.1 3DFIM

By sufficiently increasing the voltage applied on the tip during imaging it is possible to field evaporate constituent surface atoms from the specimen. In the field evaporation process, a surface atom is field-ionized and removed from the surface of the sample. The full details of the process are not fully understood [111], but it is believed to occur as an ion escapes a field-reduced potential barrier by either tunnelling or thermal agitation. Transformation from an atomic to an ionic state is thought to occur following either the one-step ionization 'hump model' or the

progressive charge drain model [111]–[113]. For recent reviews on the debate over the field evaporation process, the reader is referred to [114]–[116].

Removal of surface atoms enable FIM to operate in a mode such that the surface of the specimen is continually evolving as the next layer of atoms is progressively uncovered. This process is described in Figure 1.9. Images a-d are time ordered. In the red circle in image a, outer terrace atoms of the upper (110) plane are imaged. Since these atomic positions develop a stronger field around them than central-plane atom, more imaging gas atoms are absorbed and ionized from these sites and thus they are preferentially imaged. As the voltage is increased and these atoms are evaporated, the inner atoms of the plane are imaged, and the ring seems to shrink, as seen in image b. The same process happens as the surface is evolved from image b to c, right before the plane is fully evaporated, and the plane beneath is exposed in image d.

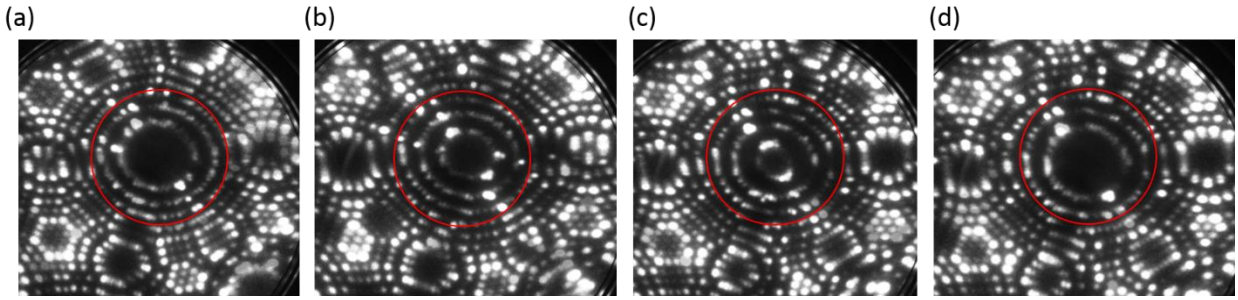

$$t_a < t_b < t_c < t_d$$

Figure 1.9: The evaporation process of a (110) plane as appears in FIM images. A-d are time ordered pictures of the (110) pole at different stages of the evaporation of one layer. The red circle marks the upper plane as it is evaporated.

1.2.1.1.1 3DFIM reconstruction and analysis

The output of a 3DFIM experiment is typically a large stack of time-ordered 2D images, tracking the surface as it is evolved by controlled field evaporation. This type of data poses several challenges in analysis. Firstly, the large number of images per experiment (typically thousands for the modest depths of several tens of crystallographic layers' evaporation) yields difficult and

laborious data analysis. Secondly, information can exist in the data that is not visually clear on a single 2D image, and requires a wider, 3D analysis. The next section explores data analysis techniques previously employed to different materials explored by FIM.

1.2.1.1.1.1 Atom-by-atom approach

The first 3DFIM experiments were demonstrated by David Seidman's research group in a series of papers investigating crystal defects in metals [56], including self-interstitials in BCC metals [117], post-irradiation defect distributions in Pt alloys [118],[81], [119], and radiation damage in tungsten [79],[80]. In these works, due to the lack in computational power and capacity for routine digitization of images, the data acquisition, analysis and reconstruction procedures were especially challenging. FIM images were recorded on film. The film later had to be developed, and was analysed using a motion analyser that helped switching between sequential images in a semi-automated way. Positions of atoms and vacancies were each identified by human eye, and their coordinates were recorded with an x-y cross hairs position reader and recorder. All coordinates were recorded in relative to a fiducial mark that had been set on the phosphor screen, to help avoid errors in coordinates measurements caused due to slippage of the film either in the recording or analysis stage. These studies resulted in important insights into atomic-sized defects characterisation that were impossible by any other experimental technique. In particular, they significantly contributed to the study of primary stages of irradiation damage. The very high spatial resolution imaging provided by FIM makes it the leading, possibly only, tool to extract information on primary stages of damage, both then and still today.

A characteristic case study is described in [119], where the vacancy structure of ion irradiated platinum-4 at.% gold alloy was studied as caused by a single 30keV W+ ion. Specifically, one

depleted zone found to contain 31 vacancies is reconstructed in 3D. This vacancy cluster was identified across 751 successive atomic planes, consisting of approximately 900 frames recorded over the total evaporation of the vacancy cluster. On each image, all atoms and vacant sites were identified manually as exemplified in Figure 1.10 . Next, a ball model was constructed and used for the assigning of the recorded coordinates to 'theoretical' atomic positions. In this procedure one atom (or vacancy) was chosen as the origin, and its neighbours were assigned theoretical coordinates according to their relative positions. Finally, this information was brought together by the ORTEP computer program to create the 3D reconstruction seen in Figure 1.10b. The ORTEP program was originally developed at the Oak Ridge National Laboratory to visualize large biological molecules [120]. The circles represent the positions of the detected vacancies only, with the connecting lines symbolizing vacancies that lie within nearest neighbour's distance from each other.

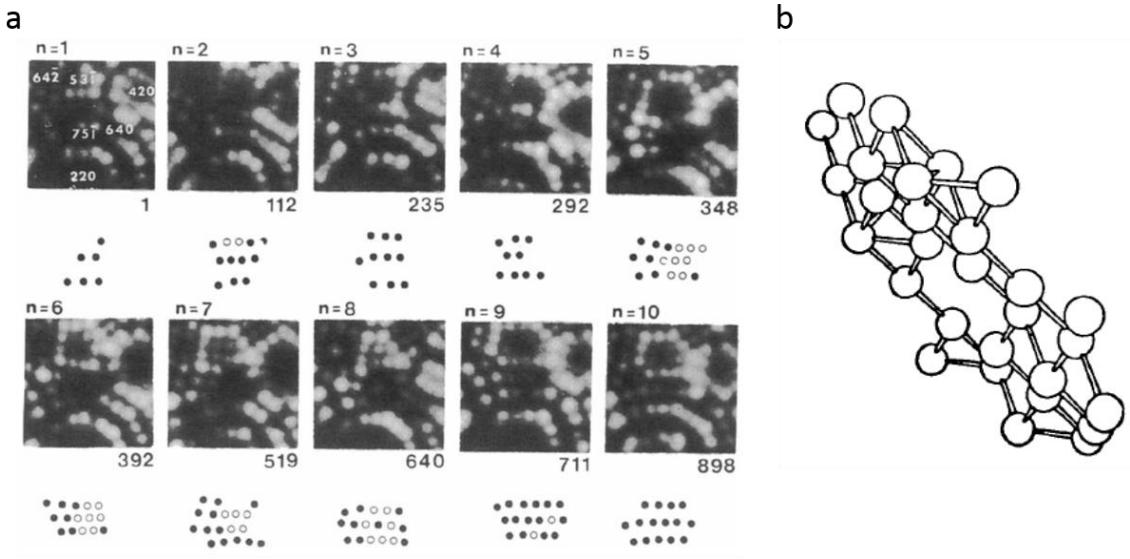

Figure 1.10: [119] (a) Selected images of planes 1-10 . The frame number is indicated by the number below each image. Atoms are identified on each image and are schematically plotted below. Full circles represent detected atoms; open circles represent missing atoms. (b) 3D reconstruction of manually recorded coordinates of a 32 vacancies cluster in Pt-4% Au alloy. Lines represent nearest neighbour's distance.

1.2.1.1.1.2 Stacking approach

3DFIM was further advanced by the development of a procedure for the digital-stacking of time-ordered FIM images [121]. In a series of experiments, 3DFIM data was recorded in movies describing the evolution of the specimen surface. By keeping the voltage variation linear, a near-constant evaporation rate was assumed, and the effective depth increment between two consecutive FIM images can be assumed constant. The sequence of images comprising the movie was then effectively stacked to create a tomographic reconstruction of the material. Slices of the 3D data in different directions can be easily explored this way.

This reconstruction scheme provided an intuitive, clear visualization of 3DFIM data. Due to contrast variations between different phases on FIM images and along the stack, this method was successfully applied to the imaging of a wide range of systems. Among first demonstrations were the imaging of chromium enriched regions in a FeCrCo alloy [122], followed by investigation of GP zones in steels [70], nitrides in Fe-Cr alloys [71] , carbides in steels [123] ,fine scale precipitates in CuFeNi [72]. It has enabled the detection of precipitates, grain boundaries and crystallographic planes [121]. Even dislocations that did not display clear contrast on the 2DFIM images were successfully identified using this method, whereby an appropriate directional slice was chosen which exposed contrast variations across the depth of the sample. Selected examples of 3D reconstructed microstructural features are presented in Figure 1.11.

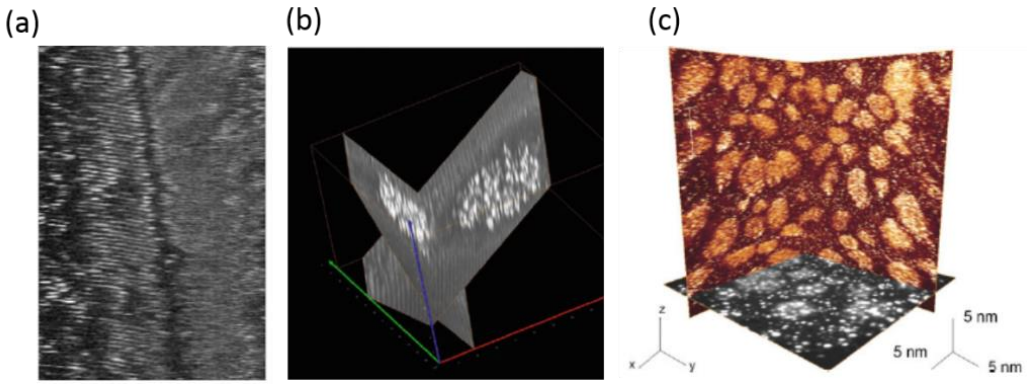

Figure 1.11 : Examples of 3DFIM reconstructed volumes by the image stacking procedure. (a) A grain boundary inside reconstructed Fe volume [121]. (b) 3DFIM reconstruction of a brightly imaged GP zone in model steel [70]. (c) Fine-scale precipitates in CuFeNi system [72].

The resulting reconstruction can be better calibrated using prominent crystallographic features in the specimen. An example of this procedure is shown in Figure 1.12 for the reconstructed FIM analysis of an iron sample. In Figure 1.12b a longitudinal slice is shown from the reconstructed structure in a. Atoms are imaged and are recognized to comprise two sets of high index crystallographic planes: (113) and (112). The measured angle between the two does not match the theoretical one, and can be corrected by adjusting the depth increment corresponding to two consecutive images. As a result of this calibration, individual atoms appear in an ellipsoid shape in c, attesting to the resolution limits of the technique, estimated in this work to be 3Å laterally, and 0.5Å in depth.

However, this simple approach will only yield correct results locally and will not necessarily reflect the true angular relation between planes detected on different parts of the tip. This is because remote planes can be influenced by the non-uniform curvature of the surface between them. The highly curved nature of the sample is also the reason why reconstructed planes may appear to be curved as seen in Figure 1.12d. A more accurate procedure for the stacking of the images

was therefore proposed to account for the highly curved shape at the apex of the specimen, and the non-linear magnification.

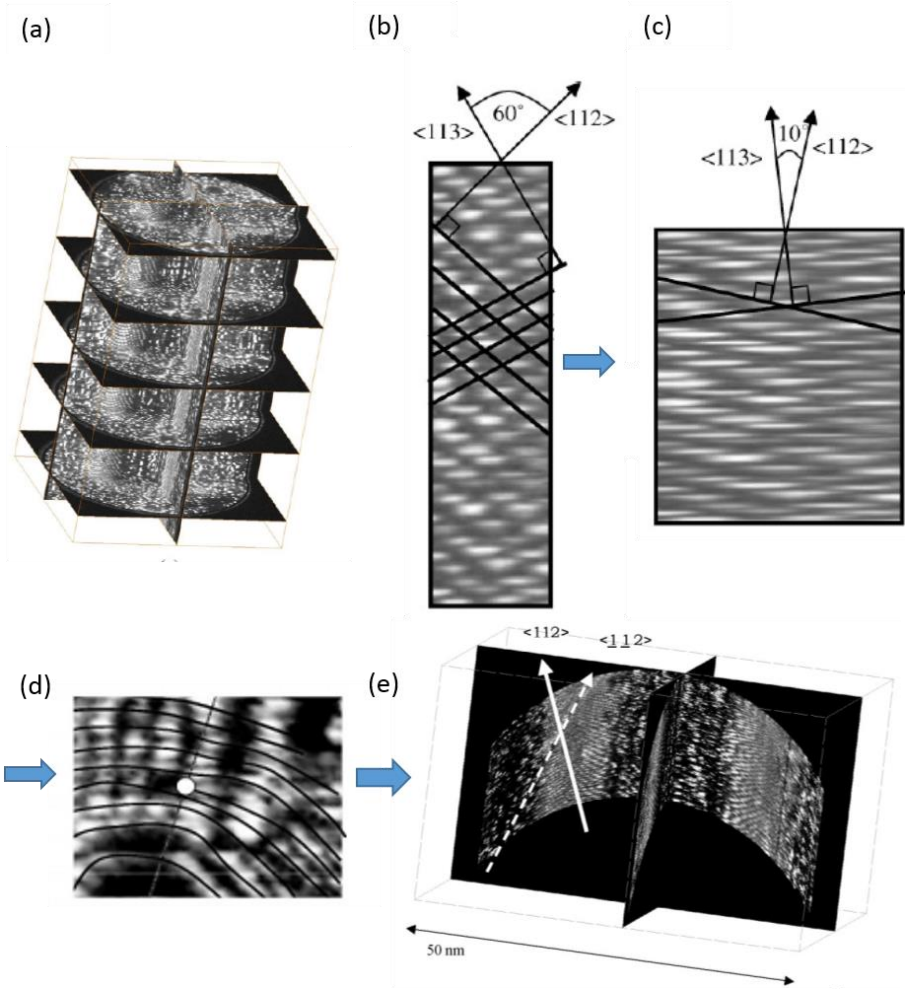

Figure 1.12: Adapted from [121]. (a) Stacking of FIM images of an iron sample. (b) Crystallographic planes are identified (c) The depth dimension of the stack is altered to generate the correct angle between the planes. Atoms appear as ellipsoids after the correction. (d) Planes appear to be curved as a result of the stacking procedure and the curved geometry of the tip. (e) Projection corrected stacking resulting in a bent stack, and un-bent planes.

Using the same projection laws utilized in traditional atom probe reconstruction, the lateral transformation for the FIM images can be calculated, and a mapping between light intensities recorded on the images and the original (x,y) sample coordinates can be drawn. Considering the projection law:

$$L = k\theta$$

where L is the distance to the centre of the image, k is the geometric compression factor estimated from the measured angle between indexed poles, and θ is the angle from the tip axis[110]. A connection between the coordinates of an arbitrary point on the surface $P(x, y, z)$ and its imaged position is then derived to be:

$$\theta = arcos(\frac{\sqrt{x^2 + y^2}}{R})$$

where R is the radius of the sample.

A second adjustment is then made for the more accurate calculation of the z depth coordinates. It is assumed here that the z coordinates are given by the sum of two contributions. The first is a constant depth increment that is applied with each FIM image, given for i^{th} image to be

$$\Delta z_e = \frac{Z_T}{N_T} \times i$$

z_T is the total depth of the analysed volume and N_T is the total number of images. The second contribution is a depth shift caused by the hemispherical shape of the tip, given by

$$\Delta z_R = R - \sqrt{R^2 - x^2 - y^2}$$

These corrections were shown to successfully reconstruct angles between planes across a large spatial range and eliminate un-desired artefacts. An example of a corrected volume can be seen in Figure 1.12e. It can be seen that the integration of the curvature of the sample into the calculation of reconstructed coordinates, effectively bends the stack of images, and eliminates un-desired artefacts of bent planes.

1.2.2 Atom probe tomography

Atom probe tomography (APT) is based on the concept of field evaporation. Much like FIM, a needle shaped specimen is introduced to an ultra-high vacuum chamber, and a DC voltage is applied [12], [124]. The two methods firstly differ in the absence of the imaging gas from the atom probe system. Instead, a pulsed voltage is applied, resulting in an electric field that is high enough to ionize surface atoms of the sample itself. Alternatively, in the case of brittle or less conductive materials the voltage pulse can be replaced by laser pulse [12]. The ionized atoms of the specimen are then projected onto a position-sensitive detector. Since actual atoms are removed from the surface of the tip, every pulse allows a deeper look inside the bulk of the tip.

The use of voltage/laser pulses for evaporation enables time-of-flight measurements of ions striking the detector. These are used to estimate mass-to-charge state ratios and enable chemical identification of the atoms. The conversion from time of flight to mass to charge ratios is done by considering the kinetic energy the ion is evaporated with. This is given by

$$qV = \frac{1}{2}mv^2,$$

as all the electic potential energy qV is converted into the ion's kinetic energy. By assuming the velocity of the atom stays constant through its journey to the detector, the mass to charge ratio is then simply given by:

$$qV = \frac{1}{2}mv^2, v = \frac{t}{d} \rightarrow \frac{m}{q} = 2V\left(\frac{t}{d}\right)^2$$

where q is the charge of the ion, m its mass, t is the time of flight, V the voltage, and d the distance of the tip from the detector.

From the positions recorded on the detector, using reverse-projection protocols, an accurate estimation of the 3D coordinates of the impacting ions is achieved, resulting in a 3D atom-by-atom reconstruction of the needle [125],[126]. The depth coordinate is determined by the atom evaporation order, and can be later rectified by calibrating the reconstructed volume to recognized crystallographic features within it [127], [128].

Data analysis in the atom probe is routinely performed by using the IVAS software, to handle data from the commercially available Local Electrode Atom Probe system [129]. The reconstruction is not straight forward however as many geometrical and physical factors need to be taken into account. The complex field-evaporation process, and non-uniform sample geometry result in aberrations to the final reconstruction and composition measurements. For example, local magnification effects may distort the final reconstruction in a system where different phases have different evaporation fields. This can cause a precipitate to be either preferentially evaporated compared to the matrix, or retained on the surface [130]. Furthermore, particularly when molecular ions are evaporated (as opposed to single ions), multiple ions can reach the detector at the same instant, resulting in un-resolved events, therefore biasing composition measurements [131].

Further limitation of atom probe data results from detection efficiency restrictions, originating from the instrument, detector and micro-channel plates design. Depending on the specific instrument design, a random loss of 30-70% of the evaporated atoms is expected [82]. Detection efficiency limitations of atom probe will be further discussed in chapter 3 as those limit the ability to identify atomic-scale defects in atom probe data.

1.3 APT/FIM radiation damage studies in tungsten

This section aims to describe some of the noticeable FIM / APT studies of radiation damage in tungsten. The technique's contribution to this field will be demonstrated across all types of radiation damage mechanisms, and placed in the context of studies performed with other techniques.

Figure 1.13 shows the detection range and spatial resolution of APT in comparison to other commonly used microscopy techniques in materials science. As can be seen, atom probe (marked by APM- atom probe microscopy) provides depth profiling with a high detection range. Also apparent from the figure is the potential of combining TEM and APM analysis for the study of fine structured materials.

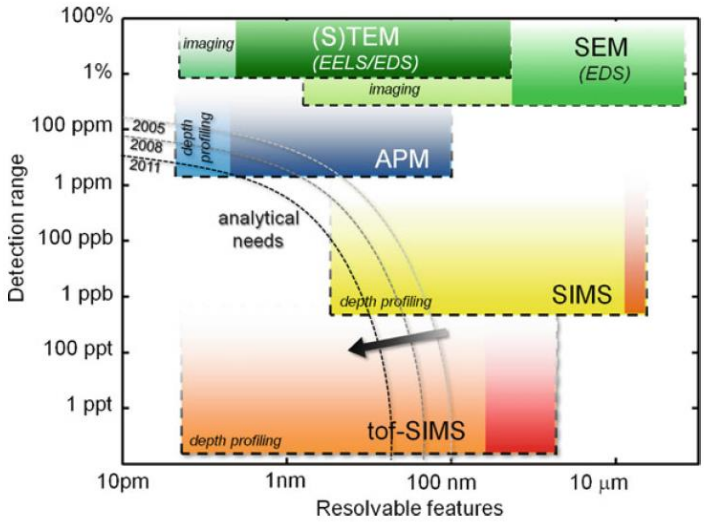

Figure 1.13 [12]: Comparison of detection range and spatial resolutions between common characterisation techniques.

1.3.1 FIM/APT of displacement damage

In the field of atomistic study of radiation damage, the most fundamental phenomena to study are the primary states of damage, resulting from a single projectile ion hit. The primary state of damage is a term used to describe the spatial distribution of point defects that are present in the lattice once all the kinetic energy of a hitting ion has been transferred into the PKA and dissipated. FIM's high resolution makes it the leading, if not only tool to extract such information in 3D. [78]–[80] all employ 3DFIM to characterise the point-defects profile in tungsten under different temperature and energy conditions, resulting in a 3D map of vacancies distribution such as seen in Figure 1.14. Information such as the absolute number of vacancies within each depleted zone (DZ), the average diameter of the DZ and orientation with respect to the ion beam, the average vacancy concentration, nearest neighbour vacancies fraction estimate, average depth from the irradiated surface, and number and concentration of vacancies found near the surface of the specimen were collected in these cases and attest to the powerful detailed characterisation capabilities of the technique. This work also proved that dislocation loops commonly observed in TEM studies of tungsten are only a fraction of the vacancy population in the material.

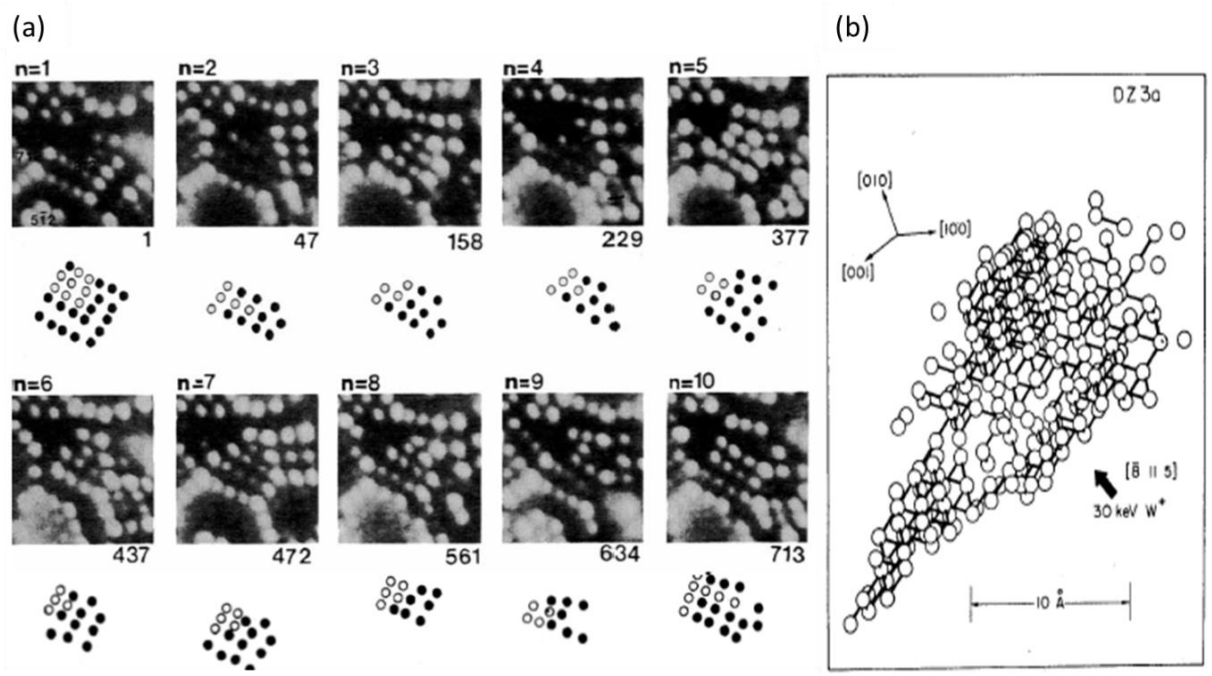

Figure 1.14 [79]: Example of a depleted zone in tungsten created by a 30 keV W+ projectile ion. (a) Marking atoms coordinates on a series of FIM images during the evaporation of the depleted layers. The black dots indicate actual atoms; the blank circles represent vacancies. (b) 3D representation of the depleted zone. The rods represent the nearest neighbours distance.

Another FIM work was concerned with the influence of the impacting ion mass and energy on the resulting damage profile [78]. Different ions were implanted at 30keV, as well as Kr ions implanted at increasing energy levels from 15 to 70keV. In a detailed characterisation of DZs, results were compared between the different energies and different implanted ions. it was found that the average diameter of DZs increased as the mass of the implanted ion decreased, while the number of vacancies contained within each DZ was found to be independent of the ion's mass. In accordance, the fraction of single vacancies within the DZs increased as the ion's mass decreased. These conclusions are schematically demonstrated in Figure 1.15. It was also found that as the energy of the colliding ion increased, the resulting number of vacancies in each DZ increased linearly. The average diameter of DZs increased as well with increasing ion energy.

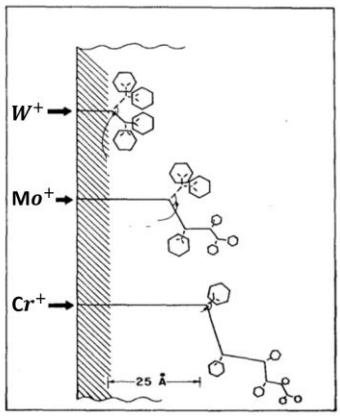

Figure 1.15 [78]: Effect of mass of implanted ion on the resulting vacancy structure of depleted zones. As the mass increases the diameter of the DZ decreases, and less single vacancies are observed, as can be seen for the heavy W ion in comparison to the lighter Cr ion.

The effects of irradiation dose were studied in [132] for tungsten implanted with 50keV W ions at room temperature between 0.01,0.1 and 5 dpa. In this study no interstitial clusters were reported, as those might have escaped to the surface, yielding vacancy concentrations of 80% of the original number of vacancies according to the authors estimate. Overlaps between damage cascades originating from different ions were reported at an initial dose of 0.1 but not in the 0.01 case. Voids as small as 10Å were reported in all three doses, as well as vacancy clusters which increased both in size and total volume as the dose was raised, from 10^3a^3 to $1.5x10^4a^3$, where a is the lattice parameter. The total number of displacements as a result of one colliding ion was estimated at 300. For the two larger doses, vacancy clusters were reported to start at the surface of the sample and extend to 90 and 130Å into the bulk's depth. This result is somewhat inconsistent with traditional SRIM analysis, according to which the expected maximal penetration depth of a 50keV tungsten ion into a tungsten matrix is at 68Å, with the total damage profile extending to approximately twice the depth, however the curved shape of the FIM samples is expected to influence the damage profile as discussed in depth in chapter 9.

Another FIM work followed the changes in damage distribution in fission experimental reactor-irradiated tungsten through its annealing post irradiation up to 700℃ [55]. Samples here were irradiated as wires, and electropolished post-irradiation. This is not common practice when performing FIM of ion implanted samples because the penetration depth of ions into the sample is smaller than neutrons, and later electropolishing can remove any implanted layers. It was found that at temperatures higher than 400℃, vacancy migration takes place, to change the form of damage from single vacancies to di-vacancies and small clusters, while maintaining a constant overall concentration of vacancies.

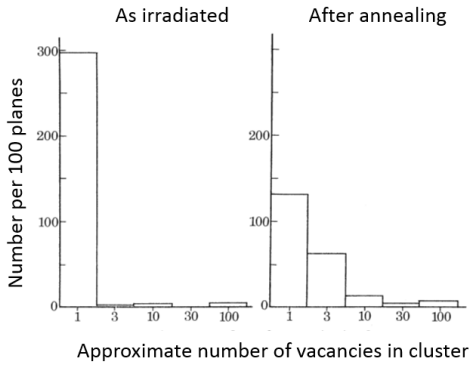

Figure 1.16: [55]: FIM measured histograms of vacancies number in cluster before and after annealing. After annealing at 400℃ for 3 hours, larger clusters are created, confirming vacancy migration

Several TEM observations were made of defect distributions after irradiation, studying both neutron irradiation and ion implantations [57], [133]–[136]. Single vacancies and interstitials remain below the resolution limit of conventional TEM techniques and therefore the defects reported in these studies are mostly voids and dislocations. In a recent series of papers, a thorough study of the statistics of dislocations following self-ion implantations in tungsten was done using diffraction contrast imaging. In a temperature range of 300-750°C, and doses equivalent to 0.4-3.6dpa, the types of defects identified were dislocation loops with a diameter

of 6-20nm [137]. It was found that larger loops were formed as the irradiation temperature increased, correlated with a lower loop density. Orientation of the implantation was also found to influence defects as implantation along low index directions resulted in a reduced number of observable defects. Characteristic results of the TEM study are shown in Figure 1.17. In a dislocations are shown on TEM micrographs, exhibiting a larger density at the higher 1.2 dpa dose in comparison to 0.4dpa. A similar statistical analysis to the vacancies distributions in FIM was done on the loop sizes observed in TEM. Characteristic results are seen in Figure 1.17b as a histogram of loop sizes at 750°C, 1.2dpa. However, while the FIM analysis was done on defects of the size of single atoms, the TEM analysis was done on loops with a minimal size of 1-2nm. Here too, similarly to the FIM results on vacancy clusters, it was found that at a constant dose, an increase in temperature resulted in larger loop sizes.

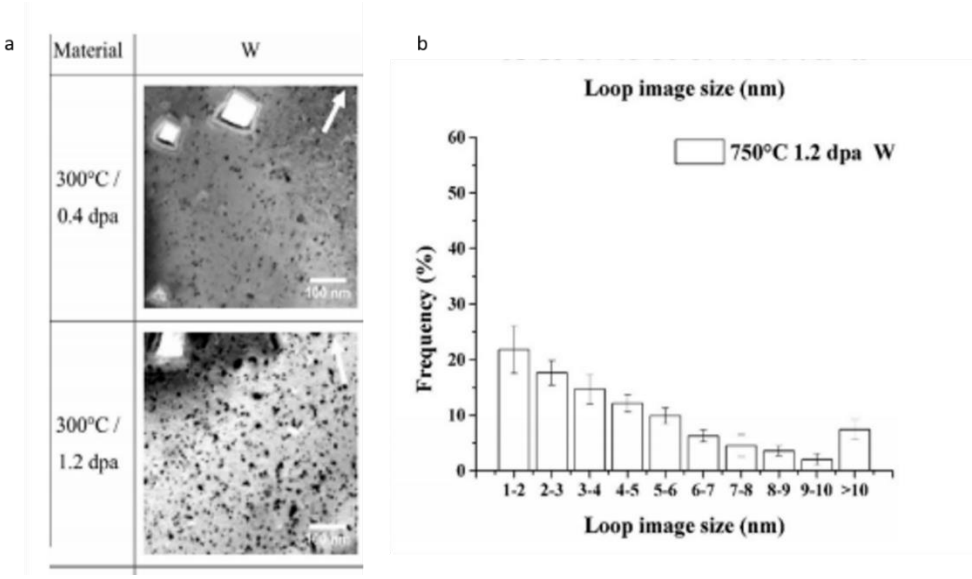

Figure 1.17[138]: (a) TEM micrographs of tungsten after tungsten ion implantations. Density of dislocation loops is higher as the dose is increased from 0.4 to 1.2 dpa in a steady 300 C° temperature. (b) Histogram of sizes of dislocation loops observed at 750 C°, 1.2 dpa.

A second TEM study was focused on low energy, 150keV self-ion implantation of tungsten [136]. Implantations were done in-situ, and defect formation was tracked. The influence of irradiation temperature, dose, alloying elements and grain orientation on the resulting damage were all studied. Vacancy loops were identified at a low dose of 0.01 dpa, corresponding to primary stages of damage. The overall concentration of point defects retained in loops was found to decrease by a factor of 17 as temperature was raised from -240℃ to 800℃. This estimation was done by evaluation of the number of loops and their diameter, as a measure to evaluate vacancies number. At higher doses, damage cascades were found to interact and form complex networks. The displacement of loops was captured on TEM movies, revealing interactions with increasing dose. Loop densities were found to be larger in WRe5 and WTa5 alloys in comparison to bulk tungsten.

TEM/FIM: From comparing the nature of FIM and TEM studies it is apparent that the detection of crystal defects by traditional TEM relies on the gathering of vacancies to form bigger structures with high strain regions around them such as dislocation loops or large clusters. In case small point defects do not collapse into such strained structures, they will not be visible in conventional TEM, but will easily detectable in 3D by FIM. Recent TEM work in [8] was able to produce the atomic coordinates of tungsten atoms from the tip of a tungsten needle, using advanced tomography reconstruction from a tilt series of an aberration corrected STEM. This work is a first proof of concept that higher resolution information than the one presented in the TEM studies above could be obtained by TEM. The detection of a vacancy however, could not be determined in this study with great certainty, as another tilt series would have to be performed to distinguish between the suspect vacant site and substitutional light atoms.

With a resolution limit of ~1.5nm, conventional diffraction-contrast TEM enables the study of larger volumes and provides better statistics than FIM on the densities of dislocation loops. Further, most of the observed loops in TEM are glissile and expected to be easily lost to the free needle surface, resulting in a much lower concentration observed in FIM samples. Combined, the two techniques are particularly powerful for successfully characterising a wide range of displacement crystal defects.

1.3.1.1 Self-interstitials characterisation

To capture self-interstitials, several FIM studies employed 20keV tungsten ion implantation at very low temperatures (-265℃-(-255℃)) [42], [56]. In-situ implantations of tungsten were employed where samples remained in vacuum after implantation and imaged with FIM immediately after. This method provided a clean sample surface by field evaporation immediately before implantation, greatly reducing contaminant issues. It also enabled implantation at very low temperatures, and observation of SIAs migration during the heating stage of the FIM chamber. Initial analysis at -258℃ showed a linear relation between the implanted dose and SIAs concentration (see Figure 1.18a), indicating that they are not mobile at -258℃, as well as that no field induced mobility is biasing the experiment. Isochronal heating was then performed while FIM images were continuously taken across -267℃-(-153℃). As interstitials became mobile and arrived to the surface they were easily detectable. SIAs were found to be immobile below -255℃. At -245℃, they were found to perform long range migration as distances of 200 Å were measured. The recovery FIM spectrum of the number of defects appearing on the surface as a function of temperature can be seen in Figure 1.18c. Further in this study impurities were found to delay recovery processes, by occupying SIAs in impurity-SIAs complexes.

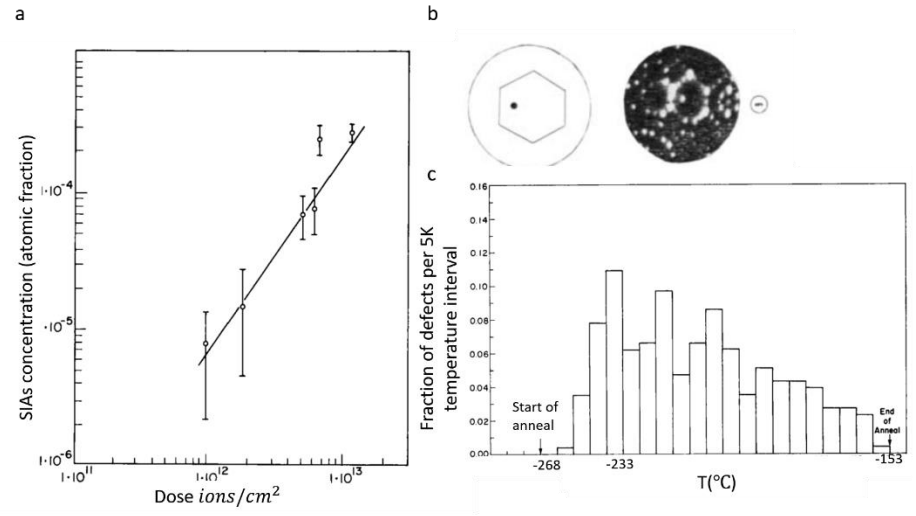

Figure 1.18[42]: (a) Atomic fraction of SIAs as a function of dose, for implantation of tungsten 20keV tungsten ions, at -258℃. The linear relation indicates no mobility of SIAs at this temperature. (b) Contrast of SIAs in FIM image. (c) SIAs fraction as a function of temperature during heating.

1.3.2 FIM/APT of tungsten alloys

Radiation induced clustering had been recognized as a mechanism for increased hardness in irradiated W-Re alloys [6],[60], [139]. In a TEM study W-3Os, W-5Re-3Os, and W-5Re samples were neutron irradiated for a year in the fast test reactor to levels of 0.4-1.54 dpa, at irradiation temperatures of 400-750℃ [6]. Vickers hardness tests showed an increase in hardness after irradiation with a positive linear correlation between the increase in hardness and concentration of rhenium in the alloy, for dpa levels above 0.4 and temperatures above 740℃. TEM microstructure observations using thin foil specimens showed that in the W-Re alloy case the hardening mechanism was irradiation induced precipitations. It was concluded that the effect of precipitation on irradiation hardening increases proportionally to rhenium content in W-Re alloys. In the case of the ternary W-Re-Os, it was found that rhenium suppresses irradiation hardening in the presence of osmium when irradiated to less than 0.17 dpa at 400℃ or below, and when the mass percentage of osmium is less than 5. However, when irradiation conditions

are above 0.4 dpa and 740℃, osmium dominates the irradiation hardening, independent of rhenium presence. This TEM study shed light on irradiation hardening in tungsten alloys, identifying clustering behaviour, however the exact compositions of precipitates could not be identified in this work due their small size and TEM limitations.

The complementary capabilities of APT and FIM have proven to be highly efficient in the study of radiation-induced precipitation in tungsten alloys. Detailed composition and structural study of such precipitates was performed using a combination of a FIM and a 1D atom probe device [140] (the 1D atom probe is an earlier version of the technique employing time of flight spectroscopy from a small selected region of a previously FIM imaged sample). FIM enables the easy detection of precipitates with sufficient difference in evaporation field from the bulk, particularly useful for very small precipitates (~1-3nm). Precipitates sizes, as well as density and spatial distribution inside the bulk can be measured. Also FIM can be used to determine the relative orientation, or coherence level between the precipitate and the matrix. Atom probe enables the exact chemical characterisation of the precipitates, as well as reveals details of the nucleation mechanism, by detecting correlations between precipitation sites and defects/impurities.

In [141], [142] ,W-25at.%Re and W-10at.%Re alloys were implanted with tungsten ions to generate approximately 8.6 dpa damage level and then tested utilizing a combined atom probe FIM instrument. First, FIM images were taken (Figure 1.19). Once a precipitate was identified on the FIM image, the specimen was rotated to be aligned with the 1D atom probe detector. The chamber was then evacuated to remove the imaging gas for the purpose of an atom probe measurement. Time-of-flights measurements were performed, and the rhenium content of the precipitates was found to be 50% and 75% for the WRe10 and WRe25 alloys respectively. For the

10% alloy, FIM images revealed the precipitates to be disc-shaped, having a thickness of between 1-2 atomic planes. The density of the precipitates was calculated from the FIM images to be ~10^{16} cm^{-3}, and it was found that coherent, semi-coherent and incoherent precipitates were all formed. Since no voids were detected this work supported the notion that the presence of rhenium suppresses void formation in irradiated tungsten.

Figure 1.19 [142]: A precipitate in a W-10%(at)Re alloy as it appears on a FIM image before evaporation by atom probe.

In a more recent work, the new generation 3D atom probe was employed to further investigate clustering behaviour in WRe and WReOs alloys in lower compositions of rhenium (1,2,5%) [60]. This was one of the first investigation of clustering after ion implantations (other similar studies can be found in [139], [143]). Precipitation of rhenium rich phases was investigated and was found to be similar to previous neutron irradiation results. Statistical cluster analysis incorporated in the APT reconstruction software was employed to accurately and consistently quantify cluster behaviour [144],[145]. This automated procedure enables characterisation of cluster size, density, and chemical compositions. Clusters as small as 1nm were detected. It was found that osmium significantly suppresses rhenium clustering in samples implanted to 33dpa. Comparison of cluster analysis between implantations performed at 300℃ and at 500℃, below

and above the stage 3 vacancy recovery temperature revealed larger, fewer rhenium clusters in the 500℃ case as can be seen in Figure 1.20.

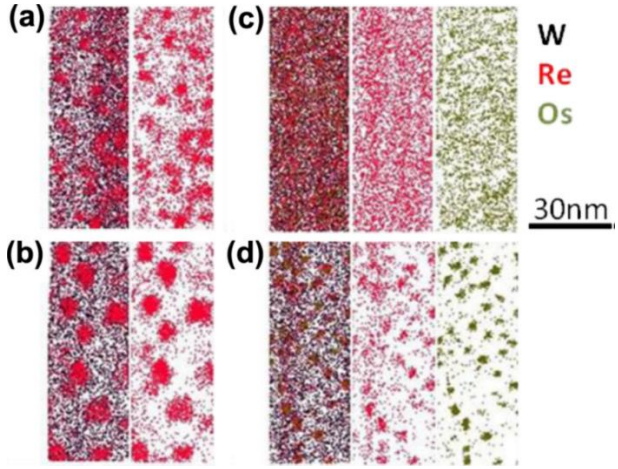

Figure 1.20 [60]: Atom probe distribution maps of tungsten rhenium and osmium post tungsten ion implantations at 33dpa (4nm think sections). (a) W-2Re implanted at 300℃ (b) W-2Re, 500℃ (c) W-1Re-1Os, 300℃ (d) W-1Re-1Os, 500℃.

1.3.3 FIM/APT of helium damage

FIM and APT were also employed to study helium damage in tungsten. Helium effects on tungsten can be divided into two regimes. In the first case the tungsten lattice contains crystal defects either due to displacement damage originating from previous neutron/heavy ion bombardment, or as a result of the helium ions themselves, if implanted above the threshold energy for vacancy formation (42eV is the minimum energy required for the creation of a stable Frenkel pair [146]. This value was found to depend on the crystallographic direction in which the displacement occurs, and was measured to be 42 eV for the [001] direction, and 68-70 eV for the [011] direction in tungsten [35]). In the second regime, no crystal defects are present in the tungsten matrix, and the retention of helium in the lattice is therefore of a different nature.

While several TEM /SEM/XPS experiments have shown the formation of helium bubbles [147],[148],[149], 'fuzz' (porous surface layer) [59],[150],[151], suggesting retention of helium in voids and dislocations [147], smaller retention sites were beyond the resolution limit to observe. In [5] nano-indentation tests showed increased hardness in tungsten implanted with helium. TEM micrographs showed no damage to explain the hardness change.

Positron annihilation spectroscopy (PAS) and nuclear reaction analysis (NRA) were previously employed to study interaction of helium with small defects, as PAS is sensitive to the formation of small clusters of vacancies and even single vacancies, and NRA to the amount of retained helium in the sample and its distribution. In NRA experiments in [152], different helium desorption behaviours were found for samples implanted with helium at energies of 0.3keV and 60keV (below and above the threshold required for defect creation in tungsten). The desorption in samples implanted to higher energies started at a higher temperature of 1277℃ in comparison to 127℃ at the low energy implantation case. This difference was attributed to the dissociation of helium-vacancy complexes in the high energy case. The 75% and 60% maximal desorption fractions for high and low energy implantation respectively indicated a second type of helium trapping site. In a complementary PAS study of the same implantation conditions in [153] it was suggested that the migration and release behaviour of helium during annealing of the samples is controlled by the concentration of defects and the ratio between helium atoms to trapping vacancies (high helium/vacancy ratio for low energy implantation). While the positron annihilation technique is sensitive to the existence of vacancies, its spatial resolution is limited in finding their exact location. Further, the assessment of the number of single vacancies, di-

vacancies and larger structures depends on fitting the overall positron annihilation spectrum to contributions from all these configurations, which is of subjective nature.

FIM/APT combination of atomic resolution and mass resolution enables the estimation of the vacancies structure in the material as well as the retained helium levels. In [146], an in-situ helium implantation APT/FIM study was able to demonstrate the retention of helium atoms in a defect free tungsten matrix, as isolated, immobile interstitials. This was the first demonstration of helium retention in a defect-free lattice (the ability to confirm a defect free matrix in FIM is straightforward) as the implantation energy was 300eV, below the threshold for defect creation[1]. He^4 ions were implanted in the sample. The 1D atom probe was used to determine the helium concentration profile from a region restricted to the centre of the (011) pole by an aperture. The depth coordinate was estimated by detecting the evaporation of (011) planes of tungsten, therefore depth resolution was limited by the interplanar spacing, equal to approximately 2 Å. The helium profile measured for the range of -213℃-(-183)℃ is seen in Figure 1.21, was found to be the same within this temperature range. This fact confirmed the helium interstitial to be immobile within these temperatures as the helium profile only depended on the energy of the implantation. Complementary to the helium concentration measurements performed by the 1D APT, FIM mode was then utilized to study the defects distribution in the sample, and found it to be un-correlated with the helium distribution, further supporting the notion that helium is not trapped in vacancies but is retained as interstitials.

[1] While the implantation energy, 300eV, is higher than the minimum Frenkel-pair creation energy in tungsten, reported previously to be 42 eV, some of the implantation energy will be lost to nuclear and electronic interactions, leaving less than the required energy for the collision to create a stable Frenkel-pair. Thus, a 300eV He atom will transfer a maximum energy of 25 eV to a tungsten atom in a head on elastic collision [146].

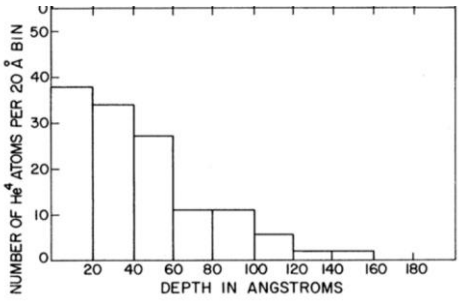

Figure 1.21[146]: Helium depth profile as measured by 1D atom probe after 300 eV helium implantation at -213℃. The profile was found to not change as temperature increased to -183℃, indicating helium retention is not related to crystal defects.

In conclusion: FIM and APT were proven to be highly valuable tools in the study of all types of radiation damage in tungsten. In displacement damage studies traditionally performed with TEM, FIM's superior resolution power allows the spatial characterisation and quantification of single vacancies and interstitials, un-resolved by conventional TEM. On the other hand, the analysed volume with FIM is much smaller, and the extended free surface provides easy escape for dislocations, making TEM and FIM highly complementary techniques. The obvious advantages of APT in comparison to TEM are the straight forward chemical analysis and 3D reconstruction, proven highly useful for the study of clustering behaviour in tungsten alloys post irradiation. While certain TEM systems might be comparable in spatial resolution power to APT, the information in TEM is obtained from the entire thickness of the sample, therefore restricting its depth resolution.

Positron annihilation spectroscopy and FIM can also act as highly complementary techniques, both sensitive to single vacancies, proven to significantly influence helium retention in irradiated tungsten. In fact, since positron annihilation relies on fitting the resultant spectrum to the different contributions from single vacancies, di-vacancies etc., the direct quantification of those in FIM can actually help inform PAS studies. While FIM is mostly utilized for surface studies up to

10s of nm's depth, PAS is very limited in analysing volumes close to the surface, however, with changing positron energies, can characterise samples up to several hundred microns in depth.

Finally, it is important to note that in spite APT's mass and spatial resolution, the quantitative characterisation of helium distribution is still a challenge in modern APT devices. The use of laser pulsing in brittle samples will cause helium atoms to move around on the surface of the sample before evaporation, resulting in false spatial characterisation, making it only possible to characterise in voltage mode pulsing. Further issues arise in cases where helium forms bubbles in the sample. The evaporation behaviour of helium in these cases is un-determined and can be a cause for concern when measuring helium content in APT.

2 Experimental methods

2.1 Materials

Two forms of tungsten were used for this work: bulk tungsten and tungsten wire. For the bulk tungsten samples ultra-high purity tungsten was used, produced by Metals Crystals and Oxides (UK) at a declared purity level of 99.99%. The tungsten wire was produced by GoodFellow (GF) at a purity level of >99.95%. Typical mass spectra for both types of materials are shown in Figure 2.1 and Figure 2.2, measured by atom probe tomography in laser mode pulsing, as well as their resulting background corrected[1] bulk composition measurements in Table 2-1-Table 2-2.

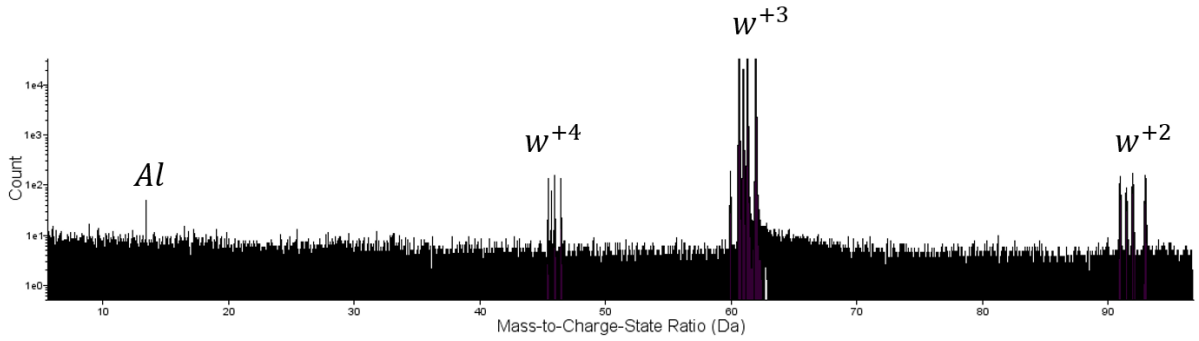

Figure 2.1: Atom probe mass spectrum of the GF tungsten wire used for electropolished needles.

Ion Type	APT concentration (%)
W	99.994%
Al	0.006%

Table 2-1: Background corrected bulk composition of the as received GF tungsten wire.

[1] Background correction is an automated estimation of the background level performed by the IVAS software. Here the local range assisted background model was used, where contributions from both DC evaporated ions, and from the thermal tail of each peak are subtracted from the mass spectrum for bulk composition measurements.

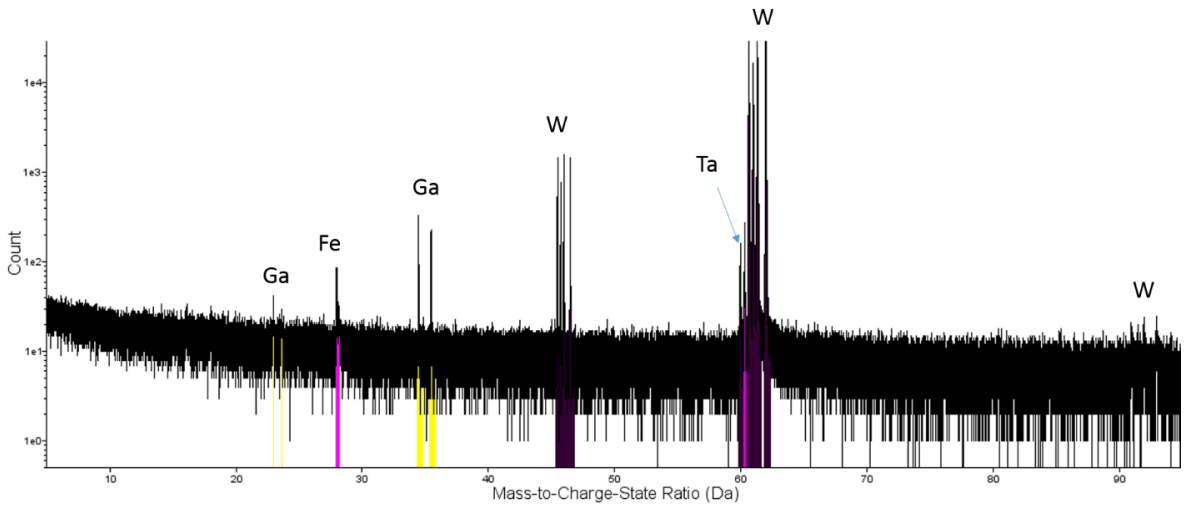

Figure 2.2: Atom probe mass spectrum of the bulk tungsten used in this thesis. Gallium peaks are the result of FIB sample preparation. Tantalum is present after tantalum implantation. Iron is the only impurity found in the original bulk material.

Ion Type	APT concentration (%)
W	99.943%
Fe	0.005%

Table 2-2: Background corrected bulk composition of the as received bulk tungsten. Concentration % is given in relation to all ranged peaks excluding gallium and tantalum.

2.2 Heat treatment

Some of the samples studied in this thesis had been heat treated in order to anneal any pre-existing defects prior to ion implantations. Wire samples that are specified to be annealed have been heat treated in vacuum, for 20 hours at 1400°C. Annealing of bulk samples was performed at 1800°C for 2 hours.

2.3 APT and FIM sample preparation techniques

The requirements for both APT and FIM samples are identical. Both require a needle shape with an apex of the order of magnitude of tens of nanometers in radius. This unique shape can be achieved in two ways: needles can be made out of wires through an electropolishing procedure,

or can be lifted out and shaped out of bulk (or wire) in the focused ion beam (FIB) instrument. Both techniques have been utilized in the experiments described in this thesis, and will be described in the following section. Each technique carries its own advantages and dis-advantages, some which are specific to radiation damage studies and will be briefly discussed.

2.3.1 Electropolishing

Electropolishing is used in this research to produce most of the examined samples out of tungsten wires and is usually done in a standard procedure [124] illustrated in Figure 2.3. In this work, the electrolyte utilized was 5 %wt NaOH solution, with the application of 5-8 V AC voltage between the specimen and electrolyte. Galden® was chosen as the inert layer, on top of which a 1 cm layer of the electrolyte was placed. This configuration allowed the formation of a bottleneck in the wire sample as voltage was applied, since only the part of the wire that was in contact with the solution was being polished. To create the preferred shank angle of the needle the sample was continuously moved up and down around the bottleneck formation point until finally broke into two very sharp needles. The samples were then cleaned with acetone followed by distilled water.

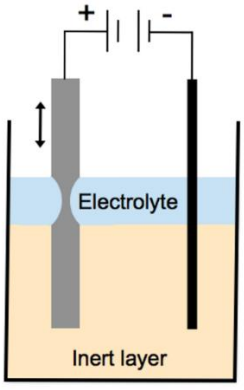

Figure 2.3: Electropolishing setup for the preparation of APT/FIM samples[12]. 5%wt NaOH water solution was used as the electrolyte and 5-8 AC voltage.

2.3.2 Focused ion beam (FIB) lift out

Bulk tungsten samples have been shaped into FIM/APT needles using the lift out procedure [154]. The FIB used was a Zeiss 'Auriga' dual-beam SEM-FIB machine with a gallium source. The steps in the lift out process are illustrated in Figure 2.4 : First, a region of interest at a typical size of $2x20\mu m$ is selected and coated with a platinum layer to protect from gallium beam damage during the milling process. Once a platinum layer is deposited the bulk material around it can be milled to create the cantilever shape seen in Figure 2.4b. Next, using a micromanipulator, the cantilever is lifted out of the bulk, and placed on the flat top of a pyramid shaped atom probe doped-silicon post, seen in c. It is then welded onto the post by platinum deposition, and the small volume directly on top of the post can be sliced free from the remaining cantilever. An atom probe coupon substrate, holding 36 such posts is seen in Figure 2.5a. A typical sized cantilever is long enough to produce 5-6 APT samples.

Finally, the sample is sharpened using annular FIB milling to create the desired final apex of an atom probe tip as described in Figure 2.4e-f. The starting current for the sharpening procedure is usually 700pA, at a voltage of 30kV, and is gradually lowered as the tip shape gets thinner. The final shape is achieved after a low kV (10-5kV) polishing to remove most of the FIB-damaged layer of the sample. This limits the amount of gallium incorporated in the final specimen, as well as removing any remaining platinum. This step is done in 'imaging' mode as opposed to active milling mode to gain better control over the very gentle tip geometry.

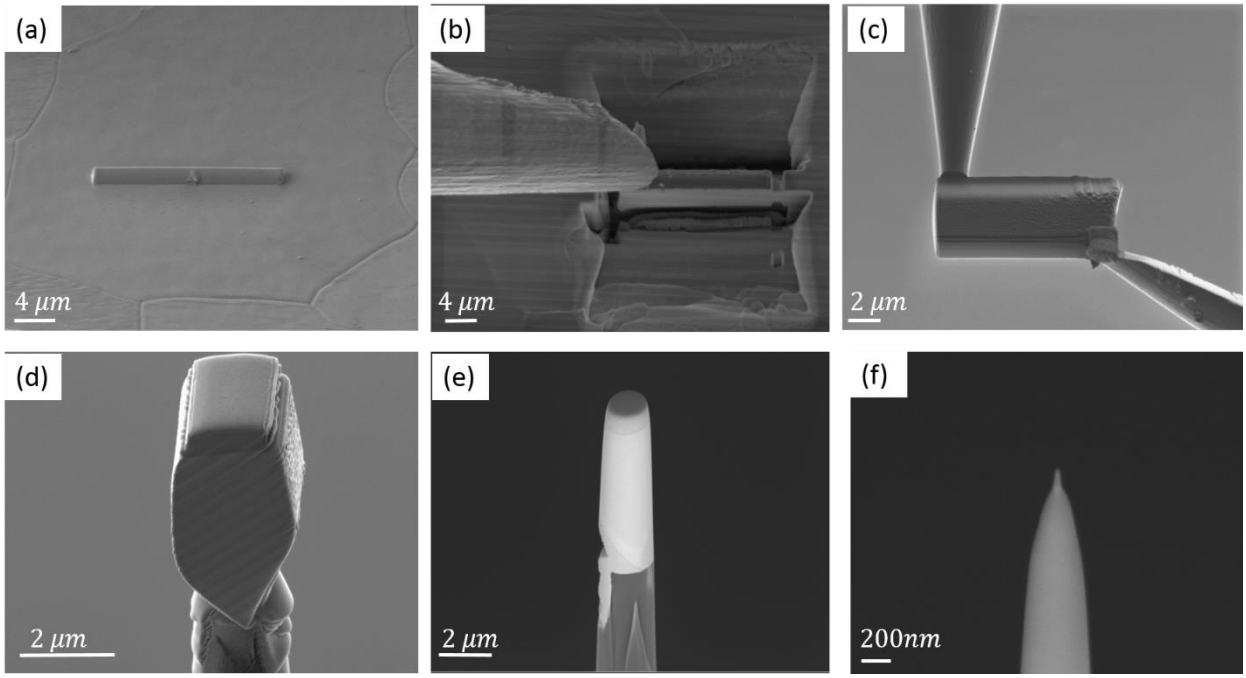

Figure 2.4: FIB lift out stages. (a) Deposition of protective layer on region of interest. (b) Lifting out a cantilever. (c-d) Mounting cantilever onto APT post. (e-f) Sharpening with annular milling.

As seen in Figure 2.5a, the APT posts are pyramid shaped, and provide a tapered post for the lift out, such that it is not deposited straight onto a flat surface. This is done in order to increase the field generated at the top of the sample, reversely proportional to the radius and field factor, k_f.

The field factor is dependent on the geometry of the specimen as well as the instrumental design of the atom probe itself. For example, the presence of a local electrode in the LEAP APT machines used in this work will lower k_f, therefore increase the field around the tip. On the other hand, the presence of a flat surface close to the tip will enhance the field factor and lower the resulting field.

The 3DAP machine used for FIM experiments was not designed to accept specimens created on microtip array coupons. Therefore, in order to characterise bulk samples in the 3DAP, electropolished tungsten samples were used as 'mounts' for FIB liftouts. The needles are

prepared by a first-stage electropolishing procedure and are then inserted to the FIB where the apex of the needle is removed to create a 2 micron wide flat surface onto which the lift out is to be mounted. An example of a tungsten needle with a mounted lift out can be seen in Figure 2.5b. In the small window on the right its FIBed flat surface end is shown.

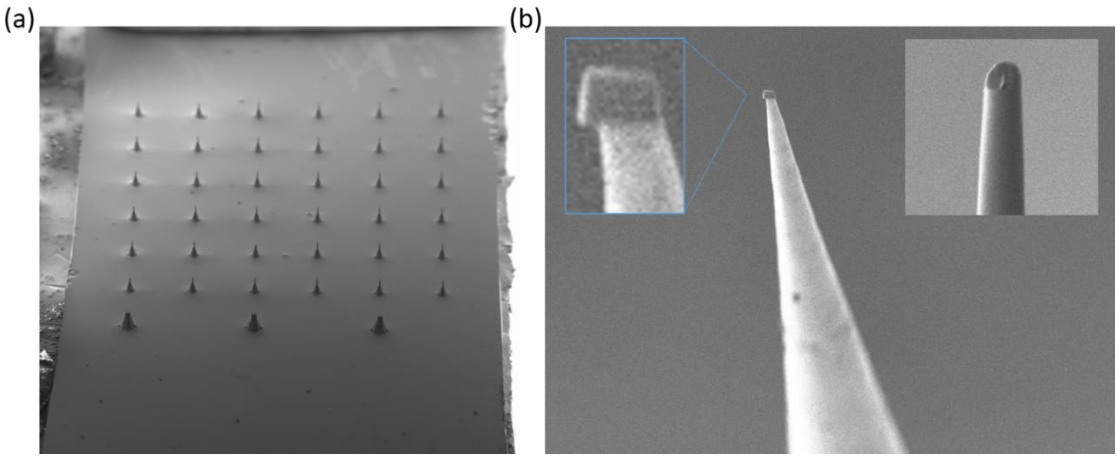

Figure 2.5: (a) APT silicon posts for FIB liftouts. (b) Electropolished tungsten needle with a lift out on top. On the right side window, the needle is seen before the lift out was attached, as its tip removed in FIB to create a flat surface.

2.3.3 Electropolishing vs FIB

Electropolishing is often considered as the faster, easier way to produce samples in comparison to FIB lift outs. With a quick first stage procedure sharp samples can be produced within minutes. However, the electropolishing method can become limiting. Unlike FIB lift-outs, it requires an initial shape of a wired sample or matchsticks, and cannot produce samples out of any randomly shaped bulk. Moreover, it is important to note that it is not possible to perform electropolishing on a wire after it has been implanted, since the technique is not precise enough so as not to remove the entire damage layer in the sample. Therefore, ion implantations can be performed on the samples only after they had already been shaped into needles. This raises some questions

regarding the effect of sample geometry on the resulting implantation profile. This issue will be addressed in chapter 9.

FIB lift outs in comparison offer a very high level of precision to incorporate very specific regions of the material in the final specimen and hence can be performed after ion implantation. In radiation damage studies this property is useful in order to select a specific depth out of the expected implantation profile for investigation. However, FIB itself can generate ion damage within the sample. While in APT the chemical identification helps to indicate regions of the data free of gallium implantation induced damage, it is more of a problem in FIM. Therefore, the FIM samples in this work are electropolished.

2.4 Ion implantations

All 'irradiated' specimens characterised in this thesis underwent ion implantations to simulate displacement damage caused by fast neutron irradiation. Self-ion implantations of tungsten in tungsten are considered as the most suitable proxy to simulate displacement damage, since no effects of the atomic-size difference are expected. Tantalum and vanadium implantations into tungsten were also performed, which will be explained in chapter 9.

All ion implantations were performed at the University of Surrey Ion Beam Centre. Ions were electrostatically accelerated and focused into a $10^{-6}Pa$ vacuum chamber. Inside the chamber there was a temperature controlled stage, where bulk samples were held perpendicular to the direction of the ion beam. Needle implantations were performed with the needles aligned parallel to the incoming ion beam. Figure 2.6 shows pictures of the set up. Needles are mounted on the rails in a. One needle is marked by a red circle as an example. The stage is then mounted

into the implanter as seen in b. Finally, as the door is closed, the stage is situated at $90°$ to the incident ion beam, schematically marked by red arrows on the right.

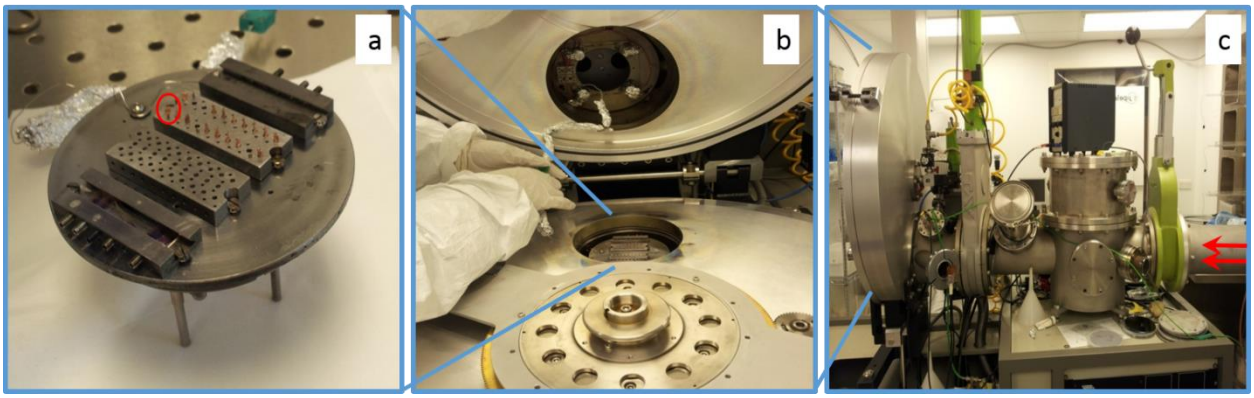

Figure 2.6: Ion beam set up at the Surrey University Ion Beam Centre. (a) Needle samples are mounted on rails. One needle is marked in a red circle. (b) The stage holding the needles seen in a is mounted onto the implanter. (c) As the door onto which the stage had been mounted is closed, the stage is perpendicular to the incident ion beam. The direction of the ion beam is marked with red arrows. The needles are therefore aligned parallel to the incident beam.

2.4.1 Implantation parameters

SRIM-Stopping Range of Ions in Matter 2013 software [155] was used to determine the experimental parameters for the desired implantation. Firstly, the stopping range tables are employed for each ion/target couple tested, to select the energy for the incident ion according to the resulting projected range (highest probability penetration depth). For example, for a tungsten/tungsten pair, 2 MeV beam energy will result in a projected range of 200nm, which is well within the atom probe sampling capabilities.

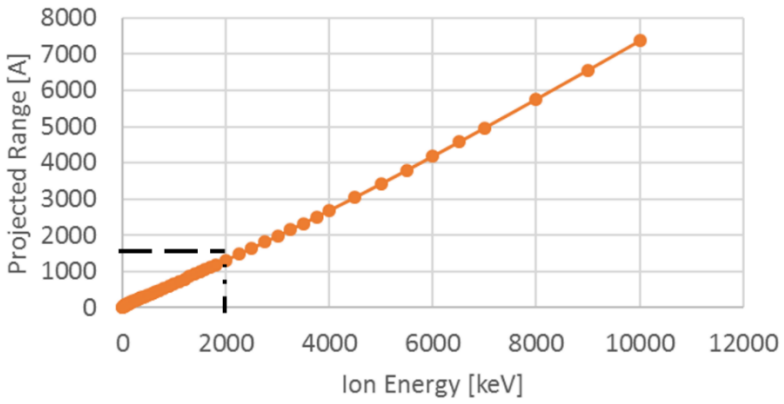

Figure 2.7: Expected projected range (mean depth of implanted ions) for self-implantation of ions in tungsten as a function of the implanted ion energy.

Once the energy of implantation is selected, a full cascade calculation is carried out, taking into account all displacements inside a collision cascade. The displacement ranges can then be plotted as presented in Figure 2.8, and used to extract the dose implantation parameter according to the desired dpa level. The relation between the two is given by:

$$dpa = \frac{dose \times \varphi}{N_{at}}$$

Where φ is the maximum number of collision events per penetrating ion, taken as the maximum value of the plot in Figure 2.8, and $N_{at} = 6.35 \times 10^{28} \frac{atoms}{m^3}$ is the crystal atomic density for tungsten. Since φ is taken as the maximal value of collisions, the calculation yields the peak dpa value.

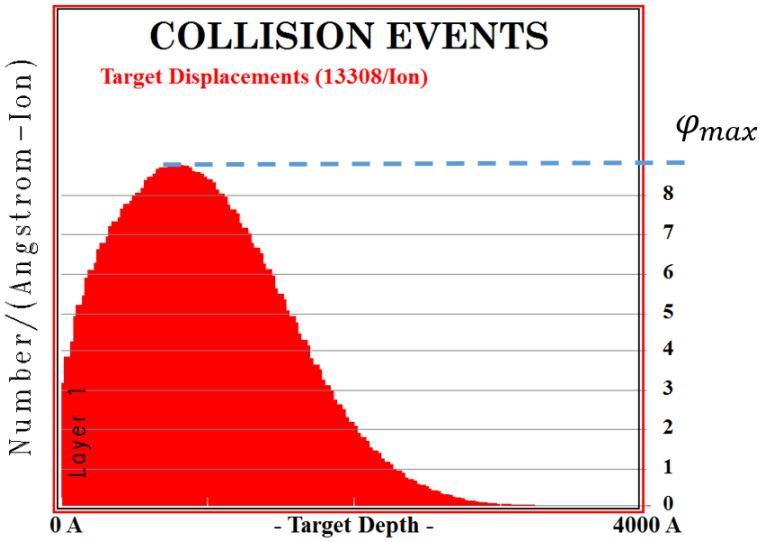

Figure 2.8: SRIM full cascade calculation profile of collision events as a result of a simulation of 10,000 2MeV tungsten ions implanted into a tungsten matrix.

The full cascade model was used in the calculations here as opposed to the quick model. While the quick calculation only takes into account initial displacements caused by the original impacting ion, the full cascade computes the displacements originated from all recoil events of sample atoms initiated by the first ion. Neither take into account migration and recombination processes. The two models will result in a different number of peak displacements, and therefore in a different dpa to dose conversion [51]. However, since the importance of the dpa term is in the ability to assess radiation exposure in-dependent to the radiation environment and compare between different implantation experiments, this discrepancy is not very important for a comparative study as long as the same SRIM model is used between compared cases.

The displacement energy used as SRIM input for the tungsten matrix is 68eV. This value was previously obtained by averaging the displacement energy across different crystallographic directions [35].

2.5 Atom probe

2.5.1 Device and run parameters

Two Local Electrode Atom Probe (LEAP) machines were utilized for the atom probe experiments; a LEAP 3000XHR and LEAP 5000XR. Both are reflectron [156] fitted instruments, with detection efficiencies estimated at 37% and 50% respectively. Both instruments are equipped with a laser pulsing system that allows the user to analyse brittle or poorly conductive samples. No change in the reported compositions measured is expected between the two machines, specifically in the samples studied in this thesis where no issues of complex molecular ions or overlapping mass spectrum peaks arose. Initial atom probe analyses were carried out at a specimen temperature of 50K. The run temperature was later increased to 55K to improve the yield of successful analyses of post-implantation brittle samples. The temperature was not raised by more than 5K to keep similar temperature conditions between the APT and the following FIM experiments performed at 50K.

All APT experiments were performed in laser mode. While for the sake of the completeness of the analogy to the FIM experiments voltage choice might have been the ideal choice, in practice voltage mode experiments yielded poor results as the analyses were very short before the specimen failed. This is due to the fact that samples post annealing and post implantations become brittle and thus more difficult to run in the atom probe. Table 2-3 summarizes the run parameters on both LEAP devices used.

	Laser wavelength	Pulse energy	Pulse rate	Detection rate
LEAP 3000	$532nm$	$0.5nJ$	$200kHz$	0.2%
LEAP 5000	$355nm$	$50pJ$	Automatically controlled $150-220\ kHz$	0.2%

Table 2-3 : LEAP 3000 and 5000 machine and experiment parameters.

Since the samples examined were either tungsten or tungsten alloys, free from overlapping peaks and complex mass spectra, no restrictions were imposed on the energy pulse as a result of different evaporation fields. The energy used was found to be high enough to reduce stress caused by high voltage on the sample, and low enough as to still maintain signal from crystallographic features like poles, needed to accurately calibrate the reconstruction.

IVAS 3.6.12 software was used to reconstruct and interpret all APT data.

2.5.2 Calibration of the 3D reconstructions

Spatial distribution maps (SDMs) are commonly employed in atom probe data analysis to detect crystallographic information and use it to calibrate reconstruction parameters [127],[157]. Other Fourier based methods also exist for this purpose [128], [158], [159], however SDMs are employed within the IVAS software due to their need for reduced computational resources [127].

SDMs are used in this thesis for two purposes. The first is in the calibration of routine atom probe reconstructions. Each atom probe reconstruction presented in this thesis uses information derived from SDM analyses to assure that the z coordinates are reconstructed correctly, according to identified crystallographic planes. For the second application, SDMs are computed independently, outside of the IVAS software, to evaluate the distortion of reconstructed FIM data, similarly to previous APT work in [157].

SDMs can be thought of as 3D histograms of inter-atomic distances. For each atom, the distance vector from all neighbouring atoms within a defined volume is calculated. For APT data, calculations are usually restricted to a 1-2 nm isotropic volume around each atom. The SDMs calculated for the FIM data in this thesis include the whole volume of the data. The resulting histogram is a 3D array, and by taking 2D slices equivalent to constants $\Delta X, \Delta Y, \Delta Z$ values, crystallographic information can be discovered. Since crystallographic information is limited in APT data and is usually observed in the direct vicinity of crystallographic poles, SDMs are usually calculated from a volume around visible pole patterns in the data.

Figure 2.9 demonstrates how SDMs are employed in APT reconstructions. In this example, a tungsten sample is analysed. Already from the hit detector event histogram in a, the central pole is evident. This is the (011) pole, which corresponds to the direction of the drawn wire. The xz ($\Delta y = 0$) and yz ($\Delta x = 0$) SDMs in b,c exhibit an ordered pattern corresponding to the contrast from (011) planes. By taking an intensity profile of the SDMs along the z direction, the plot in d is maintained, such that the distance between intensity peaks corresponds to the plane-spacing of the detected planes. A combination of the correct radius of curvature, and the image compression factor will result in the correct spacing between the planes.

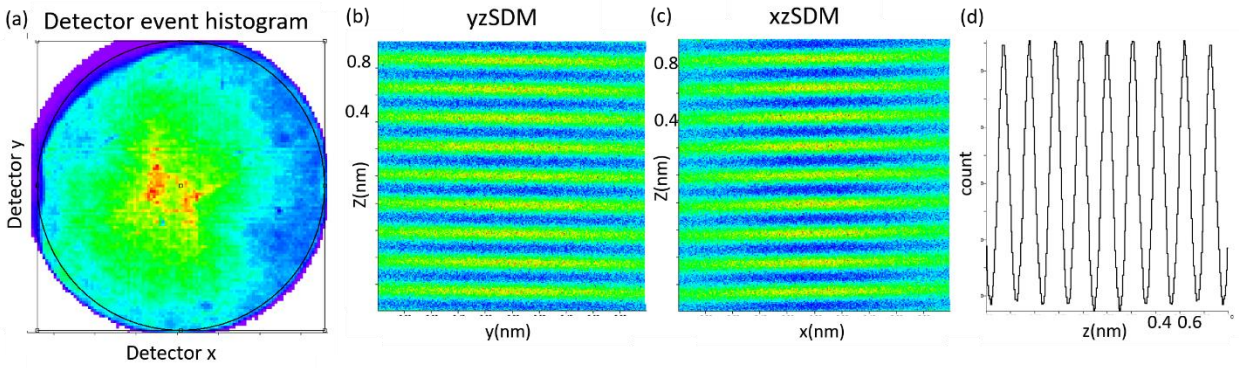

Figure 2.9: SDMs in APT reconstruction. (a) Detector hit events histogram. A crystallographic pole is evident in the centre. (b,c) yz and xz SDMs around the central pole. (d) 1D SDM along the z direction. The distance between consecutive peaks represents the plane spacing.

2.6 Field ion microscope

FIM experiments were performed on the '3 dimensional atom probe' (3DAP) instrument. The machine has a dedicated phosphor screen to preform FIM experiments, and a digital camera (AVT Stingray) was used to record all images. The phosphor screen image is intensified by a multi-channel plate, and the tip to screen distance is 56 mm. The device is not equipped with a local electrode. While imaging is performed by the application of a DC voltage on the sample, for the controlled evaporation of surface atoms a voltage pulser was additionally employed. The use of the voltage pulser allows setting of the DC voltage to the 'best image voltage' (BIV) for a specific combination of image gas and tip radius, whereby the resulting image contrast is then optimal. The BIV will be high enough to produce a suffice imaging gas ion current to produce sufficient intensity in the image, but low enough such that ionization does not occur uniformly over the tip surface which would decrease image contrast [124], [160]. This condition is usually achieved at a DC voltage that is slightly below the voltage required for the evaporation of sample surface atoms, and is assessed visually. The pulser then provides the needed additional voltage to evaporate constituent atoms from the surface, without compromising the quality of the image.

Unless stated otherwise, the DC voltage had been set manually by eye based on the quality of the resultant image, slightly below the voltage required for evaporation during FIM experiments. The voltage pulser was also changed manually and was increased as the surface evolved to a maximum of 30% of the base DC voltage. At this point, the DC voltage would be ramped up again, and the entire pulser range would be once again manually scanned. Experiments were performed with voltage pulses at a frequency of 100 kHz. Images were taken at SNR (signal to noise ratio) mode of either 8 or 4 image[2] and a frame rate of 15 fps, resulting in approximately 2/4 images respectively per second.

Experiments were performed at a specimen temperature of 50K. Helium was used as the imaging gas for all tungsten samples. Figure 2.10 demonstrates the choice of temperature and imaging gas on the resulting FIM images. For the temperature of 80K, the best image voltage was determined to be at 7.6kV. The voltage was then kept constant, and the temperature was dropped to 50K before taking another image, then again at 20K. The change in image quality is evident, with the image appearing to be at its best at 20K.

FIM's lateral resolution had previously been defined as the size of the smallest spot on the FIM screen, and was estimated at 0.3nm at favourable conditions [121], [161] . An expression for FIM's resolution, δ , was derived [12], [162], [163] and includes three major contributions:

$$\delta = \{\delta_0^2 + 16\left(\frac{\varepsilon^2 k_B T R}{k_f e E}\right) + 4\left(\frac{\varepsilon^2 \hbar^2 R}{2 m k_f e E}\right)^{\frac{1}{2}}\}^{\frac{1}{2}}$$

[2] In this mode the camera grabs and averages a set number of images and out-puts one image to reduce noise.

Where δ_0 is the size of the ionization zone above surface atoms (dependent on the field and has a lower limit size of the order of magnitude as the size of an image gas atom), ε the image compression factor, k_B the Boltzmann constant, T the temperature of imaging gas, R the tip radius, k_f field factor, e the elementary charge, E the electric field, m the mass of the imaging gas atom, and $\hbar$ the Planck constant.

The second term in the resolution equation describes the influence of the imaging gas atom's lateral velocity on resolution. As the temperature of the tip is higher, the distribution of velocities of imaging gas atoms ionized from the same atomic site is larger. Imaging gas atoms ionized with different lateral velocities will follow different trajectories, creating a larger spot size on the final FIM image. However, as the temperature is lowered, the evaporation of sample atoms requires higher voltage, therefore the samples are harder to evolve, and are more prone to fracture. 50K was chosen for experiments in this thesis as the temperature that produces a good compromise between image quality and sample yield. Argon was not considered as an imaging gas since its condensation temperature is ~80K which is higher than the selected specimen temperature. Finally, neon was tested at 50K and found to produce lower quality images. The third term in the δ equation expresses the inherent Heisenberg's uncertainty.

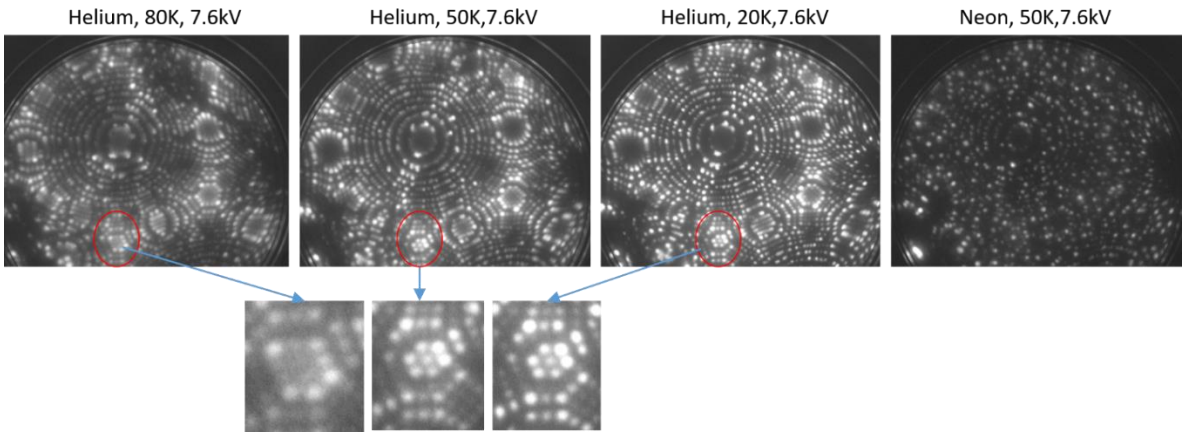

Figure 2.10: FIM temperature and imaging gas selection. Image contrast is improved as the temperature is dropped, however evaporation requires higher voltage. 50K is chosen as optimal.

Most of the analysis techniques used for FIM data are developed in this work and are presented at dedicated chapters.

2.6.1 Evaluation of tip radius

It is possible to estimate the radius of the sample from the FIM image by calibrating known theoretical angles between crystallographic poles observed to actual pixel distances on the image [12].

As schematically shown in Figure 2.11, the n'th plane in depth from the surface of the sample corresponds to the n'th ring around the centre of the FIM image. if θ_n is the angle between the $[h_1k_1l_1]$ direction and the n'th ring around the pole, and each concentric ring around pole 1 indicates a depth increment of the theoretical planar spacing between the $(h_1k_1l_1)$ planes, $d_{h_1k_1l_1}$, then the radius of curvature R_0 of the tip is given by [164]

$$R_0 \approx \frac{nd_{h_1k_1l_1}}{1-cos\theta_n}$$

where n is the number of concentric ring around pole 1 and $d_{h_1k_1l_1} = \frac{a}{\sqrt{(h_1^2+k_1^2+l_1^2)}}$, $a = 3.16\text{Å}$, tungsten's lattice parameter.

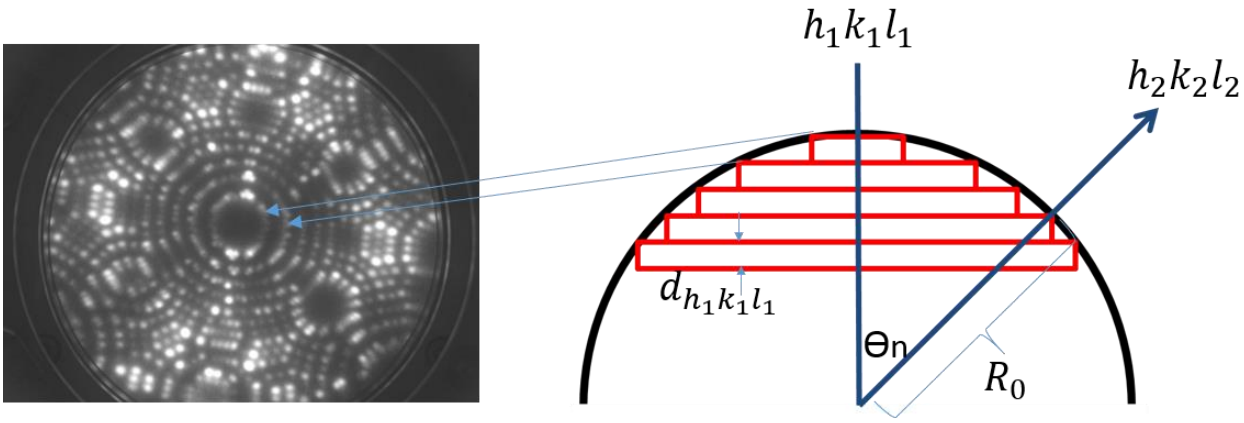

Figure 2.11: Simplified schematic description of a tip apex. Each plane along the depth of the sample symbolizes a ring around the pole in the FIM image.

To deduce θ_n from a given FIM image, a calibration is made between the theoretical angle between the $[h_1k_1l_1]\ and\ [h_2k_2l_2]$ directions, and their separation distance in pixels. Once this calibration is in place, the image radius of the n'th ring around the($h_1k_1l_1$) pole (in pixels) will be enough to estimate θ_n and in turn, the radius of curvature.

A simple matlab code was written to perform these measurements and calculations for the digital FIM images, and is demonstrated in Figure 2.12. One of the tungsten samples is shown here, with two poles indexed. The theoretical angle between the [011] and the [121] directions is 30 degrees. The centres of both poles are determined by the user's input of four points around a concentric ring of each pole. The pixel size distance on the image between the two centres of the fitted circles is then measured (in this case found to be 308 pixels). Next, the user is asked to mark 4-8 points on one of the concentric rings of the central pole, and specify the ring number. In this case, the second ring is chosen. A circle is then fitted by the code to the ring, and its radius

found to be 148 pixels. From the measured radius of the second ring, θ_n is calculated: $308 \rightarrow 30^o \gg 148\, pixels \rightarrow \theta_n = 14.4$, and the radius of curvature of the tip is then found to be$\sim 14\, nm$. Variance in such radius measurements is expected and could be the result of measurement error in calibrating distances by fitting the poles to perfect circles. Further, as the tip is not a perfect sphere, calibration according to different poles might result in different 'local' radius of curvature. The procedure described above was repeated twice for the same poles, using the n=2 ring of the central pole, and the n=3 ring of the central pole the second time. Two more measurements were performed, calibrating angles to distances using a different {121} pole on the image, marked with a green circle. The average and error estimates for these 4 measurements were found to be: $14.4\, nm \pm 0.96$ (the error estimate given here is the standard deviation from the 4 measurements).

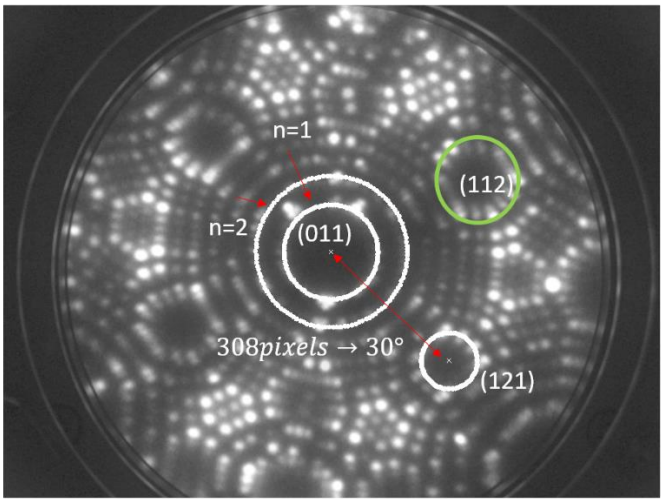

Figure 2.12: Demonstration of radius calculation procedure on a tungsten FIM image. The angle between the [011] and [121] directions is calibrated to the pixel distance between the two poles. This calibration is used to convert the measured radius of the n=2 ring around the (011) pole to an angle between the edge of the terrace and the [011] direction, which is in turn used to determine the radius of curvature, found here to be approximately 14 nm. A third pole marked in green is used to repeat the measurements using a different pole for calibration.

3 Imaging of radiation damage using complementary field ion microscopy and atom probe tomography

In this chapter potential complementary applications of FIM and APT are explored in the study of radiation damage in tungsten. A combined APT/FIM study of radiation-induced crystal damage is demonstrated to characterise the effects of self-ion implantations of increasing dose levels and explore limitations of both techniques. Contributions from both FIM and APT approaches are compared and discussed in relation to corresponding TEM and Nano indentation analysis.

3.1 Experiment

Table 3-1 summarizes the implantation parameters for all self-implantation experiments explored in this chapter. All samples were electro polished to the desired needle shape from a tungsten wire prior to the implantations.

	Material	Implanted ion	Implantation energy $[MeV]$	Implantation temperature $[c^o]$	Dose $[^{ions}/_{cm^2}]$	Damage level $[dpa]$	Preparation method
Sample 1	W	W	X	X	0	0	Electropolished
Sample 2	W	W	0.15	25	10^{12}	0.01	Electropolished
Sample 3	W	W	2	500	4.7^{15}	6	Electropolished
Sample 4	W	W	2	500	2.6^{16}	33	Electropolished

Table 3-1 : implantation parameters for samples examined in this chapter.

All samples had been tested in both FIM and APT in order to characterise the types of microstructural changes that are visible in each of the techniques. Since these are destructive,

separate specimens had to be prepared for each. At least three specimens were analysed in each technique for each implantation condition to ensure the results were representative.

Both APT and FIM experiments were performed at 50K, with helium used for FIM imaging.

3.2 Results

Figure 3.1 represents results from the FIM and APT analyses of the control un-irradiated tungsten samples. As expected, the reconstructed APT data in Figure 3.1a reveals a homogenous distribution of tungsten atoms. A clear crystal structure can be seen in the corresponding FIM image in Figure 3.1b, fully characteristic of an undamaged body-centred cubic (bcc) lattice.

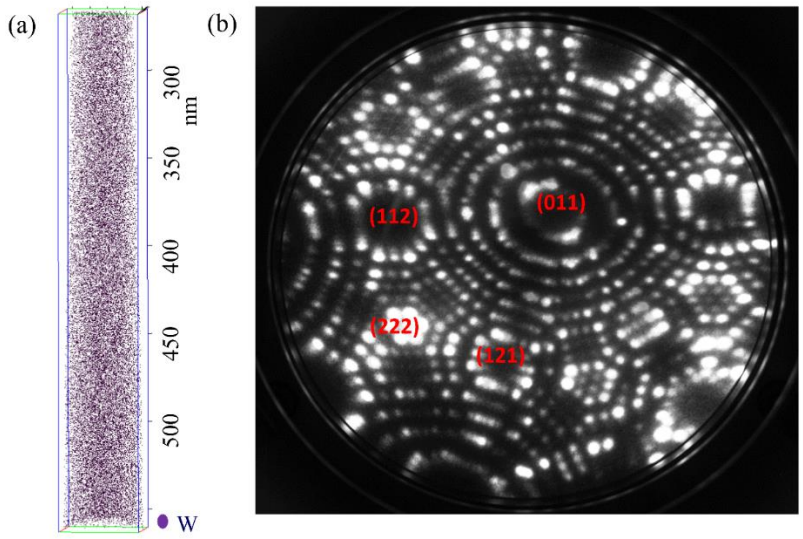

Figure 3.1: APT and FIM results obtained for the reference un-implanted tungsten sample. (a) Homogenous tungsten matrix in the APT reconstruction. For clarity, 0.3% of the atoms are imaged in a characteristic 300 nm long section of the reconstruction. (b) Characteristic bcc lattice imaged with FIM. Some of the main poles are indexed.

It is only when comparing the results of the implanted samples to the reference samples that the differences in the relative strengths between the two techniques are made apparent. Figure 3.2 presents results of APT analyses of the samples implanted to a level of 0.01 dpa. The tungsten distribution within the APT reconstruction again appears homogenous, very similar to that in

Figure 3.1, with no significant indication of crystal damage caused by the implantation. However, by carefully examining the complementary FIM images in Figure 3.2b-d, deviations from the perfect crystal structure can be detected. Very fine features of crystal damage in the form of single vacancies are observed throughout the evaporation process through the depth of the sample. These vacancies are straightforward to image with FIM, however are undetectable to APT analysis, due to it's limited detection efficiency.

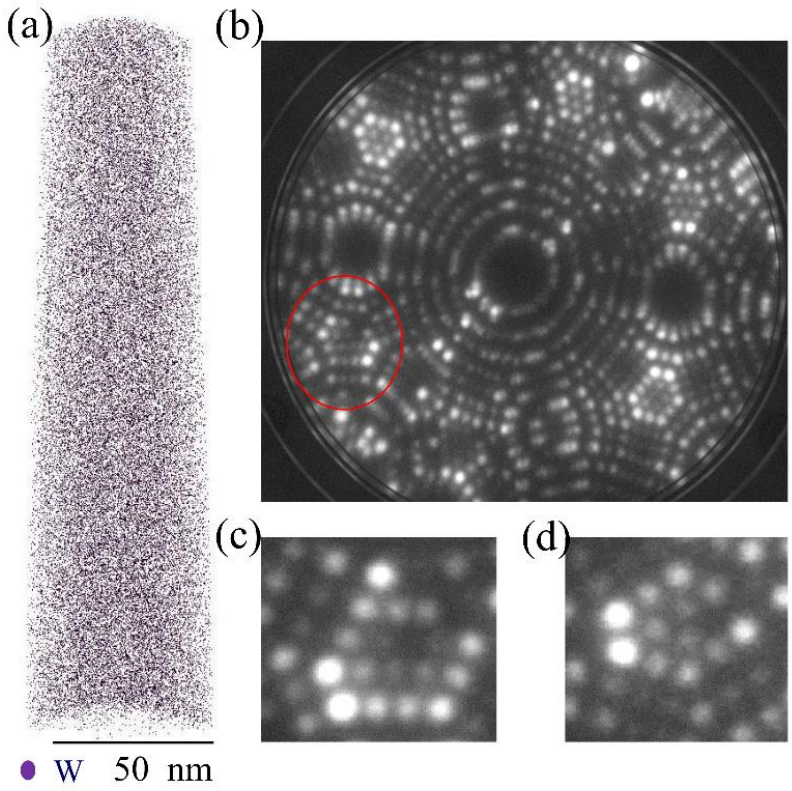

Figure 3.2: Results from sample 2, tungsten implanted to a 0.01 dpa level. (a) Homogenous tungsten matrix seen in the APT reconstruction. 0.2% of the atoms are shown for clarity. (b-d) FIM images of sample 2. Single vacancies can be seen throughout the evaporation.

Larger features of crystal damage are prominently visible via FIM analysis of the samples implanted to a higher damage level of 6 dpa, as shown in Figure 3.3d-e. The concentric ring structure defining the central (011) pole in Figure 3.1b has been replaced by a spiral (Figure 3.3d). This is clear evidence of a dislocation emerging at the surface from the (011) plane [11]. On

examining the complementary APT reconstruction, in Figure 3.3a, the homogeneous distribution of tungsten atoms is once again very similar to that observed for the previous irradiation conditions, and provides no direct evidence of damage to the crystal lattice. Interestingly, however, in this sample, small amounts of carbon were also detected (0.13 at. %) in the APT analysis. Much smaller traces of carbon (<0.01at %) were observed at the surface of the control specimen, whereas, the samples implanted to 6 and 33 dpa were found to contain increasing amounts of carbon (0.13-0.41 at % respectively). It is likely that this carbon is an unintentional impurity. If present in the implantation chamber, the beam itself, or on the surface of the needle samples, carbon atoms can be knocked into the depth of the sample during the implantation by the energetic tungsten ions. From the APT reconstruction of carbon atoms in the 6dpa sample (Figure 3.3b) it is apparent that this carbon impurity is in fact useful for revealing damage to the lattice that is not detectable from the examination of the tungsten atoms. Carbon will segregate to the implantation induced lattice defects, making them observable in the APT reconstruction as regions of high carbon concentration. Indeed, the decoration of solutes facilitating the observation of crystallographic dislocations is well-established in the APT investigation of a wide variety of material systems [165]–[170]. Looking more closely at the distribution of tungsten atoms of the 6 dpa sample, there are regions of the data where the in-depth spatial resolution of the APT reconstruction is high enough to resolve ordered (011) crystallographic planes, as demonstrated in Figure 3.3c. In such regions a departure from the well-ordered planes structure can be observed in the vicinity of carbon atoms (marked as red spheres). This further strengthens the notion that the observed distribution of carbon correlates to radiation induced lattice damage. The dislocations observed with the field ion microscope in the 6 dpa samples help to

identify the defects seen in Figure 3.3b,c as dislocations. Smaller damaged regions in the size of several vacancies were also observed with FIM, but these are apparently too small to be highlighted by carbon segregation in the APT data, either due to the small amount of carbon segregating to these locations, or due to no segregation occurring to such small size defects.

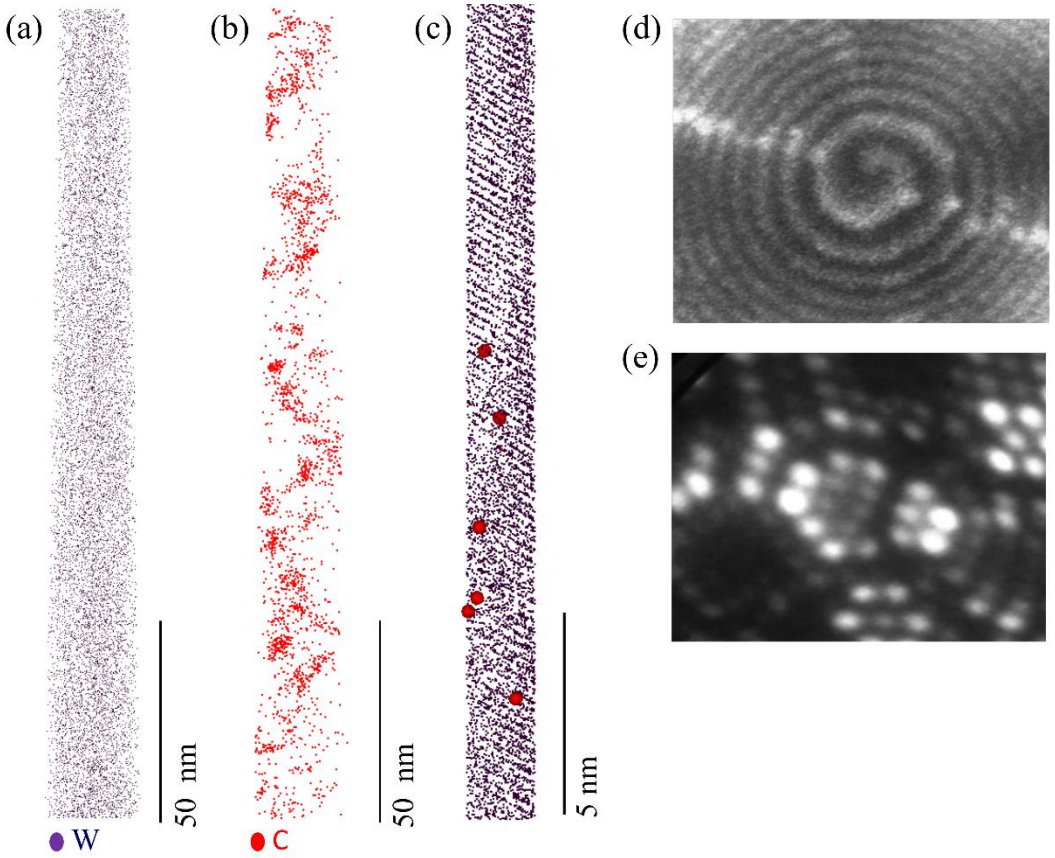

Figure 3.3: Results from sample 3, tungsten implanted to a 6 dpa level (a) Tungsten APT reconstruction still appears to be homogenous For clarity, 1% of the atoms are shown here in a 200 nm long characteristic region. (b) APT reconstruction of carbon atoms present in the sample as a result of carbon contamination during tungsten ion implantation. (c) 2x2x20 nm^3region of the tungsten matrix reveals (011) crystallographic planes. Carbon atoms are seen in red. (d-e) FIM images presenting larger features of crystallographic damage than in previous samples. The spiral in d is a dislocation emerging from a (011) plane.

It is only in the case of the highly damaged, 33 dpa sample, that the spatial distribution of tungsten in the APT reconstruction appears to be different from that of the corresponding control sample. Figure 3.4a exhibits high density regions in the tungsten reconstruction of the 33 dpa

sample. These regions, highlighted by red circles, can be attributed to trajectory aberrations in the atom probe caused by local areas of lower curvature at the surface of the tip [130] [171]. Reports in the literature indicate that the field evaporation in defective areas, such as around dislocations [11], [172] or interstitials [173], occurs at lower electric field. Fortes an co-worker attribute a lower evaporation field to interstitial atoms due to the lattice strain [11]. The local neighbourhood of these atoms is also likely to be affected by the binding energy of surface atoms in these areas [174], [175]. In addition, this is supported by the carbon distribution in the sample, seen in Figure 3.4b. The carbon exhibits segregation behaviour similar to that observed in the 6 dpa sample and in many other materials, as recently reviewed by Smith *et al.* [176]. In this case, as seen in Figure 3.4a-b, a correlation between carbon segregations and regions of tungsten high density is also revealed, further confirming the origin of the apparent high density tungsten regions as regions of extensive crystal damage. FIM images of sample 4 in Figure 3.4c-f reveal a considerably higher level of damage to the ordered lattice, with many dislocations, dislocation loops (d) and depleted zones appearing throughout the evaporation process.

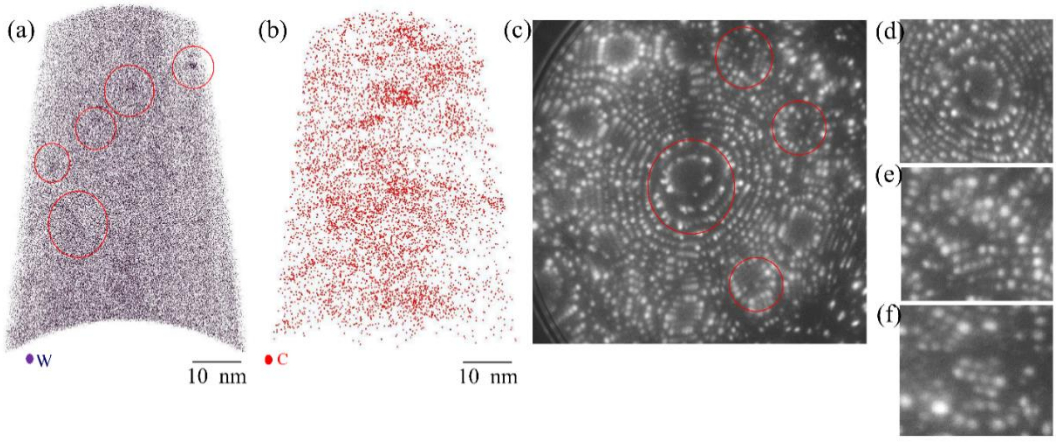

Figure 3.4: Results from sample 4, tungsten implanted to a damage level of 33 dpa. (a) Tungsten APT reconstruction reveals regions of high apparent density highlighted in red circles. For clarity, 80% of the atoms are shown in a 3.5x50x69 nm^3 slice of the data (b) Carbon segregation appear to spatially overlap with the high density tungsten regions. (c-f) FIM images presenting substantial degree of crystal damage.

3.3 Discussion: APT/FIM

From the results presented in Figure 3.1-Figure 3.4 it is clear that crystallographic information pertaining to radiation induced lattice damage is readily available in the FIM data. The atom probe data requires more careful analysis approaches and may not be successful in cases of low implantation levels where small features of damage are expected. It was shown that from the APT reconstructions of the tungsten matrix, no crystal damage was apparent up to a damage level of 6 dpa. At 33 dpa, large crystal defects manifested in the APT data in the form of density variations that can be attributed to trajectory aberrations.

The fundamental reason for this difference in resolution power lies with the use of imaging gas in FIM. In both FIM and APT, there is a random loss of 30-70% in detection efficiency due to the micro-channel plates (MCP) utilized at the entry of the detectors. In the case of a reflectron-fitted instrument such as the LEAP-3000HR used for experiments in this chapter, approximately 63% of the atoms evaporated from the specimen are stochastically omitted from the final analysis [82], [177] due to an additional reduction in detection efficiency originating from the design of the reflectron. Such limitations prevent the identification and characterisation of atomic scale crystallographic features such as vacancies, interstitials, and the direct imaging of dislocations by the atom probe. However, the FIM image is dynamic, and is in fact the result of a continuous stream of gas ions field evaporated from the tip. At any given time, each illuminated spot, representing an individual atom is made up from the contribution of thousands of gas ions striking the detector. Hence, even though a similar fraction of ions is detected in both devices, hundreds of imaging ions originating from each prominent surface site will still be detected in FIM, assuring the representation of every surface atom, while APT remains a single shot chance

for detection. In regions of high index planes effectively every atom is precisely imaged on the lattice and consequently crystal defects, including the smallest of them all, the single vacancy, can be directly observed. This difference in detection power is demonstrated in Figure 3.5. In Figure 3.5a, a simulation of the expected ion hit map around the main pole of APT data of a perfect bcc tip, aligned along the [011] direction. A concentric ring structure is obtained, representing the configuration of the kink sites, most prominent for evaporation, resulting from the intersection of the spherical shape of the tip with the crystal lattice. In Figure 3.5b, a real reconstructed tungsten dataset is shown, constructed of a 10nm (in depth) layer of ions that hit the detector in the region of the (011) pole. The reduced detection efficiency is immediately apparent. In comparison, Figure 3.5c shows a FIM image of a tungsten sample aligned at the same direction. The obvious concentric ring structure is very similar to the perfect crystal simulation, demonstrating the superior efficiency and resolution power of FIM vs the APT.

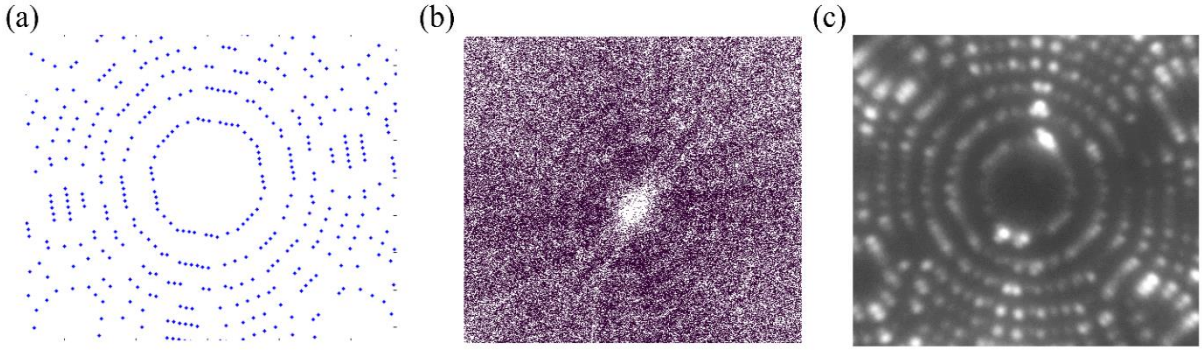

Figure 3.5: FIM vs APT detection efficiency comparison. (a) Simulation of the surface ion hit map around the (011) pole assuming 100% detection efficiency. (b) Reconstructed Ions around the (011) pole of a real tungsten APT dataset analysed in voltage mode, constructed from a 10nm layer, 4-14 nms below the surface. (c) FIM image of the (011) pole of a tungsten tip.

3.4 Discussion: complementary TEM/Nano-indentation

As the Tokamak divertor is expected to experience doses of 20-30 dpa/year [178], it is important to understand how the microstructure changes observed in this work with FIM will effect

tungsten's mechanical properties. Armstrong *et al.* have performed nano indentation tests on pure tungsten self-implanted to different doses corresponding to damage levels of 0, 0.07, 0.4, 1.2, 13, 33 dpa at 300℃ [139]. The average hardness was measured for each of the samples at a depth of 125 nm indenter displacement corresponding to the peak damage depth predicted by SRIM, and a region free from both surface effects and the underlying un-damaged depth of the sample. Their findings are summarized in Table 3-2. It can be seen that hardness increases at 0.07dpa, and increases again more drastically at 0.4 dpa, however saturates at higher doses.

dpa	Hardness at 125nm (GPa)	Change in hardness (GPa)
0	7.62	-
0.07	7.97	0.35
0.4	8.45	0.82
1.2	8.35	0.73
13	8.35	0.73
33	8.55	0.92

Table 3-2[139]: Hardness results of tungsten implanted to increasing levels of dpa at 300℃. Saturation is observed past 0.4dpa

Corresponding TEM analyses were carried on tungsten foils implanted at the same conditions. According to the TEM results, loop volume number densities observed for 0.4,1.2 and 33 dpa levels seem to match the saturation trend observed in the mechanical tests, with only a small increase in loop density between 33 and 0.4 dpa. Most of the reported damage revealed by TEM is reported to be in the form of dislocation loops of 2nm in diameter, with no voids observed. Unlike the TEM observations, FIM results in this chapter demonstrate an increase in microstructure damage across the range of implantation doses. While saturation is detected in the TEM data, FIM is still able to resolve increasing levels of damage between the 6dpa and the

33dpa samples. While those were implanted at higher temperature than the samples in [139], a trend of increase in damage levels can still be discussed in comparison to micromechanical and TEM results .The temperature difference between the two cases means that additional recovery mechanisms are active at 500℃, and as vacancies are above their migration temperature, larger structures of vacancies cluster are expected along with a decrease in individual vacancies population. However, this is true for both 6 and 33 dpa cases, therefore an increase in damage levels between the two samples can be determined.

While TEM reports dislocations to be the prominent form of damage microstructure [139], these features seem to be less commonly visible in FIM. This could be due to the needle geometry, resulting in large surface/volume ratio, causing increase loss of dislocations to the surface. This phenomenon was simulated for TEM foils [179], but could be expected to influence FIM samples possibly in a more significant manner. Indeed, field induced displacements of dislocations in field emitters had been previously reported with regards to FIM/APT samples and is an established phenomena [180], [181], one that needs to be considered when characterizing crystal defects using these techniques.

Finally, by comparing FIM results to the mechanical tests it could be suggested that the additional damage features observed at higher doses, corresponding mostly to large vacancy clusters are in fact not dominating the hardening mechanisms in tungsten, and the concentration of the dislocation loops measured in TEM seem to be following the trend better. Of course under real conditions of a fusion reactor, where tungsten is also exposed to helium surroundings and transmutation damages, the additional defects seen in FIM could have a very significant effect on hardness. In ion-implanted tungsten – rhenium alloys hardness was shown to be dominated

by the formation of rhenium clusters [60], [139]. The formation mechanism of these clusters was shown to depend on temperature and irradiation dose, implying the importance of crystal defects accumulation as these enhance diffusion and may also act as nucleation sites for the solute clusters. In another example, helium implanted tungsten samples exhibited increased hardness in comparison to samples implanted by both helium and tungsten [5]. Supported by positron annihilation studies [38], [153], these suggest that stronger hardening is achieved when helium is present in the sample as vacancy-helium complexes, rather than bound to dislocations. It is therefore another example of a tungsten system where vacancies, and vacancies clusters such as the ones observed with FIM in this chapter, have a significant effect on resulting mechanical properties. Table 3-3 summarizes the effects of different alloying elements, and crystal defects, discussed above and in the introduction chapter, on the hardness of tungsten, demonstrating the indirect, yet important effects that vacancies have on tungsten's hardness:

	Characterization techniques	Effect of implantation dose on hardness in tungsten	references
Dislocations	TEM	$dose \uparrow \rightarrow H \uparrow$, H saturates~dpa $= 0.4$	[139]
Vacancies	FIM	$dose \uparrow \rightarrow H \sim constant$, $measure\ up\ to\ 33dpa$	[15], [139]
He+ vacancies/ dislocations	$TEM, FIM, PALS, NRA$	$dose \uparrow \rightarrow H \uparrow$, $H_{He+vacs} > H_{He+dislocations}$ $\rightarrow He\ is\ more\ tightly\ bound\ to\ vacancies\ structures$	[5], [146], [152], [153], [182]
Re + vacancies	FIM, APT, TEM	$dose \uparrow \rightarrow H \uparrow$ $precipitation\ hardening$ $Re\ clusters\ formation\ assisted\ by\ vacancies$ $measured\ up\ to\ 33dpa$	[6], [60], [139], [142], [143]
Re + Os + vacancies	FIM, APT, TEM	$dose = 33dpa \rightarrow H_{Re} \uparrow < H_{Re+Os}$ $Os\ supresses\ Re\ clustering \rightarrow$ $Os\ probably\ more\ strongly\ bound\ to\ vacancies$ $dpa>0.4,\ Os\ dominates\ hardening\ not\ through\ precipitation$	[6], [60]

Table 3-3 : Summary of the effects of crystal defects and alloying elements/impurities on the hardness properties of irradiated tungsten.

In conclusion: complementary APT/FIM study of self-implanted tungsten has demonstrated the additional atomic scale information available with FIM that is below the detection efficiency limits of APT and TEM. Single vacancies, small vacancy clusters, and dislocations are all straight forward to image in 3D with FIM. While vacancies do not give any contrast in APT data, dislocations are sometimes detectable via impurities segregation. At the high dose of 33dpa, trajectories aberrations from highly damaged regions in the specimen can indirectly suggest the presence of crystal defects in APT data. Since FIM had been established as a worthwhile technique to utilize for the studies of radiation damage, the next chapters will establish working methods and data analysis techniques for the robust use of FIM in radiation damage studies.

4 Automated reconstruction of 3D field ion microscopy data

4.1 Introduction

In chapter 3 APT and FIM were demonstrated to be powerful, complementary techniques, that combined can contribute unprecedented chemical and spatial resolution to the atomic-scale characterisation of radiation damage. FIM was shown to provide unique insights into the atomic arrangement of defects in irradiated samples, information that is not available in atom probe data due to its restricted detection efficiency.

In the 1960s and 1970s 3DFIM experiments revealed a tremendous potential to contribute to the study of radiation damage in materials. However, since this time, use of FIM has been almost entirely replaced by the development of atom probe tomography. While 3DFIM still provides increased resolution power in comparison to current APT machines, it is the lack of automated, digital, convenient tools for the analysis of FIM images that have led to very little further development compared to APT.

A typical 3DFIM experiment will produce a very large number of FIM images. For example, for an analysis that probes a modest depth of 10nm into the sample, with an imaging frame rate suitable to track controlled evaporation, the resulting total size of all acquired data will typically reach tens of thousands of images. Some form of automated analysis is therefore required to map the configuration of the features of interest in the data set, whether those are several nm in size (dislocations, precipitates), or the size of a single atom (vacancies, interstitials). To make full use

of the ultimate resolution power, such analysis will need to maintain the atomic nature of the data. For this purpose, it will have to identify *all* atoms in the region of interest, and correctly place them in terms of their relative depth from the initial surface.

In order to fully utilize the unique imaging capabilities of FIM and routinely explore larger volumes accurately and consistently, this chapter introduces the first automated 'atom-by-atom' approach to 3DFIM data reconstruction. The procedure relies on minimal underlying assumptions, is sensitive to atomic information and results in an atomically resolved 3D reconstruction of the crystalline lattice. The proposed reconstruction procedure is demonstrated here for the analysis of tungsten, however the method is equally applicable to a wide range of materials which can be imaged by FIM such as steels [70], [183], superalloys [184], [185] and catalyst metals [186], [187] for example. The main stages of the reconstruction algorithm are demonstrated, as well as highlighting significant challenges in the reconstruction procedure.

4.2 The experiment

A tungsten sample was electropolished from a wire oriented along the [011] direction into a needle shape with a final specimen apex radius estimated to be less than 20 nm. Figure 4.1a is a FIM image of the analysed sample, with its main poles indexed. The sample was subject to self-ion implantation to a dose consistent with primary stages of radiation damage, whereby damage cascades caused by the implantation of individual ions are not interacting. However, since the focus of this chapter is to illustrate the 3D basic reconstruction algorithm, for a 'perfect-crystal' type system, the analysed volume of the sample discussed here is an un-damaged region of this sample. Reconstruction of damaged volumes will be discussed in chapter 8.

Since 3DFIM's greatest complementary contribution to APT data is its ability to resolve individual atoms, and since these are the smallest features on FIM images, the reconstruction algorithm demonstrated here was developed to reconstruct the atomically resolved poles of FIM images, where, in damaged samples, single vacancies can be located.

4.3 Imaging and evaporation sequence

The imaging and evaporation sequence of the atoms is demonstrated Figure 4.1b, which is fundamental to the accuracy of the reconstruction procedure. The terrace patterns are created as a result of the higher electric field generated above the more exposed surface sites at kink positions around the crystallographic poles. Outer terrace atoms protrude to a greater extent than inner plane atoms, therefore higher imaging gas ion current will be generated at these locations, resulting in brighter imaging and desired surface contrast. As the evaporation of constituent atoms progresses, the outer terrace is removed by preferential evaporation due to the higher electric field, exposing the inner plane atoms for imaging. The layer-by-layer field evaporation process is demonstrated in Figure 4.1b-c.

As the imaging and evaporation sequence progresses through the depth of the specimen, the repeating pattern provides a distinct, reoccurring metric to enable automatic detection of distinctive atomic planes as evaporated within the stack of FIM images. Figure 4.1c presents the integrated intensity measured from pixels within the central region of the (222) pole, marked with a red square in Figure 4.1b, across the first 500 consecutive FIM images. As can be seen in Figure 4.1b, each crystallographic layer will first exhibit low intensity in the middle of the pole, as terrace atoms at the periphery of the plane are preferentially imaged. Once these atoms have

evaporated, the field re-distributes such that central atoms within this plane are now imaged, corresponding to an increase in the integrated intensity of that region. Progressing further, once the final atoms on this plane have evaporated, and a lower layer is now exposed to the surface, the intensity at the centre of the pole drops again. This drop in intensity is usually sharp, since the final 3 atoms of a plane tend to field evaporate almost simultaneously, or at least within a time frame shorter than the experiment resolution.

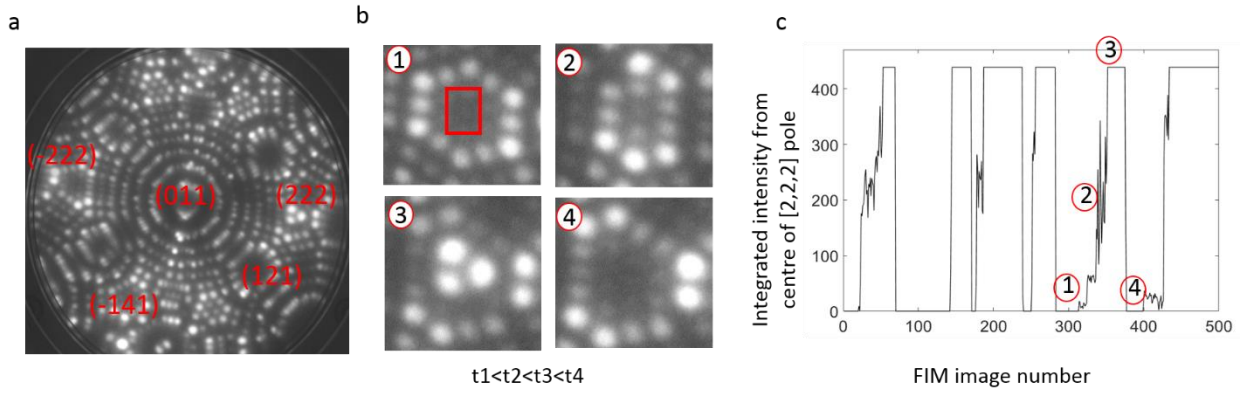

Figure 4.1: (a) FIM image of the analysed tungsten sample, with its main poles indexed. (b) Close up view on the (222) pole. Images numbered 1-4 are time ordered and describe the evaporation and imaging sequence of the plane. The plane imaged in (1-3) had been fully evaporated in (4), and the layer below is now exposed. (c) Integrated intensity from the centre of the (222) pole across 500 FIM images, measured from the region of the pole marked in a square in (b). Points 1-4 correspond to the contributions from points in time 1-4 marked in (b).

Each intensity interval in the integrated intensity plot in Figure 4.1c therefore represents the imaging and complete evaporation of a crystallographic layer. From the plot in Figure 4.1c it can therefore be concluded that in the first 500 FIM images, 6 (222) planes are imaged, and 5 of them have been fully evaporated. From the points at which the intensity drops, the final FIM image in this sequence corresponds to a particular plane which can be deduced, for example one image prior to the point labelled 4 for the fifth complete layer imaged. Since the images are taken at a constant rate, the width of each intensity interval corresponds to the evaporation duration of

each plane. This will change throughout the experiment due to changing field conditions as the shape of the specimen evolves.

4.4 Reconstruction stages

The procedure is demonstrated on a tungsten dataset comprising 7771 images, capturing the evaporation of 69 crystallographic layers in depth into the material and containing 2450 tungsten atoms. The reconstruction algorithm consists of the following key steps:

- Atomic positions are identified automatically across all images.
- A tracking algorithm is implemented in order to identify the same atom as it appears in several images across the data set.
- The relative crystallographic plane of each atom is determined, completing the coordinates needed to create the final 3D reconstruction.

These analysis stages are each discussed in detail in the following sections.

4.4.1 Gaussian filter and automated detection of atomic coordinates

In the first stage of the process, a Gaussian filter is applied in the Fourier space of each digital image to remove high frequency noise. To this end, the fast Fourier transform of each image is calculated and multiplied by the Gaussian filter (GF) given by

$$GF = e^{-\frac{\left(x-\frac{w}{2}\right)^2+\left(y-\frac{h}{2}\right)^2}{2\sigma^2}}$$

where w, h correspond to the width and height dimensions (in pixels) of the image, and σ determines the width of the Gaussian filter, set here to 40. The inverse Fourier transform of the multiplication product is then calculated, and serves as the filtered image. The atomically

resolved poles of interest are then selected and the same region is automatically cropped out of all FIM images to reduce the size of the data and increase calculation speed.

Next, within each FIM image the intensity values of all pixels are scanned and local intensity maxima coordinates are identified. These maximum-intensity pixels represent coordinates of all atoms appearing within the stack of images. Note that a threshold value is defined for the intensity peaks to be identified as atoms to avoid false identifications due to remaining noise. In the analysis demonstrated here, the threshold was set at 60% of the maximum measured intensity.

Figure 4.2 demonstrates the effects of varying the Gaussian filter and intensity cutoff values on the resulting intensity peaks that are identified as potential atoms, for the same FIM image. In the table in this figure, for each of these analysis conditions, the number of peaks that were ultimately identified across the same sequence of 100 FIM images is stated. It is evident that without the application of filter and an intensity cutoff, many intensity peaks on the images are falsely identified as atoms, due to contributions from the high frequency noise contained in the images. A large portion of these false-positives are removed by setting a threshold value for the intensity peak, beneath which any peak is not considered as a potential atom. The inclusion of the cutoff in this case has eliminated most of the points identified in the background of the image, but there are many that still remain in high intensity regions of the image, over-representing the same atom. With the application of a Gaussian filter significant improvement is achieved.

The best result is achieved for this data set when applying a Gaussian filter with $\sigma = 40$, and a cutoff of 0.6 of the normalized intensity. In this case, as can be seen from the two images on the

right in Figure 4.2, the cutoff has eliminated several correctly identified atoms. However, due to the imaging sequence of the atoms, these atoms will be identified in later images as the evaporation process continues. The elimination of detection of atoms at low intensities is actually preferred as these atoms tend to image inconsistently until they attain a more uniform intensity, i.e. they are typically detected in one image but not in the next. Furthermore, their edges are difficult to precisely determine, which in turn creates inaccuracies when attempting to estimate their size as is required in the next stage of the algorithm. All these will make the task of tracking these atoms across the stack of images more difficult. The tracking algorithm developed here is described in more detail in later sections of this chapter, but relies on assumed proximity of identified coordinates of the same atom on both the image plane, and across the timeline axis. Thus, the inconsistency in imaging, characteristic of low intensity imaging will only complicate the tracking step.

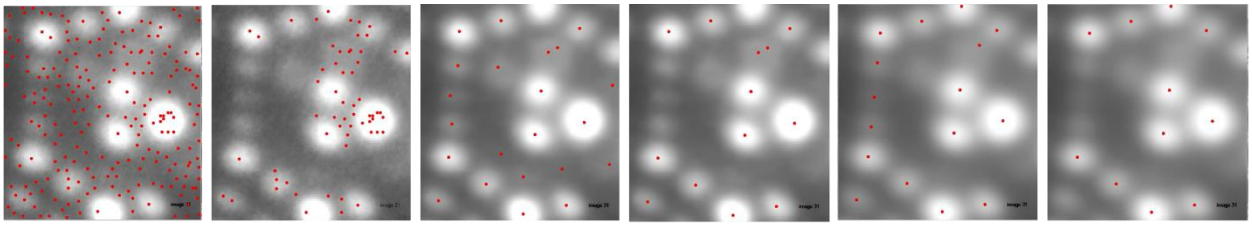

No filter, No cutoff	No filter, 0.6 cutoff	$\sigma = 100$, No cutoff	$\sigma = 100$, 0.6 cutoff	$\sigma = 40$, No cutoff	$\sigma = 40$, 0.6 cutoff
21317	4886	2735	1411	1578	1255

Figure 4.2 : Effect of Gaussian filter and intensity cutoff on identified intensity peaks. Each red dot on the images represents intensity peak on the image. In the last row of the table the number of identified coordinates for each of the stated conditions across the same sequence of 100 FIM images.

In Figure 4.3a, such unidentified atoms are marked manually using white circles. It is the local field that is responsible for atoms being imaged with different intensities. A higher field will result in an atom imaging more brightly, and will also increase the probability of evaporation for that atom. Thus, atoms are usually imaged with the highest intensity directly before evaporation. The

evaporation process continues from the image in Figure 4.3a to the point in time represented by Figure 4.3b. Two brightly imaging atoms in Figure 4.3a have evaporated, as indicated by the red circles in Figure 4.3a,b. Subsequent to the evaporation of these atoms, the intensity of the un-identified atoms increases above the identification threshold. Therefore, while not all atoms will be positively identified across all images in which they appear in, all atoms will be identified eventually prior to their evaporation by application of these values for the Gaussian filter and intensity cutoff.

Figure 4.3c plots the coordinates that were automatically detected in the first 80 FIM images, corresponding to the first crystallographic plane to evaporate from the surface of the specimen. To create the plot, the measurement of atomic positions is repeated across the first 80 images, and the detected atomic coordinates are effectively stacked in the 3D plot. The z coordinate in Figure 4.3c represents the serial number of the image in which the atoms were identified. For clarity only the first plane is shown here.

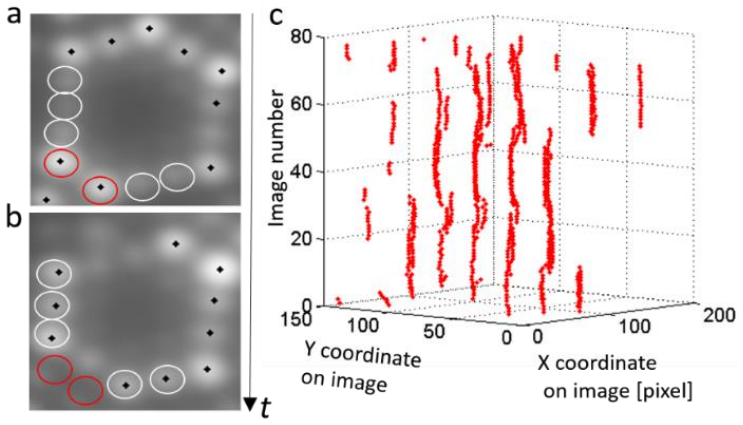

Figure 4.3: (a,b): Time ordered FIM images of the (222) pole. A Gaussian filter has been applied to remove high frequency noise. Intensity maximum points are identified and marked in black dots. (a) The intensities of atoms marked in white circles are below the set threshold. (b) As the evaporation process progresses, the atoms marked in red circles in (a) have evaporated, and the ones marked in white circles are now imaging with intensities above the identification threshold. (c) All atomic coordinates identified in the first 80 images, corresponding to the

evaporation of the first crystallographic layer. The x-y coordinates are set by the pixel coordinates, and the z coordinate at this stage represents the serial number of the image in which every peak was identified.

4.4.2 Consolidating contributions from individual atoms across the sequence

Once all intensity peaks have been identified across the sequence of images, the next step is to separate these signals into contributions from distinct atoms. The 3D 'point cloud' of information to be analysed at this stage represents every atom detected across all images, but is not the list of atom coordinates for the final reconstruction. Each atom will typically appear in multiple images from the time that it is first exposed at the surface until it is ultimately evaporated. In fact, the number of images in which each atom appears is dependent on its local field conditions and varies from atom to atom.

The association of a collection of identified intensity peaks with related x-y coordinates to a specific individual atom is carried out through analysis of the relative position of each peak both within the image plane and across the sequence of images. Under the influence of instantaneous field conditions, the imaged positions of atoms may shift from their original recorded positions and their measured position from one image to the next can thus change. The imaging intensity of each atom can also change from image to image, dropping below the threshold for identification at times. These changes make it necessary to use an adjustable tracking algorithm to identify and group together intensity points describing the same atom across different images.

4.4.2.1 Image-plane consolidation

First, peaks from all images are separated according to their x-y spatial coordinates (in the image plane). This is a challenging task in practice due to fluctuations in atomic coordinates of the same atom recorded from image to image. An example of such displacements can is shown in Figure

4.5a, where the coordinates of one atom across the entire sequence of images is seen to fluctuate. In order to identify the same atom as it is displaced between images, an estimation of atom image size is made, which is then used as a characteristic maximum distance separating two intensity peaks that can represent the same atom in different images. This atomic radius can be regarded as a measure of the spatial resolving power. If the distance separating the imaged coordinates of the same atom on two consecutive images is greater than the atomic size, then there is no way (automated or not) of knowing for certain whether this is indeed the same atom migrating more than one atomic site displacement between the two images, or whether these are instead two neighbouring atoms – one appearing right after the evaporation of the other.

A calibration of 'size' of the imaged atoms in pixels is carried out on each image, for each identified intensity peak. This calibration is done for every atom, on every image since as the evaporation process progresses, local magnification conditions change which impact on measured atomic sizes on the images. Thus, the last few atoms on a plane will often appear to image larger than other atoms previously evaporated from the same plane, and even larger than their own size on earlier images, where more atoms were present. Further, the total magnification of the image can also change during the evaporation process as the surface is evolving and the radius of the tip becomes larger. These two effects are demonstrated in Figure 4.4. The measured sizes of the atoms are defined here by the edge of a circular area surrounding identified atomic coordinate where peak intensity drops to 0.875 of the respective measured maximum. In Figure 4.4a the sizes in pixels of three atoms out of the remaining six atoms on the plane are marked. Figure 4.4b shows a very similar configuration, where the last six atoms on the imaged plane are marked. Figure 4.4b was taken at a later stage of the evaporation process, after

the removal of 30 layers. As can be seen from the measured sizes of atoms, the average size of an atom in this configuration has decreased as the magnification of the image decreases. In Figure 4.4c the same central atoms of the plane in b are shown. When comparing measured atomic sizes between b and c, a shorter time-scale local magnification effect becomes apparent. As neighbouring atoms are evaporated and the final three atoms of the plane are left on the surface, their imaged size becomes larger, with an increase in diameter of 53% (from 15 to 23 pixels) and 23% (from 17 to 21 pixels). Furthermore, it evident from Figure 4.4c that atoms on the same image can appear with significant size differences. Here, a terrace atom from a lower plane is seen, imaging at approximately 50% the size of the remaining three atoms on the plane above.

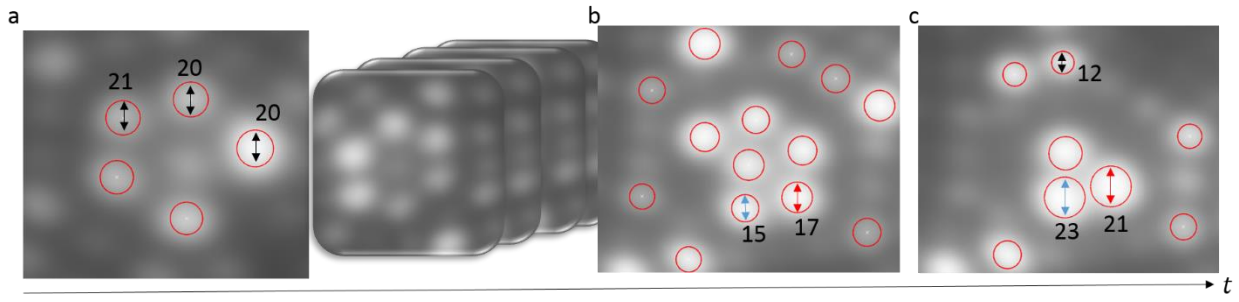

Figure 4.4 : Imaged atomic sizes as they change throughout the evaporation process. Size is defined here as a circle where intensity drops to 0.875 of the detected peak intensity. (a) Final six atoms on a plane with the measured sizes of three in pixels stated. (b) After the evaporation of 30 layers, the final six atoms of a plane are shown and have decreased in size due to decrease in magnification and increase in tip radius. (c) The same plane as in (b) is imaged, with the remaining three atoms. The coloured arrows in (b) and (c) match and represent the same atoms. It can be seen that their size has increased. Also can be seen in (c) that kink atoms from a lower plane are imaged with smaller size.

The defined 'resolution' distance (defined here as half the atomic size) provides a method for accounting for small displacements in the coordinates of the imaged atoms throughout a series of images, as demonstrated in Figure 4.5b. Each atomic coordinate is compared using this calibration distance to all atomic coordinates found on the consecutive image. Intensity peaks

that are found to be positioned within the defined x-y 'atom-sized' region will be grouped together at this stage as demonstrated in Figure 4.5c. Each colour represents a group of intensity points associated to the same atom-sized x-y region on the images. Note that atomic positions are compared between adjacent images, and not to the initial position in which the atom was first recorded. This is because recorded coordinates of atoms can gradually drift over a distance comparable to a characteristic atomic radius within the whole course of their exposure to the surface, but are unlikely to move by such a distance between adjacent images.

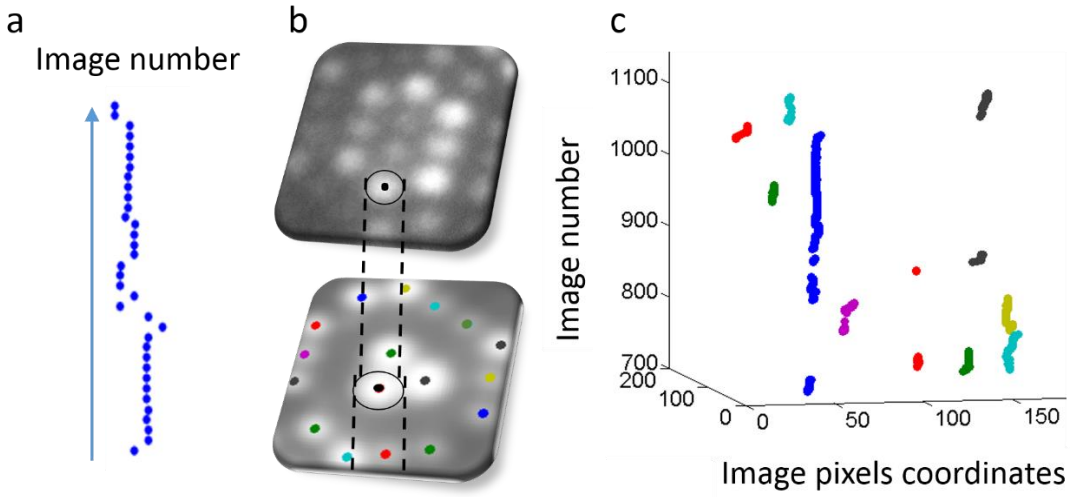

Figure 4.5: (a) Recorded coordinates of one atom across all FIM images it appears in. (b) For each measured coordinate the size of the atom around it is estimated and used to examine identified coordinates in the next image. (c) Selected atomic coordinates that are grouped together according to their x-y positions. Each colour represents a group of atomic coordinates classified as the same atom.

4.4.2.2 Planar separation

In the next step, the distribution of points within each group is examined with respect to the z direction. Figure 4.6 shows a close-up of one such identified group. It can be seen that this particular group does not continuously contribute a peak to every image across the sequence. The apparent discontinuities could of course indicate the evaporation of an atom, and the

subsequent imaging of another atom from the plane below. Hence, on first inspection the analysis in the z direction would seem to be straightforward; contributions in a sequence of images from the same atom can be separated in the z direction according to the identification of a discontinuity within each x-y group of points. Moreover, it would appear that by combining the integrated intensity measurement, exemplified in Figure 4.1c, the relative plane to which each atom originates can be deduced according to the image number in which it was lastly identified before the discontinuity. However, the analysis is not as simple as it would first seem. Frequent deviations from the simple model of layer-by-layer uniform evaporation sequence result in the need for a more sophisticated analysis and the intervals of integrated intensity alone cannot provide a reliable determination of the relative plane number for all atoms. Furthermore, instantaneous changes in field conditions, or the presence of impurities in gas atoms or in the system, can also cause the intensity of one atom positively identified in one image to temporarily drop below the detection threshold value in a subsequent image, which would yield a discontinuity such as shown in Figure 4.6. An example of such an atom 'blinking' between images, is marked with an arrow in the lower close-up in Figure 4.6, but could also extend over a larger number of images.

The continuously changing imaging intensity therefore necessitates a metric to define the minimum number of images that is likely to separate the imaging of two distinct atoms from different crystallographic planes, as opposed to the blinking of the same atom. Furthermore, this metric should not be a fixed constant across the whole sequence of images, since, as can be seen from Figure 4.1c, the evaporation rate at which an entire plane is evaporated varies significantly from plane to plane. To determine the appropriate metric, the time of occurrence of a blinking

event is correlated to the corresponding image on the integrated intensity plot. The metric required to separate an evaporation event from a blinking event can therefore be assessed with respect to the total interval width in the integrated intensity plot. In the example in Figure 4.6, a close-up view reveals that there are two relatively long breaks in the sequence between identification of intensity points in respect to the number of images describing the evaporation of the respective planes. This can be interpreted as two separate evaporation events as occurring in the sequence and the overall imaging of three distinct atoms. Thus, the blue group will be further separated into 3 atoms. In comparison, blinking, observable in the close-ups of Figure 4.6 is found to be relatively short to the determined metric and therefore the groups of atoms will not be further divided.

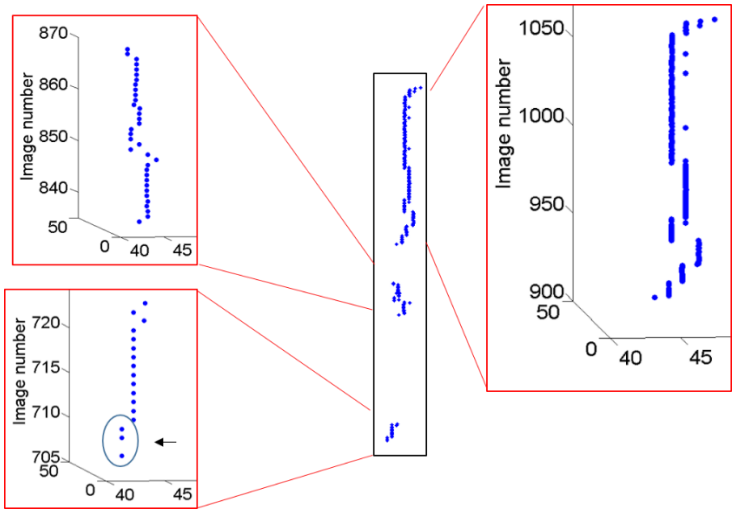

Figure 4.6 Zoom-in view on the blue group of peaks, actually describing three atoms that are placed in the same x-y region, in different crystallographic planes. This can be automatically concluded from the long pause in detection across the image series, corresponding to the evaporations of the separate atoms. A short intensity fluctuation 'blinking' event is marked with an arrow.

Finally, once all atoms have been tracked across all images, the total displacement in the recorded coordinates of each atom is calculated (displacement between the last and first recorded positions of the atom) as well as the duration of each atom on the surface (the number

of images it appears in). These can then be used to identify and resolve 'suspicious' atoms that seem to have very large displacements or are apparently imaged for very long durations in comparison to the lengths of their correspondent intensity interval, however these are highly uncommon.

4.4.3 Separation to crystallographic planes

The final step in the reconstruction procedure is placing the atoms in their correct crystallographic planes, or in other words, correctly determining their in-depth, z coordinate. Again, this is not a straightforward task due to the frequent divergence from the simplified 'layer-by-layer' evaporation sequence. According to this over-simplified model, a kink atom from an upper layer will evaporate prior to an atom in the layer below, and prior to an atom in the centre on the same plane. In this case, all that is needed to determine which atoms belong on the same plane is given by the plot in Figure 4.1c as atoms can be classified to the different layers according to the number of image in which they were last identified. However, the true nature of the evaporation sequence is that of a stochastic process. While centre atoms will rarely evaporate prior to a kink atom on the same layer in the absence of a close-by defect [188], it is more common for kink atoms from lower planes to evaporate prior to the removal of the entire atomic layer above them. Example of this behaviour can be seen in Figure 4.7. Atoms marked with the number '2' are kink atoms from a lower plane than the three central atoms marked with the number '1'. In Figure 4.7b, one of the kink atoms marked with a white arrow, has evaporated prior to the atoms from the plane above. In fact, out of all the atoms that were analysed for this study, approximately 27% were found to be such 'cross-layer' evaporation events.

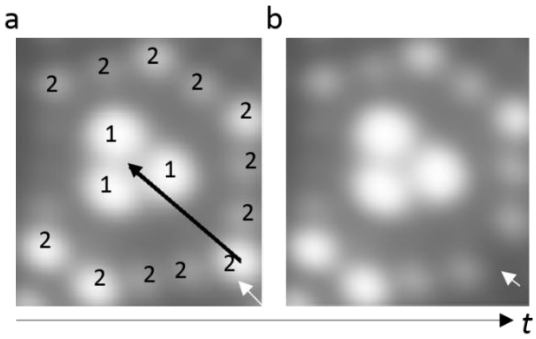

Figure 4.7: (a) Two planes are imaged here. The final 3 atoms from the higher plane are marked with the number '1', and outer terrace sites from the lower plane are marked with '2'. (b) An atom from a lower layer (marked with a white arrow) is evaporated prior to the three central ones of the upper layer. The two layers can be resolved by detecting decrease in intensity across the black line in a.

In light of these frequent deviations from an over-simplified 'layer-by-layer' evaporation model, a different approach must be taken to determine which crystallographic plane to assign to each atom. In the example in Figure 4.7, the outer terrace of the lower plane can be spatially distinguished from the final 3 centre atoms of the higher plane, by the 'dark' region in the image, separating the two. By examining the intensity profile across the black line in Figure 4.7a from the evaporating atom on the outer terrace to the centre of the pole, this dark region is evident. Such measurements were found to demonstrate highly consistent profile shapes in several atomic configurations. The characteristic configurations have therefore been incorporated into the reconstruction algorithm, and characteristic intensity and derivative behaviours of events breaking the 'layer-by-layer' sequence are used to identify such atoms. Figure 4.8 summarizes characteristic intensity profiles of repeating evaporation events. The profiles are always taken across a straight line from the atom at question to the centre of the pole, and are calculated according to intensities of pixels along this line on the image where the highest intensity was recorded for the atom (usually directly before evaporation). In Figure 4.8a, a characteristic profile is shown for an 'out of sequence' event. This intensity profile clearly demonstrates the decrease

in intensity corresponding to the transition across the image from a kink atom belonging to a lower plane to the central atoms contained within the plane above it. For comparison, Figure 4.8b shows the same profile for a terrace atom that obeys the simple layer-by-layer evaporation pattern, with its final imaging within the correct intensity interval of the plane on which it resides. Unlike the profile in a, the decrease in intensity towards the centre of the pole is not followed by an increase, since all the atoms from the plane above have already been evaporated, and thus do not appear in this image. The cases present in c and d however, demonstrate an additional complexity to the problem. Both atoms here exhibit very similar intensity profiles. However, while the atom in c is a central atom evaporating 'in sequence' with its plane, the atom in d is a kink atom from a lower layer, evaporating 'out of sequence' and ahead of central atoms of the plane above it. In order to distinguish between these cases, it is necessary to examine not only their intensity profiles, but also the corresponding derivatives of these profiles. This is illustrated by the black curves in Figure 4.8, on the same plot as their respective intensity profiles. It can be seen that an additional condition for the identification of an 'out of sequence' kink atom, is that the rate of intensity change along the transition between the two planes will be sufficiently large. This condition is specifically illustrated by comparing intensity profiles and their derivatives on the same figure as shown in Figure 4.8; the derivative should change significantly enough within the transition region between the two planes so that it then crosses the intensity profile when plotted on the same axes. The algorithm therefore scans for such profiles and derivatives shapes across all atoms examined. Once a 'cross-layer' event is identified, the atom will be assigned to the plane below the one under active consideration.

Note that the 'z' coordinate determined here represents the serial number of the crystallographic layer to which the atoms are assigned, from the surface and into the depth of the sample, in a direction normal to the plane. Thus, in the conversion from plane numbers to actual z coordinates, each layer will be separated from the next by the theoretical plane constant of the (222) plane spacing in tungsten. The x-y coordinates plotted until now had been described in 'image coordinates', corresponding to the image pixels where atoms were found to be located. These can be transformed from 'image dimensions' to real tungsten lattice dimensions by calibrating average interatomic distances to the corresponding theoretical values on a tungsten (222) plane (Details on the exact calibration process can be found in chapter 6).

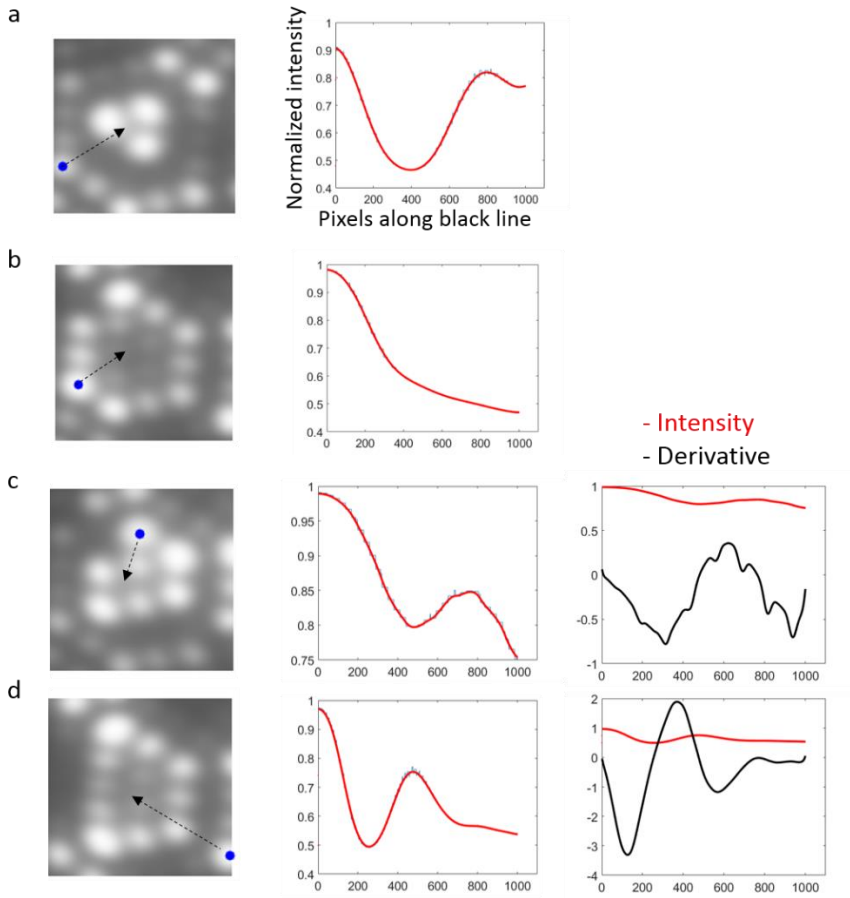

Figure 4.8 : Characteristic evaporation patterns for kink and central atoms. In red plots are intensity profiles of the atoms marked in blue, across black arrows, connecting the atom to the centre of the pole, on their highest intensity image. (a) Terrace atom evaporating 'out of sequence'. (b) Terrace atom evaporating in sequence with this plane. (c) Central atom evaporating in sequence, exhibiting similar intensity profile to the 'out of sequence' terrace atom in (d).C and d can be distinguished by the intersection behaviour of the intensity and derivatives along the black arrows.

To summarise the method, Figure 4.9 shows all the key stages of this reconstruction approach as applied to all of the analysed images. Figure 4.9c presents the final reconstruction, once all atoms have been identified, tracked, and placed in their crystallographic planes. During the analysis, positions of atoms on all images they appear in are recorded. For the final reconstruction, only one coordinate per atom is chosen. Here all atoms are placed in the initial positions, corresponding to the positions recorded for each atom on the first image in which detected.

Alternatively, final positions of atoms can be chosen, or any other along the way. The difference between initial and final coordinates can be seen in the 'close-up' view of plane number five in Figure 4.9d. Further discussion on the origin for this discrepancy can be found in chapter 5. Note that as the final reconstruction is rotated and tilted, additional crystallographic planes other than (222) are also clearly resolvable as demonstrated in Figure 4.9e. It is also important to note that it is only the evaporated layer number that sets the depth coordinate here, without incorporating the tilt angle of the surface with respect to the tip axis. Such reconstruction will result in a slight 'shear' of the reconstructed data.

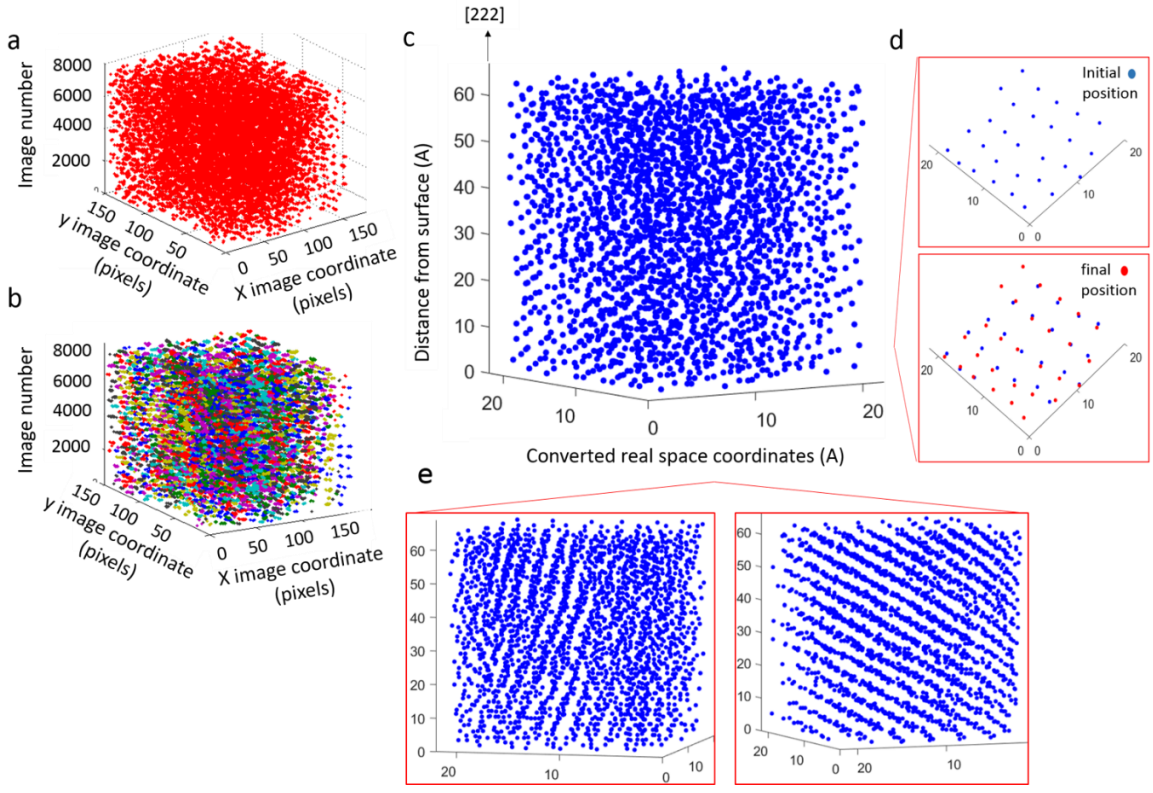

Figure 4.9: The three steps of reconstruction demonstrated across the entire analysed data set: (a) Intensity peaks are identified on all images. (b) Intensity peaks are grouped according to atoms. (c) Final reconstruction: each atom is positioned in its crystallographic layer in its initial position, coordinates converted to real space. (d) The 5th plane is shown. Initial positions (blue) of the atoms on this plane and final positions (in red) are shown together for comparison in the lower window. (e) As the final reconstruction is rotated and tilted, additional crystallographic planes are evident

5 Sub-angstrom displacements of atomic coordinates

5.1 Introduction

As field conditions change from image to image, lateral displacements in recorded atomic coordinates are observed. These displacements are discussed in chapter 4 with regards to the reconstruction process, as they necessitate a tracking algorithm to identify the same atom across different images. The algorithm allows high resolution tracking of these very subtle sub-angstrom displacements. Note that these displacements will be referred to in this chapter as 'atomic displacements', however, they are in fact displacements in the imaged positions of the atoms on FIM images, and cannot yet be determined as representing actual surface atoms displacements.

Measurements of atomic movements in FIM have previously been utilised to great effect to track the successive positions of atoms during surface diffusion [189]–[191] and laser illumination [192]. However, the displacements measured in this study represent subtler effects.

While atoms appear to constantly change their positions slightly between images, a more prominent effect is detected in the local neighbourhood around the former location of an evaporated atom directly after its removal from the surface. Atomic displacements on the surface of the sample prior to evaporation are a known phenomenon [193]–[196], having been recognized as a limiting factor in the spatial resolution of the atom probe.

In this chapter, a detailed study into the nature of the movements following evaporation events is undertaken, and their possible origin is discussed. The displacements in recorded atomic positions are analysed quantitatively, characterising their average size and their dependence on

the voltage applied, atomic imaging intensities and the remaining number of atoms on the plane in question.

5.2 The phenomena

A prominent example of the effect of nearest neighbour evaporation on such displacements is seen in Figure 5.1 a–c. The last remaining 6 atoms on one of the (-222) planes of a tungsten tip are shown with their peak intensities tracked across a series of FIM images in Figure 5.1 c, from the point when only those 6 atoms remained on the surface and until the first one of these atoms is evaporated. The position from which this single atom was observed to evaporate is marked by the green circle in Figure 5.1a, while its imaged position is tracked across the series of images and is presented in green in Figure 5.1c. Upon evaporation of this atom, the imaged coordinates of the five remaining atoms are displaced towards the final location of the sixth prior to field evaporation, with the relative magnitude of this displacement correlating with each atom's proximity to the position of the evaporated atom. The sizes of the displacements are expressed in percentage units relative to the average nearest neighbour distance (NN) measured across all images prior to evaporation, with the largest displacements estimated at 0.5 Å (estimated by calibration to the theoretical nearest neighbour distance on the (222) plane, equal to 4.4Å. Of course the accuracy of this estimation is also affected by precisely these movements, limiting the resolution of FIM, as will be addressed later in this chapter). The converted size of the displacements to real space coordinates can be seen in Figure 5.1b. Since the imaged positions of the atoms are constantly changing, even prior to evaporation, the average displacement of the 5 remaining atoms was calculated prior to the evaporation of the green atom across the same

range of images. It was found to be 1.8 % of the nearest neighbour distance, and is considered as the error estimation for the post-evaporation displacements shown in Figure 5.1a.

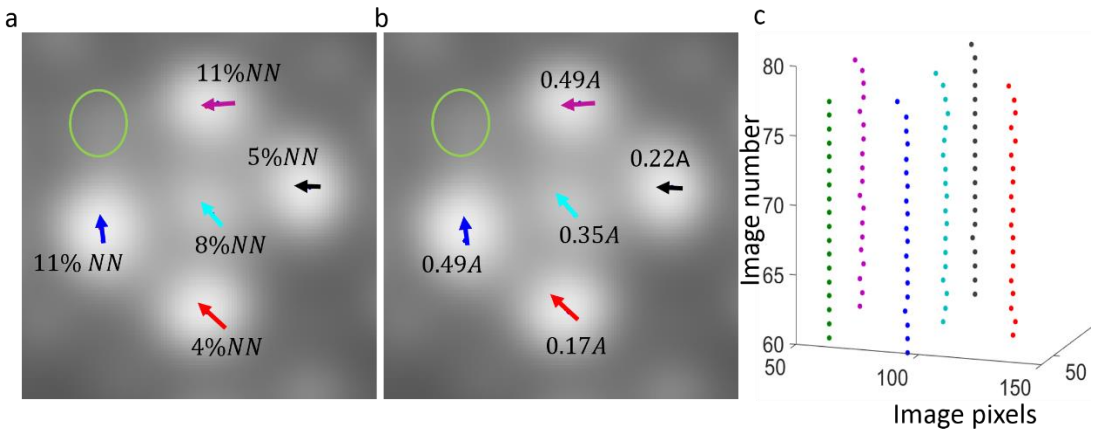

Figure 5.1: Displacements of atomic coordinates post an evaporation event. (a-b) The last five atoms to evaporate from a (-222) plane of a tungsten sample. The green circle marks the location of the sixth atom of this layer, before it had evaporated. The arrows mark the displacement direction of the remaining atoms. The displacements are converted to real space coordinates in (b) according to the average NN distance. (c) Tracking of the atom's positions across all images from the moment where only they are left on the plane, and until the green atom evaporates. The colours in which they are plotted match the colours of the arrows in (a,b), to symbolize the same atoms in all 3 images.

Figure 5.1 highlights two important facts. Firstly, atoms (or atom's images) react to the evaporation of another atom in their vicinity in a very small movement towards the evaporated atom. Secondly, by utilizing the reconstruction code on FIM data, it is possible to detect and measure these displacements.

5.3 Experiment

The experimental data used here for the analysis of the displacements is the result of the same experiment and the same sample tested in chapter 4, with the (-222) pole analysed this time.

The threshold value for detection of an atom has been reduced in the code to the minimal value (40% of maximum intensity) that does not trigger false identification of atoms in the small

analysed volumes. As a result, the presence of an atom at the surface will be automatically identified by the algorithm in FIM images earlier than when using a higher threshold. This is done in order to increase the number of position measurements for the analysis.

5.3.1 Quantifying the phenomena

In order to examine the consistency of this effect, and to quantify any correlation between the number of remaining atoms on the plane and the resulting magnitude of the displacements, the same analysis described above was repeated 3 times for the same plane, tracking the displacements of atoms after the rate-controlled evaporations of the final 7, 6, 5-4 atoms (atoms number 4 and 5 evaporated within a time difference too small to be resolved by the frame rate in which images were taken), respectively. Each interval described in Figure 5.2-Figure 5.3 represents a series of images starting with the first image recorded after the evaporation of one atom, and ending with the first image recorded after the evaporation of another. For each image interval the following information is displayed:

- 'displacement after evaporation' – the position difference measured between the first image after evaporation and the last image before evaporation. Distances are presented here as measured, in pixels.
- 'average displacement before evaporation' – displacements measured between consecutive images over image interval between evaporation events. This number is used to estimate the error of the evaporation displacement measurement, can be considered as 'background displacements noise'.
- 'intensity before / after' – intensities of the remaining atoms before/after evaporation.

5.4 Results

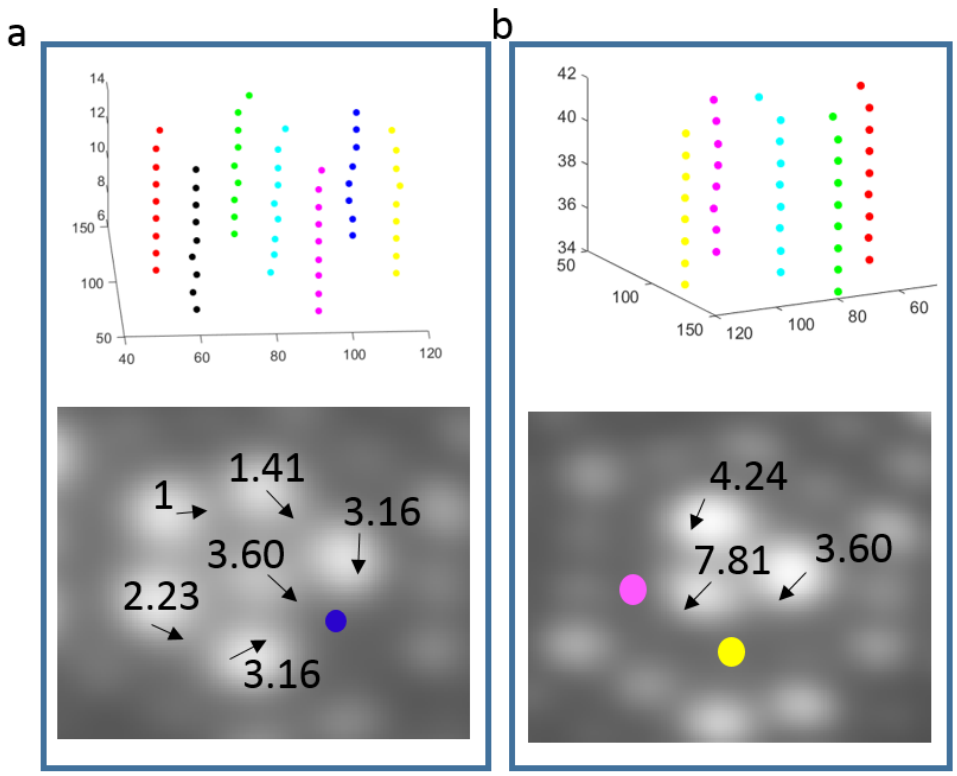

	Displacement after evaporation [pixels]	Intensity ratio after/before evaporation
●	3.16 ± 0.48	0.89/0.86=1.03
●	2.23 ± 0.43	0.91/0.89=1.02
●	1 ± 0.83	0.85/0.85=1
●	1.41 ± 0.14	0.85/0.79=1.06
●	3.16 ± 0.48	0.88/0.82=1.07
●	3.6 ± 1.15	0.76/0.68=1.11
●	± 0.8	/0.87

	Displacement after evaporation [pixels]	Intensity ratio after/before evaporation
●	3.60 ± 0	0.96/0.94=1.02
●	4.24 ± 0.57	0.97/0.93=1.06
●	7.81 ± 0.85	0.86/0.78=1.02
●	± 0.71	/0.94
●	± 0.14	/0.93

Figure 5.2 : (a,b) Post evaporation displacements in positions of the last remaining 6 and 3 atoms respectively of the same plane. The evaporated atoms are marked on the FIM images, in the same colour code as the respective coordinate maps and tables. Atoms closest to the evaporated atoms are displaced the most. Error estimations are done by averaging the displacements recorded for each atom on images between evaporation events.

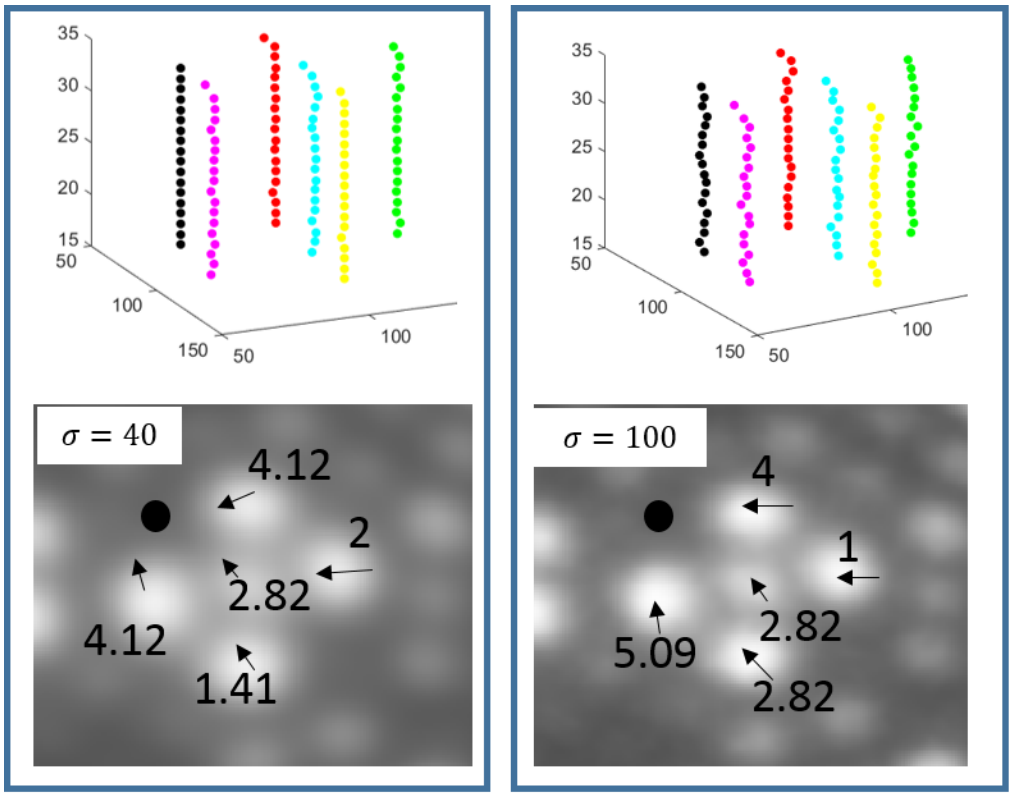

	Displacement after evaporation $\sigma = 40$ [pixels]	Displacement after evaporation $\sigma = 100$ [pixels]	Intensity ratio after/before evaporation $\sigma = 40$	Intensity ratio after/before evaporation $\sigma = 100$
●	1.41 ± 0.11	2.82 ± 1.23	0.91/0.89=1.02	0.97/0.95=1.02
●	2 ± 0.92	1 ± 1.33	0.9/0.87=1.03	0.97/0.94=1.03
●	4.12 ± 0.82	5.09 ± 1.41	0.93/0.91=1.02	0.97/0.96=1.01
●	4.12 ± 0.64	4 ± 0.81	0.88/0.83=1.06	0.94/0.90=1.04
●	2.82 ± 0.87	2.82 ± 1.45	0.77/0.74=1.04	0.81/0.79=1.02
●			/0.87	/0.94

Figure 5.3 : Post evaporation displacements analysis of the last remaining 5 atoms. The data was analysed twice, one with a Gaussian filter level of $\sigma = 40$, the standard filter used for reconstruction, and once with a reduced filtering level of $\sigma = 100$. While the absolute size of the displacement in pixels is slightly changed, the general phenomenon is consistent in both cases.

By examining Figure 5.2 and Figure 5.3, several trends are easily detectable. Firstly, it becomes evident that this is a highly repeatable, prominent effect, detected with every evaporation event. This is further confirmed by examining the error estimations on the displacements measurements. These errors are the average displacements of the atoms between evaporation events, and are clearly smaller than the displacements measured immediately after an evaporation event, meaning the post evaporation displacement measured is above the 'displacement noise level'.

There does not seem to be a very consistent correlation between the intensity of the imaged atoms before and after evaporation events, and the extent of their displacements. In some cases, atoms that are displaced the most will have also experienced the larger increase in intensity after evaporation of a neighbour, but this phenomenon is not very consistent throughout these limited statistics. There also does not seem to be a very strong indication that the atom that exhibits the highest intensity on the image prior to an evaporation event is the atom that necessarily evaporates, but this could be due to the resolution response time of the camera (sometimes the evaporated atom will exhibit a stronger intensity one image before), and the probabilistic nature of the field evaporation phenomena.

The overall magnitude of the displacements of all remaining atoms appears to increase with increasing proximity to the final position of the evaporated atom, with the nearest neighbour displaced the most. Additionally, the displacement also appears to depend on the number of remaining atoms on the plane. As this number becomes smaller, the displacements measured are larger reaching ~8 pixels for the last remaining three atoms, as opposed to 3-4 pixels measured for NNs in case of 6 remaining atoms (however the 8 pixels' displacement was

measured after the evaporation of more than one atom). In order to eliminate any possible local magnification bias to the displacements measurements that might occur as fewer atoms are left on the plane, Figure 5.4 shows the displacements for each of the three evaporation events analysed in Figure 5.2-Figure 5.3, normalized for each atom by its radius size in pixels (as measured right after the evaporation event). The radius is taken here as defined by a circular area around the centre of the atom in which intensity drops to 0.875 of the peak intensity. As can be seen from Figure 5.4, all previously stated trends regarding the size of the displacements are still observed for the normalized displacements.

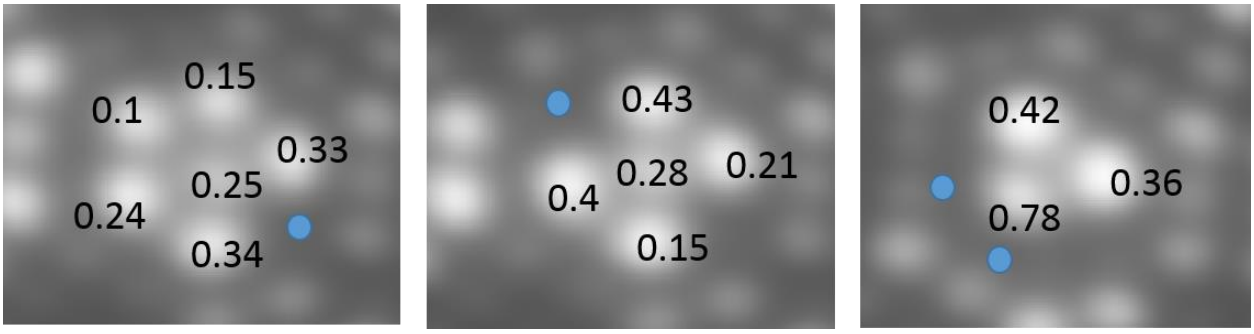

Figure 5.4 : Normalized displacements for the three evaporation cases analysed above. Blue dots correspond to the coordinates of the evaporated atoms. The size of the measured displacements after evaporation events is normalized here according to the size of each atom (estimated as a circular region around the peak intensity point of the atom where intensity drops to 87.5%).

Furthermore, in order to rule out any unintentional influence that the filter used on the images for analysis might have on this effect, evaporation events were examined twice. Once with the standard degree of smoothing used for the reconstruction code as conventionally applied, and then repeated using a lowered degree of filtering. The Gaussian filter is defined as

$$GF = e^{-\frac{\left(x-\frac{w}{2}\right)^2+\left(y-\frac{h}{2}\right)^2}{2\sigma^2}}$$

where w, h correspond to the width and height pixels dimensions of the image, and σ determines the width of the filter. The two cases examined are $\sigma = 40$ (the higher level of filtering usually employed for the 3D reconstruction), and $\sigma = 100$. The comparison has been made on all cases examined between the two filters, however, as a demonstration, results are presented here in Figure 5.3, for the case of the 6th atom evaporation. It can be seen from the comparison that the 'displacement background noise' is larger with the lower level of filtering, but that the effect is still visible, and all identified trends are still evident.

Next, some statistics were generated on NN distances for each evaporation case before and after evaporation, to try and detect any trends towards a more (or less) 'ordered' configuration. These are summarized in Table 5-1. For each configuration of atoms, the NN distances were measured on the first image where only those atoms (including the atom to be evaporated) were present on the surface, and then a second time on the first image after the evaporation event. For each configuration, only the NN distances between the atoms remaining on the surface are calculated, not including the evaporated atom, so that a direct comparison can be made of before and after evaporation. The variance and standard deviation are then calculated for each case respectively as well as the 'normalized standard deviation' given by $\sigma_N = \sigma/\sqrt{N}$, where σ is the standard deviation and *N* is the number of NN distances measured. The normalized standard deviation is given to better compare the results as different number of atoms are analysed.

Number of atoms left on plane	Average NN distance before evaporation [pixels]	Variance/standard deviation before evaporation	Normalized standard deviation before evaporation	Average NN distance after evaporation [pixels]	Variance/standard deviation after evaporation	Normalized standard deviation after evaporation
6	35.8	9.04/3.0072	$\frac{3.0072}{\sqrt{9}} = 1.0024$	36.04	20.03/4.47	$\frac{4.47}{\sqrt{9}} = 1.49$
5	35.57	20.42/4.51	$\frac{4.51}{\sqrt{6}} = 1.8412$	35.55	23.5/4.85	$\frac{4.85}{\sqrt{6}} = 1.98$
3	34.39	23.74/4.87	$\frac{34.87}{\sqrt{3}} = 2.8117$	36.08	14.05/3.75	$\frac{3.75}{\sqrt{3}} = 2.165$

Table 5-1 : NN statistics before and after every evaporation event.

The most obvious trend apparent from Table 5-1 is that both the standard deviation, and the normalized standard deviation increase as the number of atoms that remain on the surfaces decreases. This, in turn, could indicate that the structure is closer to that of a theoretical lattice when more atoms are present on the plane. It could indicate that with every evaporation event, the balance of inter-atomic forces characteristic to that of a perfect crystal structure changes, resulting in a slightly more distorted structure. For the cases with 6 and 5 atoms remaining, it is also evident that post-evaporation, the standard deviations increase relative to before the evaporation event. This could indicate the same phenomena, as before evaporation an extra atom was present on the surface (even though it was not included in the statistics), and was contributing to a more balanced structure. However, this is not the situation for the final evaporation event where three atoms are left on the surface. Here the standard deviation

decreased after evaporation of two atoms. It could be that the last remaining 3 atoms of a plane are in a somewhat unstable state and will possibly yield less consistent results.

5.4.1 Voltage effect on displacements

Finally, a comparison has been made between the 'regular' and post evaporation displacements of atoms from two (-222) planes, at different voltage conditions.

The two planes selected here are of the same pole, only a few crystallographic layers apart, to minimise the influence of any other possible parameters. They were chosen such that the evaporation sequence in both is as similar as possible going from five to four and three atoms. The four atoms configuration seems to be significantly less frequent at low voltage conditions, and while it was easily found in the high voltage conditions, was difficult to achieve at low voltage conditions. The rate of evaporation is therefore different between the two cases, where in the low voltage case there are less readings between the 4-3 atoms transition.

The two analysed planes are seen in Figure 5.5, along with the very clear voltage increase between them. The voltage increase can be identified due to the lowered contrast between the atoms on the image, the higher background intensity, and the general blurring effect on the image. The last atoms on the plane right after voltage increase are analysed and compared to the last atoms on a plane separated by one crystallographic layer, imaged before the voltage increase. Note that a contribution to the contrast difference between beginning and end of an evaporated layer could also arise from the fact that the pulse fraction used for evaporation is elevated as the evaporation progresses. However, since the evaporation processes discussed here are only of a few atoms per plane, this effect is expected to be very small.

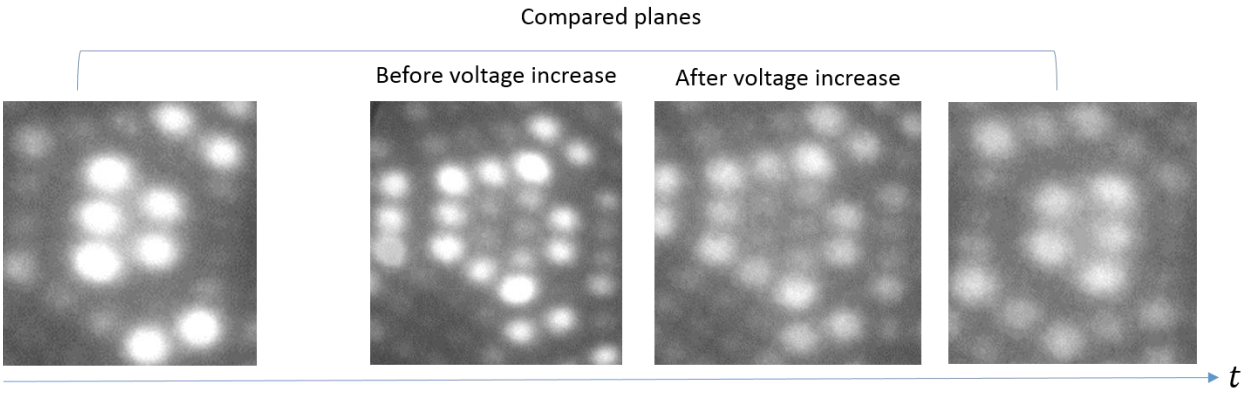

Figure 5.5: Voltage comparison: The compared (-222) planes are separated by one plane. In the middle, the same intermediate (-222) plane before and after voltage increase. The voltage increase beyond the best imaging field is evident in the lessened contrast between the atomic features on the plane, and the increased overall background intensity level.

The average displacements between evaporation events as well as the instantaneous displacements immediately after evaporations have been recorded for both planes, and are presented in Figure 5.6. The displacements are presented as normalized displacements according to the imaged atomic radius measured right after evaporation. This is to eliminate any magnification/ blurring effects that might be caused by the change in the imaging voltage. As can be seen, the general trend discussed in the previous section of this chapter is apparent in both voltage cases. The atoms closest to the evaporated atom are displaced by the largest amount. However, there is no definite, consistent trend to the difference between the high voltage and low voltage cases (this is also the case for the un-normalized results). The average normalized displacements are also shown as measured for the last remaining three atoms in both cases, across the same number of images. Here, too, no significant differences are observed between the two cases.

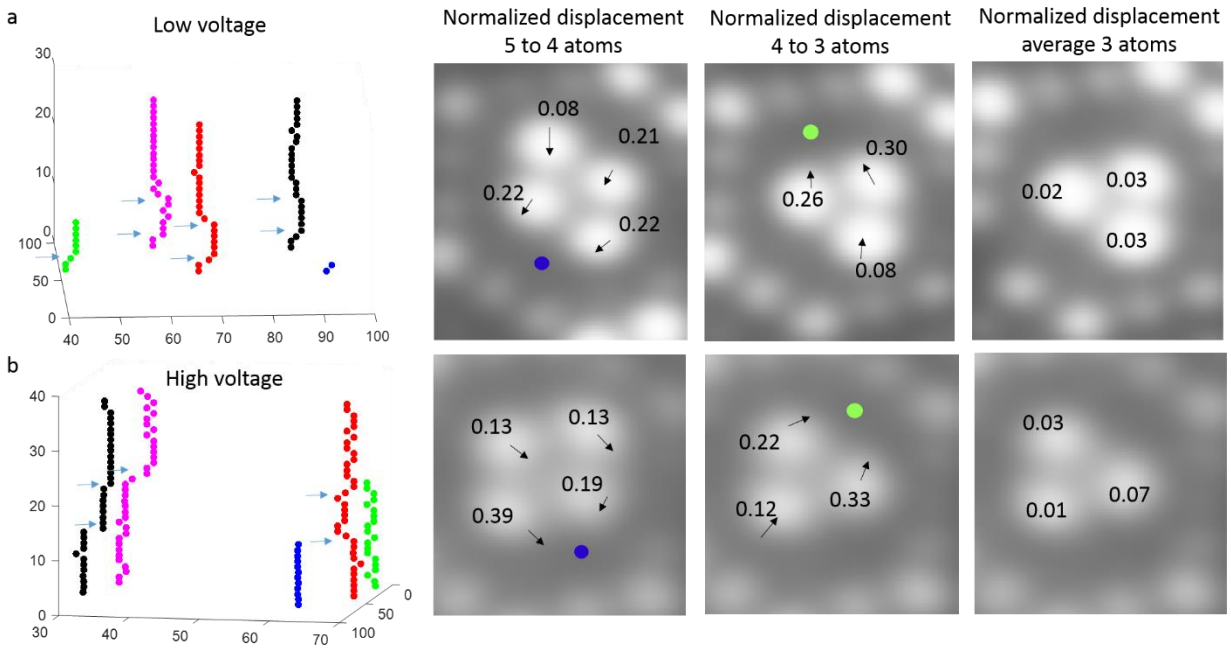

Figure 5.6 : Voltage effect on displacements. (a,b) Low and high voltage imaging of (-222) planes respectively, showing the displacements after evaporation of the last 5th and 4th atoms. The evaporated atoms are marked on the images with the same colours as they appear on the coordinates plots on the left. The average displacements of last three atoms are shown for each plane on the right. The displacements are normalized by the size of the atoms.

5.5 Origins of the measured displacements

The question remains as to the precise origin of these displacements. To address this, one must discriminate between the displacements measured continuously from image to image (these displacements are regarded here as the 'error' estimation) and the larger displacements following evaporation events. The more commonly observed, smaller displacements most likely originate from experiment limitations. The imaging gas statistics that contribute to every spot on every image are an important factor to consider. Each spot is generated by a large, yet finite number of helium atoms evaporating from the vicinity of the same surface atom. Each of those will have an inherent Heisenberg uncertainty in position as well as some lateral momentum and thermal agitation [12]. In addition, there exist several scattering mechanisms for the helium atom en route to the detector, including scatter due to trajectory change resulting from lateral thermal

energy distributions, and slight scatter from the channel plate. Other than statistics, it is also important to acknowledge that the precise theoretical field adsorption behaviour of the gas is not fully understood. Multiple sites for gas absorption representing the same atom, as well as the presence of helium atoms above the directly adsorbed layer could potentially influence the final imaged coordinate of atoms [101].

However, by all the numerical demonstrations shown above, it is clear that a more significant, larger scale effect is occurring with each evaporation event. One possible explanation for the post evaporation displacements is that these are in fact displacements in the 'imaged' coordinates originating from artefacts due to how the imaging gas atoms arrange themselves on the surface, i.e. the actual configuration of atoms on the surface remains the same, however, the image is changing. Imaging gas atoms adsorbed on atomic sites on the surface will have induced dipole moments, repelling one another, that could cause the adsorbed gas atoms to be slightly displaced outward of the centre of the pole. It is possible that as one of the atoms evaporates, gas atoms adsorbed on the remaining atoms will relax their positions, and may result in such displacements. While the surface binding energy of tungsten atoms is 8.6eV [197] (likely to change as atoms are evaporating), the binding energy of a field adsorbed helium atom is 0.14eV [198]. These numbers suggest that the tungsten atoms are kept in their place more strongly than the imaging gas atoms and so could support the case that these displacements are indeed caused by image gas relaxation.

An alternative option can be the actual re-arrangement of the tungsten atoms themselves. Previous FIM [194] and field desorption studies [196] have indicated atomic movement of the evaporated atom prior to evaporation. In [196] and references therein, a broad review about this

type of phenomena can be found. Discrepancies between FIM and desorption images of the (110) pole in tungsten were explained by a roll-up motion that kink ions perform prior to their evaporation, assuming a short-lived metastable position. The motion was found to depend on the NNs configuration of the evaporated atom, as these induce polarization forces on the rolled atom, determining its movement direction and the tangential kinetic energy it may acquire during this movement. This energy in turn could change the atom's trajectory to the screen. Unlike previous work, the study in this chapter focuses on the displacements of NNs to the evaporated atom, however the work discussed in [196] reinforces the possibility that such movement of surface atoms is possible under characteristic FIM experimental conditions.

To try and resolve the possible effects of gas atoms reactions and atomic movement experimentally, evaporation behaviours in different voltage conditions were examined, with no consistent changes found. As the DC voltage is raised, the reduced contrast of the FIM image indicates that gas atoms are ionized from more sites on the surface, as well as from a further and larger area above the atoms. This will cause a reduction in gas supply to each specific atomic site. In case the displacements observed are the result of gas atoms relaxation, increased voltage could potentially reduce the observed displacements. The fact that no significant change has been observed reinforces the option that these displacements correspond, at least in part, to an additional effect other than image gas movement, such as movement of actual surface atoms.

Finally, a third mechanism for the observed displacements could involve little to no displacement of gas atoms or surface atoms, and potentially result from the very quickly changing equilibrium charge distribution post an evaporation event. This in turn can result in changes to the location

of the ionisation zone above near atoms, and in the observed displacements. Out of the three possible mechanisms, this is probably the one occurring on the fastest time scale.

Of course the three possible explanations suggested here are not mutually exclusive, and may contribute both to the observed displacements. Molecular dynamics simulations may prove successful in describing such a system and resolving the origin of the observed displacements, and are therefore to be considered a possible next step. Atom-probe simulations are currently incorporating these effects in order to yield more accurate ion trajectories calculations and ultimately more accurate reconstructions [199]–[201], [171]. The approach employed in [200] where the local charge distribution is recalculated with the evaporation of every atom is particularly interesting to consider to simulate the results observed in this chapter. If the displacements observed in this study are in fact describing the movement of tungsten atoms, then this type of FIM analysis demonstrates the potential to directly measure and quantify this effect as well as a range of atomic interactions. By resolving the gas contribution, insights into the field adsorption mechanism of the gas are also possible.

6 Investigations of distortions in reconstructed FIM volumes

6.1 Introduction

When closely examining the resulting reconstructed 3D structure in chapter 4, it becomes evident that it deviates from the expected crystallographic structure. It was demonstrated in chapter 5 that atoms move on the surface of the specimen prior evaporation. At which point, then, do the observed coordinates reflect the true position of the atom, the one which is the closest to its expected lattice site, and how compatible are those two positions?

The automated reconstruction procedure enables the quantification of the deviation from the theoretical structure at specific time points. Here we address the dataset reconstructed in chapter 4, a defect-free volume taken from the (222) pole of a tungsten sample, and by considering the initial and final positions recorded for every atom, evaluate the distortion of the structure in each case by analysing the nearest neighbours distance distribution. This procedure is done to estimate the distortion level in the reconstructed volume, but is also useful to perform an as accurate as possible calibration of image pixels to real space coordinates, considering all measured NN distances.

Next, a wider analysis is done in the form of spatial distribution maps, which spans across atomic distances in the entire dataset. SDMs are also calculated for a different pole, the (-141) pole, to examine crystallographic effects on the distortion measured.

Finally, a comparison is made between the reference dataset from the (222) pole, and a dataset containing vacancies, taken from the (-222) pole of the same tungsten sample. This comparison will provide insights into the contribution of single vacancies to distortion of the final reconstructed structure.

The distortions analyses presented in this chapter are preliminary and explore the new probe now available with the atomistic reconstruction into the image formation mechanisms in FIM. In combination with the results in chapter 5, these lay ground for future work shedding light into the complexity of the FIM experiment, with the final image depending on both surface processes, surface-gas interactions, and the ionization zone above the atoms.

6.2 Nearest neighbour's analysis

Due to the imperfect nature of the reconstructed planes, identifying all 'theoretical' nearest neighbours of every atom is not a straight forward task, precisely because the atoms are not consistently spaced from each other in accordance with a crystal structure. In Figure 6.1a, one of the reconstructed planes is shown with the atoms in their final coordinates. Atoms in red mark the six closest NN's found for the atom highlighted with a circle around it. As can be seen, one of these (marked with an arrow) is not a correct 'theoretical' NN, however its distance was found to be shorter than the true last NN of the atom. Therefore, a code was written to locate the theoretical NN's of all detected atoms, taking into account their angular spread, and will be briefly explained in the appendix 1. The correct NNs found by the algorithm can be seen in Figure 6.1b.

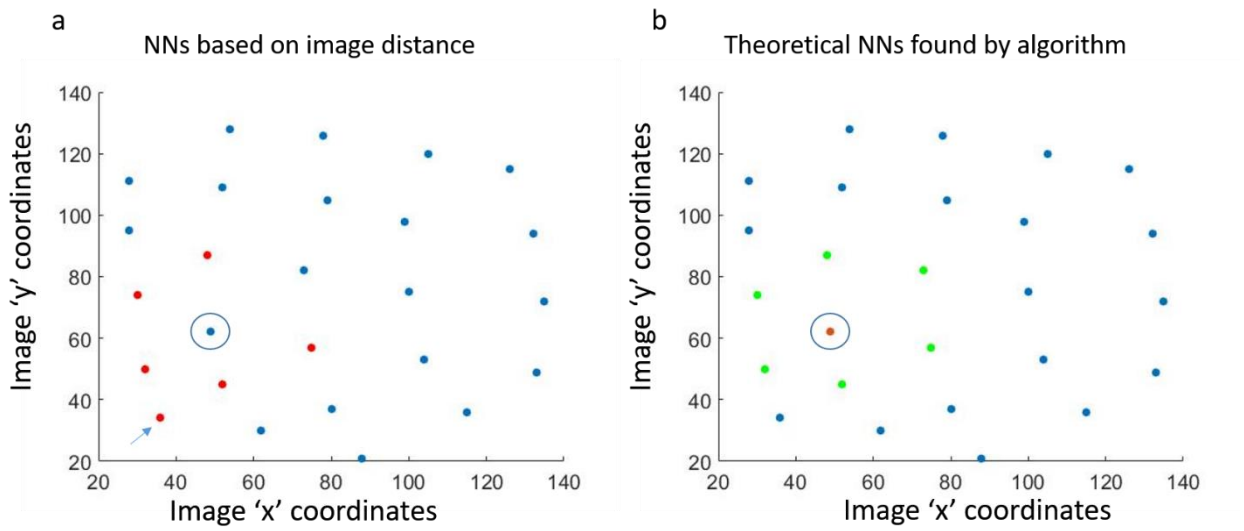

Figure 6.1: (a) Reconstructed (222) plane. In red are the six closest atoms found to the central atom marked with a circle. The one marked with an arrow is not compatible with the crystallographic NNs. (b) Marked in green are the NNs found by an algorithm written to identify the 'theoretical' NNs defined by the crystallography.

Note that the NN analysis is performed only with regards to neighbouring atoms from the same XY plane. This is due to the fact that the 'Z' coordinate was set 'artificially' here to be equivalent to the known d-spacing of the corresponding plane, and is not a measured quantity.

Firstly, the average distance of NNs is employed in order to re-calibrate distances from image pixels into real space coordinates. The NN distances were measured across the whole data set for both initial and final positions of the atoms, employing the algorithm described in appendix 1. The dataset referred to here is the one reconstructed in chapter 4, consisting of 69 crystallographic tungsten layers similar in size, containing 2450 tungsten atoms altogether (average of 35 atoms per layer). The results are shown in Figure 6.2. For each of these cases, the average NN distance in pixels was used to calibrate the measured NN distance in pixels to the theoretical $d_{NNtheoretical} = \sqrt{2}a, a = 3.16\text{Å}$, as can be seen in the lower parts of Figure 6.2a, b for final and initial positions respectively.

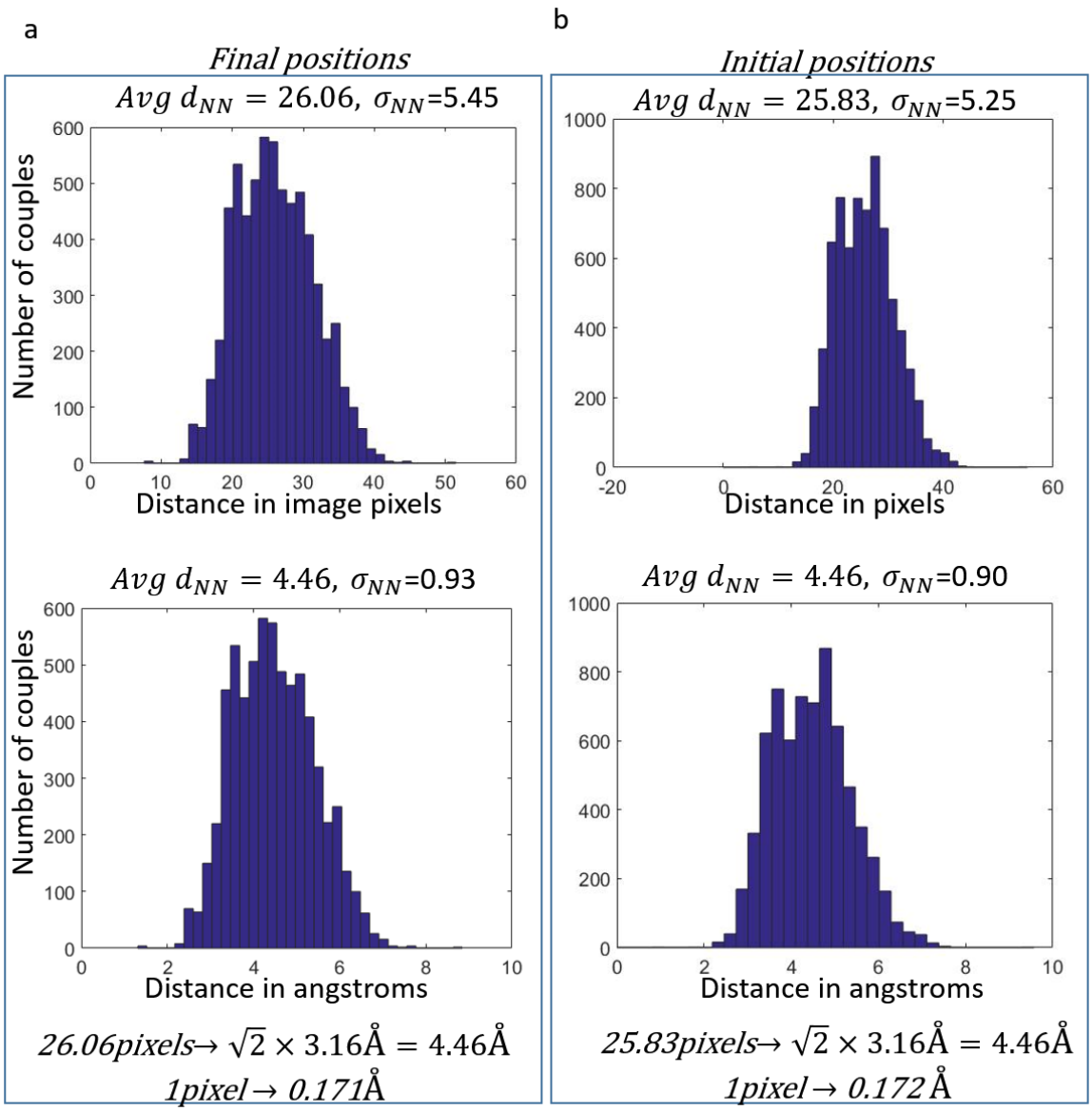

Figure 6.2 : Nearest neighbours distance histograms of recorded atomic coordinates of final (a) and initial (b) atomic positions. The average of the distance in pixels is used to calibrate the data so to match the theoretical NN value on the (222) plane in tungsten.

Comparison of the two distributions (final and initial) reveals no major differences. The average NN distance pixel value shows almost no difference between final and initial positions. The more interesting point of comparison is the standard deviations of the two distributions. The narrower the distributions are, the better the reconstructed structure fits the expected theoretical value.

By comparing the standard deviations of the two results, it can be seen that here too, the two are very similar. There is a 4% difference between the two cases, where the final positions distribution was found to be slightly wider.

Further, the NN distance was computed along the x and y axis separately. The results are given in Table 6-1. As can be seen, in both cases of final and initial coordinates there exists an asymmetry between the two directions, with the distances measured along the x axis found to be ~ 13% longer than the averaged distance measured in the y direction. The variance in the measured distances along the x direction was found to be significantly larger than in the y direction. The x-y axes are defined as the image axis and are marked on the FIM image in Table 6-1.

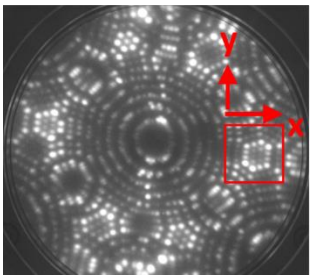

	NN distance in X direction		NN distance in Y direction	
	Initial positions	Final positions	Initial positions	Final positions
Average [pixels]	16.99	17.16	14.98	15.08
Variance/standard deviation	129.2/11.36	129/11.36	57.28/7.56	57.92/7.61

Table 6-1：A-symmetry is observed between the x and y directions in the reconstructed structure of the (222) pole. NN distances in x are found to be longer and wider distributed than in the y direction for both final and initial coordinates.

6.3 Spatial distribution maps

As a wider estimate of the distortion of the structure, spatial distribution maps were calculated. Spatial distribution maps (SDMs) are commonly used in atom probe reconstruction to identify the limited amount of crystallographic information retained by the analysis and then adjust the reconstruction calibration parameters accordingly. The concept of spatial distribution maps is explained in chapter 2. SDMs were calculated for the FIM reconstruction using both final and

initial atomic imaging positions, and are presented in Figure 6.3 a, b respectively. For each case, three cross sections are shown, describing the distribution of measured atomic separations for a constant zero distance in either x, y, z direction. For example, the $\Delta z = 0$ cross section shows the distribution of distances and directions measured on the x - y plane for atoms that are on the same plane, meaning, that have the same z coordinate. As can be seen once again, the two cases of initial and final positions are very similar, and neither is apparently preferential.

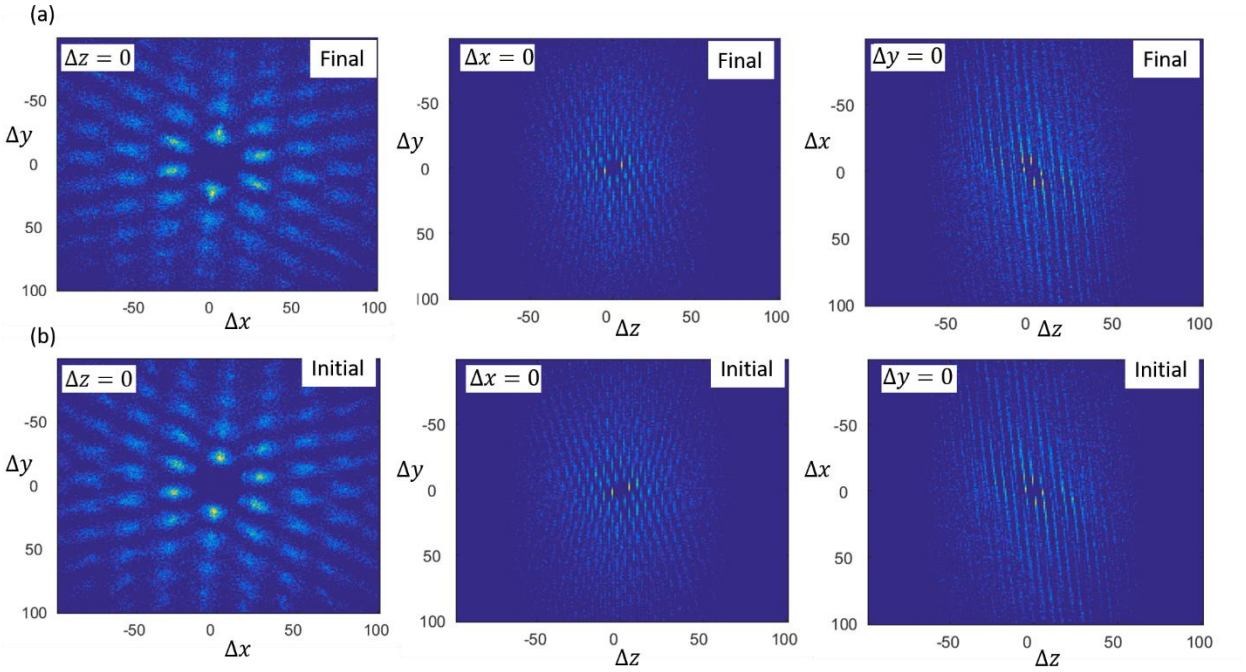

Figure 6.3 : Spatial distribution maps for the reconstructed volume from the (222) pole of a tungsten sample (in image pixels distances). (a) Distances calculated from final positions. (b) Distances calculated from initial positions. In both cases, three cross sections are seen, describing neighbours distances distribution on the XY,XZ YZ planes from left to right.

When observing the SDM for the $\Delta z = 0$ cross-section, the previously detected asymmetry between the x and y directions is once again apparent. The difference in both distances and standard deviations are evident once more, as can be seen in Figure 6.4. Each cluster on this map represent a group of measured distances between atoms on the same plane. The position of each

cluster corresponds to the actual measured distance. The spread of each cluster represents the variance in the measured distance and can be seen to be much wider in the x direction than in y for the chosen 'close-up' cluster. Observing the whole SDM reveals that the 'smearing' seem to be aligned in a radial direction from the centre of the pole. When comparing the highest intensity coordinates from two such clusters, seen in the lower zoom-in window in Figure 6.4, a 30% difference is measured, and a 25% difference when comparing the centres of mass coordinates. This is higher than the difference measured in the NN calculation, but is also not computed specifically between the x and y directions, but along the axes dictated by the SDM.

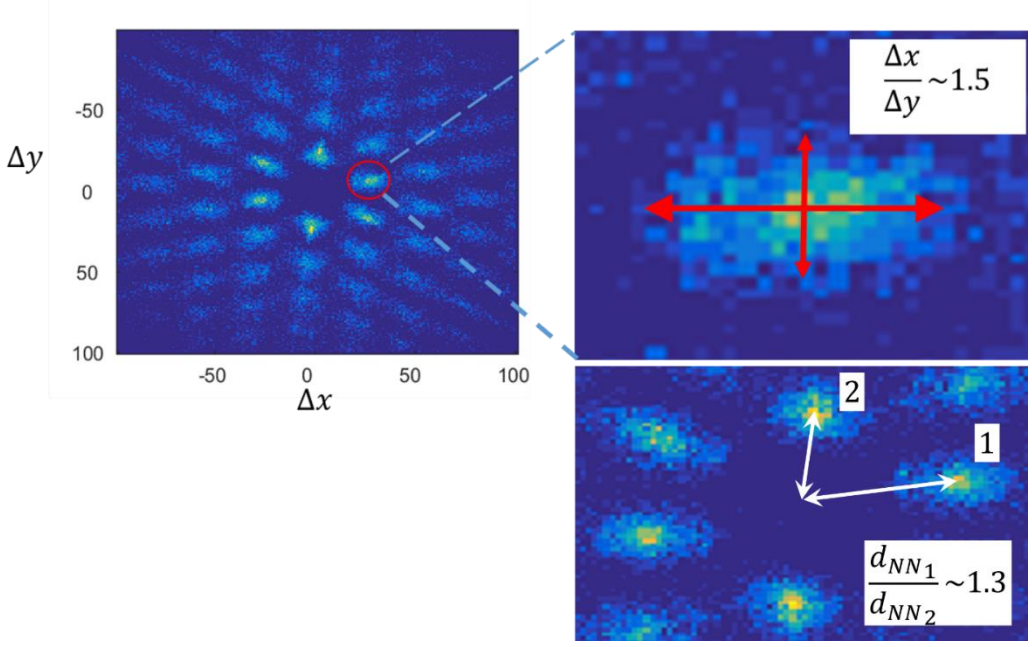

Figure 6.4: A-symmetry between the x and y directions is apparent from the $\Delta z = 0$ SDM. The variance of distances is approximately 50% larger in a radial direction to the centre of the pole than in the perpendicular direction. 30% difference between two NNs distances is measured according to highest intensity points of clusters 1 and 2.

6.3.1 Crystallography effect on measured distortion

To examine the effect of the local atomic arrangement on the measured distortion, SDMs were calculated for final atomic positions from the same sample for the (-222) and the (-141) poles.

Representative SDMs of the three poles are seen in Figure 6.5 in relation to their position on the FIM image. The (-222) exhibits precisely the same characteristics of the (222) pole. The (-141) pole however, was found not to be as distorted when comparing the positions of the clusters. The measured ratio between the distances seen on the lower SDM, marked in R1 and R2 closely matches the expected 1.17 theoretical value illustrated next to the SDM in Figure 6.5 (calculated from both high intensity points, and centre of mass, yielding very similar results). The angles between NN atoms also match on the (-141) pole. All poles exhibit smearing in a direction radial to the centre of the pole.

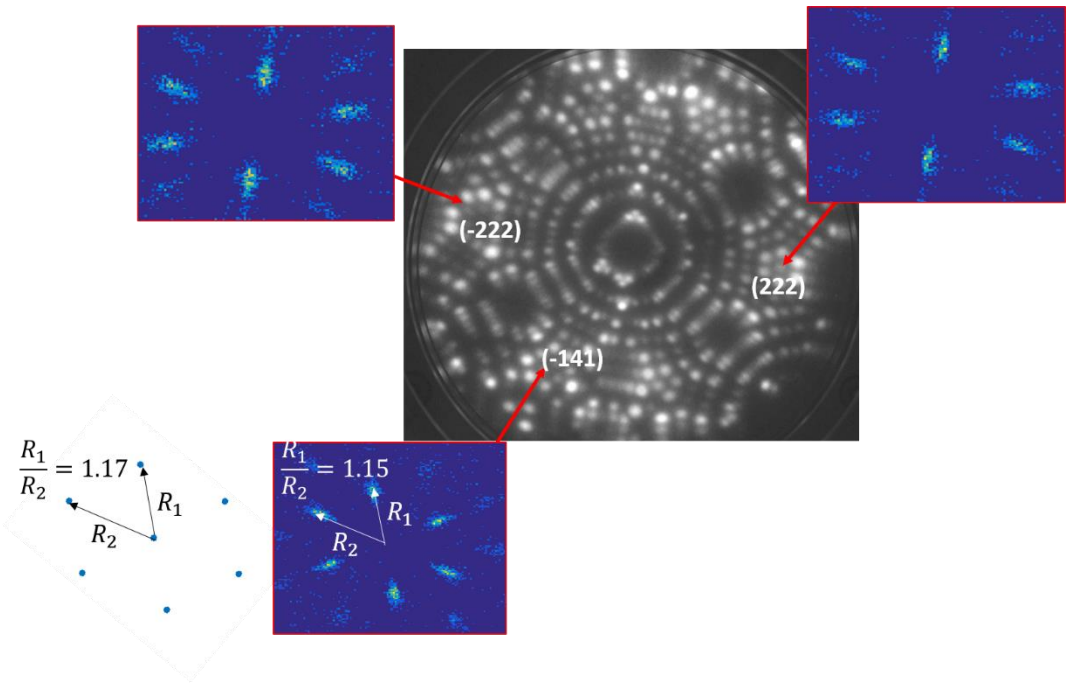

Figure 6.5: SDMs derived from the (222), (-222) and (-141) poles of a tungsten sample. Next to the (-141) SDM, an illustration of the theoretical (141) plane is seen. While all poles exhibit the same radial smearing in atomic positions, the positions of clusters in the (-141) pole better fit the theoretical structure, than the (222) and (-222) poles.

6.4 Distortions in damaged tungsten dataset

The distortion measured in a non-damaged tungsten dataset can account for the intrinsic limitations of the FIM technique when it comes to extracting true crystalline structures. However,

such measurements can also be used to evaluate the distortion that might be expected around crystal defects. Such distortions are readily visible in some cases from the FIM image itself, as seen in the example in Figure 6.6, where a plane containing a vacancy is displayed. The red arrow represents the position of the vacancy (some of it's NNs are already evaporated in the image), and the blue arrow connects the same atom on both the FIM image and the reconstruction for clarity.

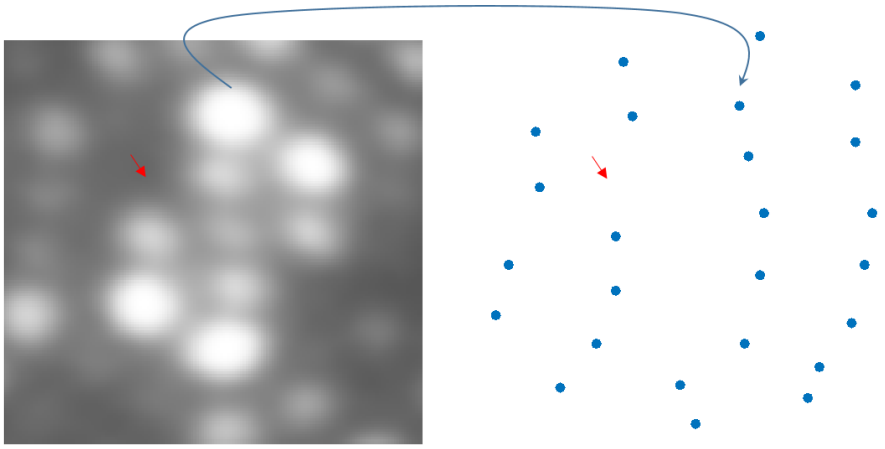

Figure 6.6 : A (-222) plane on a tungsten tip with a vacancy. The vacancy position is marked with a red arrow. In the FIM image, several of it's NN's had already evaporated. The distortion in atomic positions is evident in both the FIM image and the reconstruction. One of the atoms is marked on both for the easy comparison between the two images.

For a more comprehensive, quantitative analysis, SDMs were calculated and compared between two datasets: The first one is a data set reconstructed from the same tungsten sample discussed above, however from the (-222) pole where several vacancies were observed. The analysed volume consists of 504 atoms detected across 20 planes with 8 vacancies detected on 7 planes out of the 20. To compare the distributions of the calculated SDMs, a similar volume was cropped from the un-damaged dataset, taken from the (222) pole of the same sample. A sub-section of 20 planes, comprising of exactly 504 atoms was located and used for comparison. The SDMs for

both data sets are shown below in Figure 6.7, both based on the final atomic coordinates measured in each dataset for each atom.

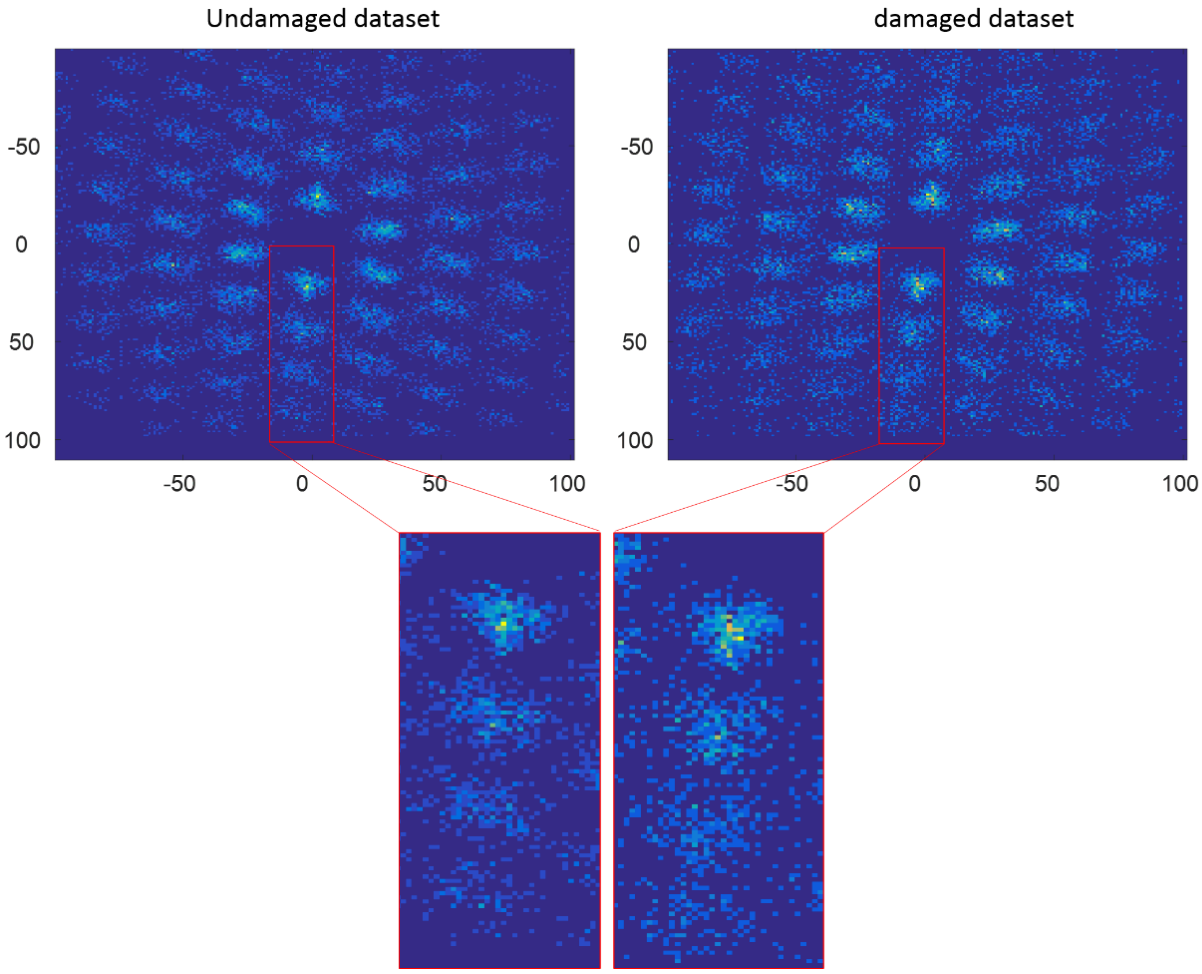

Figure 6.7: xySDMs calculated from both damaged((-222) pole) and un-damaged ((222) pole) data sets of a tungsten sample, both containing 20 planes and 504 atoms. The damaged dataset seem to exhibit a more 'noisy' SDM.

As might already be evident from the SDMs, the SDM for the defects case seem to have more background noise, attesting to a wider distribution of intra-plane distances in comparison to the non-damaged case. Notice that the colour map in each case was determined according to the pixel with the highest intensity on each map separately. This value was found to be higher for the non-damaged dataset. To make the comparison more quantitative, an analysis of the background

levels in each SDM was performed. Firstly, to make sure that the effects seen are not a result of a different number of distance entries between the two SDMs, the number of calculated distances contributing to each of the maps was calculated and found to be very similar (6157 distances calculated for the un-damaged dataset, and 6172 distances calculated for the un-damaged dataset, the difference originates from the fact that while the number of atoms and planes in each dataset is equal, the number of atoms on each plane may be slightly different). Even though the total number of distances was found to be very similar in the two cases, each SDM was normalized by this number, corresponding to the sum of all pixel intensities on the SDM. The normalized SDMs were then analysed to create the plot in Figure 6.8. The x axis represents intensity values on the SDM. The intensity of the SDM in turn represents the number of atomic couples found to be in a specific direction and distance from each other. The y axis is the sum of all pixels found to have that intensity, normalized by the total sum of entries contributing to the SDM. The sum of the bars in both cases is therefore 1 (the y axis are shown on the figure in a log scale). For example, the bars corresponding to x=1, represent all pixels on the SDM where only one couple of atoms was found at a specific distance and direction. As can be seen, this is the highest value, corresponding to background noise, and is also the only bar in which the count of pixels in the damaged structure is larger than the un-damaged structure. As the values of x increase, the plot sums the number of pixel found to have higher intensities, corresponding to a more ordered structure. It can be seen that both plots decrease, however the plot for the damaged structure decreases faster, corresponding to a lower level of order. The un-damaged structure exhibits the highest intensity pixel of 12 (as opposed to 9 for the damaged case).

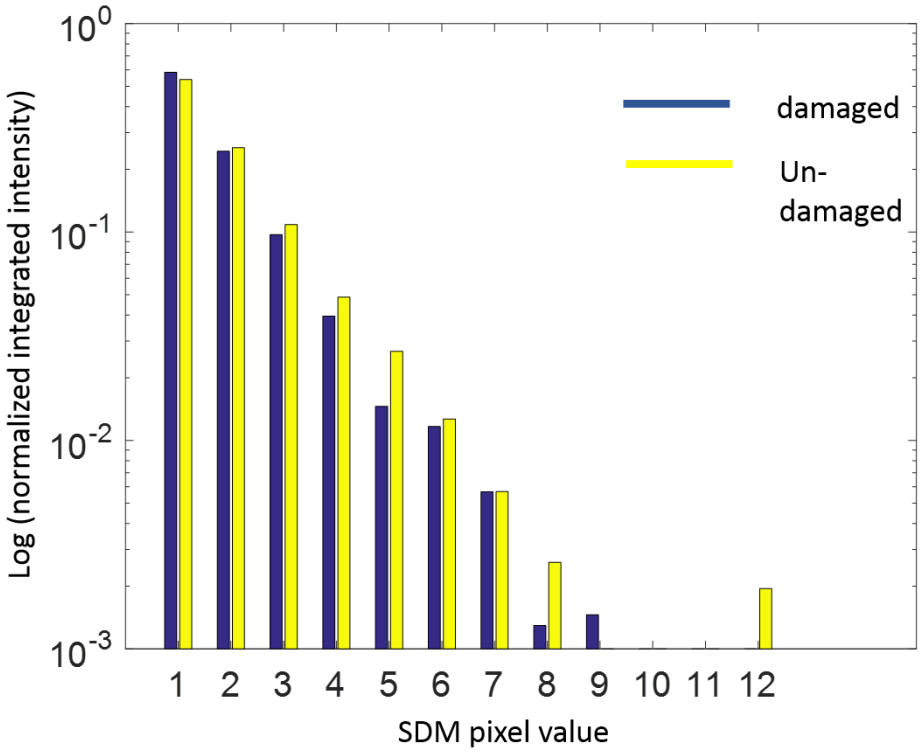

Figure 6.8 : Histogram of intensity of SDM pixels. For each possible intensity bin, the intensity of all pixels found is summed, normalized by the total number of distances calculated to construct the SDM. Only in the case of intensity=1 the damaged region is found to have a larger count of pixels corresponding to this intensity, attesting to the increased noise in the damaged structure SDM.

6.5 Discussion

In this chapter, NN analysis as well as SDMs were employed to investigate the distortion of reconstructed FIM structures. SDMs were previously proven to be a useful tool in measuring trajectory aberrations and distortion in APT reconstructions [127], [157], [193]. With the new reconstruction procedure for FIM data, the SDM analysis can now be easily employed on FIM data as well.

Both the NNs analysis and the SDMs of the un-damaged tungsten dataset demonstrate that the reconstructed structure deviates from the expected crystal lattice. The distortion is evident in both un-even NN distances measured for the (222) pole (as seen in Figure 6.4 and Table 6-1), and

the variance measured for these distances. When considering the final positions vs the initial positions of the atoms, the analyses do not indicate a preference of one set of coordinates over the other. As seen in chapter 5, displacements in atomic coordinates are observed following evaporation events in FIM data. Whether due to the response of imaging gas atoms, or 'rollup' of tungsten atoms previously discussed as a limiting factor to the resolution of FIM/ APT [196], these displacements could indicate that there will be no single time frame where all atoms will assume positions that best fit the theoretical structure. Changes in local magnification effects during the measurement can also play a role in the measured variance. As previously demonstrated in chapter 4, the dimensions of the imaged atoms can change instantaneously as the evaporation process continues. Further, as was simulated specifically for FIM experiments, highly anisotropic magnification could arise simply from the faceted nature of the tungsten FIM sample [202]. This will result in the need of local re-calibration of image pixels to real space coordinates. Indeed, earlier FIM experiments [75] oriented towards characterising surface diffusion were using consecutive recorded absorptions sites of the diffusing atom to calibrate the NN distance for each local surrounding, not satisfied by one such measurement for the entire range of diffusion.

Since no single set of coordinates measured at a specific time was found preferential, only final coordinates will be discussed from this point onwards. This is due to the fact that unlike final positions, initial positions are somewhat subjective, in the sense that they are dependent on the threshold that is chosen in the initial stage of the reconstruction for the identification of peaks.

Similar distortions in NN distances had been previously reported from APT SDMs analysis for the (110) pole of tungsten [127] and were regarded as the result of lattice strains. A different

explanation to the anisotropic 'stretching' evident in the FIM SDM could be the anisotropic magnification effects, computed in [202] to range between 0.64-10, depending on crystallography. Indeed, the distortions measured in this chapter across all SDMs exhibit a dependence on crystallography. This is evident by the fact that the SDM calculated for the (-222) pole is found to have the same ratio between the NN distances measured as the one measured for the (222) pole as seen in Figure 6.7. The SDM calculated for the (-141) on the other hand shows less distortion as the ratio between the two closest distances measured is similar to the expected theoretical one as well as the angles between them. An anisotropic shape of the overall tip, deviating from the perfect sphere model is of course another factor to consider that can possibly cause image distortions, however the agreement between the findings for the (222) and (-222) poles on opposite sides of the tip indicates a more crystallographic origin to the distortion.

Asymmetry was also observed in the distribution of distances, with a higher variance measured in a radial direction to the centre of the pole, estimated at a maximum value of 0.2nm for the (222) pole, similar to the FIM resolution estimated in [121]. Similar effects had been previously observed for APT SDMs and were considered as an estimate to the spatial resolution limit of the technique [127], [157], [193].

Several limiting factors to APT and FIM's spatial resolution were previously identified and discussed. APT simulations re-calculating the electric field distribution with every evaporation event were able to reproduce prominent features such as zone lines and depleted low index poles, proving that the variation of electric field at the atomic scale is a main cause of the aberrations [203]. Crystallography was shown to play a role in determining the trajectory aberrations of the evaporated ions, as those are influenced by the configuration of NNs. In 1981,

Moore showed by desorption images that trajectories of evaporated ions depend on the immediate crystallographic surrounding from which the ions are evaporated from [204]. This is due to repulsion powers between the evaporated ion and its neighbours. In [193] it was shown from calculation of APT SDMs in the vicinity of different poles, that changes to the variance of the atomic positions can be seen, limiting the resolution around some poles more than others. Unlike the APT SDMs in [127] that exhibited smearing in a direction perpendicular to the line connecting the analysed area to the central pole, the smearing direction in FIM was found to be radial towards the centre of the pole. While APT and FIM are similar in many ways, the intermediate presence of gas atoms in FIM complicates the image formation mechanism further, and the latter is not fully understood to this day. As gas atoms are ionized at a critical distance from the surface, it was shown that it is the field conditions at this distance that will dictate trajectory aberrations for gas ions [196],[163]. The new reconstruction algorithm now allows SDM investigations in FIM data, similar to those previously done in APT and can potentially resolve some of the additional complexity added by the presence of the imaging gas.

Finally, it was shown that even though defect-free tungsten dataset was already found to deviate from the expected structure, it is still possible to resolve further ‘disorder’ originating from crystal defects. The additional distortion found in the dataset containing vacancies can also be the result of actual change in atomic positions around a vacancy, or, in increased displacements of the imaged atoms during the FIM experiment in the presence of a vacancy.

7 3DFIM reconstruction of microstructural features

The 3D FIM reconstruction algorithm presented in chapter 4 was designed with the goal of developing a highly accurate, atom by atom approach, for the study of very subtle damage features common to primary stages of radiation damage. Optimal implementation of this algorithm requires high quality data underpinned by a high level of control in the evaporation process, atomic resolution and a 'layer-by-layer' evaporation structure. However, it can also be implemented on FIM datasets that do not possess all of these properties. Depending on the microstructural features of interest in the data, 'feature oriented' reconstruction can be adapted, such that a specific microstructure in the data is reconstructed 'atom-by-atom' with this method. In this chapter, two such examples are presented and discussed. In both examples the 'layer-by-layer' sequence cannot be used to estimate the 'z' coordinate and the reconstructed features extend across larger portions of the tip.

7.1 Example 1: Carbides in M50 bearing steel

In the first example, carbides are reconstructed from FIM data of a M50 bearing steel, with a composition given in Table 7-1. These carbides are designed to play an important role in the resistance of the steel to hydrogen embrittlement, which is a common problem given the lubricated environments these components operate in [205]. Carbides compositions, size, shape, can all affect the way in which carbides trap hydrogen, limiting its diffusion through the matrix, and hence influencing the steel's resistance to hydrogen embrittlement, however these need to

be accurately characterised. Atom probe tomography is a suitable technique to study these carbides and determine their phase and relative abundances. However, the evaporation field required for carbides is often higher than that of the matrix, resulting in retention of the carbides on the surface, and in turn, distortions to their depth coordinate in the APT reconstruction. Further, retention and migration of carbon on the surface were shown to result in high percentage of carbon multiple hit events and bias to the APT measured carbon concentration [206],[207]. Carbides size and volume fraction are usually determined from APT data using iso-surfaces, however those rely heavily on a subjective carbon level used to define them. FIM was proven as a highly complementary technique to atom probe in the study of such carbides. In a previous FIM/APT study, 3DFIM stacking was used to study the size and morphology of carbides in a martensitic steel while APT was used to extract their chemical composition [123].

C	Cr	Mo	V	Si	Mn	W	Co	Fe
3.84	4.38	2.4	1.05	0.37	0.2	0.003	<0.0004	87.48

Table 7-1 : Composition (at.%) of the M50 bearing steel analysed in this section

As the carbides image more brightly than the iron matrix, by keeping the DC voltage low and using only high pulsing voltage to evaporate through the samples it is possible to image only the carbides for a limited amount of volume, as can be seen in Figure 7.1a. By increasing the DC voltage as seen in Figure 7.1b-c, the carbides can also image along with the matrix, and so it is possible to determine the relation between the carbides and the matrix, as well as to use crystallographic matrix features to estimate the size of the carbides.

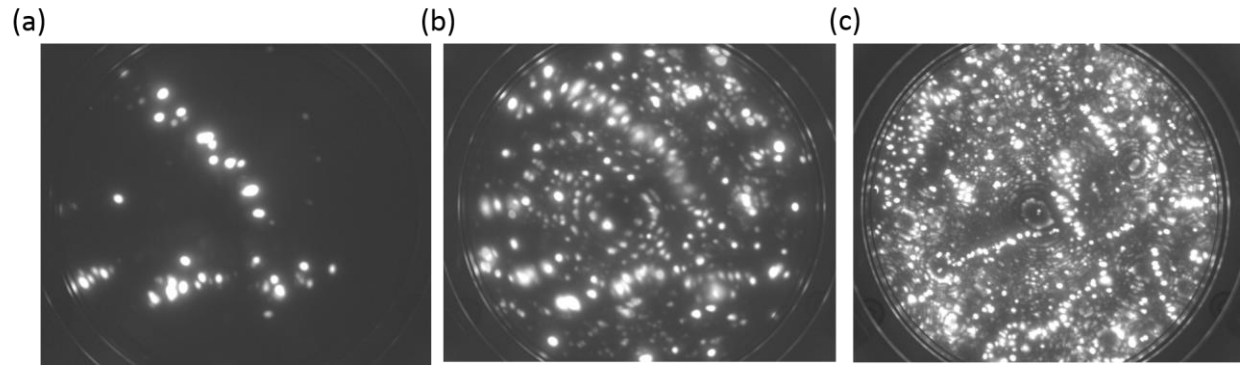

Figure 7.1: FIM of carbides in a M50 bearing steel, neon is used as imaging gas. (a) DC voltage below the best image voltage for the matrix – only carbides are visible. (b) DC voltage raised, the matrix is starting to image. (c) Both matrix and carbides are imaged.

Further, since FIM provides a more direct view of the surface than APT reconstruction, migration of carbon atoms [208] and the retention of carbides can be detected and accounted for.

To apply the atomistic reconstruction to this data set in 3D, the same reconstruction procedure described in chapter 4 had been applied with some straightforward adjustments to account for the different nature of the data: In the first stage all atomic coordinates are identified, and the x-y separation to individual atoms is undertaken in the same way described earlier. Next, to separate atoms in the 'z' direction, the 'break' in imaging between two atoms at the same x-y position is used. The procedure for the analysis of a single pole compared the duration of this break with the evaporation time of the whole plane. Here this 'time' scale reference is not available, and so atoms are separated in the z direction by setting the number of images likely to separate two atoms that lie on top of each other. Since the carbides are imaged very brightly, this number was chosen for this analysis to be 3 images, and yields accurate results as carbide atoms rarely drop in intensity below the detection threshold. However, its application is more limited when attempting to reconstruct matrix atoms, that are imaged less brightly. The intensity threshold set for the analysis of this dataset is chosen such that it is low enough to detect matrix

atoms. Because the carbides are imaged much more brightly, setting the threshold to be low also guaranties that any 'breaks' in imaging of a carbide atom that extend longer than a couple of images are due to evaporation events. A higher threshold is chosen at the end of the reconstruction to discriminate between the carbides and matrix. Finally, in the absence of a 'layer-by-layer' obvious sequence to employ here, the assignation of the z coordinate will yield less accurate results than in the single-pole tungsten example. Z coordinate will therefore be determined in a similar way to the atom probe data, however, while in APT it is assigned according to the relative evaporation time, in this FIM reconstruction the initial detection time was chosen to set the z coordinate. This choice was made to account for the tendency of these carbides to be retained on the surface.

A demonstration of the 3D FIM reconstruction procedure applied to this point in the algorithm is presented in Figure 7.2. Here a low intensity threshold has been chosen such that both carbide and matrix atoms are identified in the initial scan in Figure 7.2a. The reconstructed structure in Figure 7.2b is composed from atoms recorded from a 500 image sequence. The points in this figure represent individual atoms, after their multiple contributions from different images had been taken into consideration and consolidated to one point on the figure. The z axis here represents the first image in which an atom was detected. High intensity imaged atoms mostly corresponding to carbides in the dataset are coloured in red here, while lower intensity matrix elements in yellow.

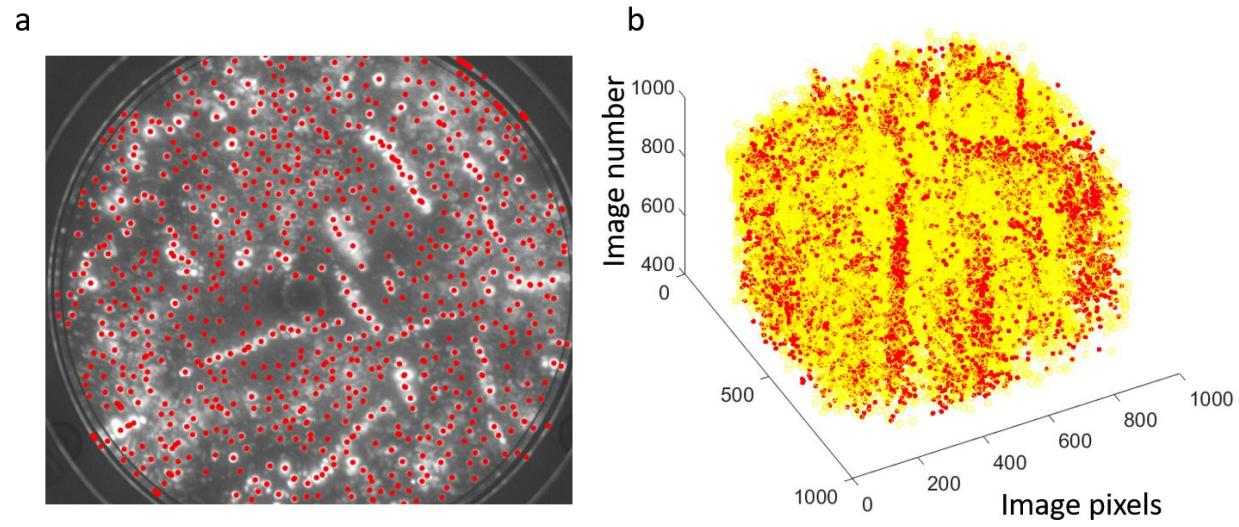

Figure 7.2 : 'Atom-by-atom' reconstruction of carbides in FIM. (a) All atoms above a threshold of 40% maximal intensity are identified (not all matrix atoms are identified since the matrix is imaged less brightly) (b) Reconstructed coordinates in image pixels. Red atoms are atoms imaged above an intensity threshold set at 95% – comprise mostly the carbides in the sample. Yellow atoms are low intensity atoms, mostly matrix atoms.

Next, a calibration is performed to convert to real space coordinates. Here the x-y coordinates are converted by evaluating the radius of the tip as detailed in chapter 2. The radius of the tip was estimated to be 68 nm and this was used to calibrate the range of x-y pixels into real space coordinates, ranging from 0-90nm. The z coordinate however requires a different approach as an estimate needs to be made regarding the depth increment between successive images. Since the evaporation rate is not uniform, the stacking and bending approach described in the introduction to 3DFIM in chapter 1 will yield inaccurate results. To calibrate the depth increment between the different images, the integrated intensity plots are employed, which provide improved sensitivity to the instantaneous changes in evaporation rate. Those are calculated from a crystallographic pole of the matrix that is found to exhibit ordered signal through the dataset and can be seen in Figure 7.3b, along with the pole from which they were calculated, marked with a circle in a. From the intervals of intensity identified, a depth increment can be extracted

between initial and final image of each interval. This results in depth increments of equal size (the plane spacing in this crystallographic direction) being assigned to different width image intervals. The 'local depth increment' is then calculated between every adjacent two images, such that the sum of all local increments will yield the correct depth increment across the whole image interval. While the evaporation rate of other poles may be slightly different than the pole examined, this procedure is still found to produce a good scaling metric for the z coordinate, as intensity plots taken from different poles yield similar numbers of plane counts in the dataset. The curvature of the tip was not accounted for, and can be enforced on top of the crystallographic calibration described here.

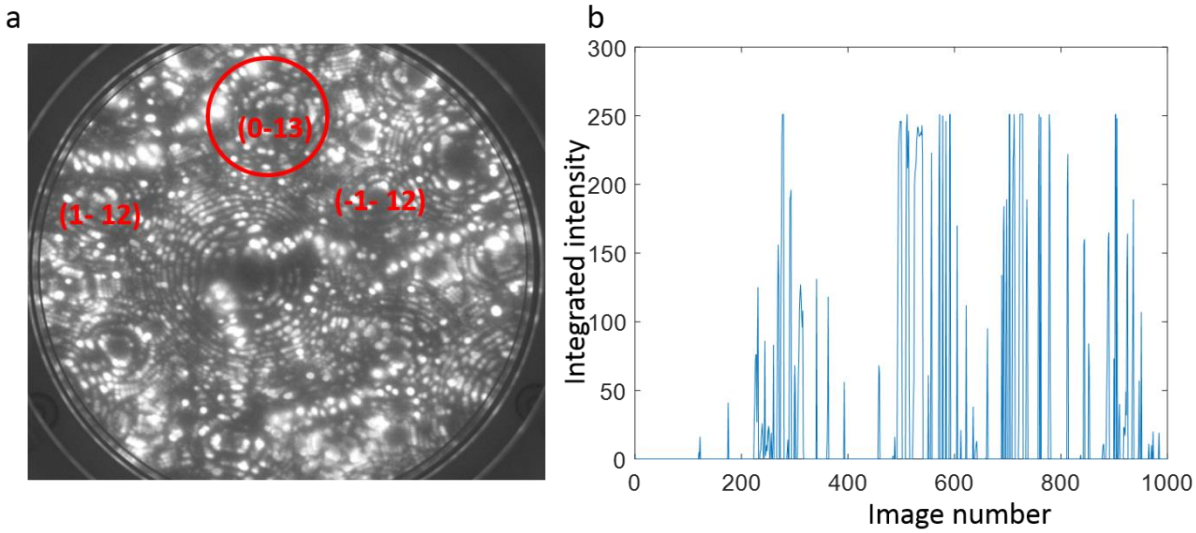

Figure 7.3: Scaling reconstruction to real space coordinates. (a) X-Y scaling is done by evaluating the radius of the tip from indexed poles (b) Depth estimations are performed from integrated intensity plots of a prominent pole, marked in a circle in (a).

Figure 7.4 plots the high intensity pixels in the dataset, mostly corresponding to the carbides, calibrated to real space coordinates. It can be seen that some 'background noise' exists as a result of high intensity coordinates that do not seem to correlate with the carbides. These were

recognized in [123] as substitutional or interstitial atoms commonly observed in alloys. Using the stacking approach in [123] these features were discriminated from the carbides by the assumption that their depth extension in comparison to those of the carbides is small. A different option possible with the 'atom-by-atom' approach is to discriminate those based on their local density. For this purpose, the number of atoms within a small area around each atom was calculated and considered as the local density of the atom. In Figure 7.4b only high density atoms are shown, with the density threshold chosen visually. It can be seen that some of the background atoms are now eliminated, however between the existing features remains a brightly imaged matrix pole. A combination of more than one image gas may be attempted in the future to resolve better contrast between the matrix and the carbides [123].

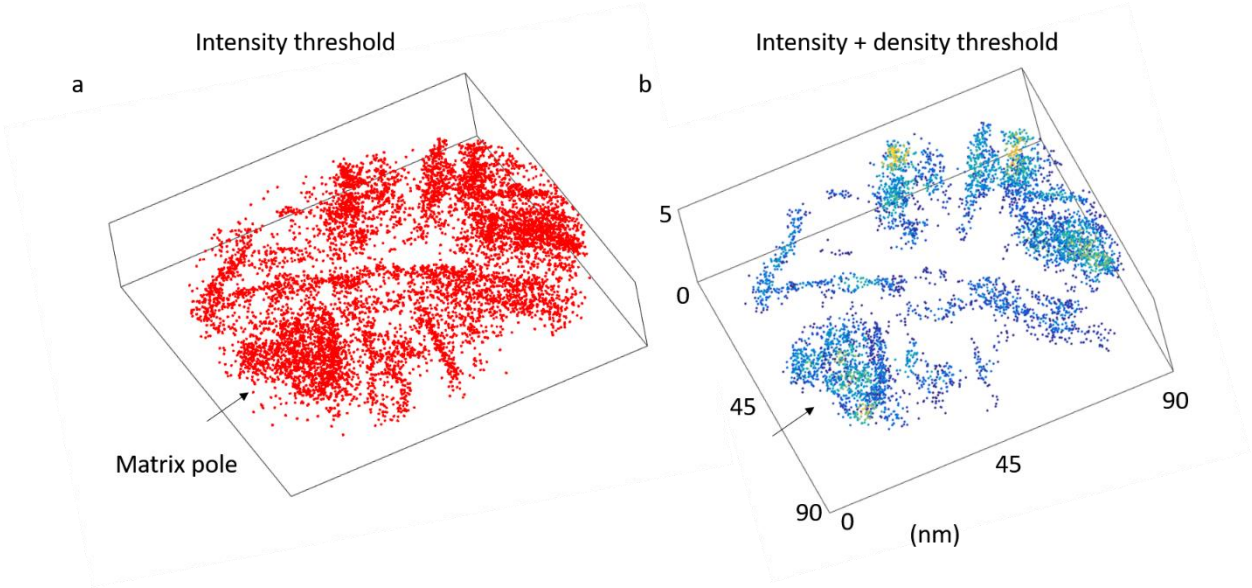

Figure 7.4: (a) High intensity pixels (>0.95 normalized intensity) including mostly carbides but also background noise from brightly imaged alloying elements and a matrix pole. (b) After the application of high density filter on the coordinates in a, the background noise has been reduced.

The analysis of this dataset is brought here to exemplify the possibilities of the atomistic reconstruction approach and could be further optimized. As the procedure transfers FIM images

into a 3D point cloud, the final list of atoms in this dataset could potentially be further analysed with any appropriate software such as IVAS or 3Depict [209], for quantitative characterisation of the carbides.

7.2 Example 2: Grain boundary in tungsten

The second example is a reconstruction of a grain boundary in tungsten. In this case the atomic resolution around the boundary exists, and the quality of the data is high, however, the feature extents along several poles, and therefore the 'layer-by-layer' reconstruction approach cannot be easily employed.

As grain boundaries play an important role in determining the mechanical properties of metals and alloys, the atomic arrangement along grain boundaries is of significant interest to the materials science community. Specifically in the field of radiation damage, it was recently shown that grain boundaries in tungsten play an important role in hydrogen retention, as they change the number and distribution of vacancies, as well as the size of the hydrogen-vacancy complexes formed [210]. Several models exist that predict the arrangements of atoms along common boundaries recognizing the notion of depleted zones that are created in several regions of the boundary along with islands of 'joint' atomic sites, where atoms either fit the atomic arrangement of both grains, or present in compromised sites between the two [74].

FIM enables an atomically resolved view of grain boundaries and had been previously utilized to characterise them [74]. With 3DFIM, it is possible to track the boundary in 3D.

Figure 7.5 shows FIM images of the grain boundary from when it was first detected (a), to the last image where the boundary can be observed, (b). Between b and c, a small un-controlled

burst of evaporation occurred, exposing the new, single grain surface seen in c. It can be confirmed from the similarity of b and c that the evaporation burst corresponds to the removal of only a few layers of the material, and so effectively this boundary is tracked almost until its end. It can also be seen that the final structure imaged after the full evaporation of the boundary is that of grain 1 (one of its main poles is marked in the same location in b and c as an example).

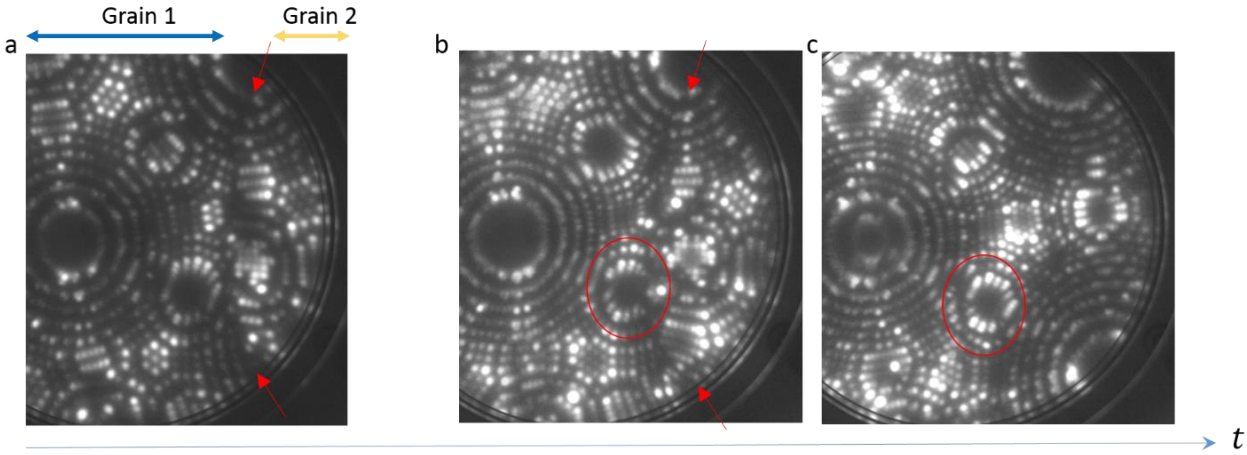

Figure 7.5: (a) FIM of grain boundary in tungsten. The boundary is outlined by a depletion zone. (b,c) Right before and right after the full evaporation of the boundary. The underlying structure is shown in (c) and seems to be aligned with grain 1 as reflected from the unchanged position of the pole marked in red.

From the 2D images it is possible to detect the depleted and joint atomic regions. Figure 7.6 plots cross sections of a simple 3D stacking of all FIM images, from the x coordinates marked in a. The first case shows a cross section along a depleted zone, and the second case shows a cross section along an atomic site at the boundary.

Grain boundaries are known to cause erroneous density distortions in the reconstructed atom probe data due to the local change in evaporation fields between the two grains and segregated atoms to the boundary, as well as morphology changes on the surface of the boundary. Simulations have recently predicted the formation of a depleted zone around grain boundaries

[171] in APT data. Similar aberrations are probable to contribute to the depleted zone seen in this FIM data, however as the atomic resolution around the boundary is not reduced, and no other indication of distortion of the atoms around the boundary is observed, the depletion could also be physical.

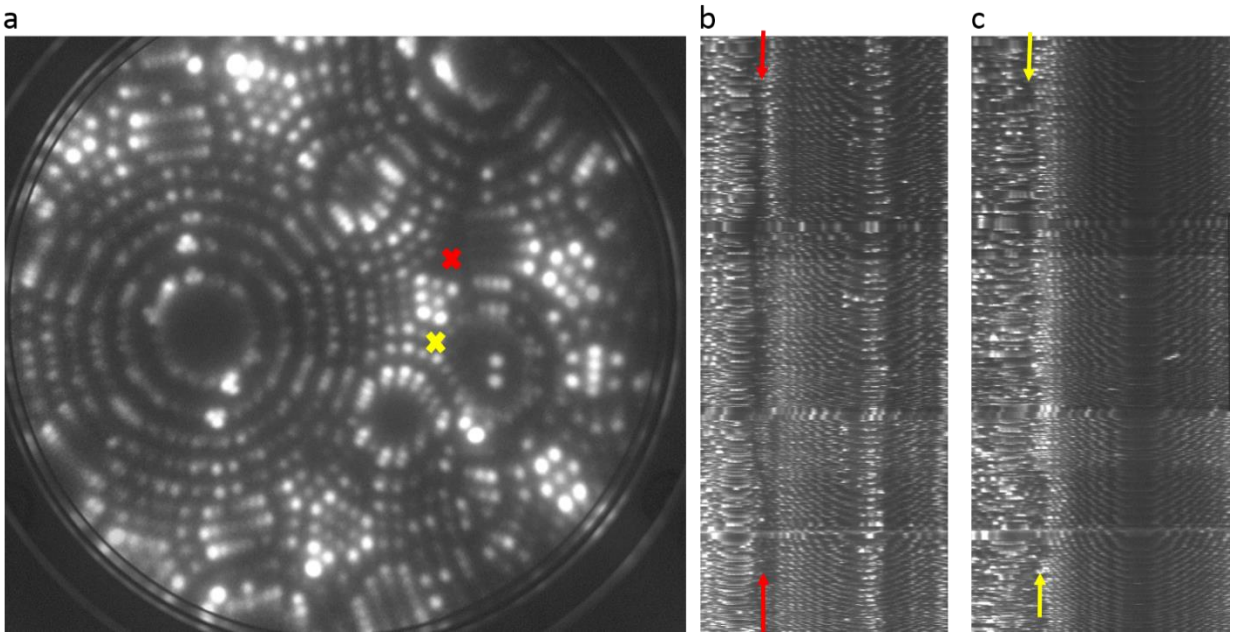

Figure 7.6: 3DFIM stacking along cross sections at the red and yellow points in (a). (b) The depleted zone is seen in 3D (c) A cross section along a joint atomic region is seen to be less depleted along the depth of the grain.

To analyse the data, high intensity coordinates are found normally. X-Y plane tracking is performed in the same way as before. Since there is no 'layer-by-layer' sequence to generate the integrated intensity plots that are used to separate the atoms in the z direction, each discontinuity event lasting for over 3 images is considered as marking the evaporation of an atom, and the appearance of a new atom. This constant number of images was chosen visually. To improve the accuracy of this approach, the intensity threshold used to identify atoms was decreased from 0.6 (used in chapter 4) to 0.4 of the maximal intensity. The 'z' coordinate is taken

here as effectively the sequence of evaporation, meaning the last image in which the atom is recorded to appear.

Figure 7.7b plots the reconstructed coordinates surrounding the grain boundary from a view down the z axis. Atoms evaporated in the first 500 images are displayed here for clarity. The volume represented here corresponds to the evaporation of 32 (222) planes of grain 1 and similar number of planes of other poles according to the integrated intensity plots. Over 6000 atoms are reconstructed here from the region seen in Figure 7.7a. Several features of the grain boundary are evident already at this stage. The depleted zone is easily seen between the grains. In grain 2 (on the right) a family of very prominent concentric rings is visible from the reconstructed data. This feature is not clearly visible when looking at individual FIM images such as in Figure 7.6a. Next, histograms are calculated from the reconstructed coordinates to estimate the amount of atomic depletion along the boundary. These are shown in Figure 7.7c, for coordinates reconstructed from all 2000 images. In the upper case, atoms from images 1-1000 are analysed, and in the lower part, atoms from images 1000-2000 are analysed, corresponding to the part of the grain boundary closer to its end. As can be seen from the resulting histograms, the depletion seems to diminish as the boundary is progressively evaporated to its end where only one grain is visible.

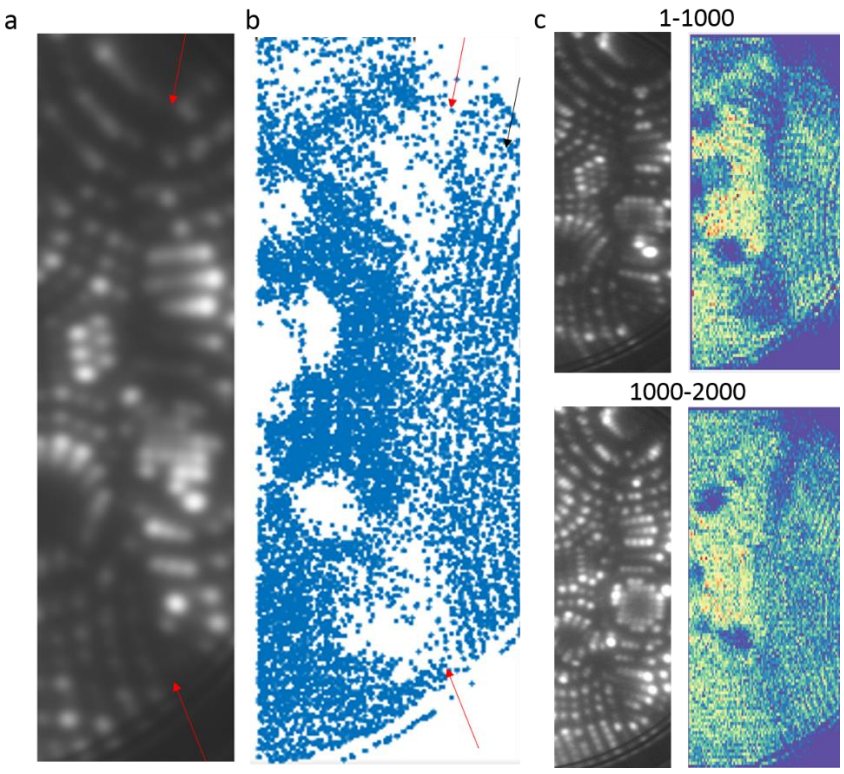

Figure 7.7 : (a) Cropped region around the grain boundary to be analysed. (b) Atomic coordinates from the first 500 images, view from the z direction. (c) Histograms calculated from the reconstructed atoms. The depleted zone is more evident in the first half of the data, and seems to close as the boundary is evaporated towards a one grain structure.

Figure 7.9 shows the 3D reconstruction of all atoms in the dataset. There are over 50000 atoms in this reconstructed volume, evaporated from over 140 crystallographic layers (estimated from the 222 pole, and confirmed against other poles). For each atom, an intensity profile along a line crossing the atom and the grain boundary horizontally was calculated and employed to assign each atom to the correct grain by detecting the depletion area. Of course, there are limitations in this analysis as the depleted zone defining the boundary is not uniform along the boundary, with joint sites, and intensity drops corresponding to crystallographic poles. To correct for these mistakes, the NN code was employed until convergence, correcting the assignment of atoms

placed originally in one grain, but fully surrounded by atoms of the other. The results of the NN correction are exemplified in Figure 7.8.

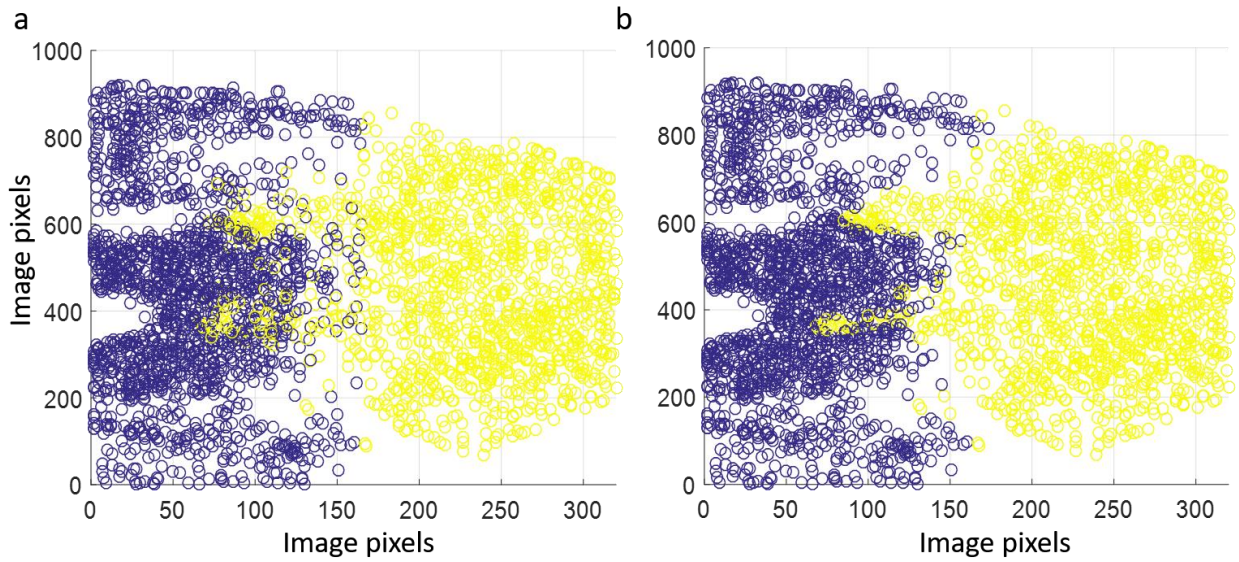

Figure 7.8 : View along the z axis of coordinates reconstructed from the first 200 images. (a) Grain separation before NN correction. (b) After NN correction. Atoms assigned to one grain that are found to be fully surrounded by atoms of the other grain are corrected.

Finally, the NN code was employed again to identify atoms on the edge of the boundary such that are surrounded by atoms of grain 1 from one side, and of grain 2 from the other side. These atoms are plotted in red in Figure 7.9 with some example atoms plotted on top of their FIM images in c. The atoms seen in c are difficult to assign to one grain over the other, corresponding to the 'joint sites' or to segregated impurities to the boundary.

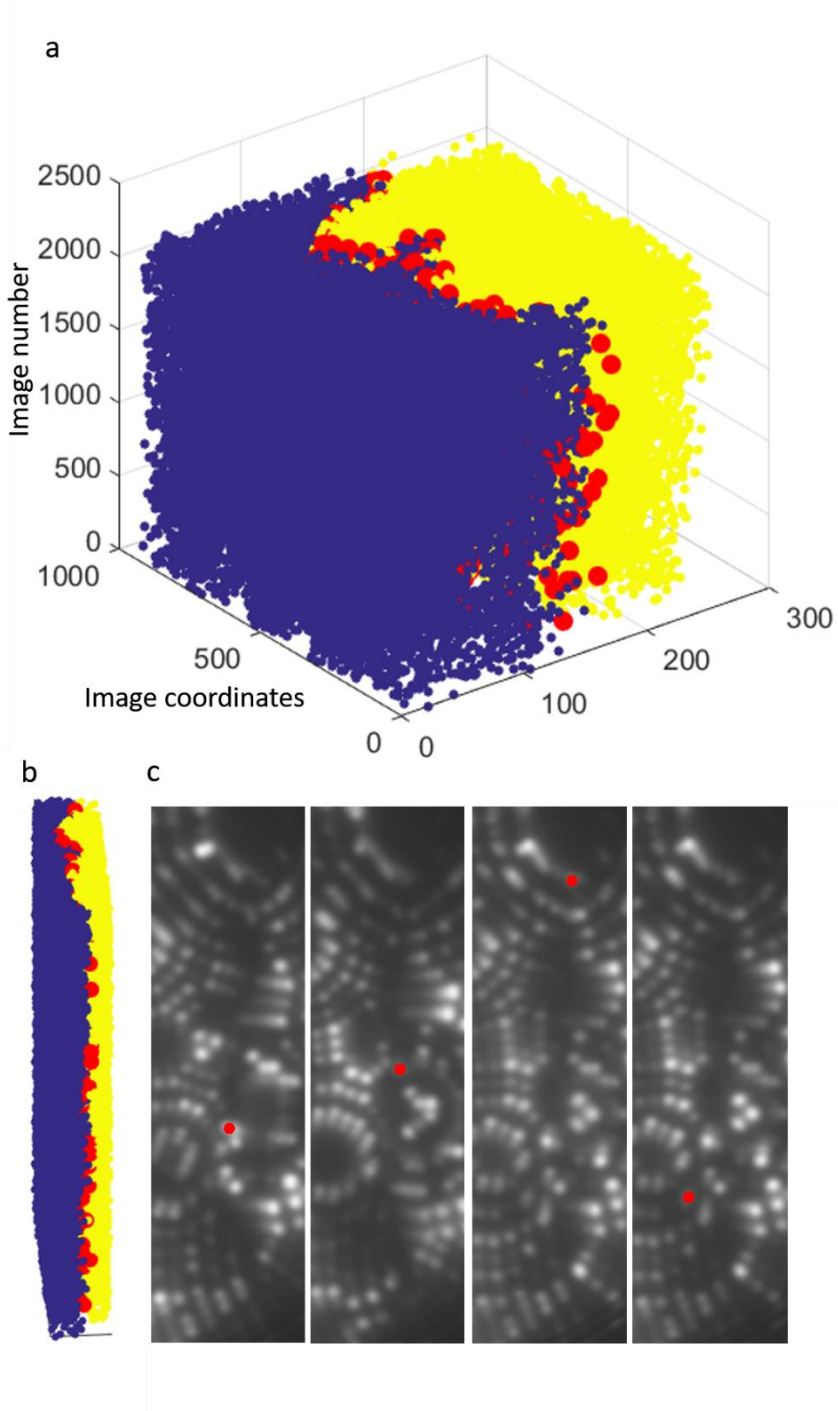

Figure 7.9: All atoms in their detected image coordinates. The different grains are marked by blue and yellow. Red atoms represent atoms on the boundary, possibly joint atoms. (b) Side view of the reconstruction with scaled axis. (c) Examples of some of the atoms marked in red at positions along the boundary that are not obviously assigned to one grain or the other, and can correspond to impurities segregation or joint atomic sites to the two grains.

8 Automated reconstruction of crystal defects

8.1 Introduction

The reconstruction methodology described in detail in chapter 4 has deliberately been developed using a known standard specimen, i.e. a defect-free tungsten lattice. The ability to identify and image the 3D location of every atom in the examined region represents a significant step towards the automated 3D FIM reconstruction of point defects inside the lattice. Since instantaneous field conditions determine which atoms will be imaged at any given time, it is not possible to confidently identify the presence of a vacancy by observing a single FIM image, but only by analysing the full time-ordered sequence. This was well acknowledged in previous FIM studies [55], which emphasised the importance of taking several FIM images of the same plane in order to identify a vacancy, but also commenting on the tedious data analysis this entails due to the lack of automated tools.

Out of sequence imaging and evaporation events, for example, can result in FIM images similar to those resulting from the actual presence of vacancies. Such cases have previously been observed on (222) planes due to the presence of vacancies within underlying planes [188], and in the presence of alloying elements, such as tantalum in a tungsten matrix [15]. An example of such an effect is presented Figure 8.1. In a-b are two similar FIM images from separate experiments, both of which appear to contain vacancies in the middle of the imaged planes. Figure 8.1a shows a (114) plane of a WRe5 sample implanted with tantalum, while Figure 8.1b represents a (222) plane of a tungsten sample implanted with tungsten. The difference between

the two cases becomes evident when observing the evaporation process as it progresses. Figure 8.1 (c-d) were imaged at a time subsequent to a-b, however still represent the same planes, respectively, after the removal of some of the atoms surrounding the suspected vacant site. As can be seen, the two different situations can now be resolved. In Figure 8.1c, the evaporation of neighbouring sites has led to the imaging of an atom in the previously thought to be vacant space. This is most likely due to the presence of a rhenium or tantalum atom in this site, which leads to a change in the usually reliable imaging sequence of the tungsten matrix. In Figure 8.1d the vacant site is still empty, and is observed to remain empty until the final removal of all atoms from this plane. In other cases, when a vacancy is present close to the outer terrace of a plane, it is common for adjacent outer terrace neighbours to evaporate prior to the imaging of inner plane neighbours. This results in a series of images highlighting the immediate surrounding of the vacant site, without the vacancy ever being clearly visible in one single image.

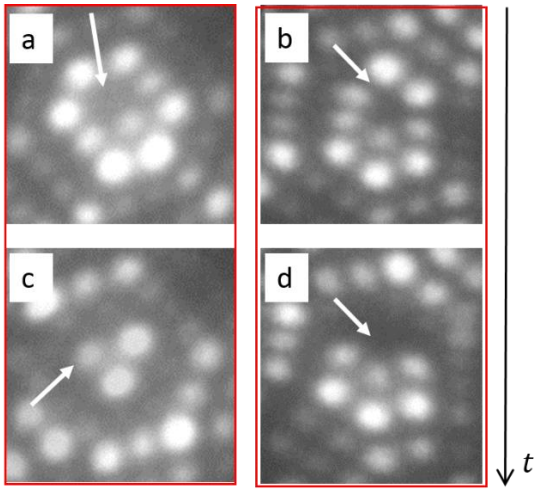

Figure 8.1 : Vacancy vs 'out of sequence' imaging event. (a,c) The (114) pole of a WRe5 sample implanted with tantalum. (b,d) The (222) pole of a tungsten sample implanted with tungsten. From (a-b) it appears as though in both cases there is a vacancy present, marked by the white arrows. (c-d) Images of the same planes imaged in a,b respectively, with the arrows marking the same 'vacancy suspected' positions. In c it is now clear that an atom is present in this position. In d no atom is seen as the evaporation process continues.

Therefore, for the reliable automated reconstruction of defects in 3D, all atomic positions must be mapped and reconstructed, and a simpler, 2D analysis of a single image will not suffice. The reconstruction demonstrated in chapter 4 is hence an important step towards accurate lattice defect characterisation.

However, the presence of crystal defects poses additional challenges to the 3D FIM reconstruction algorithm and requires modifications to robustly reconstruct all damaged regions in an accurate manner. Once all atoms are correctly reconstructed, further data mining steps are required to then locate the defects inside the reconstructed volume. The additional steps required for the successful reconstruction of crystal volumes that contain defects are described in this chapter.

8.2 Modifications to the existing algorithm

Before taking further steps to automate the identification of vacant sites in the reconstructed volume, it is important to examine the existing algorithm and determine its applicability in the case of damaged regions. An immediate concern arises regarding the validity of the integrated intensity plots step to estimate image intervals describing different planes. This step is based on a 'layer-by-layer' evaporation trend, and an 'outside-in' assumption regarding the imaging sequence of atoms. If these assumptions both hold, this results in the integrated intensity at the centre of the plane peaking right before the evaporation of the final central atoms. However, defects are known to change both the imaging and evaporation sequence [188] [174]. Hence, it is important to establish that this step is still reliable in identifying the evaporation of different planes. Figure 8.2 shows the integrated intensity plots as a function image number for two cases

of (222) planes containing defects. In both cases the planes selected are characteristic of maximum extent of damage observed in the samples around the atomically resolved poles. FIM images corresponding to the imaging of the initial outer terraces of the planes are presented, together with a subsequent image highlighting centre of the plane, for each case respectively. The first set of FIM images is taken from a 7dpa vanadium implanted tungsten sample, while the second is from the analysis of a 33dpa self-implanted tungsten, corresponding to the highest damage level seen in experiments included in this thesis. As can be seen in both cases, the planar interval indicated by the plots is less 'clear cut' than the respective plots for the un-damaged case in Figure 4.1c, with the noise increasing with damage level. However, the planar intervals are still resolvable, and so no modifications are needed at this stage.

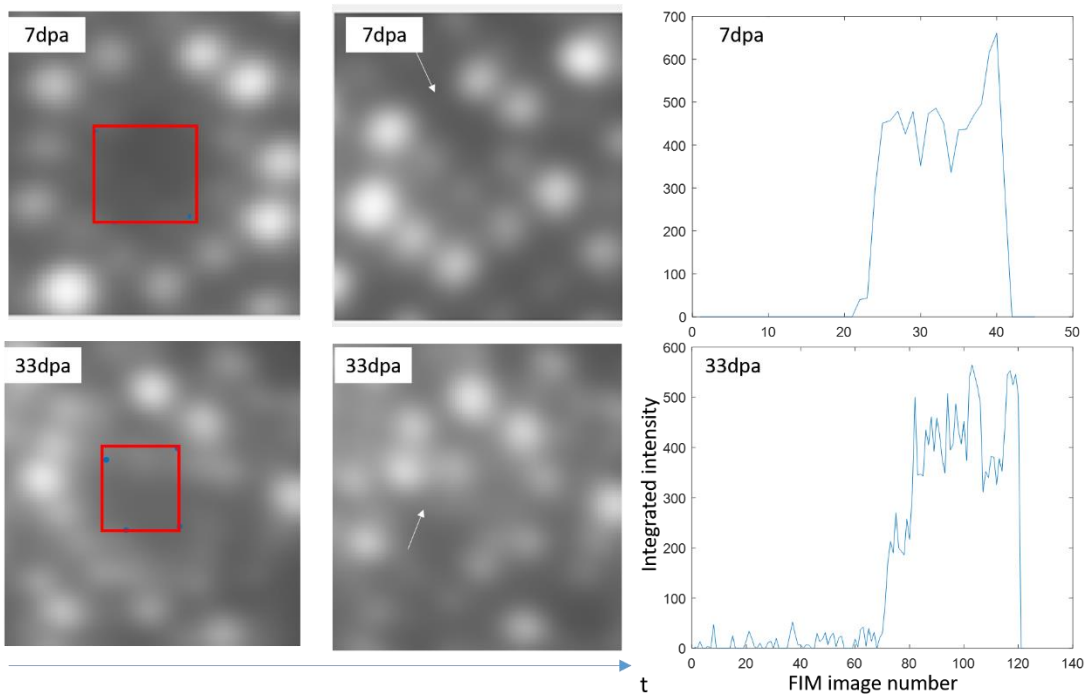

Figure 8.2: Integrated intensity plots as they are employed on datasets containing defects. Even at 33 dpa, the most severely damaged structure recorded still exhibits signal good enough for automated planar separation.

The next obvious step in the algorithm that might require modification is the final step in which 'out-of-sequence' events are identified by examining their intensity profile across a line connecting the atoms to the centre of the pole. This step is also based on repeating intensity profile patterns that result from the established imaging and evaporation sequences. By detecting a rapid enough decrease in the intensity profile directly followed by an increase, the transition between two terraces belonging to different planes is established. The presence of a vacancy along the path on which the line intensity profile is measured can also result in a detected intensity decrease, in which case an atom that belongs to the same layer as the vacancy, can be erroneously placed in the layer below. Figure 8.3 demonstrates such a case. In Figure 8.3a, the measured x-y coordinates for all atoms that were evaporated across a set of images belonging to the same intensity interval are plotted together. Atoms that are marked in red are atoms that were found to belong to the plane represented by the current intensity interval. Atoms marked in blue are atoms that were found to evaporate out of sequence, and were placed in the plane below in the resulting 3D reconstruction. The FIM image of the plane shown in Figure 8.3b demonstrates the presence of vacancies in the centre of this plane. These vacancies result in four central atoms of the plane being incorrectly coloured in blue, i.e. assigned with a z coordinate of the layer below. These atoms are marked in red circles for clarity in Figure 8.3b. Intensity profiles for the atoms marked in a are seen in c,d along with the images from which they were calculated. While one of those, seen in c, is a terrace atom from the plane below, the other, in d, is a central atom of the current plane, erroneously assigned to the plane below as well. It is evident from the FIM image in Figure 8.3d that vacancies can lead to profiles that before were attributed only to out of sequence events.

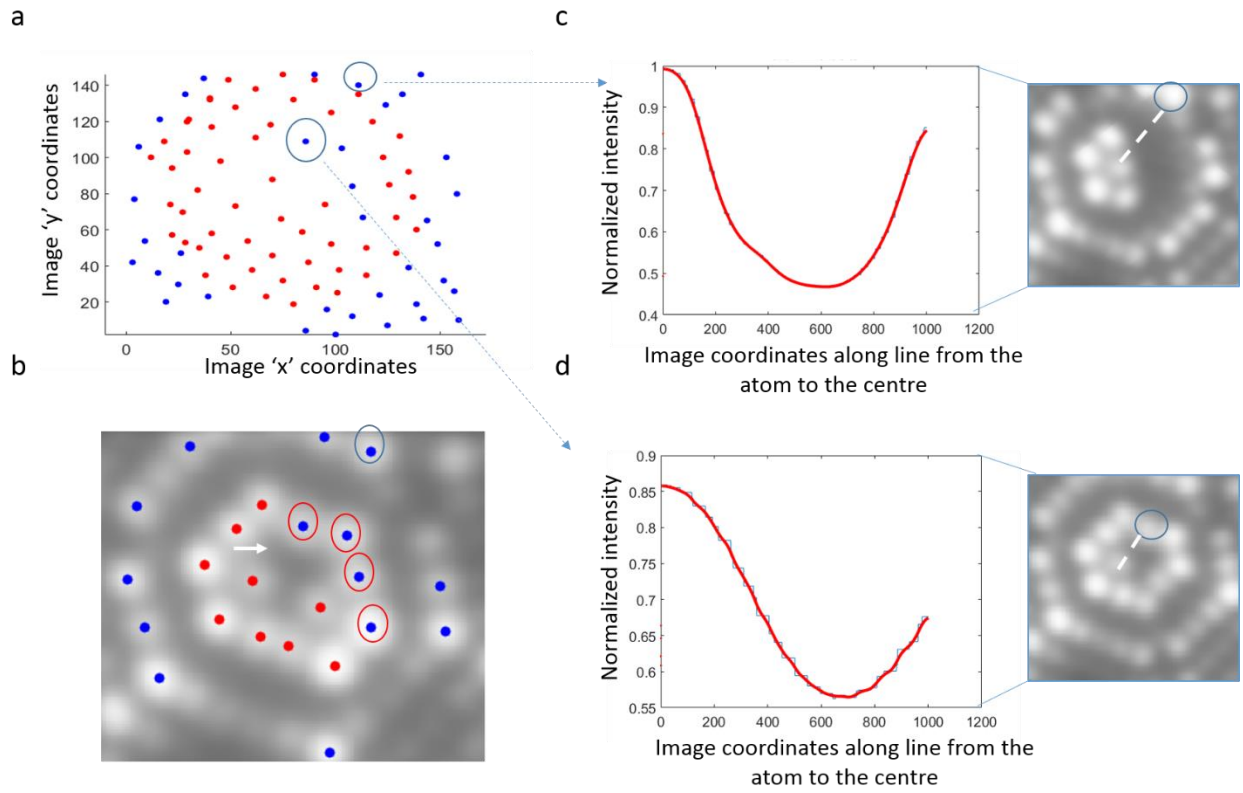

Figure 8.3: (a) Atoms evaporated in images from one intensity interval are plotted together. In red are atoms found to belong to the current plane, in blue atoms that were identified as out of sequence events. (b) Some of the atoms in (a) placed on top of a FIM image from the intensity interval. (c,d) Intensity profiles from the two atoms marked in circles to the centre of the pole. The images on which the profiles are calculated are shown in the small windows in c, d. Both profiles appear to be characteristic of out of sequence events, but the one in d is actually a central atom next to a vacancy.

In order to resolve these two situations, a further 'post-processing' step has been added after the initial reconstruction, that utilizes the algorithm that was originally developed to locate the 'theoretical' nearest neighbours of each imaged atom. This algorithm is described in appendix 1. In this case, the NNs of every blue atom in Figure 8.3 are identified from within the set of atoms evaporated in this interval of images. Next, in order to isolate the cases where central plane atoms are mistakenly coloured in blue, i.e. assigned to the incorrect plane, the algorithm will evaluate the distribution of red and blue NNs around the atom in question. As can be seen from Figure 8.3a, if a blue atom is mostly surrounded by red atoms, it is likely to be falsely classified as blue. Any blue atom that is found to be surrounded predominantly by red atoms will be identified

and its ‘z’ coordinate will be corrected at this stage, to correctly place it in the same plane as its red neighbours. This step is repeated until no further changes in atomic planes are made.

8.3 Detecting vacant sites in the reconstructed volume

In order to effectively characterise the damage features in the sample, after all atomic positions are mapped and placed correctly in their 3D positions, the next stage is to automatically identify the vacant sites. This will allow easy visualization and analysis possibilities of the damaged regions.

The most obvious approach to the automation of this problem would be to search for vacant volumes inside the reconstructed space that are large enough to accommodate an atom (or more accurately, a vacancy). However, since the reconstructed crystal structure deviates from the theoretical ‘perfect crystal’ (see chapter 6), this task is not straightforward. Even in the case of the defect free reconstructed volumes, variance in the NN distance could be measured between atoms on the same plane. In fact, variance between the NN distance along orthogonal directions was found to be different in chapter 6. In a volume containing defects, this distortion is expected to increase further, resulting in gaps between atoms that can potentially be large enough to accommodate a vacancy even when no atoms are missing. The identification of vacant volumes that actually contain vacancies is therefore challenging, necessitating constant evaluation of the NNs distances in the immediate surrounding of the atoms analysed. The algorithm described here re-evaluates the local surrounding of every atom on every plane for this reason. The approach benefits from making no assumptions about the theoretical crystallographic structure of the data.

8.3.1 Step 1: Assigning each atom an 'effective' volume

Since a discrete z coordinate is given to the atoms according to their plane number, it is sufficient to perform this analysis on the XY plane, and essentially search for a large enough area to accommodate vacant site (rather than volume). Thus, every plane is considered separately.

Due to the variance in NN distances across the plane, each atom is assigned with a different 'effective area'. Since NN distances measured in orthogonal directions were found to be different in variance, the optimal volume was found to be in the shape of an ellipse rather than a circle. The process is demonstrated on a vacancy-free plane presented in Figure 8.4. To determine the radii of the ellipse, first the NNs of each atom are detected. NNs found for the red atoms in Figure 8.4 are marked in green. The distance and direction of the closest NN is chosen as the small radius of the ellipse, r_1. Next, prospective 'orthogonal' neighbours are located, such that their coordinates are within a 45° area centred around the orthogonal direction to r_1. From these atoms the closest NN is selected, and its distance is set as the r_2 radius. This process results in the selection of two radii, derived from approximately orthogonal directions, and is repeated for each of the atoms on the plane. Identification of the r_1 and r_2 values for the two atoms seen in the example presented Figure 8.4 a and b, on the same plane, demonstrate once again the possible variance in NN distances across the plane.

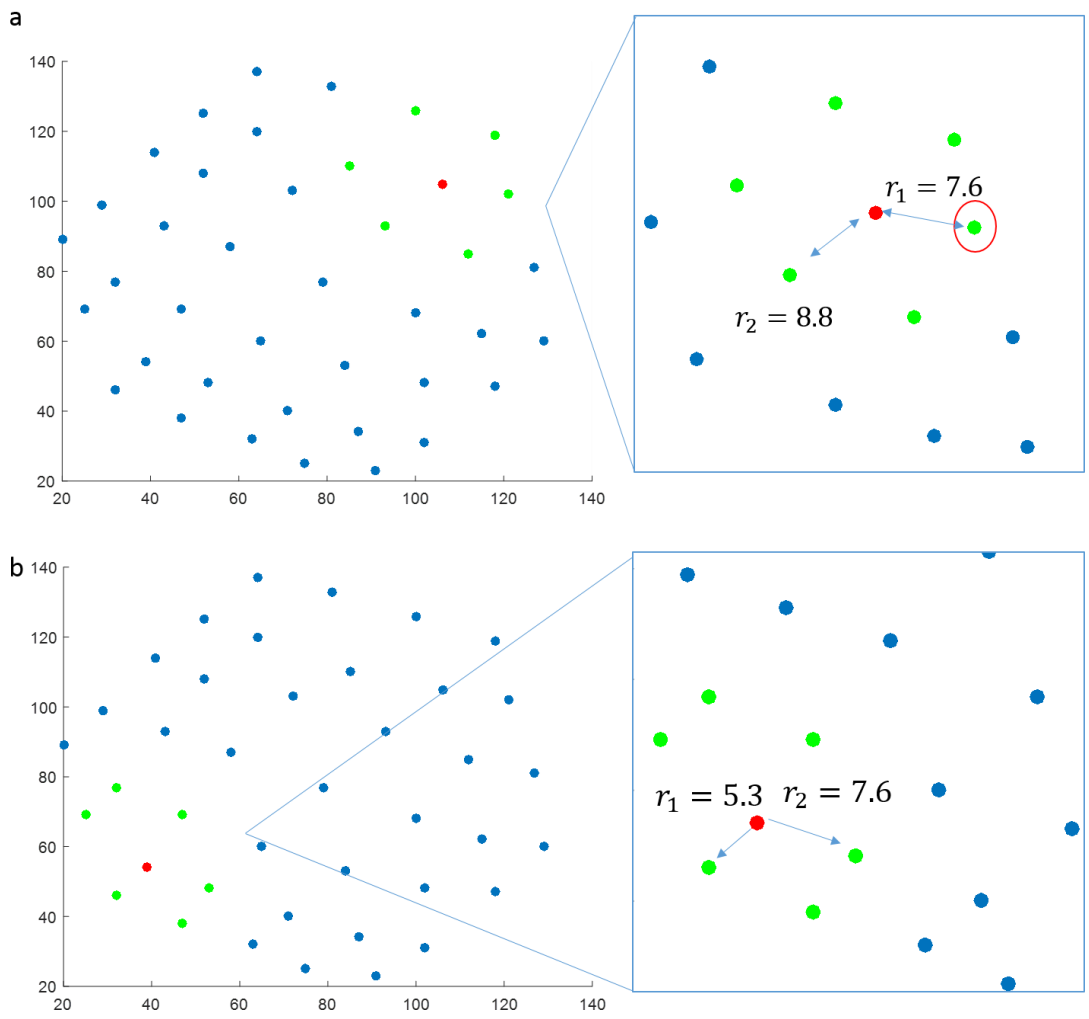

Figure 8.4 : Effective ellipse surface assignment for each atom on the plane. (a,b) Examples of two atoms marked in red. NNs are found for the red atoms, marked in green. The closest neighbour's distance is chosen as the small ellipse radius, and the closest approximate orthogonal neighbour's distance is chosen as the second radius.

The radii assigned at this stage are not the final radii that will ultimately define the effective area of the atoms. Since the presence of a vacancy can bias the radii assigned for atoms around the vacancy, a further step is taken to minimize this effect. Therefore, for each atom the values of both radii are averaged across the radii measured in the respective orthogonal directions for the NNs of each atom, and the median for each direction will be the final radii assigned for the atom in each direction. Figure 8.5 demonstrates the need for this step. The plane in the image contains

a vacancy, marked by a black dot on the right hand side of the figure. The plane is shown twice, with the ellipses defining the area around each atom. On the left are the original radii for each atom, as defined without taking into account the median among NNs. As can be seen, due to the presence of a vacancy, the effective areas assigned to atoms around it are larger and more eccentric than those assigned for other atoms. This is of course incorrect, and as a result it will prevent successful detection of a vacancy in the next step of the analysis. The next step in the algorithm attempts to fit into the vacant areas a vacancy, with a size defined by the average size of its surrounding atoms. Therefore, the bias of an enlarged ellipse is twofold: it reduces the size of the free area next to an atom, but also increases the expected effective size of a potential vacancy. In Figure 8.5 on the right, median of the radii were taken into account, and are seen to significantly reduce the bias caused by the vacancy.

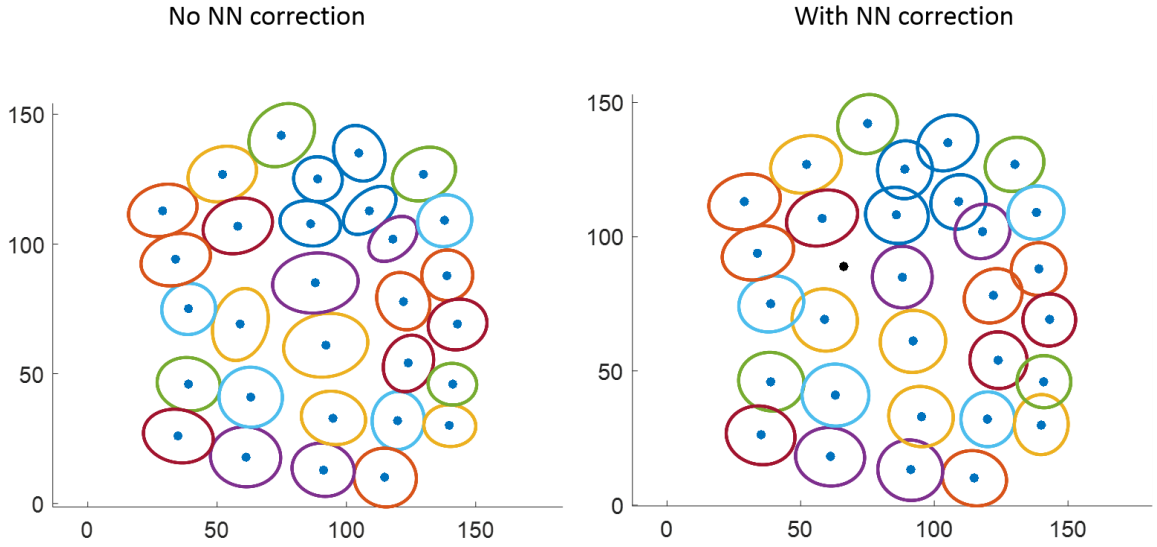

Figure 8.5: Vacancy effect on 'effective area' assigned to each atom. On the left each atom is given the radii estimated by distances from NNs, without taking the median of the values measured for NNs. On the right the median of NNs radii is taken, the ellipses are less eccentric, and the vacancy is detected.

Figure 8.6 demonstrates the rationale as to why ellipses were chosen and not circles to define the effective area around each atom. The same plane is shown three times, each with a different choice of effective-surface for the atoms. The plane does not contain a vacancy. On the left, circles were used to define the area occupied by the atoms. The same radius was used for all atoms and was determined by the average NN distance measured between all atoms on the plane. A similar sized vacant surface was located, and the presence of two vacancies was incorrectly identified. A second approach was implemented, and is illustrated in the middle graph of Figure 8.6. In this case, circles were used again, however, this time with the average NN distance calculated among each atom's NNs. In this case three vacancies were erroneously identified in the same region as the previous case, a region within which a significant asymmetry is evident along image axis. Finally, on the right of Figure 8.6, ellipses were assigned, taking into account NNs in both distances and directions. This time no vacancies were detected, which is the correct result as none exist on this particular plane.

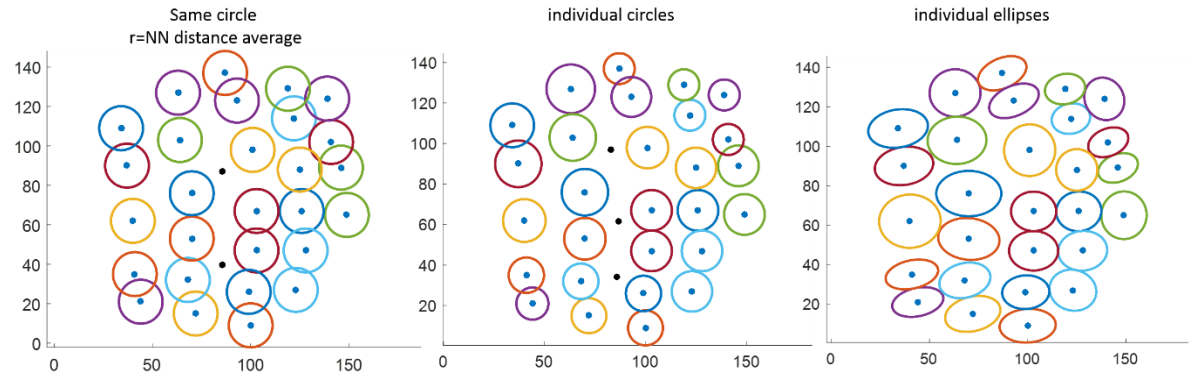

Figure 8.6: Three approaches to define effective areas around atoms. On the left – the same circle was used for all atoms, its radius determined by NN average – 2 vacancies were wrongfully identified, marked by black dots. In the middle, circles were used with a radius determined by NN distance average for each atom locally-3 wrong vacancies detected. On the right – ellipses were used, calculated locally for each atom, yielding the correct approach – as no vacancies were detected.

8.3.2 Step 2: Locating potential vacancies coordinates

After all the 'occupied' areas on the plane have been mapped by the ellipses, potential spots for vacancies are located. As a first step, 'suspect points' are defined at the centre point of the distance between any two atoms on the plane. A second group defined as suspect points are centre points between atoms on the adjacent planes above and below, respectively. These points are added in order to identify vacancies at the edges of planes, that are not fully surrounded by atoms, For example in Figure 8.7a, approximately half of an entire row of terrace atoms is missing.

At this stage of the algorithm the 'suspect points' seen in Figure 8.7b constitute a large group of points that must now be further examined and sorted.

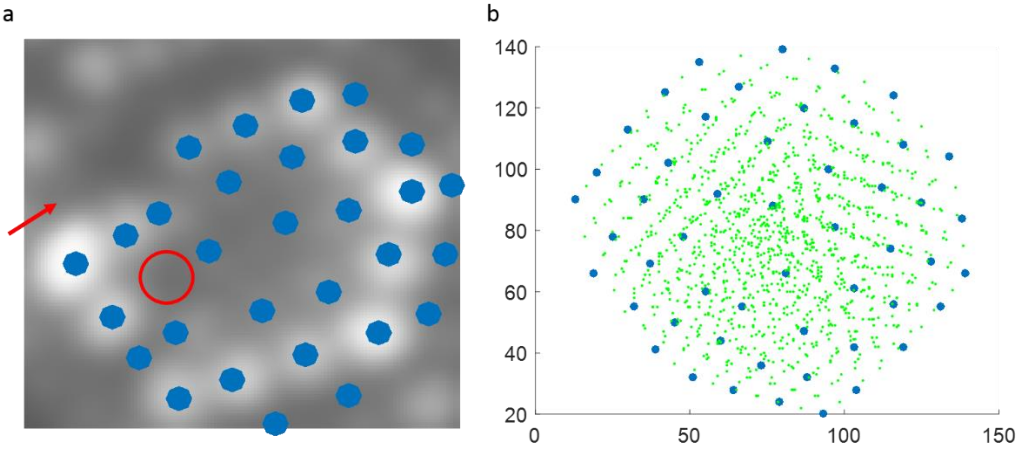

Figure 8.7: (a) Two types of vacancies on the same plane. Marked with a circle is a vacancy fully surrounded by plane atoms. Marked with the arrow are several vacancies on the edge of the plane. (b) All suspect points marked with green on an example plane. Points are defined at centre points of between any two atoms on the plane and on immediate planes below and above.

The next step is to estimate whether the area around each suspect point is large enough to be defined as a vacancy. To determine the effective size of the suspected vacancy, it is important to regard its immediate surrounding in a similar process as before. Therefore, atomic NNs are found

for every suspect point. The suspect point is then compared to each NN, and is assumed to have an ellipse with a radius equal to 90% of the neighbour's radius in the direction that connects the two as seen in Figure 8.8. If the two ellipses do not overlap, the suspect point is confirmed to fit in the vacant space with regards to this neighbour. The analysis is repeated for all the NNs, where each time the suspected vacancy is assigned an effective area according the neighbour examined. Note that the examined canter point is assigned with a radius of 90% of that of the neighbouring atom. This parameter was found experimentally to provide optimal results in vacancy detection, however can be interpreted as a further expression to the distortion of the local surrounding of a vacancy. In fact, the algorithm failed at times to fit 'full sized' vacancies into areas clearly identified as vacancies on the FIM images, suggesting either slight distortions of atomic positions around vacancies, or, very subtle local magnification increase near vacancies for the surrounding atoms.

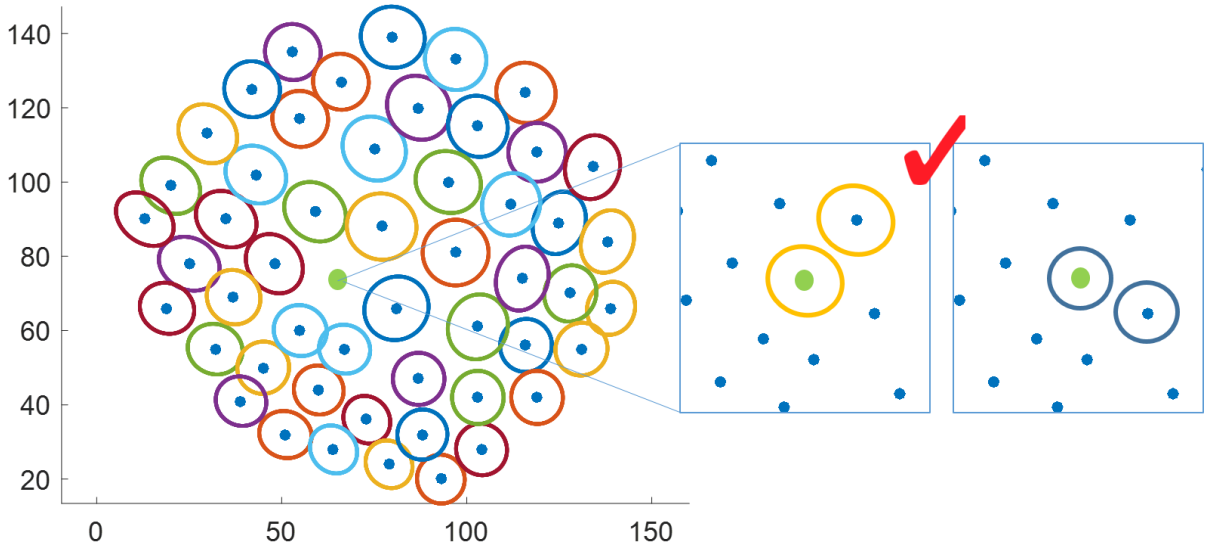

Figure 8.8: Testing the green potential vacancy point with regards to its NNs. The vacancy is assigned an ellipse with 90% of the neighbour's radius. If their ellipses don't overlap, the point is verified as a vacancy.

The process is summarized Figure 8.9, and will result in the reduction from a very large group of suspect points to several vacancy candidate points.

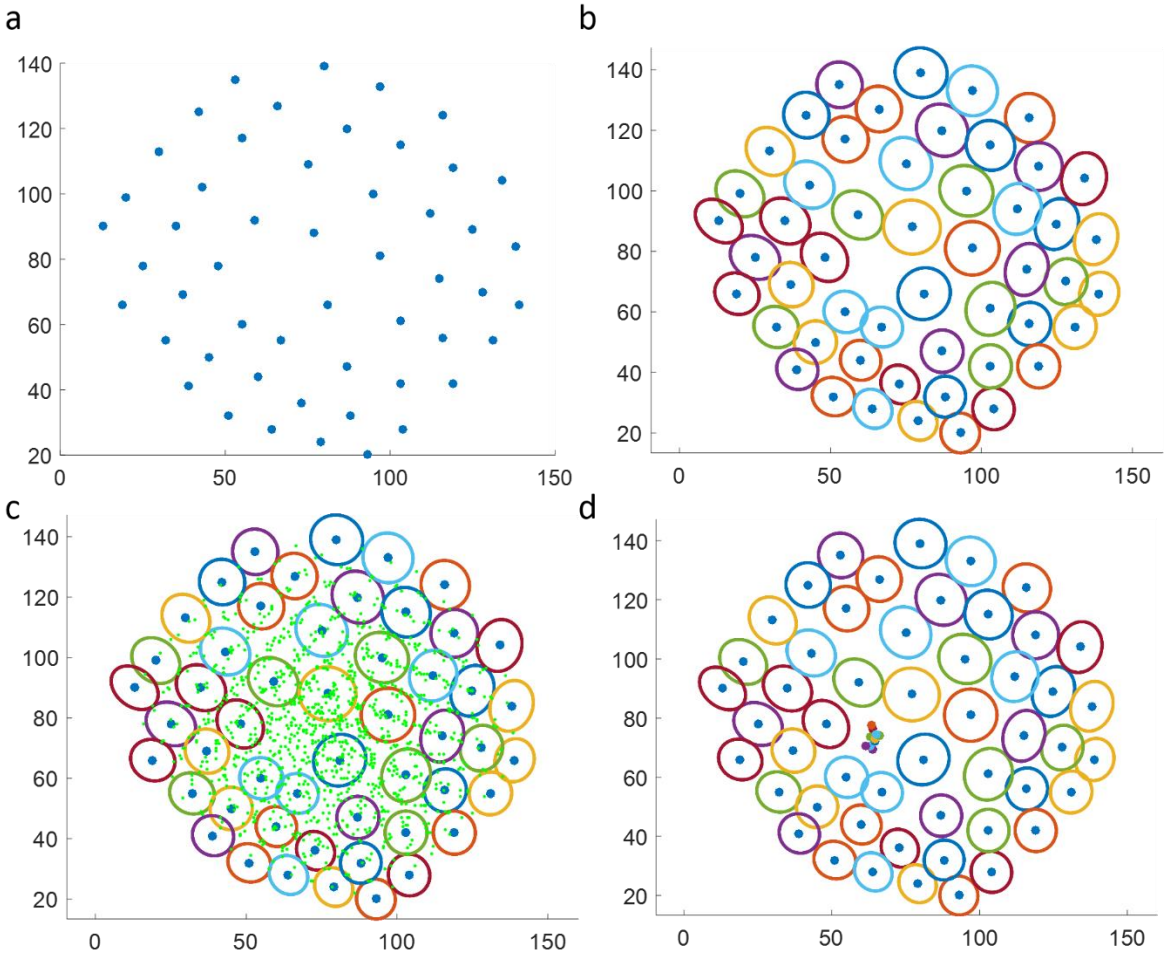

Figure 8.9: a-d Stages in locating vacancies. (b) Atoms are assigned effective areas on the plane according to their local neighbours. (c) Suspect points are defined at the centre points between every two atoms on the plane. (d) Suspect points in c are reduced by trying to fit ellipses around them of similar sizes to their local neighbours.

While in the case of the plane seen in Figure 8.9 it is clear that all the remaining candidate coordinates correspond to the same single vacant site, in the case of the plane seen in Figure 8.10, the free space corresponds to two vacancies. In order to choose the coordinates that reflect

the most accurate position of the vacancy and determine the number of vacancies present within the space, the next step is further taken.

8.3.3 Step 3: Identifying exact locations of vacancies

For each remaining point the atomic NNs are identified, and effective radii are defined by the median of the NNs radii in the appropriate directions. (The minor axis direction is chosen according to the position of the closest NN). The point with the largest effective size is considered first as the best candidate for the vacancy's location. This single point will be replaced by two other coordinates only if two points are found such that their ellipses overlap with the largest one, but not with each other. All other coordinates within the ellipse defined by the chosen vacancies (either initial one or the replacement couple) are erased from the list of potential vacancies. At the end of this analysis, if there are any remaining potential vacancy points left on the list the process is repeated again, starting with the new largest ellipse. At the end of this step, the final list of vacancies coordinates is complete.

A post processing step is then applied, comparing all vacancies found to the full list of atomic coordinates recorded at the initial stage of the reconstruction, to make sure that no atoms were identified that correspond in position to the identified vacancies. While the atomic reconstruction stage provides a highly reliable reconstruction, this step, where vacancies are located, is tolerant to mistakes in the atomic reconstruction. This is useful in cases where evaporation rate was momentarily too high, and some atoms were omitted from the final reconstruction.

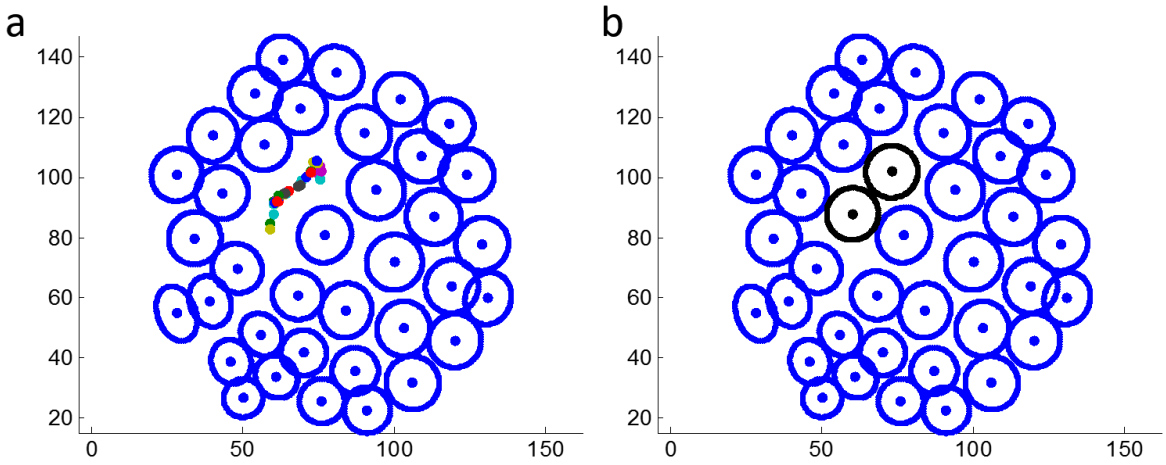

Figure 8.10: A plane with two neighbouring vacancies. (a) Reduced list of candidate vacancies. (b) The final two vacancies identified, as the point with the largest effective area in a was replaced by two others.

8.4 Limitations to the algorithm and future improvements

While every attempt has been made to optimize the algorithm for the successful identification of all vacancies, several challenges still remain to improve the accuracy and reliability of the approach.

A particular challenge arises in planes where a number of NNs vacancies are present. An example to such a plane is presented in Figure 8.11. By manually counting the atoms in each row of the plane, one could claim that 3 atoms are missing from the centre of the plane, however, when applying the automated algorithm only one vacancy is identified. This is due to the fact that the 'vacant area' defined by NNs atoms of this vacancy cluster is simply not large enough to contain 3 additional atoms with sizes similar to the sizes of atoms in their immediate surrounding. In the reconstruction example presented in the next section an additional post processing step was implemented in order to resolve some of these cases. This step is based on the analysis of a representative image such as the one in Figure 8.11a. The process is briefly described in appendix

2 and was helpful to resolve some of these cases. However, there remains un-resolved cases where no representative image exists.

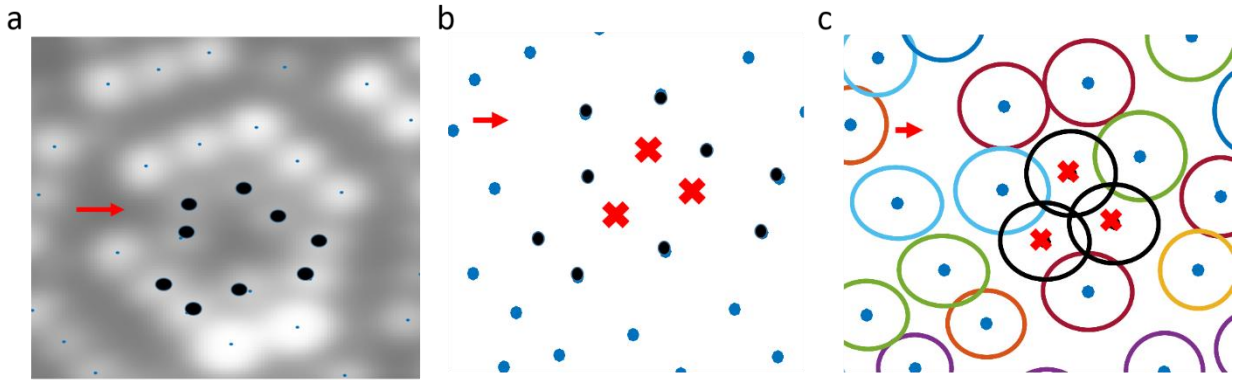

Figure 8.11: (a) FIM image of a tri-vacancy and a fourth vacancy marked with the arrow. (b) Manual attempt to complete atomic rows, 3 vacancies can be fitted in the centre. (c) In black are the ellipses that would have been found by the NNs algorithm. Since they overlap with each other, only one vacancy is automatically detected in the centre. The fourth vacancy remains un-detected since its neighbours do not have enough neighbours of their own to correctly define their ellipses.

An additional challenge for the current algorithm are cases where the vacancy is in close proximity to the terrace of the plane, or to a cluster of other vacancies, as the vacancy marked with an arrow in Figure 8.11. In several of these cases the algorithm failed to detect the vacancies. This is due to the fact that the ellipses assigned to the outer terrace atoms were often distorted by the presence of the vacancy. Since these atoms are not fully surrounded by NNs, the median step in determining the ellipse radii was not sufficient to reduce the bias induced by the vacancy. The fourth vacancy in Figure 8.11 has both terrace atoms NNs as well as NNs bordering the tri-vacancy.

These challenges highlight the need for further work to achieve an accurate as possible detection of vacancies in the reconstructed volume. While the method presented here benefits from no crystallographic assumptions, it is possible that to improve the accuracy of vacancy detection,

the incorporation of theoretical crystallographic information is necessary. Such an approach might include lattice correction steps where reconstructed atoms are fitted back to their 'theoretical' locations.

Finally, it is important to note that the presence of vacancies on outer terraces is always difficult to determine with absolute certainty. As seen many times during a 3DFIM experiment, the removal of the last remaining atoms on a plane at the surface can be accompanied by an almost simultaneous burst of terrace atoms from a lower plane. This was brought as evidence in [196] to the fact that the evaporation of central atoms raises the field at the edges of a lower plane, and in turn, the field at the edges of the second plane below. The presence of vacancies on these edges is therefore uncertain, even in an experiment with a highly controlled evaporation rate.

8.5 Vacancies distribution in ion-implanted tungsten

The reconstruction code followed by the vacancies detection algorithm had been applied to study the vacancies distribution in a tungsten sample implanted with vanadium. The sample was annealed prior to implantations as a needle with 400keV vanadium ions at 300℃, to a level of 7 dpa. The vanadium distribution inside the sample was studied using APT and discussed in chapter 9. In this chapter the reconstruction procedure was utilized to study the vacancies distribution.

During the 3DFIM experiment approximately 23,000 images were recorded and over 570 planes evaporated. In this example the (222) pole was reconstructed, as it was visually found during the experiment to contain a high concentration of the overall crystal damage seen in the sample. Since the few first atomic layers of the surface of the sample usually contain some defects, and generally do not produce high quality images, the first 20 (222) planes were not reconstructed

but taken into account in determining the 'z' coordinate. 555 planes of the (222) pole were reconstructed here. The reconstruction is seen in Figure 8.12, where all reconstructed atoms are seen in red. The corresponding 2D xy-SDM seen in Figure 8.14 confirms the successful reconstruction. Since uncertainty always exists in the detection (automated or not) of vacancies that lie on the outer-terrace of a plane, the vacancy search was conducted on data that excludes atoms that had evaporated 'out of sequence', essentially reducing the data to 'central atoms'.

The reconstructed volume was calibrated to an approximate volume of $50\times4\times4\ nm^3$. A total of 175 vacancies were located in the reconstructed volume and are plotted in black in Figure 8.12. Since the pattern of tri-vacancies was often observed during the experiment, the additional correction in appendix 2 was applied to identify the vacant positions detected that contained more than one atom. Finally, since the algorithm suggested here still requires improvements, a final step of manual correction of the vacancies was performed.

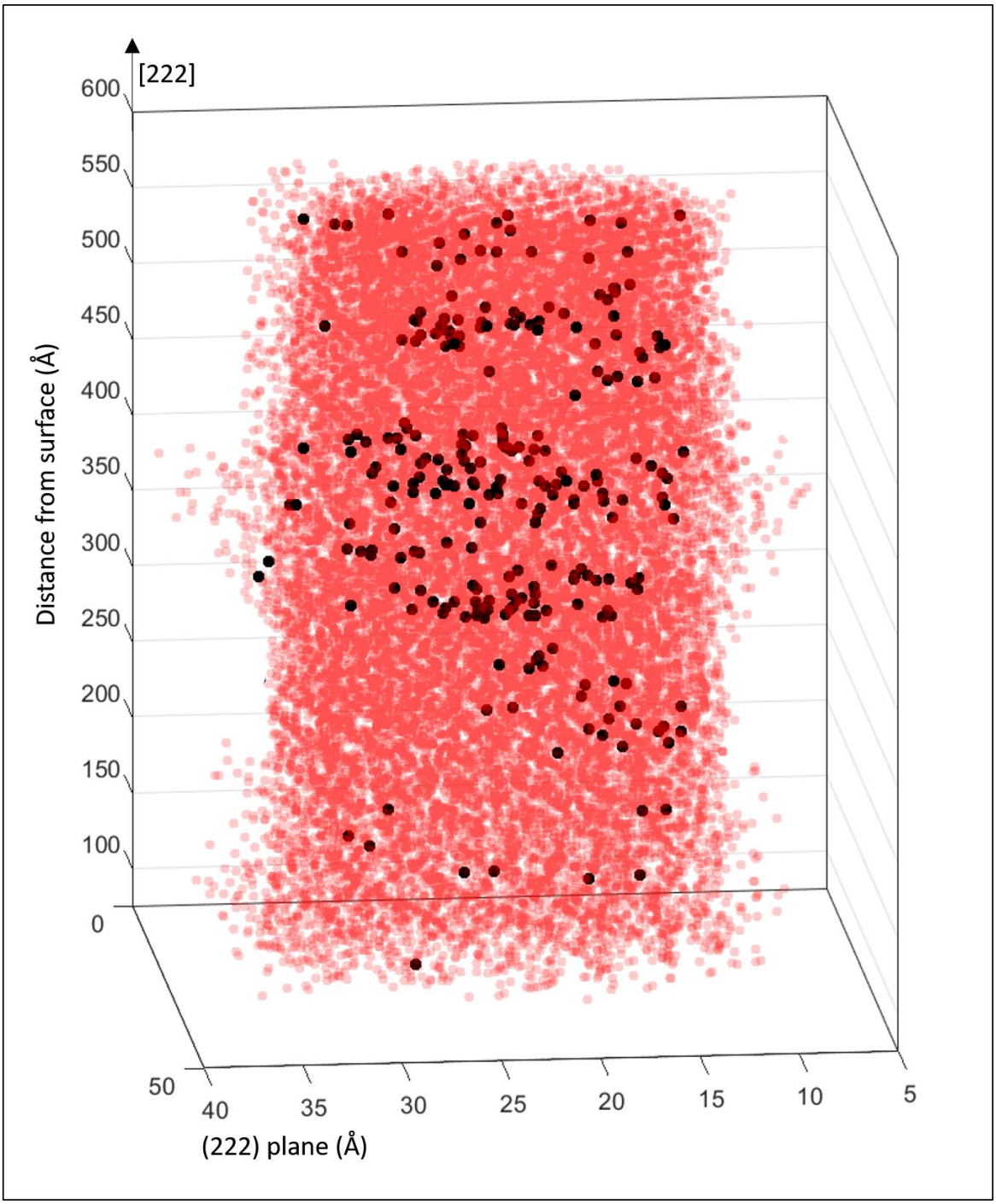

Figure 8.12: Reconstruction of over 555 (222) planes imaged across over 20,000 images. Atoms are plotted in red, vacancies in black.

Figure 8.13a plots the depth profile of the vacancies distribution as measured by FIM and in comparison to the SRIM profile. As discussed in chapter 9, the many assumptions incorporated

into the SRIM profile are expected to result in deviations in the measured damage profile. SRIM does not take into account any recombination and migration processes that occur between the initially created defects. In fact, the profile is computed at a temperature of 0K. For the comparison in Figure 8.13a, the SRIM profile was calibrated to be on the same scale as the FIM profile, and it is only the general trend of the profiles that is comparable. Unlike the vanadium ion distribution that was found to be flat in the needle samples in chapter 9, the damage does seem to be shallow at the surface, and increase into the depth of the sample, similarly to the SRIM profile.

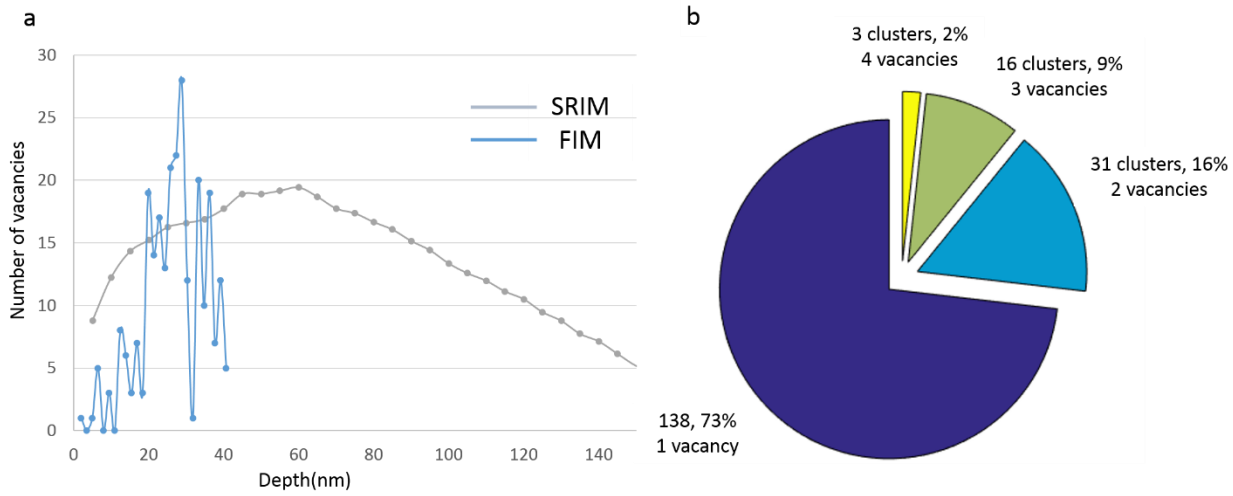

Figure 8.13 (a) Depth profile of vacancies as measured in FIM in comparison to SRIM profile. SRIM profile is scaled for comparison. (b) Vacancies cluster histogram, calculated across (222) planes. Majority of vacancies are found to be single vacancies on their (222) plane.

Figure 8.13b plots the spatial distribution of vacancies as a histogram of the number of vacancies observed as NNs to each other. The NNs are computed within each (222) plane and do not extend across several planes in this analysis. The reconstructed vacancies are seen again in Figure 8.14, this time coloured according to the number of NNs vacancies on their plane, following the colour map of the histogram in Figure 8.13b. The measured distribution of vacancies into small clusters

is difficult to compare to previous results as it is highly dependent on the conditions of implantation. In Reference [79], the structure of depleted zones following ion implantation in tungsten was studied as a function of the mass and energy of the impacting ion. One of the implanted ions was Cr, which is similar in atomic mass to vanadium. In that experiment single vacancies were also found to be much more common than a complex of 2,3 and 4 vacancies. Further comparisons are difficult to make as the energy of the ions was an order of magnitude lower, the temperature (-263℃) and dose much lower.

Current radiation damage simulation studies in tungsten are usually designed to predict the behaviour of larger defects such as voids and dislocations [179],[211]. These often disregard the population of single vacancies, and rely on TEM experiments to determine the voids population which only partially describes the vacancies population in the sample. Automated FIM experiments as demonstrated in this chapter can yield unique and highly valuable statistics to inform such damage simulation studies.

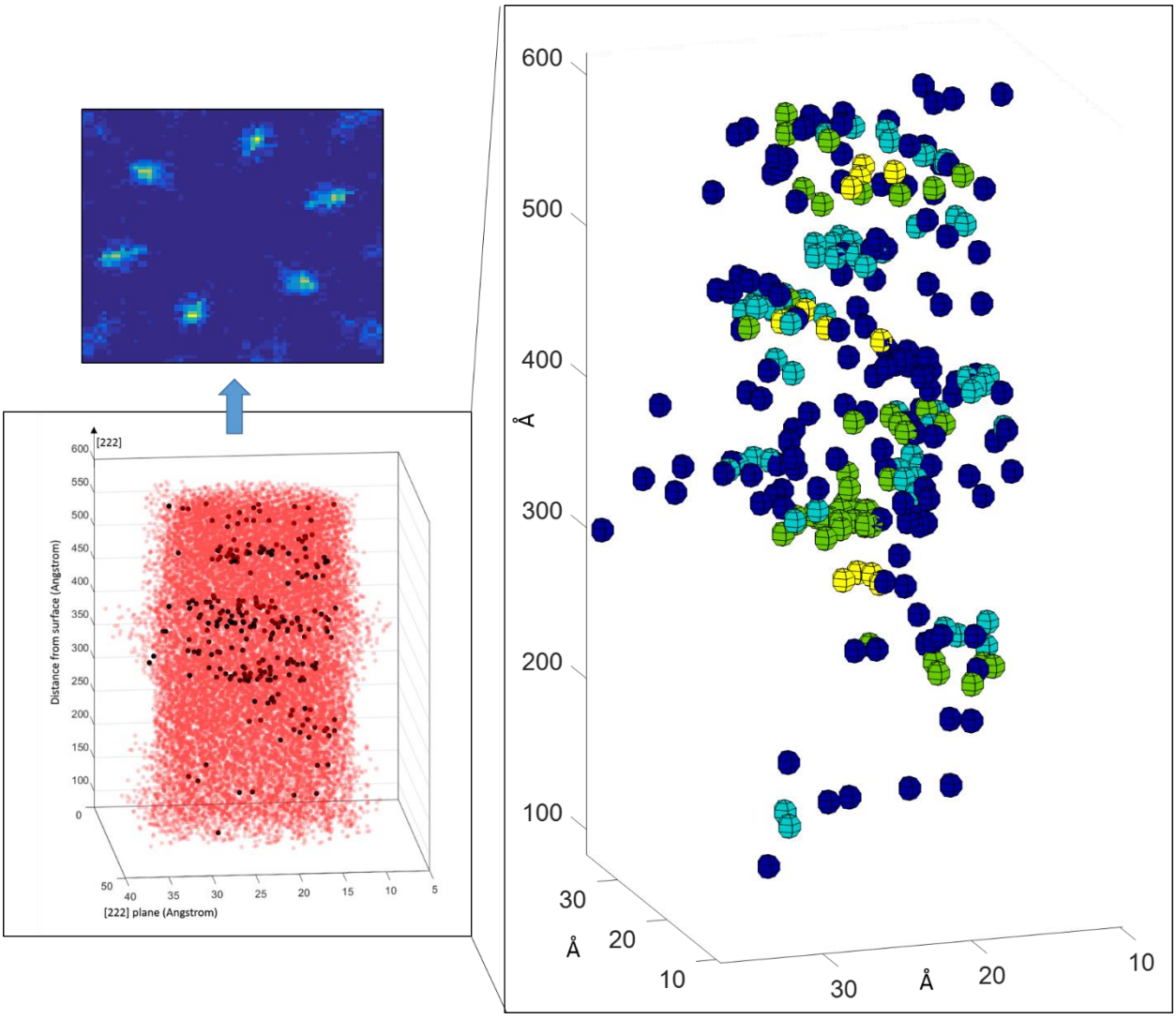

Figure 8.14 : Close up on the vacancies distribution. The vacancies are coloured according to the colour map in figure 8.13, such that the colours represent the number of vacancies inside the vacancy cluster for each case. Note that the z axis is not equally scaled in comparison to xy, for the sake of the illustration. The xySDM of the reconstructed atoms is also shown, demonstrating the successful reconstruction of the volume.

9 Influence of sample geometry on ion implantation profile

9.1 Introduction

As discussed in chapter 2, the two sample preparation techniques utilized for APT/FIM are electropolishing and FIB, and each has its own strengths and weaknesses with regards to characterisation of radiation damage. As can be seen in the example in Figure 9.1c, the distribution of Ga, C, Pt ions, that can be introduced to the specimen during a typical FIB preparation is straightforward to characterise in the resulting APT reconstruction and exclude from analysis. However, more significantly for this study, the FIM images in Figure 9.1a,b demonstrate that the lattice damage caused by the FIB procedure manifests as atomic-sized features, ranging from single vacancies to several-vacancy clusters. Furthermore, brightly imaged atoms that display a different contrast to the tungsten lattice are observed (such as the one marked with the left red arrow) can potentially highlight Ga/Pt/C atoms. Atoms that break the characteristic evaporation pattern around a crystallographic pole and are retained on the surface are marked with the right arrow. These too are potential impurities atoms resulting from FIB treatment, but unlike in the APT data, they are more difficult to resolve in FIM, as they might also correspond to irradiation-induced features such as the implanted ions themselves, or interstitials. Such features were typically observed in FIM images even following evaporation of 50 (011) layers.

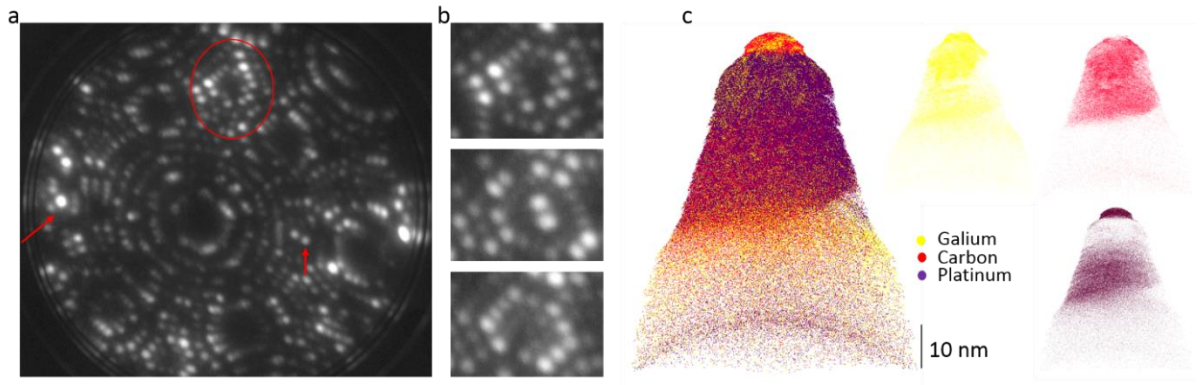

Figure 9.1: FIB damage during sample preparation as seen in FIM (a-b) and APT (c). From (a-b) it is clear that FIB induced damage is comparable to the type of damage detected in ion-implanted needles, and may pose a problem for radiation damage studies. In the APT data in (c) APT reconstruction of a tungsten FIBed sample. FIB products gallium, carbon and platinum are shown.

The FIB induced crystal damage seen here is thus comparable in nature to the type of damage caused by intentional ion-implantation experiments. It is therefore very difficult to unambiguously characterise radiation damage in FIB-prepared FIM samples. Hence, the preferred sample preparation technique for atomic-scale FIM damage studies will be electropolishing of wire-form materials.

This methodology does raise questions regarding the expected implantation profile into needle-shaped samples. In particular; how does the highly curved shape of the electropolished samples effect the damage profile and the distribution of the incident ions inside the sample? Furthermore, how will these change in comparison to an implantation performed under the same conditions into a bulk sample? Or in other words, how well does implantation of needles represent the bulk case? A final complication emerges concerning the extent to which SRIM predictions provide a good estimation of implanted ion depth profiles and material damage in both sample geometries.

This chapter aims to examine the use of electropolished needles sharpened *prior* to implantation for FIM experiments, in comparison to bulk samples that are FIBed into needles *after* implantation. The implanted ion depth ranges in samples implanted as bulk will be compared to the ones measured from samples implanted as needles. The final concentration of ions implanted into the samples is also compared as measured by APT. The effects of specimen geometry are discussed, as well as the comparison to the calculated SRIM profile.

9.2 The experiment

Ion-implantations were performed on both bulk tungsten and electropolished tungsten wire. Samples were prepared according to the lift out (for bulk) and electropolishing (for wire) procedures described in chapter 2.3. All samples were annealed prior to implantation and analysed by APT. The agreement between SRIM predictions, and the implantation profiles experimentally measured for bulk and needle implantations, respectively, was investigated for two cases:

- tungsten samples implanted with vanadium ions, to examine the case of lighter ions hitting a heavy element matrix.
- tungsten samples implanted with tantalum ions, which are comparable in mass to the tungsten matrix atoms. Tantalum ions were used instead of the traditional self-ion tungsten implantations in order to be able to distinguish between the matrix and the implanted ions in APT data.

A third type of needle-implanted sample was also implanted with the same tantalum conditions, but in this case using a WRe25 at% alloy. This enabled comparison of the alloy with pure tungsten

to determine any composition effects on the irradiation response, as well as possible insights into the damage profile inside the sample, as a number of studies have shown extensive implantation-induced clustering in W-Re alloys [60], [139], [143], [212], [213].

Table 9-1 summarizes the implantation parameters for the analysed samples. Implantation energies were set such that the maximum concentration depth of impacting ions lay within reasonable ranges to detect in the APT runs. As the mass of the ion is lower, It's penetration depth will be larger, therefore, vanadium was implanted at lower energies in comparison to tantalum. In all implantations ions were implanted perpendicular to the bulk surface, and 'head-on' to the needles orientation, as illustrated in Figure 9.3 and Figure 9.4.

	Material	Implanted ion	Implantation energy $[MeV]$	Implantation temperature [℃]	Dose $[^{ions}/_{cm^2}]$	Damage level $[dpa]$	Preparation method
Sample 1E	W	V	0.4	300	2×10^{15}	7	Electropolished
Sample 1F	W	V	0.4	300	2×10^{15}	7	FIBbed
Sample 2E	W	Ta	2	300	6.34×10^{15}	80	Electropolished
Sample 2F	W	Ta	2	300	6.34×10^{15}	80	FIBbed
Sample 3E	WRe25	Ta	2	300	6.34×10^{15}	80	Electropolished

Table 9-1 : implantation conditions

SRIM predictions for both ion-type implantations are presented in Figure 9.2. The profiles shown were taken from a calculation averaged across 10,000 incident ions[1]. The SRIM profile for the WRe25 alloy was very similar to the one predicted for tungsten.

[1] Notice that the units of the profiles are given in $\frac{atoms}{cm^3} / \frac{atoms}{cm^2}$. When multiplying these units by the dose $[\frac{ions}{cm^2}]$, the concentration is given.

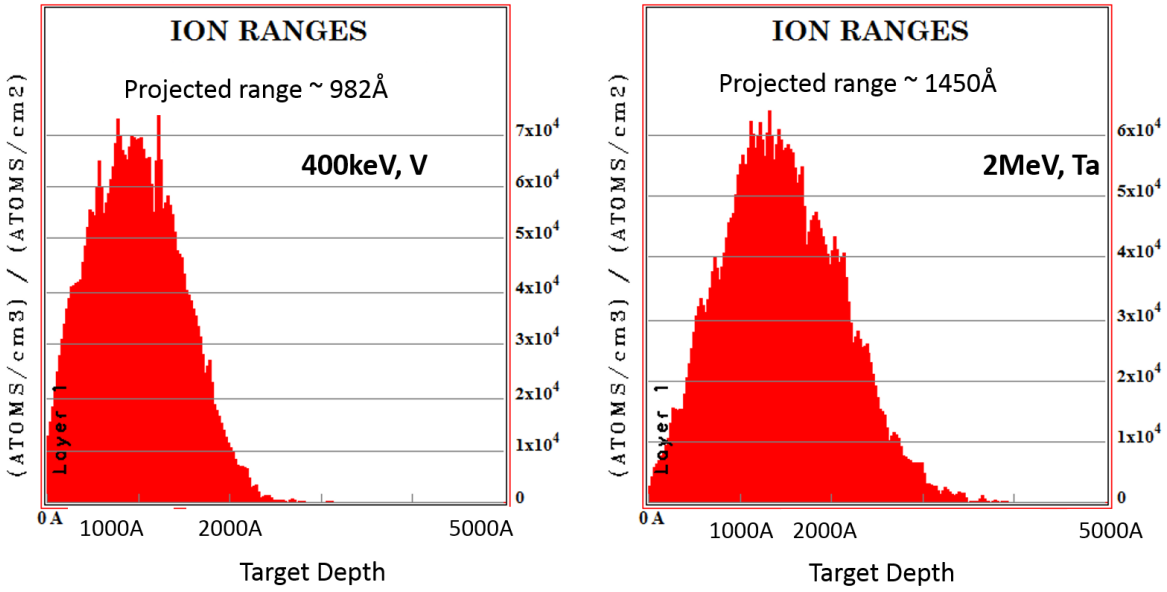

Figure 9.2: SRIM predictions for implanted ions distribution of the different implantations performed. Each simulation consisted of 10,000 ions.

9.3 Tantalum implantation into tungsten

APT results for the tantalum implantations are presented in Figure 9.3-Figure 9.5**.** Figure 9.3 plots atom maps for tantalum, carbon and a vertical slice of the tungsten atoms as measured for the electroplished sample. It can be seen that the tantalum visually appears to be distributed uniformly. The carbon distribution possibly indicates some damaged regions, highlighted through the segregation to a region near the sample apex. Furthermore, a region of high tungsten density can also be observed, similar to those observed in the 33dpa tungsten implantation case (chapter 3), which indicates damaged regions in the crystal from the observed trajectory aberrations**.** Figure 9.4 plots the atom maps of the same implantation for the FIB-prepared sample. Here again, the tantalum seems to be uniformly distributed. Figure 9.5 plots 1D tantalum concentration profiles measured from the APT reconstructions from both types of samples, plotting concentration as a function of depth from the sample surface.

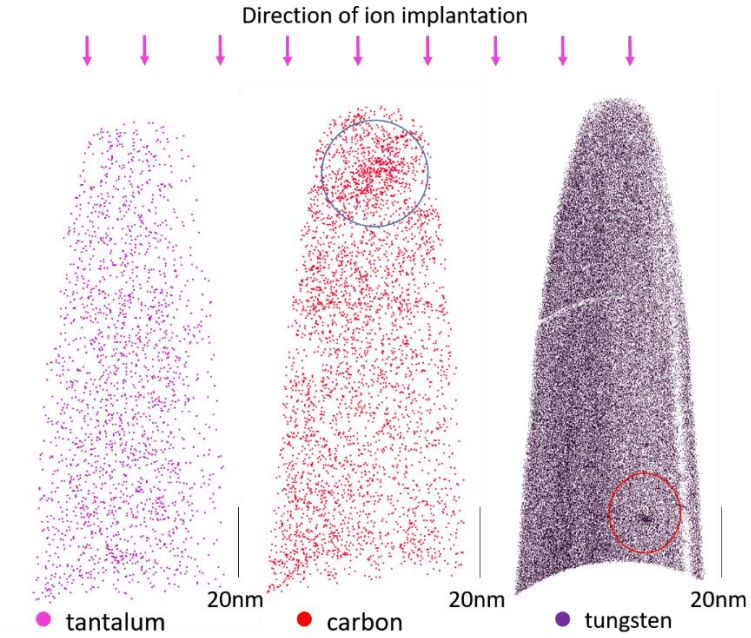

Figure 9.3 : Pre-sharpened electropolished needle results in APT following tantalum implantation. Carbon and tungsten show density variations that might correspond to defects. Tantalum seem to be distributed homogenously.

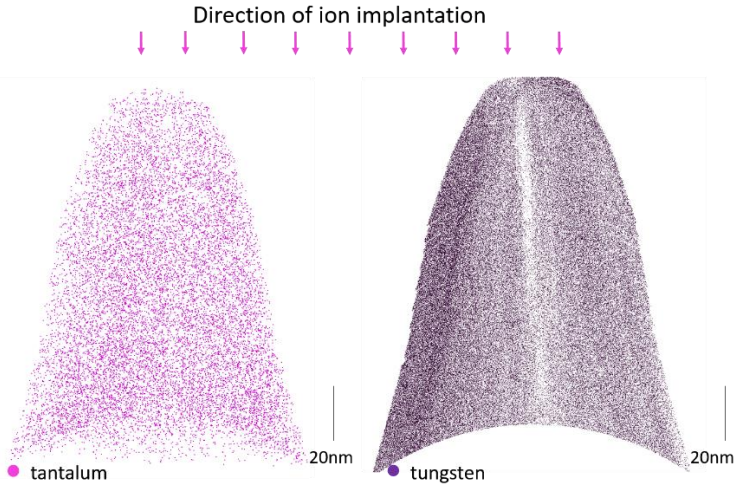

Figure 9.4: Post-implantation FIB-prepared sample, APT results following tantalum implantation. Carbon is not shown since also originates from the FIB specimen preparation process. Both tungsten and tantalum distributions seem uniform.

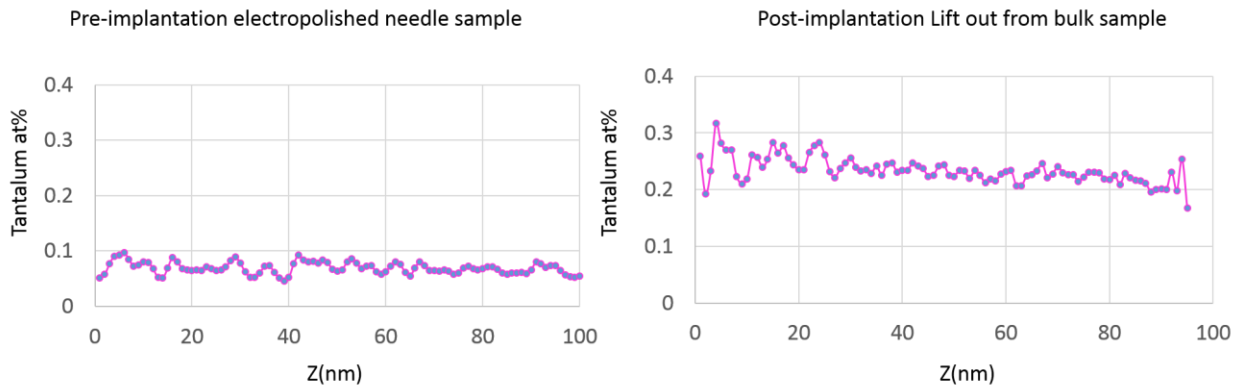

Figure 9.5 : 1D concentration profiles of tantalum along the z direction (depth) of the bulk and needle samples. In both cases the profiles seem to not vary significantly with depth. Needles exhibit lower concentration than bulk.

To ensure that these results are not influenced by any edge and/or geometry effects from the finite size of the reconstruction, the concentration profiles are plotted again in Figure 9.6, this time from a limited cylindrical region of interest (ROI) within each dataset. The ROIs were defined to be the same size for both samples, the dimensions of which are presented schematically in Figure 9.6. The resulting profiles are very similar whether they originate from within the ROIs or from the entire datasets.

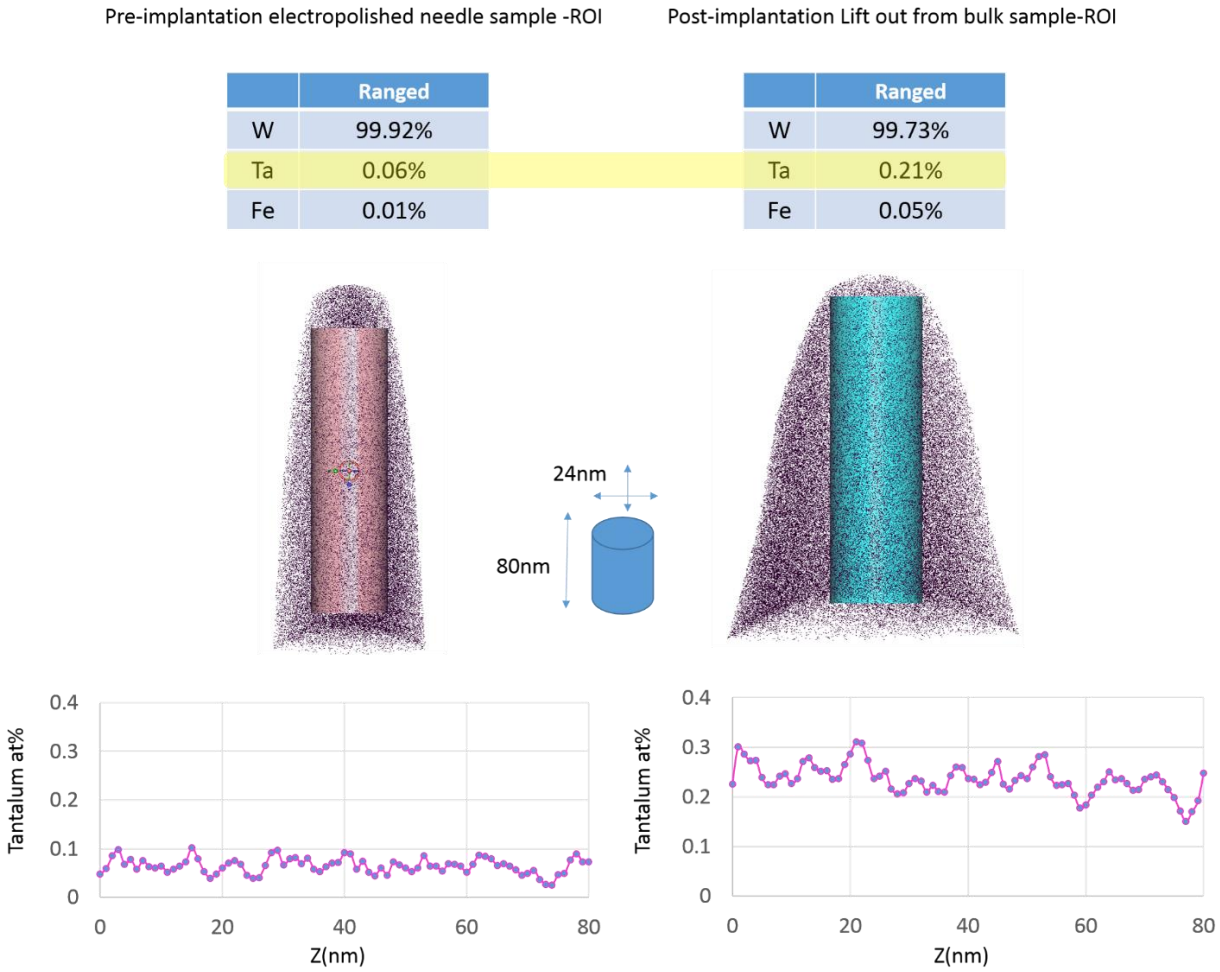

Figure 9.6: Concentration profiles from selected cylindrical region from the centre of the reconstructions. The same sized region of 24x24x80nm area has been selected in both. Resulting concentration profiles are similar to the ones measured from the entire dataset, exhibiting an approximately constant trend and a lowered concentration of tantalum in the needle case.

The concentration of tantalum ions inside bulk and needle samples was measured by APT. The average concentration for the two bulk samples examined was found to be $0.215 \pm 0.005\ at\%$, and $0.09 \pm 0.02\ at\%$ for the three needle samples (the error estimations are given by the standard deviations of the concentration values measured for the different samples of each type). When comparing the average concentrations measured in both types of samples it becomes apparent that the bulk samples contain approximately twice as much tantalum as the needle samples, even though both were implanted at exactly the same conditions during the same implantation session. Next, the tantalum distributions are compared to the corresponding SRIM predictions. The SRIM profile predicts a distribution of implanted ions with a sharp rise in concentration peaking at ~100 nm in depth from the surface, followed by sharp decrease as seen in Figure 9.2. However, both the profiles measured in bulk and needle samples exhibit a flat trend across the depth of the samples. For comparison, the APT bulk profile and the calculated SRIM profile are both plotted together in Figure 9.7. The SRIM profile was multiplied by the implantation dose, and the concentration in at% was calculated in relation to the expected theoretical density of tungsten ($6.338\times10^{22}\ \mathrm{atoms/cm^3}$). Since the protective platinum layer applied in FIB had been fully removed during the sharpening stage, it is difficult to precisely determine the starting depth in the APT bulk sample reconstruction, i.e. in the resulting measured concentration profile the depth of 0 nm does not necessarily represent the surface of the bulk sample but is actually further in depth into the specimen. However, this uncertainty in the exact depth of the measurement is estimated to be a maximum of 50nm, from examining images taken before and after the final FIB milling stages. Since a very slight trend of decreasing concentration is seen in the measured profile, the attempt to fit the APT profile to the SRIM

profile was performed on the decreasing part of the SRIM profile, and the APT depth in Figure 9.7 is set according to the point where both profiles match in concentration. However, attempts to fit the APT profile to the SRIM one at any depth will fail as a sharp change in concentration is predicted by SRIM across any region of 100nm.

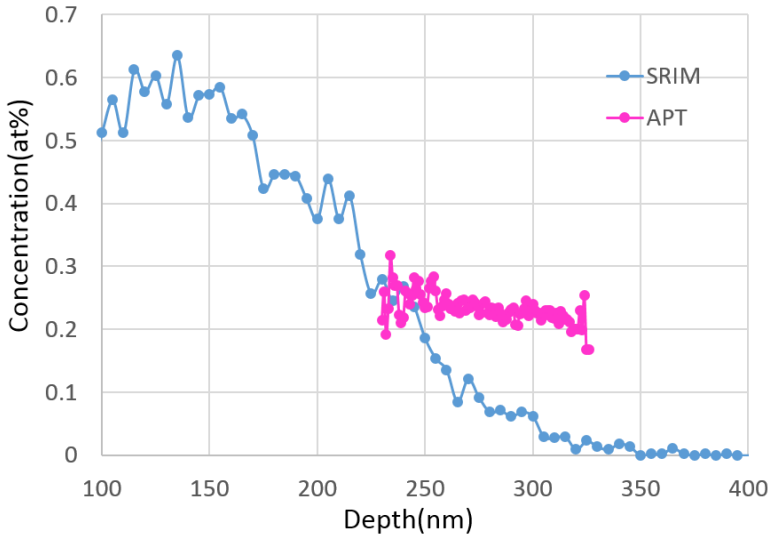

Figure 9.7: 2MeV tantalum concentration profile inside tungsten, as predicted by SRIM (blue curve) and measured in APT for the bulk sample (pink). Since the starting depth of the APT profile was ambiguous due to the removal of the protective layer during final sharpening, the start depth in the figure is set at the point where SRIM and APT concentrations match. Unlike SRIM predictions, the measured profile is almost flat across the measured 100nm, regardless of the start depth.

9.4 Vanadium implantation into tungsten

The same analysis was performed on the bulk and electropolished samples implanted with vanadium. The results for implantation into pre-sharpened needles are plotted in Figure 9.8. Here too a relatively flat concentration profile of vanadium is measured across 100nm in depth of the sample. All three samples examined in this study exhibited similarly flat profiles.

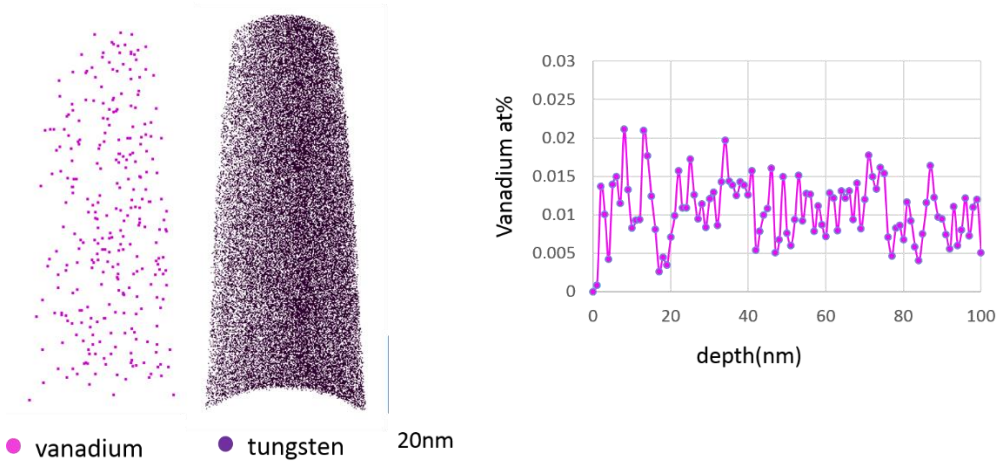

Figure 9.8: Atom maps from implantation of 400keV vanadium ions into pre-sharpened tungsten needles and resulting 1D vanadium concentration profile through the depth of the sample.3% of tungsten atoms are shown from a 15nm slice of the data for clarity.

Results of the implantation into bulk samples are presented in Figure 9.9. In this case a portion of the protective platinum layer was retained on the surface after FIB preparation, and was used to more precisely determine the actual surface of the sample, estimated at a depth of 45nm within the resulting atom probe reconstruction. This is also where the concentration of tungsten is found to plateau, further signalling the surface of the sample as seen in Figure 9.9a. A concentration profile across the relatively short depth of approximately 40nm from the identified surface of the tungsten sample to the end of the reconstruction could be measured. According to SRIM predictions even within this short region the concentration of vanadium is expected to increase significantly, which in this instance is indeed observed in the APT data. This is evident in the concentration profile and is even visually apparent in vanadium atom map presented in Figure 9.9b. In c, SRIM profile was converted as before to at% units. The depth coordinates of the APT vanadium profile in Figure 9.9c were moved by 45nm, so that the estimated surface matches the beginning of the SRIM profile. This time, the APT profile better matches expected implantation profile.

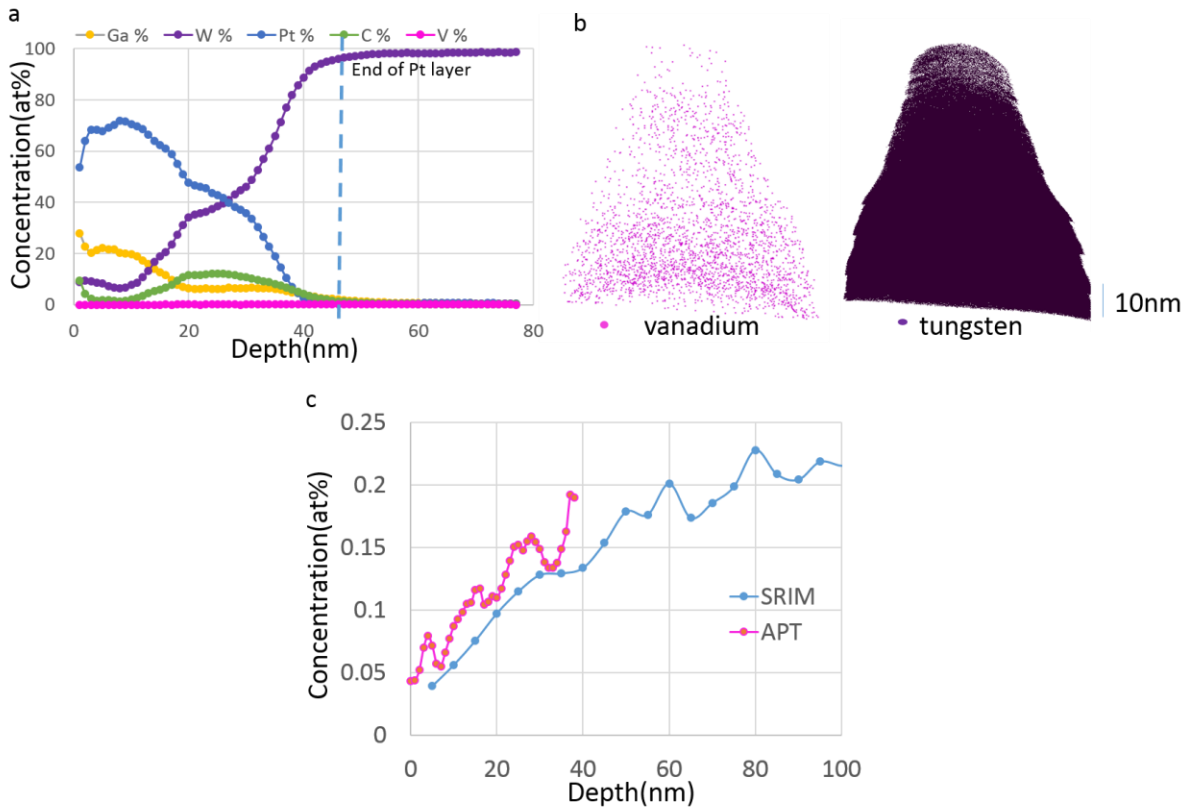

Figure 9.9: APT results of the bulk tungsten sample implanted with 400keV vanadium ions. (a) The surface of the sample was estimated at the depth where the platinum concentration was reduced to zero and tungsten concentration seem to stabilize. (b) Resulting W and V atom maps. (c) APT vanadium profile in comparison to SRIM profile.

Compositions were calculated for three needle samples, yielding an average concentration of $0.01 \pm 0.008\ at\%$ vanadium. Since the concentrations of vanadium measured are very low, the average concentrations as well as the presented profiles in Figure 9.8-Figure 9.9 incorporate the entire data set, without further reducing it to a selected ROI. However, the same concentration profile was observed for the vanadium when measured within a cylindrical ROI along the depth of the sample. The needles average concentrations results seem to be spread between the three needles examined, with one of the three exhibiting a larger, 0.027at% average concentration.

Finally, Table 9-2 summarizes the different average compositions measured for needles in both tantalum and vanadium implantations along with the doses implanted for comparison.

	average V concentration %	average Ta concentration %	Ta/V % measured	Implanted V dose $[^{ions}/_{cm^2}]$	Implanted Ta dose $[^{ions}/_{cm^2}]$	Ta/V implanted
Needle	0.01	0.09	9	2×10^{15}	6.34×10^{15}	3.17

Table 9-2: APT average concentrations measured for pre-sharpened needle samples after vanadium and tantalum implantations, along with the actual implanted dose.

9.5 Tantalum implantation into WRe25 alloy

WRe25 at% alloy in the form of electropolished needles was implanted at the same tantalum implantation conditions as the tungsten samples. The APT characterisation of the specimen is presented in Figure 9.10 and Figure 9.11. The concentration profile seen in Figure 9.10 is taken from a cylindrical ROI extending along the analysis direction, and the tantalum level is constant with respect to depth, similar to the profiles observed for the implanted tungsten needles. The average tantalum concentration however, was 0.2 at%, closer to the one measured in the bulk tungsten rather than the needles. Two such needles were analysed, exhibiting the same trend.

Figure 9.11 shows the post-implantation APT reconstruction of rhenium atoms. Irradiation-induced clustering is visually apparent while the distribution of rhenium prior to implantation was homogenous. A cluster search was performed to identify the individual clusters using the maximum separation method [144]. The parameters defining this approach were d_{max} = 0.28nm and N_{min}=17. Rhenium concentration in the clusters was found to be 70 at%, slightly lower than previous results obtained in neutron irradiated WRe25 wire [212]; however in that previous investigation implantation was carried out at an estimated level of 8 dpa and at a temperature of 500°C. Next, the number of clustered atoms was estimated as a function of depth, as a measure to the damage extent. For this purpose, after application of the clustering algorithm,

the reconstruction was divided into thin 10nm sections in depth. The number of ranged atoms detected in each of the clusters in each of the sections was summed and is plotted Figure 9.11b. Summation of only rhenium atoms detected in the clusters produced a very similar plot. This analysis was restricted to the data within a cylindrical ROI along the z direction, so that each depth increment has an identical volume. While the tantalum ions seem to exhibit a flat profile, the number of clustered atoms as a function of depth after implantation is not flat, and seem to reasonably approximate the shape of the SRIM profile of damage (Figure 9.11b), although there is significant scatter in the data from the small numbers of atoms considered. The two plots are placed in the same figure for comparison of their trends, the actual 'damage' values are not comparable.

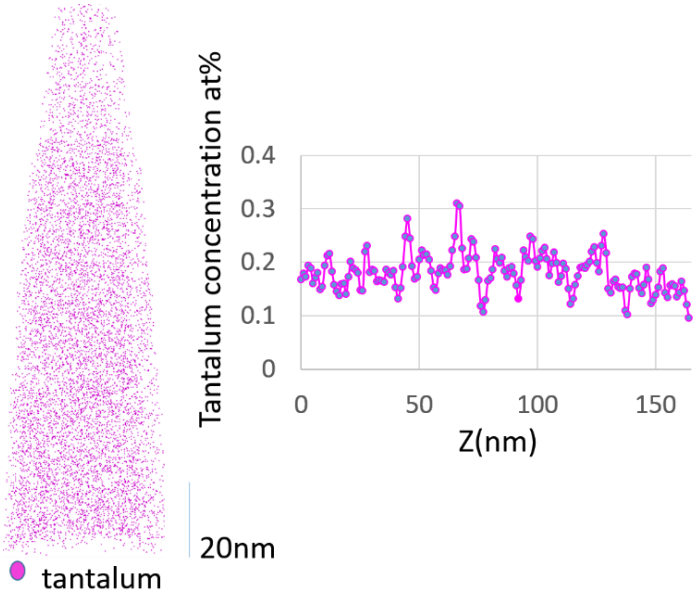

Figure 9.10: Atom map and 1D concentration depth profile of tantalum with APT reconstruction of a pre-sharpened WRe25 needle

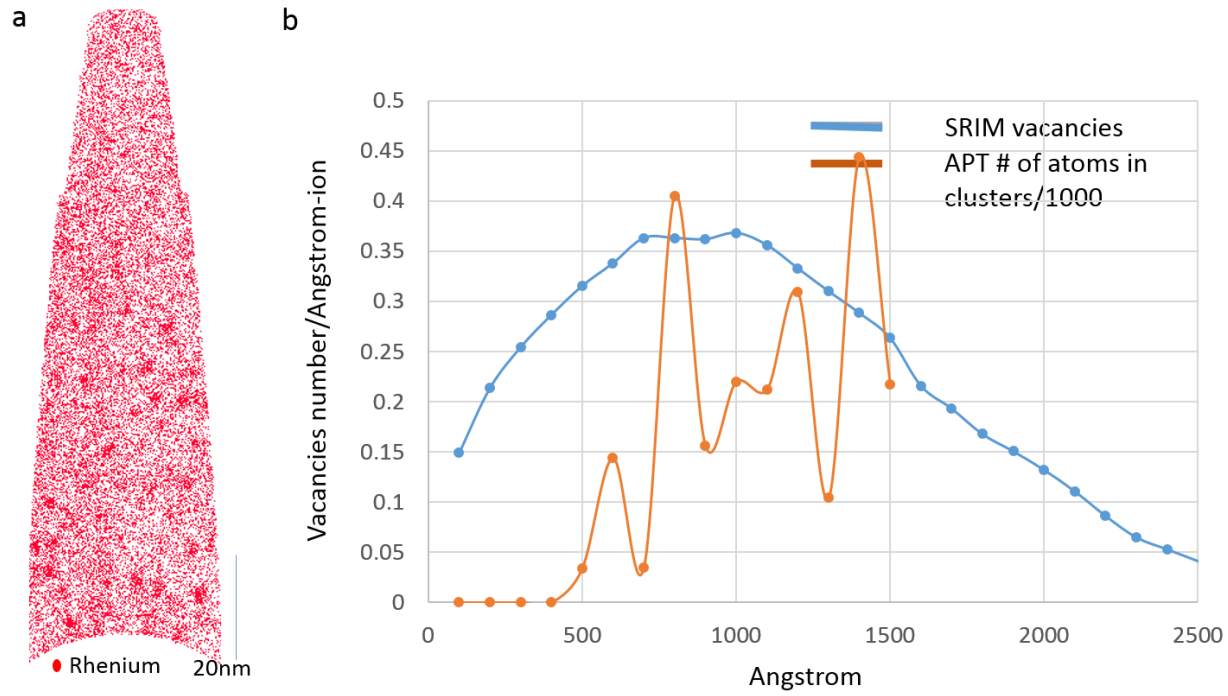

Figure 9.11: Custer analysis distribution in WRe25 alloy post tantalum implantation. (a) A 3 nm thick slice of the APT reconstruction of rhenium (taken from the x direction). (b) SRIM predicted profile for damage, compared to the volume fraction of the clusters as a function of depth. Profiles are scaled in the 'y' axis of the plot as to be presented on the same plot, the SRIM vacancies profile is presented in its original numerical values.

9.6 Discussion

From the results above several observations can be made, some more prominent than others. For tantalum and vanadium implantations it can be seen that the final distribution of implanted ions inside all electropolished needles is constant throughout the measured depth of the samples. This is in contrast to the predicted SRIM concentration profile, in which implanted ion concentration increases as a function of depth from the surface inside the sample, peaking at the mean projected range, then decreasing. This discrepancy can possibly be attributed to the highly curved geometry of the samples into which the ions were implanted. As well as from the apex of the needle, ions are also likely to penetrate the needles along their shank. Each of these ions addressing the penetration point as a local z=0 surface, convolute the measured concentration.

Hence, a flatter profile of ions might be expected. Furthermore, erosion of the surface of the samples by the implanted ions [214] may also contribute to the flat profile measured, eliminating the original surface where according to the simulations ions are less likely to be retained.

A perhaps more surprising observation is the difference in the measured APT concentration profiles of tantalum and vanadium in the bulk samples. While vanadium concentration follows the expected SRIM trend in bulk, tantalum ions appear to be distributed homogenously along the depth of the sample, across a region of approximately 100nm, corresponding to half the size of the predicted SRIM profile. There are many assumptions made in the SRIM calculations that are not suitable for this type of experiment such as 0K temperature and an isotropic displacement energy, most of them however are expected to influence the damage profile and not the implanted ions profile in the bulk. On the other hand, the assumption of an amorphous matrix used in SRIM is expected to influence the mean free path of implanted ions inside the matrix between successive collisions, creating in turn a change in their final distribution. It could be that the different mass and energy of the implanted tantalum and vanadium ions is the reason for the difference, indicating that light, lower energy ions follow the SRIM profile better. Further, as the sputtering of tungsten atoms by tantalum ions is expected to be greater than the sputtering due to vanadium ions, it could be that the eroded tungsten surface is contributing to the flat final profile observed in APT. A set of experimental conditions could possibly also cause such differences. The implantation profile is expected to depend on the quality of the surface of the bulk samples, which, if not completely smooth could result in distorted profiles. Further, as the degree of control and precision over the experimental parameters of the implantations is difficult to determine, a direct comparison between two different implantations is difficult to make with

certainty. A spread in the energies of the implanted ions for example can result in a flatter profile. Finally, while a definite non-flat profile had been observed in the bulk vanadium case, the degree of fit to the SRIM profile is dependent on APT calibration of depth, and since limited crystallographic information was found in the dataset, it is possible that the gradient of vanadium increase with depth is smaller, resulting in a less steep profile.

Another comparison parameter between bulk and needle samples are the measured concentrations of the implanted ions. The average tantalum concentration in the bulk samples was found to be approximately twice as high as the average concentration measured for needles. The vanadium implantation concentration profiles show even larger discrepancies (although more difficult to compare due to the non-flat bulk profile). A possible explanation for the differences between compositions measurements in the needles and bulk samples could be the erosion of the needle-shaped samples during implantation. Of course bulk samples will also experience some erosion, however, the sputtering yield in tungsten was found to depend on the incident angle [215]. From SRIM calculations, the number of eroded tungsten atoms per implanted tantalum ion was found to increase by 180% for an incident beam at 45° in comparison to 0° in a simulation averaging 5000 2MeV tantalum ions. While in bulk the incident angle is only 0°, the surface of the needles will experience a range of angles, resulting in increased sputtering, and in turn, decreased final concentration of implanted ions. A second possible explanation for the reduced final concentration of implanted ions in the needles samples could be the scattering of the penetrating ions out of the samples. The incident ions will undergo a series of collisions inside the sample, changing their direction with each one. It is possible that some of these ions

will be scattered out of the very narrow geometry at the apex of the needle sample, as opposed to the effectively infinite flat surface of the bulk.

The difference between vanadium and tantalum compositions can be further investigated by comparison of the average ion concentrations measured in needles and the actual dose implanted. As the tantalum dose implanted was approximately three times higher than vanadium, tantalum concentrations measured in the needles were indeed higher than the ones measured for vanadium. However, while the requested dose was 3 times higher for tantalum, the corresponding difference measured in needles was closer to 9 times higher. This observation emphasizes extensive loss of vanadium ions from the needles in comparison to the tantalum case. Preferential erosion of the needle in the case of vanadium in comparison to tantalum is not a probable explanation. SRIM simulations show lower sputtering yield in the vanadium case in comparison to tantalum for both the 0° and 45° incident cases. A second explanation could be the distribution of lateral ranges of the respective ions as a function of depth. From SRIM simulations presented in Figure 9.12a,b, performed according to the implantation energy in each case, the radial range of the ions on the XY plane (perpendicular to the incident ion beam) for the tantalum implantation increases from 40 to 100nm as a function of depth. For the vanadium case however, the radial distribution of ions is approximately constant as a function of depth and is estimated at 70nm. This distance is comparable to, if not larger than, the diameter at the apex of needles, therefore vanadium ions are prone to leaving through the surface of the specimen after a series of scattering events. A larger tip radius will therefore result in less loss of vanadium ions, and could account for the one vanadium sample exhibiting a larger average concentration. In the tantalum case, ranges start from 40nm at the surface, and reach 70nm only at a depth of 200nm,

at which point, due to the shank angle of the specimen the width of the needle is also larger. To determine if this effect is dominated by the different energies of the two implantations rather than mass, the simulations were performed a second time, with the energies exchanged between vanadium and tantalum cases. Figure 9.12c,d plot simulations for the lateral distribution of tantalum ions implanted at the lower energy, 400keV, compared to that of vanadium ions implanted at 2 MeV.

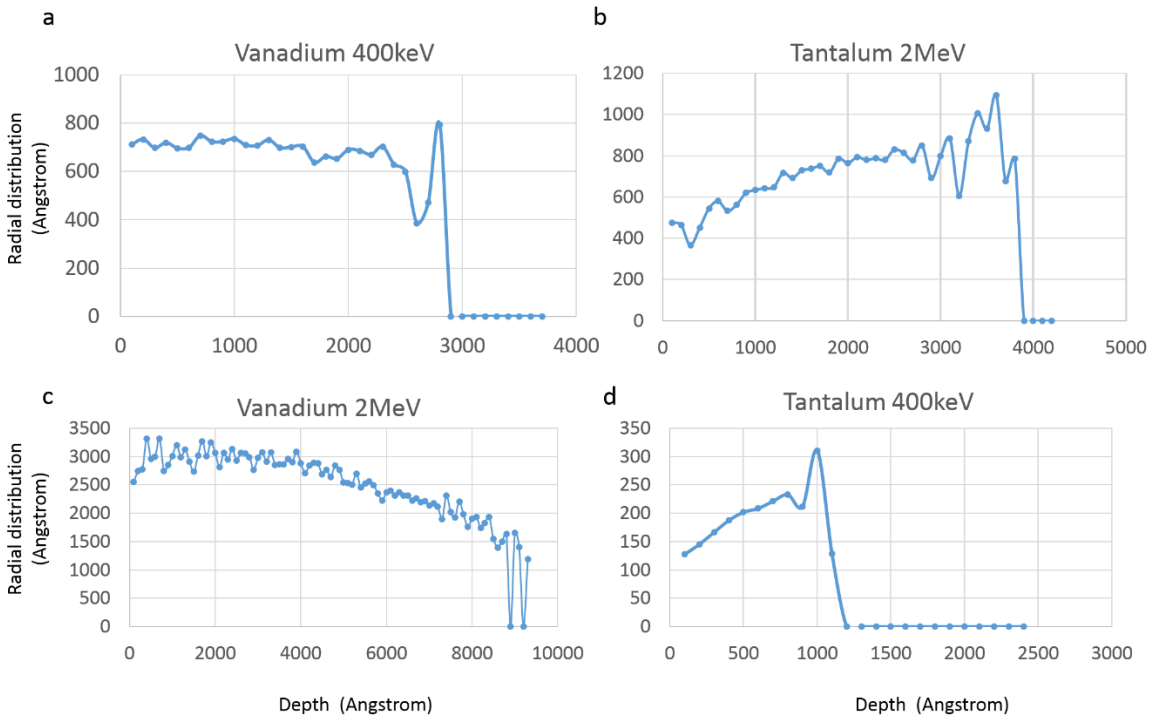

Figure 9.12: Radial distribution on a plane perpendicular to incident beam of implanted ions as a function of depth. Vanadium ions exhibit a flatter dependence on depth than tantalum in both 400kev and 2MeV energies. At 400keV, with radial distribution of 700 Å, ions can be easily scattered outside of the small needle tip dimensions.

Even with the significantly higher energy, the shape of the profile remains flatter for vanadium than tantalum, indicating that this property is dominated by the mass of the ion rather than energy. It is therefore expected to be an issue in all light ions implantations. Of course, as mentioned before, a direct comparison between the results of two different implantation

sessions is difficult to make due to the un-certainty in implantation parameters as well as the limited statistics, and small APT concentrations measured. The results brought here justify further investigations for the calibration of needle implantations. To obtain robust comparative results between different implantation sessions a second round of implantations should be made for the two cases, and the experiments repeated.

Finally, post-implantation clustering observed in WRe25 pre-sharpened needle provides an estimate of the damage profile in the sample. While the implanted ions depth profile does not match SRIM predictions, the number of clustered atoms as a function of depth appears to follow the overall shape of the SRIM profile, peaking at a slightly larger depth. A similar result was previously presented in [60] for a bulk sample as clusters profile in WRe2 alloy was found to match the trends of the SRIM damage profile after a 33dpa tungsten implantation at 500℃. In [143] clusters in WRe25 alloys had been detected post implantation at 300°C, at a damage level as low as 1.5dpa. Both bulk samples and needles were implanted in that study. The needles were found to generate a slightly flatter profile of rhenium clusters size distribution relative to the bulk. Differences were reported for the rhenium concentration inside the clusters and their sizes, however no clear trends were evident. Finally, in this study, the tantalum concentration in the needle was found to better match the one measured in bulk tungsten. SRIM calculations of sputtering yield in the alloy in comparison to tungsten did not show significant differences, as nor the radial distribution of the expected tantalum ions inside the alloy vs pure tungsten. The origin of this different behaviour exhibited by the alloy in comparison to pure tungsten in the needle samples remains unresolved and might be attributed to the small statistics, or even the needle's position on the implantation stage.

A similar observation with regards to the damage depth profile in implanted needles had been made in chapter 8. The same type of pre-sharpened tungsten needle implanted with vanadium was analysed, implanted under the same conditions and in the same session as the rest of the vanadium implanted samples studied in this chapter. The vacancy distribution of the electropolished needle was measured in FIM, and found to exhibit a non-flat profile across the depth around the (222) pole. Similarly to the WRe25 case, the vanadium concentration in the needle was found flat. It is possible then, that the implanted ions are scattered out of the needle after a series of collisions inside it, changing the observed ion profile, however, still leaving a damage trail that is not very different from the simulation prediction.

To summarize:

An APT investigation has been made into the effect of specimen geometry on the resulting implantation profile, aimed to assess the extent in which pre-sharpened needle implantations represent the bulk case:

- The concentration profiles of implanted ions into pre-sharpened needles were found flat for both light ions and self-implanted ions, therefore deviating from the expected SRIM profile.
- Concentration profiles measured for needles in the self-implantation case were found to closely describe the shape of the profile measured in bulk. For the light ion implantations, a discrepancy between bulk and needles was found and should be taken under advisement as bulk samples were found to follow the SRIM profile.

- The concentration of implanted ions measured in bulk samples was found to be higher than the concentration measured in respective needle samples. This could be due to preferential erosion and scattering in the needle case.
- The effect of reduced final concentration of implanted ions in needle samples was found more prominent in the light vanadium case, possibly due to the increased spatial straggle of the ions in this case. This should be taken under consideration when determining the dose level in light ions implantations to needles.
- The damage profile in needles was found to exhibit an increasing trend with depth in both WRe25 alloy implanted with tungsten and vanadium implanted tungsten samples, unlike the flat ion profile measured in both. This result is encouraging for prospective uses of pre-sharpened needles, optimal for FIM use, in radiation damage studies.

10 Summary and future work

Inspired by the goal of atomic-scale characterisation of radiation damage for fusion applications, new automated techniques were developed for 3DFIM reconstruction and data analysis. The new tools presented in this thesis are hoped to further establish FIM as a still relevant, highly complementary technique to APT.

In the comparative FIM/APT study presented in chapter 3, FIM was demonstrated to provide superior detection efficiency to APT as the damage evolution in self-implanted tungsten samples was investigated. While vacancies were detected in FIM data at the low 0.01 dpa damage level, it is only at 33 dpa where the APT reconstruction of tungsten exhibited evidence to crystal defects in the form of high density regions in the matrix. Dislocations were detected in APT data at 6dpa through the segregation of carbon to their vicinity.

Despite its advantages in crystallographic characterisation, the tedious data analysis required to extract the atomic 3D information from the overwhelming amount of FIM images taken in a FIM experiment has been a major obstacle in the employment of the technique.

The automated ‘atom-by-atom’ reconstruction algorithm presented in chapter 4 enables the transformation of a large stack of time-ordered FIM images into a 3D point cloud of atomic coordinates. The algorithm is designed to follow the dynamic nature of the FIM experiment, adjusting to the changing evaporation rate and local magnification conditions. It is able to track the atoms as their image coordinates shift from image to image, to detect the evaporation of one and the appearance of another, and to determine their relative depth coordinates. The algorithm

was successfully applied to the reconstruction of thousands of tungsten atoms. While optimally designed for the analysis of atomically resolved poles of the FIM image, it was shown to be successfully applied to the reconstruction of larger, less ordered datasets in chapter 7, with the reconstruction of carbides extending across the whole steel tip, and an atomically resolved grain boundary in tungsten. Future work could potentially expand the existing algorithm to analyse the entire FIM image and incorporate the radius of the curvature of the tip, the projection characteristics, and the relative angles between the different analysed poles. Further, while currently being used to automate the data analysis stage of the FIM experiment, the algorithm can be used with slight modifications to possibly automate the currently manual data acquisition stage. Un-like APT, where the evaporation rate is measured by the detection of evaporated atoms and voltage raised automatically accordingly, in FIM no such feedback currently exists. The algorithm could be used 'live' during the FIM experiment to detect evaporation events, and automatically control the voltage accordingly. Finally, a variety of simulated FIM datasets can be generated and used to systematically test the accuracy of the reconstruction algorithm and it's boundaries.

It was also shown that once the data is transformed into a reliable 3D points cloud, a variety of analysis possibilities is then available, similarly to APT data. Nearest neighbours' statistics and the more advanced spatial distribution maps are possible to implement with the new reconstruction tools. This opened the door to a quantitative inspection of the deviation of the reconstructed structures from the expected crystallographic ones. Preliminary analysis in chapter 6 applied SDMs in a similar way as was previously applied to APT data to investigate the limitations and resolution of the FIM experiment, as well as the effect of lattice defects on the resultant

distortion. Un-isotropic degree of variance in atomic positions was found around all atomically resolved poles examined, with the variance in a radial direction to the centre of the pole found to be ~150% larger than in perpendicular direction. An increased distortion in the average NNs distances recorded around the (222) pole in comparison to the (-141) pole was found suggesting a dependence on crystallographic orientation. SDMs were also shown to be sensitive to the increased distortion in reconstructions of volumes containing vacancies. Further analysis in chapter 5 revealed subtle but consistent sub-angstrom movements of the imaged positions of atoms in response to the evaporation of another atom from the same plane. The displacements were found to correlate in size to the distance from the evaporated atom, with the NNs displaced the most. As FIM images are the result of a complex convolution of the field evaporation process of surface atoms and ionization of image gas atoms, the origin of these displacements is challenging to resolve, and will require further work. The analyses performed in chapters 5-6 demonstrate high accuracy, quantitative data analysis options available as an outcome of atomic 3D reconstruction, that can shed light into the still not fully-resolved image formation process of FIM. To further explore these phenomena similar analyses can be made on data taken at different experimental conditions of temperatures/gas pressure/voltage. Coupled with advanced atomistic simulations, these can yield new insights into the dynamic FIM image formation process, quantification of surface relaxation, local magnification changes, trajectory aberrations, as well as structural information about the examined materials, and the damage evolution in them. 3DFIM atomistic data can be used to inform such simulations, and indeed molecular statics simulations are already being applied to the 3D coordinates computed in this thesis, aimed to

obtain the most accurate presentation of the reconstructed volume, which in turn will serve as input for molecular dynamics studies.

Further processing steps were developed to identify vacancies within the 3DFIM reconstruction data and employed to plot their spatial distribution and depth profile across a 50nms depth interval of the (222) pole in an ion-implanted tungsten sample. The vacancies detection algorithm suggested in chapter 8 relies on no crystallographic assumptions and is designed to overcome local distortions in the crystallographic structure. However, as the accuracy of the vacancies analysis still requires improvements, a different approach can be considered in the future, that will utilize lattice rectification methods to correct the distortions in the data and locate vacancies based on the expected theoretical lattice arrangement. Large and accurate experimental vacancies statistics are needed to inform theoretical studies seeking to understand the mechanisms in which lattice damage evolves post irradiation. As most of the current studies are validated against TEM data, the vacancies behaviour remains un-verified. Vacancies distributions such as the ones extracted in chapter 8 can be used in the future to advance such studies.

Finally, APT/FIM investigations in chapter 9 were employed to evaluate the influence of the sample's geometry at implantation time on the resultant implantation outcome. The observed implanted ion concentration was found to be significantly lower in needle-implanted samples in comparison to bulk. While needles exhibited flat concentration profile for the implanted ions, the damage profiles were found to exhibit closer resemblance to the ones predicted by SRIM simulations. Therefore, pre-sharpened needles can be cautiously utilized to characterise the damage profile in implanted materials, with an emphasis put on the correct calibration of the dose level. In future FIM work, if FIBed bulk samples are wished to be studied, the new

reconstruction algorithm could be employed to quantify the characteristic FIB damage caused during the preparation process of the samples. Once a comprehensive study of the FIB damage is done, it could be possible to de-convolve it from the radiation induced damage measured in FIBed samples.

Appendix 1: Automatic identification of nearest neighbours

The algorithm employed to automatically locate the 'theoretical' NNs of each atom is described here. For each atom, distances from all other atoms on the plane are measured and arranged in an ascending order. The algorithm then examines the closest 6 neighbours. The closest atom is assumed to be a true NN. An angular region around it is then defined, such that no other NNs can be found within this region ($60°$ used here for the analysis of the (222) pole). The algorithm then scans the list of the remaining 5 atoms. Each is examined with respect to the already occupied angular regions around the original atom. If the atom is outside of the occupied regions (see the defined region in Figure 1) then it will be verified as a NN, and an angular spread will be defined around it. This way, the atom marked in a red circle in a is eliminated from the final NN's list since it lies within the same region defined by the closer atom in that angular region.

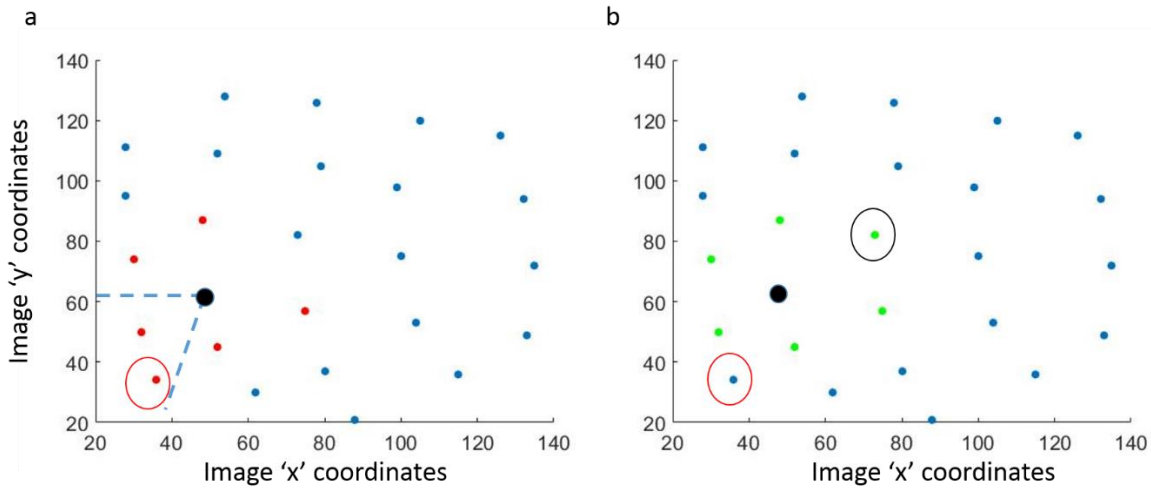

Figure 1: Locating nearest neighbours. (a) The atoms marked in red are the six closest atoms to the middle black atom. The atom marked with a red circle is not the correct 'theoretical' sixth NN. It is eliminated from the NNs list in (b) as it's within an angular region around a closer NN. (b) Atoms marked in green are the NNs found by the algorithm. The wrongfully identified atom in (a) has been removed and the correct NN (marked in a black circle) was located.

Once the closest six are sorted, the rest of the atoms are considered in an ascending order of their distance from the original atom, in case the distorted structure has placed them further from their theoretical NN atom. These atoms are considered in the same way, however the angular region defined by them will be larger. As can be seen in Figure 1b, when considering further atoms, the remaining last NN is correctly identified and is marked with a black circle. The atoms marked in green are the final six identified NN's of the black atom.

A final 'post-processing' step is taken at the end of this analysis. The list of atoms and their identified NNs is examined again, this time to assure a mutual NN connection. This means that once an atom had been identified as a NN to another atom, the other atom should be found as a NN when the algorithm is applied to find the NNs of the first atom. This step will remove most of the remaining 'false identification' mistakes.

Appendix 2: Image analysis for the detection of multiple vacancies

In order to detect and correct for cases where a small cluster of vacancies was wrongfully identified as a single vacant site, a representative image was automatically chosen and analysed (when found) for each detected vacancy. The image was chosen to be the one in which most of the identified vacancy's NNs were found to be present according to the initial list of atomic coordinates detected on all images in the reconstruction stage (if no image was found in which at least 3 neighbours were present, the vacancy was not analysed further). For cases where such an image was found, the shape of the 'dark' area around the identified vacant site was determined as seen in Figure 1. The image was binarized according to a threshold set by the intensity value at the coordinate in which the vacancy was detected by the vacancy finder code (marked by the green dot in the figure). In case the number of pixels found to be in a lower intensity was less than 200 (determined experimentally for this dataset, characteristic of a vacant site), the threshold would be raised. This process was repeated until the area defined around the vacancy (seen in grey on the images on the right in Figure 1) was larger than 200 pixels. Two cases are exemplified in the figure. A tri-vacancy in a, and a single vacancy in b. It is important to note that both were identified by the algorithm as vacant positions, and it is only the number of vacancies that is in question. The green dots in both cases represent the position of the identified vacancy, and the grey area around them, the low intensity region around it, as was found on the representative images. Already by observing the grey shapes it is evident that while the single vacancy displays a round low intensity contrast, the tri-vacancy appears to have a triangular shaped dark area around it. By looking at the ratio of circumference and the area of the dark region captured between the NNs of the vacancy (stated by 'r' in Figure 1) it is possible to

distinguish between the two cases, or generally, between the case of a single vacancy, and several vacancies (here too an experimental value of 3.14 was set for r, below this value the site was determined as a single vacancy).

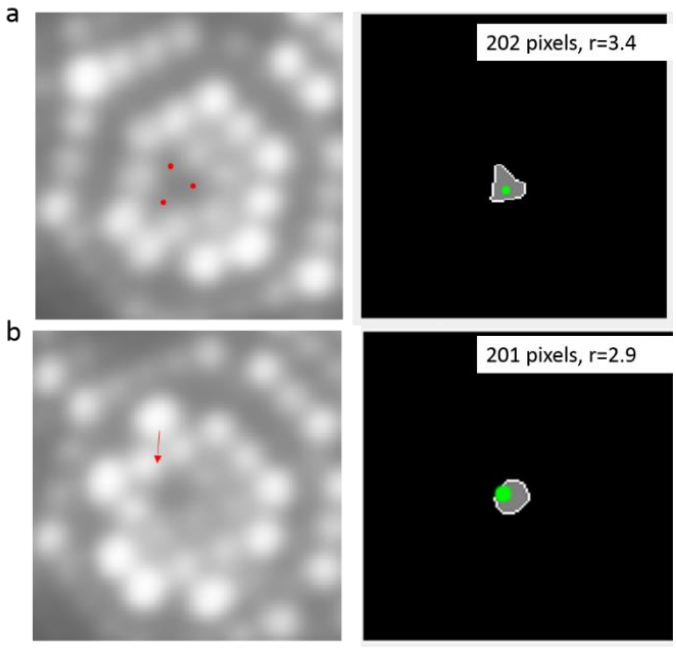

Figure 1 : Contrast patterns from a trivacancy in (a) and a single vacancy in (b).On the left are representative images for the two cases. On the right are the binraized images, with the green dot at the coordinates in which the vacancies were originally located, and the grey area around them defining the low intensity area of the vacancy on the image. A ratio, r, of circumference/area of the grey region higher than 3.14 was found experimentally to characterise a site with more than one vacancy.

Since the dataset analysed in chapter 8 exhibited repeating patterns of tri-vacancies, this step was developed and applied specifically to this vacancy configuration and utilized to replace a single site of vacancies, with three vacancies, on the furthest points on the circumference of the area found (these points are marked in red dots on the representative image in a). For other configurations, this step could at least flag the cases of identified vacancies where a larger number is expected, and require manual correction. Finally, not every case will have a proper representative image, as some NNs can evaporate prior to the imaging of others. Currently, this

post-processing step will not resolve such cases. It is possible to try and construct an 'integrated' representative image from images in which NNs were recorded, however this was not applied at this stage, and could be considered as future developments.

References

[1] J. Knaster, A. Moeslang, and T. Muroga, “Materials research for fusion,” *Nat. Phys.*, vol. 5, no. 2, pp. 424–434, May 2016.

[2] M. R. Gilbert and J. C. Sublet, “Neutron-induced transmutation effects in W and W-alloys in a fusion environment,” *Nucl. Fusion*, vol. 51, no. 4, p. 43005, Apr. 2011.

[3] S. J. Zinkle, “Fusion materials science: Overview of challenges and recent progress,” *Phys. Plasmas*, vol. 12, no. 5, p. 58101, 2005.

[4] M. Rieth, S. L. Dudarev, S. M. Gonzalez de Vicente, J. Aktaa, T. Ahlgren, S. Antusch, D. E. J. Armstrong, M. Balden, N. Baluc, M.-F. Barthe, W. W. Basuki, M. Battabyal, C. S. Becquart, D. Blagoeva, H. Boldyryeva, J. Brinkmann, M. Celino, L. Ciupinski, J. B. Correia, A. De Backer, C. Domain, E. Gaganidze, C. García-Rosales, J. Gibson, M. R. Gilbert, S. Giusepponi, B. Gludovatz, H. Greuner, K. Heinola, T. Höschen, A. Hoffmann, N. Holstein, F. Koch, W. Krauss, H. Li, S. Lindig, J. Linke, C. Linsmeier, P. López-Ruiz, H. Maier, J. Matejicek, T. P. Mishra, M. Muhammed, A. Muñoz, M. Muzyk, K. Nordlund, D. Nguyen-Manh, J. Opschoor, N. Ordás, T. Palacios, G. Pintsuk, R. Pippan, J. Reiser, J. Riesch, S. G. Roberts, L. Romaner, M. Rosiński, M. Sanchez, W. Schulmeyer, H. Traxler, A. Ureña, J. G. van der Laan, L. Veleva, S. Wahlberg, M. Walter, T. Weber, T. Weitkamp, S. Wurster, M. A. Yar, J. H. You, and A. Zivelonghi, “Recent progress in research on tungsten materials for nuclear fusion applications in Europe,” *J. Nucl. Mater.*, vol. 432, no. 1–3, pp. 482–500, Jan. 2013.

[5] D. E. J. Armstrong, P. D. Edmondson, and S. G. Roberts, “Effects of sequential tungsten and helium ion implantation on nano-indentation hardness of tungsten,” *Appl. Phys. Lett.*, vol. 102, no. 25, p. 251901, 2013.

[6] T. Tanno, A. Hasegawa, J.-C. He, M. Fujiwara, S. Nogami, M. Satou, T. Shishido, and K. Abe, “Effects of Transmutation Elements on Neutron Irradiation Hardening of Tungsten,” *Mater. Trans.*, vol. 48, no. 9, pp. 2399–2402, 2007.

[7] Z. Y. Li, N. P. Young, M. Di Vece, S. Palomba, R. E. Palmer, A. L. Bleloch, B. C. Curley, R. L. Johnston, J. Jiang, and J. Yuan, “Three-dimensional atomic-scale structure of size-selected gold nanoclusters,” *Nature*, vol. 451, no. 7174, pp. 46–48, Jan. 2008.

[8] R. Xu, C.-C. Chen, L. Wu, M. C. Scott, W. Theis, C. Ophus, M. Bartels, Y. Yang, H. Ramezani-Dakhel, M. R. Sawaya, H. Heinz, L. D. Marks, P. Ercius, and J. Miao, “Three-dimensional coordinates of individual atoms in materials revealed by electron tomography,” *Nat. Mater.*, vol. 14, no. 11, pp. 1099–1103, Sep. 2015.

[9] C. Speicher, W. Pimbley, M. Attardo, J. Galligan, and S. Brenner, “Observation of vacancies in the field-ion microscope,” *Phys. Lett.*, vol. 23, no. 3, pp. 194–196, Oct. 1966.

[10] D. A. Smith, M. A. Fortes, A. Kelly, and B. Ralph, “Contrast from stacking faults and partial

dislocations in the field-ion microscope," *Philos. Mag.*, vol. 17, no. 149, pp. 1065–1077, May 1968.

[11] M. A. Fortes, D. A. Smith, and B. Ralph, "The interpretation of field-ion micrographs: Contrast from perfect dislocation loops," *Philos. Mag.*, vol. 17, no. 145, pp. 169–176, Jan. 1968.

[12] B. Gault, M. P. Moody, J. M. Cairney, and S. P. Ringer, *Atom Probe Microscopy*, vol. 160. New York, NY, NY: Springer New York, 2012.

[13] F. Vurpillot, B. Gault, B. P. Geiser, and D. J. Larson, "Reconstructing atom probe data: A review," *Ultramicroscopy*, vol. 132, pp. 19–30, Sep. 2013.

[14] E. A. Marquis, J. M. Hyde, D. W. Saxey, S. Lozano-Perez, V. de Castro, D. Hudson, C. A. Williams, S. Humphry-Baker, and G. D. W. Smith, "Nuclear reactor materials at the atomic scale," *Mater. Today*, vol. 12, no. 11, pp. 30–37, Nov. 2009.

[15] M. Dagan, L. R. Hanna, A. Xu, S. G. Roberts, G. D. W. Smith, B. Gault, P. D. Edmondson, P. A. J. Bagot, and M. P. Moody, "Imaging of radiation damage using complementary field ion microscopy and atom probe tomography," *Ultramicroscopy*, vol. 159, pp. 387–394, Dec. 2015.

[16] U.S. Energy Information Administration, "International Energy Outlook 2016," 2016.

[17] International energy agency, "2015 Key World Energy Statistics," 2015.

[18] "Culham Centre for Fusion Energy." [Online]. Available: http://www.ccfe.ac.uk/How_fusion_works.aspx.

[19] "ITER." [Online]. Available: http://www.iter.org/.

[20] M. Shimada, D. J. Campbell, V. Mukhovatov, M. Fujiwara, N. Kirneva, K. Lackner, M. Nagami, V. D. Pustovitov, N. Uckan, J. Wesley, N. Asakura, A. E. Costley, A. J. H. Donné, E. . J. Doyle, A. Fasoli, C. Gormezano, Y. Gribov, O. Gruber, T. C. Hender, W. Houlberg, S. Ide, Y. Kamada, A. Leonard, B. Lipschultz, A. Loarte, K. Miyamoto, V. Mukhovatov, T. H. Osborne, A. Polevoi, and A. C. C. Sips, "Chapter 1: Overview and summary," *Nucl. Fusion*, vol. 47, no. 6, pp. S1–S17, Jun. 2007.

[21] T. R. Barrett, E. G, G. Pérez, M. Kovari, M. Fursdon, F. Domptail, S. Kirk, S. C. McIntosh, S. Roberts, S. Zheng, L. V. Boccaccini, J.-H. You, C. Bachmann, J. Reiser, M. Rieth, E. Visca, G. Mazzone, F. Arbeiter, and P. K. Domalapally, "Progress in the engineering design and assessment of the European DEMO first wall and divertor plasma facing components," *Fusion Eng. Des.*, vol. 109–111, pp. 917–924, Nov. 2016.

[22] F. Romanelli, "Fusion Electricity A roadmap to the realisation of fusion energy (EFDA)," 2012.

[23] S. C. Cowley, "The quest for fusion power," *Nat. Phys.*, vol. 12, no. 5, pp. 384–386, May 2016.

[24] J. Ongena, R. Koch, R. Wolf, and H. Zohm, “Magnetic-confinement fusion,” *Nat. Phys.*, vol. 12, no. May, pp. 398–410, May 2016.

[25] H. Bolt, V. Barabash, G. Federici, J. Linke, A. Loarte, J. Roth, and K. Sato, “Plasma facing and high heat flux materials – needs for ITER and beyond,” *J. Nucl. Mater.*, vol. 307–311, pp. 43–52, Dec. 2002.

[26] V. Barabash, A. Peacock, S. Fabritsiev, G. Kalinin, S. Zinkle, A. Rowcliffe, J.-W. Rensman, A. A. Tavassoli, P. Marmy, P. J. Karditsas, F. Gillemot, and M. Akiba, “Materials challenges for ITER – Current status and future activities,” *J. Nucl. Mater.*, vol. 367–370, no. 2007, pp. 21–32, Aug. 2007.

[27] S. Pestchanyi, V. Safronov, and I. Landman, “Estimation of carbon fibre composites as ITER divertor armour,” *J. Nucl. Mater.*, vol. 329–333, pp. 697–701, Aug. 2004.

[28] J. Roth, “Chemical erosion of carbon based materials in fusion devices,” *J. Nucl. Mater.*, vol. 266–269, pp. 51–57, Mar. 1999.

[29] H. Kawamura and M. Okamoto, “Proceedings of the third IEA international workshop on beryllium technology for fusion,” in *JAERI-Conf*, 1998, pp. 98–1.

[30] S. J. Zinkle, “Advanced materials for fusion technology,” *Fusion Eng. Des.*, vol. 74, no. 1–4, pp. 31–40, Nov. 2005.

[31] V. Barabash, M. Akiba, I. Mazul, M. Ulrickson, and G. Vieider, “Selection, development and characterisation of plasma facing materials for ITER,” *J. Nucl. Mater.*, vol. 233–237, no. I 996, pp. 718–723, Oct. 1996.

[32] N. Yoshida, “Review of recent works in development and evaluation of high-Z plasma facing materials,” *J. Nucl. Mater.*, vol. 266–269, pp. 197–206, Mar. 1999.

[33] V. Philipps, “Tungsten as material for plasma-facing components in fusion devices,” *J. Nucl. Mater.*, vol. 415, no. 1, pp. S2–S9, Aug. 2011.

[34] S. J. Zinkle and N. M. Ghoniem, “Operating temperature windows for fusion reactor structural materials,” *Fusion Eng. Des.*, vol. 51–52, no. 2000, pp. 55–71, Nov. 2000.

[35] F. Maury, M. Biget, P. Vajda, A. Lucasson, and P. Lucasson, “Frenkel pair creation and stage I recovery in W crystals irradiated near threshold,” *Radiat. Eff.*, vol. 38, no. 1–2, pp. 53–65, Jan. 1978.

[36] R. Dierckx, “The importance of the PKA-energy spectrum for radiation damage simulation,” *J. Nucl. Mater.*, vol. 144, no. 3, pp. 214–227, Feb. 1987.

[37] M. R. Gilbert, S. L. Dudarev, P. M. Derlet, and D. G. Pettifor, “Structure and metastability of mesoscopic vacancy and interstitial loop defects in iron and tungsten,” *J. Phys. Condens. Matter*, vol. 20, no. 34, p. 345214, Aug. 2008.

[38] A. Debelle, M. F. F. Barthe, T. Sauvage, R. Belamhawal, A. Chelgoum, P. Desgardin, and H. Labrim, “Helium behaviour and vacancy defect distribution in helium implanted tungsten,”

J. Nucl. Mater., vol. 362, no. 2–3, pp. 181–188, May 2007.

[39] Y. You, D. Li, X. Kong, X. Wu, C. S. Liu, Q. F. Fang, B. C. Pan, J. L. Chen, and G.-N. Luo, "Clustering of H and He, and their effects on vacancy evolution in tungsten in a fusion environment," *Nucl. Fusion*, vol. 54, no. 10, p. 103007, Oct. 2014.

[40] D. Nguyen-Manh, A. P. Horsfield, and S. L. Dudarev, "Self-interstitial atom defects in bcc transition metals: Group-specific trends," *Phys. Rev. B*, vol. 73, no. 2, p. 20101, Jan. 2006.

[41] T. Amino, K. Arakawa, and H. Mori, "Activation energy for long-range migration of self-interstitial atoms in tungsten obtained by direct measurement of radiation-induced point-defect clusters," *Philos. Mag. Lett.*, vol. 91, no. 2, pp. 86–96, Feb. 2011.

[42] R. M. Scanlan, D. L. Styris, D. N. Seidman, D. L. Styris, and D. N. S. An, "An in situ field ion microscope study of irradiated tungsten," *Philos. Mag.*, vol. 23, no. 186, pp. 1439–1457, Jun. 1971.

[43] G. H. Kinchin and R. S. Pease, "The Displacement of Atoms in Solids by Radiation," *Reports Prog. Phys.*, vol. 18, no. 1, p. 301, Jan. 1955.

[44] Gary S. Was, *Fundamentals of Radiation Materials Science: Metals and Alloys*. Springer Science & Business Media, 2007.

[45] M. J. Norgett, M. T. Robinson, and I. M. Torrens, "A proposed method of calculating displacement dose rates," *Nucl. Eng. Des.*, vol. 33, no. 1, pp. 50–54, Aug. 1975.

[46] L. E. Rehn, "Production of freely-migrating defects," *J. Nucl. Mater.*, vol. 174, pp. 144–150, 1990.

[47] R. S. Averback, R. Benedek, and K. L. Merkle, "Ion-irradiation studies of the damage function of copper and silver," *Phys. Rev. B*, vol. 18, no. 8, 1978.

[48] T. Hashimoto, L. E. Rehn, and M. Okamoto, "Freely-migrating-defect production during irradiation at elevated temperatures," *phys*, vol. 38, no. 18, pp. 868–878, 1988.

[49] L. E. Rehn, M. Okamoto, and A. R. S, "Relative efficiencies of different ions for producing freely migrating defects," vol. 30, no. 6, 1984.

[50] J. F. Ziegler, M. D. Ziegler, and J. P. Biersack, "SRIM – The stopping and range of ions in matter (2010)," *Nucl. Instruments Methods Phys. Res. Sect. B Beam Interact. with Mater. Atoms*, vol. 268, no. 11–12, pp. 1818–1823, Jun. 2010.

[51] R. E. Stoller, M. B. Toloczko, G. S. Was, A. G. Certain, S. Dwaraknath, and F. A. Garner, "On the use of SRIM for computing radiation damage exposure," *Nucl. Instruments Methods Phys. Res. Sect. B Beam Interact. with Mater. Atoms*, vol. 310, pp. 75–80, Sep. 2013.

[52] ASTM International, "ASTM E521-16, Standard Practice for Investigating the Effects of Neutron Radiation Damage Using Charged-Particle Irradiation," West Conshohocken, 2016.

[53] V. N. Bykov, G. A. Birzhevoi, M. I. Zakharova, and V. A. Solov'ev, "Nature and thermal

stability of radiation defects in single-crystal tungsten," *Sov. At. Energy*, vol. 33, no. 4, pp. 930–935, Oct. 1972.

[54] M. W. Thompson, "The damage and recovery of neutron irradiated tungsten," *Philos. Mag.*, vol. 5, no. 51, pp. 278–296, Mar. 1960.

[55] K. M. Bowkett and B. Ralph, "The Annealing of Radiation Damage in Tungsten Investigated by Field-Ion Microscopy," *Proc. R. Soc. A Math. Phys. Eng. Sci.*, vol. 312, no. 1508, pp. 51–63, Aug. 1969.

[56] D. N. Seidman, "The study of radiation damage in metals with the field-ion and atom-probe microscopes," *Surf. Sci.*, vol. 70, no. 1, pp. 532–565, Jan. 1978.

[57] F. Ferroni, X. Yi, K. Arakawa, S. P. Fitzgerald, P. D. Edmondson, and S. G. Roberts, "High temperature annealing of ion irradiated tungsten," *Acta Mater.*, vol. 90, pp. 380–393, May 2015.

[58] H. Iwakiri, K. Yasunaga, K. Morishita, and N. Yoshida, "Microstructure evolution in tungsten during low-energy helium ion irradiation," *J. Nucl. Mater.*, vol. 283–287, pp. 1134–1138, Dec. 2000.

[59] S. Kajita, W. Sakaguchi, N. Ohno, N. Yoshida, and T. Saeki, "Formation process of tungsten nanostructure by the exposure to helium plasma under fusion relevant plasma conditions," *Nucl. Fusion*, vol. 49, no. 9, p. 95005, Sep. 2009.

[60] A. Xu, C. Beck, D. E. J. Armstrong, K. Rajan, G. D. W. Smith, P. A. J. Bagot, and S. G. Roberts, "Ion-irradiation-induced clustering in W–Re and W–Re–Os alloys: A comparative study using atom probe tomography and nanoindentation measurements," *Acta Mater.*, vol. 87, pp. 121–127, Apr. 2015.

[61] J. I. W. Watterson, "A Review of accelerator based neutron source and their application," *Use Accel. based neutron source*, vol. 7, pp. 5–14, 2000.

[62] S. J. Zinkle and A. Möslang, "Evaluation of irradiation facility options for fusion materials research and development," *Fusion Eng. Des.*, vol. 88, no. 6–8, pp. 472–482, Oct. 2013.

[63] R. Gobin, D. Bogard, P. Cara, N. Chauvin, S. Chel, O. Delferrière, F. Harrault, P. Mattei, A. Mosnier, F. Senée, H. Shidara, and Y. Okumura, "International Fusion Materials Irradiation Facility injector acceptance tests at CEA/Saclay: 140 mA/100 keV deuteron beam characterizationa)," *Rev. Sci. Instrum.*, vol. 85, no. 2, p. 02A918, Feb. 2014.

[64] P. Vladimirov and A. Möslang, "Comparison of material irradiation conditions for fusion, spallation, stripping and fission neutron sources," *J. Nucl. Mater.*, vol. 329–333, no. 1–3 PART A, pp. 233–237, Aug. 2004.

[65] S. J. Zinkle and L. L. Snead, "Designing Radiation Resistance in Materials for Fusion Energy," *Annu. Rev. Mater. Res.*, vol. 44, no. 1, pp. 241–267, Jul. 2014.

[66] M. Shimada, Y. Hatano, Y. Oya, T. Oda, M. Hara, G. Cao, M. Kobayashi, M. Sokolov, H. Watanabe, B. Tyburska-Püschel, Y. Ueda, P. Calderoni, and K. Okuno, "Overview of the

US–Japan collaborative investigation on hydrogen isotope retention in neutron-irradiated and ion-damaged tungsten," *Fusion Eng. Des.*, vol. 87, no. 7–8, pp. 1166–1170, Aug. 2012.

[67] O. V Ogorodnikova and V. Gann, "Simulation of neutron-induced damage in tungsten by irradiation with energetic self-ions," *J. Nucl. Mater.*, vol. 460, pp. 60–71, May 2015.

[68] A. J. Melmed, "Recollections of Erwin Müller's laboratory: the development of FIM (1951–1956)," *Appl. Surf. Sci.*, vol. 94–95, pp. 17–25, Mar. 1996.

[69] S. S. Brenner, "Application of field-ion microscopy techniques to metallurgical problems," *Surf. Sci.*, vol. 70, no. 1, pp. 427–451, Jan. 1978.

[70] F. Danoix, T. Epicier, F. Vurpillot, and D. Blavette, "Atomic-scale imaging and analysis of single layer GP zones in a model steel," *J. Mater. Sci.*, vol. 47, no. 3, pp. 1567–1571, Feb. 2012.

[71] P. Jessner, R. Danoix, B. Hannoyer, and F. Danoix, "Investigations of the nitrided subsurface layers of an Fe–Cr-model alloy," *Ultramicroscopy*, vol. 109, no. 5, pp. 530–534, Apr. 2009.

[72] S. Cazottes, F. Vurpillot, A. Fnidiki, D. Lemarchand, M. Baricco, and F. Danoix, "Nanometer Scale Tomographic Investigation of Fine Scale Precipitates in a CuFeNi Granular System by Three-Dimensional Field Ion Microscopy," *Microsc. Microanal.*, vol. 18, no. 5, pp. 1129–1134, Oct. 2012.

[73] D. J. Larson and M. K. Miller, "Atom Probe Field-Ion Microscopy Characterization of Nickel and Titanium Aluminides," *Mater. Charact.*, vol. 44, no. 1–2, pp. 159–176, Jan. 2000.

[74] D. G. Brandon, B. Ralph, S. Ranganathan, and M. S. Wald, "A field ion microscope study of atomic configuration at grain boundaries," *Acta Metall.*, vol. 12, no. 7, pp. 813–821, Jul. 1964.

[75] G. L. Kellogg, "Field ion microscope studies of single-atom surface diffusion and cluster nucleation on metal surfaces," *Surf. Sci. Rep.*, vol. 21, no. 1–2, pp. 1–88, Dec. 1994.

[76] C. Barroo, S. V. Lambeets, F. Devred, T. D. Chau, N. Kruse, Y. De Decker, and T. Visart de Bocarmé, "Hydrogenation of NO and NO2 over palladium and platinum nanocrystallites: case studies using field emission techniques," *New J. Chem.*, vol. 38, no. 5, p. 2090, 2014.

[77] S. Koelling, O. Richard, H. Bender, M. Uematsu, A. Schulze, G. Zschaetzsch, M. Gilbert, and W. Vandervorst, "Direct Imaging of 3D Atomic-Scale Dopant-Defect Clustering Processes in Ion-Implanted Silicon," *Nano Lett.*, vol. 13, no. 6, pp. 2458–2462, Jun. 2013.

[78] D. N. Seidman, M. I. Current, D. Pramanik, and C.-Y. Wei, "Direct observations of the primary state of radiation damage of ion-irradiated tungsten and platinum," *Nucl. Instruments Methods*, vol. 182–183, pp. 477–481, Apr. 1981.

[79] C.-Y. Wei, M. I. Current, and D. N. Seidman, "Direct observation of the primary state of damage of ion-irradiated tungsten I. Three-dimensional spatial distribution of vacancies," *Philos. Mag. A*, vol. 44, no. 2, pp. 459–491, Aug. 1981.

[80] C.-Y. Wei and D. N. Seidman, “Direct observation of the vacancy structure of depleted zones in tungsten ion irradiated at 10 K,” *Appl. Phys. Lett.*, vol. 34, no. 10, p. 622, 1979.

[81] C. Wei and D. N. Seidman, “The stage ii recovery behavior of a series of ion-irradiated platinum (gold) alloys as studied by field-ion microscopy,” *Radiat. Eff.*, vol. 32, no. 3–4, pp. 229–249, Jan. 1977.

[82] T. F. Kelly and M. K. Miller, “Invited Review Article: Atom probe tomography,” *Rev. Sci. Instrum.*, vol. 78, no. 3, p. 31101, Mar. 2007.

[83] G. L. Kellogg and T. T. Tsong, “Pulsed-laser atom-probe field-ion microscopy,” *J. Appl. Phys.*, vol. 51, no. 2, p. 1184, 1980.

[84] A. Cerezo, T. J. Godfrey, and G. D. W. Smith, “Application of a position-sensitive detector to atom probe microanalysis,” *Rev. Sci. Instrum.*, vol. 59, no. 6, p. 862, 1988.

[85] T. F. Kelly, D. J. Larson, K. Thompson, R. L. Alvis, J. H. Bunton, J. D. Olson, and B. P. Gorman, “Atom Probe Tomography of Electronic Materials,” *Annu. Rev. Mater. Res.*, vol. 37, no. 1, pp. 681–727, Aug. 2007.

[86] D. J. Larson, B. D. Wissman, R. L. Martens, R. J. Viellieux, T. F. Kelly, T. T. Gribb, H. F. Erskine, and N. Tabat, “Advances in Atom Probe Specimen Fabrication from Planar Multilayer Thin Film Structures,” *Microsc.Microanal.*, pp. 24–31, 2001.

[87] A. Shariq, T. Al-kassab, R. Kirchheim, and R. B. Schwarz, “Exploring the next neighbourhood relationship in amorphous alloys utilizing atom probe tomography,” *Ultramicroscopy*, vol. 107, no. 9, pp. 773–780, Sep. 2007.

[88] J. W. Valley, A. J. Cavosie, T. Ushikubo, D. A. Reinhard, D. F. Lawrence, D. J. Larson, P. H. Clifton, T. F. Kelly, S. A. Wilde, D. E. Moser, and M. J. Spicuzza, “Hadean age for a post-magma-ocean zircon confirmed by atom-probe tomography,” *Nat. Geosci.*, vol. 7, no. 3, pp. 219–223, Feb. 2014.

[89] M. K. Miller and K. F. Russell, “Embrittlement of RPV steels: An atom probe tomography perspective,” *J. Nucl. Mater.*, vol. 371, no. 1–3, pp. 145–160, Sep. 2007.

[90] P. Auger, P. Pareige, S. Welzel, and J.-C. Van Duysen, “Synthesis of atom probe experiments on irradiation-induced solute segregation in French ferritic pressure vessel steels,” *J. Nucl. Mater.*, vol. 280, no. 3, pp. 331–344, Aug. 2000.

[91] J. Zelenty, G. D. W. Smith, K. Wilford, J. M. Hyde, and M. P. Moody, “Secondary precipitation within the cementite phase of reactor pressure vessel steels,” *Scr. Mater.*, vol. 115, pp. 118–122, Apr. 2016.

[92] P. D. Styman, J. M. Hyde, K. Wilford, A. Morley, and G. D. W. Smith, “Precipitation in long term thermally aged high copper, high nickel model RPV steel welds,” *Prog. Nucl. Energy*, vol. 57, pp. 86–92, May 2012.

[93] M. K. Miller, E. A. Kenik, K. F. Russell, L. Heatherly, D. T. Hoelzer, and P. J. Maziasz, “Atom probe tomography of nanoscale particles in ODS ferritic alloys,” *Mater. Sci. Eng. A*, vol.

353, no. 1–2, pp. 140–145, Jul. 2003.

[94] M. K. Miller, D. T. Hoelzer, E. A. Kenik, and K. F. Russell, “Nanometer scale precipitation in ferritic MA/ODS alloy MA957,” *J. Nucl. Mater.*, vol. 329–333, no. 2004, pp. 338–341, Aug. 2004.

[95] C. A. Williams, E. A. Marquis, A. Cerezo, and G. D. W. Smith, “Nanoscale characterisation of ODS–Eurofer 97 steel: An atom-probe tomography study,” *J. Nucl. Mater.*, vol. 400, no. 1, pp. 37–45, May 2010.

[96] S. Lozano-Perez, D. W. Saxey, T. Yamada, and T. Terachi, “Atom-probe tomography characterization of the oxidation of stainless steel,” *Scr. Mater.*, vol. 62, no. 11, pp. 855–858, Jun. 2010.

[97] D. Hudson, A. Cerezo, and G. D. W. Smith, “Zirconium oxidation on the atomic scale,” *Ultramicroscopy*, vol. 109, no. 5, pp. 667–671, Apr. 2009.

[98] T. Sakurai and E. W. Müller, “Field calibration using the energy distribution of a free-space field ionization,” *J. Appl. Phys.*, vol. 48, no. 6, p. 2618, 1977.

[99] T. Sakurai and E. W. Müller, “Field Calibration Using the Energy Distribution of Field Ionization,” *Phys. Rev. Lett.*, vol. 30, no. 12, pp. 532–535, Mar. 1973.

[100] D. G. Brandon, “Image formation in the field ion microscope,” *Philos. Mag.*, vol. 7, no. 78, pp. 1003–1011, Jun. 1962.

[101] T. T. Tsong, “Field ion image formation,” *Surf. Sci.*, vol. 70, no. 1, pp. 211–233, Jan. 1978.

[102] E. W. Muller, “Field Ion Microscopy,” *Science (80-.).*, vol. 149, no. 3684, pp. 591–601, Aug. 1965.

[103] R. Gomer, “Field emission, field ionization, and field desorption,” *Surf. Sci.*, vol. 299–300, pp. 129–152, Jan. 1994.

[104] T.T.Tsong, “field ion emission,” in *atom-probe field ion microscopy*, New York: Cambridge University Press, 2005, p. 98.

[105] E. W. Müller and K. Bahadur, “Field Ionization of Gases at a Metal Surface and the Resolution of the Field Ion Microscope,” *Phys. Rev.*, vol. 102, no. 3, pp. 624–631, May 1956.

[106] D. G. Brandon, “The resolution of atomic structure: recent advances in the theory and development of the field ion microscope,” *Br. J. Appl. Phys.*, vol. 14, no. 8, pp. 474–484, Aug. 1963.

[107] D. G. Brandon, “The accurate determination of crystal orientation from field ion micrographs,” *J. Sci. Instrum.*, vol. 41, no. 6, pp. 373–375, Jun. 1964.

[108] J. M. Walls and H. N. Southworth, “Magnification in the field-ion microscope,” *J. Phys. D. Appl. Phys.*, vol. 12, no. 5, pp. 657–667, May 1979.

[109] R. W. Newman, R. C. Sanwald, and J. J. Hren, “A method for indexing field ion micrographs,” *J. Sci. Instrum.*, vol. 44, pp. 828–830, 1967.

[110] A. Cerezo, P. J. Warren, and G. D. W. Smith, “Some aspects of image projection in the field-ion microscope,” *Ultramicroscopy*, vol. 79, no. 1–4, pp. 251–257, Sep. 1999.

[111] R. G. Forbes, “Field evaporation theory: a review of basic ideas,” *Appl. Surf. Sci.*, vol. 87–88, no. 94, pp. 1–11, Mar. 1995.

[112] R. Gomer, “Field Desorption,” *J. Chem. Phys.*, vol. 31, no. 2, p. 341, 1959.

[113] R. K. Biswas and R. G. Forbes, “Theoretical arguments against the Muller-Schottky mechanism of field evaporation,” *J. Phys. D. Appl. Phys.*, vol. 15, no. 7, pp. 1323–1338, Jul. 1982.

[114] M. K. Miller and R. G. Forbes, *Atom-Probe Tomography*. Boston, MA: Springer US, 2014.

[115] C. G. Sanchez, A. Y. Lozovoi, and A. Alavi, “Field-evaporation from first-principles,” *Mol. Phys.*, vol. 102, no. 9–10, pp. 1045–1055, May 2004.

[116] R. G. Forbes, “Field electron and ion emission from charged surfaces: a strategic historical review of theoretical concepts,” *Ultramicroscopy*, vol. 95, pp. 1–18, May 2003.

[117] D. N. Seidman and K. H. Lie, “On contrast patterns produced by self-interstitial atoms in field ion microscope images of a b.c.c. metal,” *Acta Metall.*, vol. 20, no. 8, pp. 1045–1059, Aug. 1972.

[118] P. Pétroff and D. N. Seidman, “An in situ field ion microscope study of irradiated platinum—I. Stage I recovery behavior,” *Acta Metall.*, vol. 21, no. 4, pp. 323–334, Apr. 1973.

[119] C. Wei and D. N. Seidman, “Direct observation of the vacancy structure of a (220) platelet in an ion-irradiated platinum-4·0 at. % gold alloy,” *Philos. Mag. A*, vol. 37, no. 2, pp. 257–272, Feb. 1978.

[120] K. Johnson, “OR TEP: a fortran thrmal-ellipsoid plot program for crystal structure illustrations.” .

[121] F. Vurpillot, M. Gilbert, and B. Deconihout, “Towards the three-dimensional field ion microscope,” *Surf. Interface Anal.*, vol. 39, no. 2–3, pp. 273–277, Feb. 2007.

[122] A. Cerezo, M. G. Hetherington, J. M. Hyde, M. K. Miller, G. D. W. Smith, and J. S. Underkoffler, “Visualisation of three-dimensional microstructures,” *Surf. Sci.*, vol. 266, no. 1–3, pp. 471–480, Apr. 1992.

[123] J. Akré, F. Danoix, H. Leitner, and P. Auger, “The morphology of secondary-hardening carbides in a martensitic steel at the peak hardness by 3DFIM,” *Ultramicroscopy*, vol. 109, no. 5, pp. 518–523, Apr. 2009.

[124] M. K. Miller and G. D. W. Smith, *Atom Probe Microanalysis: Principles and Applications to Materials Problems*. Materials Research Soceity, 1989.

[125] P. Bas, A. Bostel, B. Deconihout, and D. Blavette, “A general protocol for the reconstruction of 3D atom probe data,” *Appl. Surf. Sci.*, vol. 87–88, pp. 298–304, Mar. 1995.

[126] B. Gault, D. Haley, F. de Geuser, M. P. Moody, E. A. Marquis, D. J. Larson, and B. P. Geiser, “Advances in the reconstruction of atom probe tomography data,” *Ultramicroscopy*, vol. 111, no. 6, pp. 448–457, May 2011.

[127] B. P. Geiser, T. F. Kelly, D. J. Larson, J. Schneir, and J. P. Roberts, “Spatial Distribution Maps for Atom Probe Tomography,” *Microsc. Microanal.*, vol. 13, no. 6, pp. 437–447, Dec. 2007.

[128] F. Vurpillot, G. Da Costa, A. Menand, and D. Blavette, “Structural analyses in three-dimensional atom probe: a Fourier transform approach,” *J. Microsc.*, vol. 203, no. 3, pp. 295–302, Sep. 2001.

[129] “CAMECA.” [Online]. Available: http://www.cameca.com/.

[130] F. Vurpillot, A. Bostel, and D. Blavette, “Trajectory overlaps and local magnification in three-dimensional atom probe,” *Appl. Phys. Lett.*, vol. 76, no. 21, p. 3127, 2000.

[131] L. Yao, B. Gault, J. M. Cairney, and S. P. Ringer, “On the multiplicity of field evaporation events in atom probe: A new dimension to the analysis of mass spectra,” *Philos. Mag. Lett.*, vol. 90, no. 2, pp. 121–129, Feb. 2010.

[132] A. F. Bobkov, V. T. Zabolotnyi, L. I. Ivanov, G. M. Kukavadze, N. A. Makhlin, and A. L. Suvorov, “Field ion microscopy of radiation defects in tungsten irradiated with 50-keV W+ ions,” *Sov. At. Energy*, vol. 48, no. 5, pp. 331–333, May 1980.

[133] W. Jäger and M. Wilkens, “Formation of vacancy-type dislocation loops in tungsten bombarded by 60 keV Au ions,” *Phys. Status Solidi*, vol. 32, no. 1, pp. 89–100, Nov. 1975.

[134] A. Hasegawa, M. Fukuda, T. Tanno, and S. Nogami, “Neutron Irradiation Behavior of Tungsten,” *Mater. Trans.*, vol. 54, no. 4, pp. 466–471, 2013.

[135] A. Hasegawa, M. Fukuda, S. Nogami, and K. Yabuuchi, “Neutron irradiation effects on tungsten materials,” *Fusion Eng. Des.*, vol. 89, no. 7–8, pp. 1568–1572, Oct. 2014.

[136] X. Yi, M. L. Jenkins, M. A. Kirk, Z. Zhou, and S. G. Roberts, “In-situ TEM studies of 150 keV W+ ion irradiated W and W-alloys: Damage production and microstructural evolution,” *Acta Mater.*, vol. 112, pp. 105–120, Jun. 2016.

[137] X. Yi, M. L. Jenkins, K. Hattar, P. D. Edmondson, and S. G. Roberts, “Characterisation of radiation damage in W and W-based alloys from 2MeV self-ion near-bulk implantations,” *Acta Mater.*, vol. 92, pp. 163–177, Jun. 2015.

[138] X. Yi, M. L. Jenkins, K. Hattar, P. D. Edmondson, and S. G. Roberts, “ScienceDirect Characterisation of radiation damage in W and W-based alloys from 2 MeV,” *Acta Mater.*, vol. 92, pp. 163–177, 2015.

[139] D. E. J. Armstrong, X. Yi, E. A. Marquis, and S. G. Roberts, “Hardening of self ion implanted

tungsten and tungsten 5-wt% rhenium," *J. Nucl. Mater.*, vol. 432, no. 1–3, pp. 428–436, Jan. 2013.

[140] E. W. Müller, J. A. Panitz, and S. B. McLane, "The atom-probe field ion microscope," *Rev. Sci. Instrum.*, vol. 39, no. 1, pp. 83–86, 1968.

[141] R. Herschitz and D. N. Seidman, "An atomic resolution study of homogeneous radiation-induced precipitation in a neutron irradiated W-25at.% Re alloy," *Acta Metall.*, vol. 32, no. 8, pp. 1141–1154, 1984.

[142] R. Herschitz and D. N. Seidman, "An atomic resolution study of homogeneous radiation-induced precipitation in a neutron irradiated W-10at.% Re alloy," *Acta Metall.*, vol. 32, no. 8, pp. 1141–1154, Aug. 1984.

[143] P. D. Edmondson, A. London, A. Xu, D. E. J. Armstrong, and S. G. Roberts, "Small-scale characterisation of irradiated nuclear materials: Part I – Microstructure," *J. Nucl. Mater.*, vol. 462, pp. 369–373, Jul. 2015.

[144] J. M. Hyde, E. A. Marquis, K. B. Wilford, and T. J. Williams, "A sensitivity analysis of the maximum separation method for the characterisation of solute clusters," *Ultramicroscopy*, vol. 111, no. 6, pp. 440–447, May 2011.

[145] D. Vaumousse, A. Cerezo, and P. J. Warren, "A procedure for quantification of precipitate microstructures from three-dimensional atom probe data," *Ultramicroscopy*, vol. 95, pp. 215–221, May 2003.

[146] A. Wagner and D. N. Seidman, "Range Profiles of 300 and 475 eV He+ Ions and the Diffusivity of He in Tungsten," *Phys. Rev. Lett.*, vol. 42, no. 8, pp. 515–518, Feb. 1979.

[147] N. Yoshida, H. Iwakiri, K. Tokunaga, and T. Baba, "Impact of low energy helium irradiation on plasma facing metals," *J. Nucl. Mater.*, vol. 337–339, pp. 946–950, Mar. 2005.

[148] W. R. Wampler and R. P. Doerner, "Deuterium retention in tungsten from exposure to plasma," *Phys. Scr.*, vol. T138, p. 14037, Dec. 2009.

[149] N. Hashimoto, J. D. Hunn, N. Parikh, S. Gilliam, S. Gidcumb, B. Patnaik, and L. L. Snead, "Microstructural analysis on helium retention of ion-irradiated and annealed tungsten foils," *J. Nucl. Mater.*, vol. 347, no. 3, pp. 307–313, Dec. 2005.

[150] M. J. Baldwin and R. P. Doerner, "Formation of helium induced nanostructure 'fuzz' on various tungsten grades," *J. Nucl. Mater.*, vol. 404, no. 3, pp. 165–173, Sep. 2010.

[151] Q. Yang, Y. You, L. Liu, H. Fan, W. Ni, D. Liu, C. S. Liu, G. Benstetter, and Y. Wang, "Nanostructured fuzz growth on tungsten under low-energy and high-flux He irradiation," *Sci. Rep.*, vol. 5, Jun. 2015.

[152] P. E. Lhuillier, A. Debelle, T. Belhabib, A. L. Thomann, P. Desgardin, T. Sauvage, M. F. Barthe, P. Brault, and Y. Tessier, "Helium desorption in 3He implanted tungsten at low energy," *J. Nucl. Mater.*, vol. 417, no. 1–3, pp. 504–507, Oct. 2011.

[153] P. E. Lhuillier, T. Belhabib, P. Desgardin, B. Courtois, T. Sauvage, M. F. Barthe, A. L. Thomann, P. Brault, and Y. Tessier, "Trapping and release of helium in tungsten," *J. Nucl. Mater.*, vol. 416, no. 1–2, pp. 13–17, Sep. 2011.

[154] K. Thompson, D. Lawrence, D. J. Larson, J. D. Olson, T. F. Kelly, and B. Gorman, "In situ site-specific specimen preparation for atom probe tomography," *Ultramicroscopy*, vol. 107, no. 2–3, pp. 131–139, Feb. 2007.

[155] J. F. Ziegler and J. P. Biersack, "SRIM-2013 (Stopping and Range of Ions in Matter)." 2013.

[156] A. Cerezo, T. J. Godfrey, S. J. Sijbrandij, G. D. W. Smith, and P. J. Warren, "Performance of an energy-compensated three-dimensional atom probe," *Rev. Sci. Instrum.*, vol. 69, no. 1, p. 49, 1998.

[157] M. P. Moody, B. Gault, L. T. Stephenson, D. Haley, and S. P. Ringer, "Qualification of the tomographic reconstruction in atom probe by advanced spatial distribution map techniques," *Ultramicroscopy*, vol. 109, no. 7, pp. 815–824, Jun. 2009.

[158] A. Cerezo, M. Abraham, H. Lane, D. J. Larson, M. Thuvander, S. K, P. J. Warren, and G. D. W. Smith, "Three-dimensional atomic scale analysis of interfaces," *Instrum Phys Conf Ser*, vol. 161, 1999.

[159] F. Vurpillot, F. De Geuser, G. Da Costa, and D. Blavette, "Application of Fourier transform and autocorrelation to cluster identification in the three-dimensional atom probe," *J. Microsc.*, vol. 216, no. 3, pp. 234–240, Dec. 2004.

[160] E. W. Müller and R. D. Young, "Determination of Field Strength for Field Evaporation and Ionization in the Field Ion Microscope," *J. Appl. Phys.*, vol. 32, no. 11, p. 2425, 1961.

[161] M. K. Miller, A. Cerezo, M. G. Hetherington, and G. D. W. Smith, *Atom probe field ion microscopy*. 1996.

[162] C. M. C. De Castilho and D. R. Kingham, "Resolution of the field ion microscope," *J. Phys. D. Appl. Phys.*, vol. 20, no. 1, pp. 116–124, Jan. 1987.

[163] Y. C. Chen and D. N. Seidman, "On the atomic resolution of a field ion microscope," *Surf. Sci.*, vol. 26, no. 1, pp. 61–84, Jun. 1971.

[164] M. Drechsler and P. Wolf, "Zur Analyse von Feldionenmikrosop-Aufnahmen mit atomarer Auflösung," in *4th Int Conf. on Electron Microscopy*, 1958, p. 823.

[165] D. Blavette, "Three-Dimensional Atomic-Scale Imaging of Impurity Segregation to Line Defects," *Science (80-.).*, vol. 286, no. 5448, pp. 2317–2319, Dec. 1999.

[166] K. Thompson, P. L. Flaitz, P. Ronsheim, D. J. Larson, and T. F. Kelly, "Imaging of Arsenic Cottrell Atmospheres Around Silicon Defects by Three-Dimensional Atom Probe Tomography," *Science (80-.).*, vol. 317, no. 5843, pp. 1370–1374, Sep. 2007.

[167] M. K. Miller, "Atom probe tomography characterization of solute segregation to dislocations," *Microsc. Res. Tech.*, vol. 69, no. 5, pp. 359–365, May 2006.

[168] M. Bachhav, L. Yao, G. Robert Odette, and E. A. Marquis, “Microstructural changes in a neutron-irradiated Fe–6at.%Cr alloy,” *J. Nucl. Mater.*, vol. 453, no. 1–3, pp. 334–339, Oct. 2014.

[169] E. A. Marquis, M. Bachhav, Y. Chen, Y. Dong, L. M. Gordon, and A. McFarland, “On the current role of atom probe tomography in materials characterization and materials science,” *Curr. Opin. Solid State Mater. Sci.*, vol. 17, no. 5, pp. 217–223, Oct. 2013.

[170] L. Chang, S. Barnard, and G. Smith, “The segregation of carbon atoms to dislocations in low-carbon martensites: studies by field ion microscopy and atom probe microanalysis,” *Gilbert R. Speich Symp. Proc. Fundam. aging tempering bainitic martensitic steel Prod.*, 1992.

[171] C. Oberdorfer, S. M. Eich, and G. Schmitz, “A full-scale simulation approach for atom probe tomography,” *Ultramicroscopy*, vol. 128, pp. 55–67, May 2013.

[172] K. Hoummada, D. Mangelinck, B. Gault, and M. Cabié, “Nickel segregation on dislocation loops in implanted silicon,” *Scr. Mater.*, vol. 64, no. 5, pp. 378–381, Mar. 2011.

[173] M. J. Attardo and J. M. Galligan, “Radiation Damage in Platinum,” *Phys. Rev. Lett.*, vol. 14, no. 16, pp. 641–642, Apr. 1965.

[174] A. J. W. Moore and J. A. Spink, “Field evaporation from tungsten and the bonding of surface atoms,” *Surf. Sci.*, vol. 12, no. 3, pp. 479–496, Nov. 1968.

[175] X. Ge, N. Chen, W. Zhang, and F. Zhu, “Selective field evaporation in field-ion microscopy for ordered alloys,” *J. Appl. Phys.*, vol. 85, no. 7, p. 3488, 1999.

[176] G. D. W. Smith, D. Hudson, P. D. Styman, and C. A. Williams, “Studies of dislocations by field ion microscopy and atom probe tomography,” *Philos. Mag.*, vol. 93, no. 28–30, pp. 3726–3740, Sep. 2013.

[177] M. K. Miller, T. F. Kelly, K. Rajan, and S. P. Ringer, “The future of atom probe tomography,” *Mater. Today*, vol. 15, no. 4, pp. 158–165, Apr. 2012.

[178] B. Raj, M. Vijayalakshmi, P. R. V. Rao, and K. B. S. Rao, “Challenges in Materials Research for Sustainable Nuclear Energy,” *MRS Bull.*, vol. 33, no. 4, pp. 327–337, Apr. 2008.

[179] F. Ferroni, E. Tarleton, and S. Fitzgerald, “Dislocation dynamics modelling of radiation damage in thin films,” *Model. Simul. Mater. Sci. Eng.*, vol. 22, no. 4, p. 45009, Jun. 2014.

[180] B. Loberg, “Inelastic changes in specimens during operation of the field-ion microscope,” *Philos. Mag.*, vol. 24, no. 189, pp. 593–602, Sep. 1971.

[181] D. a. Smith, P. J. Birdseye, and M. J. Gorinoe, “Forces on dislocations in field-ion specimens; further analysis of some previous observations,” *Philos. Mag.*, vol. 27, no. 5, pp. 1175–1181, May 1973.

[182] S. Lee, J. Choi, and J. Gunn, “Energetics of He and H atoms with vacancies in tungsten : First-principles approach,” *J. Nucl. Mater.*, vol. 383, no. 3, pp. 244–246, 2009.

[183] M. K. Miller and M. G. Burke, “An atom probe field ion microscopy study of neutron-irradiated pressure vessel steels,” *J. Nucl. Mater.*, vol. 195, no. 1–2, pp. 68–82, Oct. 1992.

[184] D. Blavette, E. Cadel, and B. Deconihout, “The Role of the Atom Probe in the Study of Nickel-Based Superalloys,” *Mater. Charact.*, vol. 44, no. 1–2, pp. 133–157, Jan. 2000.

[185] M. K. Miller, “Contributions of atom probe tomography to the understanding of nickel-based superalloys,” *Micron*, vol. 32, no. 8, pp. 757–764, Jan. 2001.

[186] P. A. J. Bagot, A. Cerezo, and G. D. W. Smith, “3D atom probe study of gas adsorption and reaction on alloy catalyst surfaces II: Results on Pt and Pt–Rh,” *Surf. Sci.*, vol. 601, no. 10, pp. 2245–2255, May 2007.

[187] P. A. J. Bagot, T. Visart de Bocarmé, A. Cerezo, and G. D. W. Smith, “3D atom probe study of gas adsorption and reaction on alloy catalyst surfaces I: Instrumentation,” *Surf. Sci.*, vol. 600, no. 15, pp. 3028–3035, Aug. 2006.

[188] K. Stiller and H.-O. Andrén, “Faulty field evaporation at di-vacancies in {222} tungsten,” *Surf. Sci.*, vol. 114, no. 2–3, pp. L57–L61, Feb. 1982.

[189] G. L. Kellogg, “Surface diffusion and adatom-induced substrate relaxations of Pt, Pd, and Ni atoms on Pt(001),” *J. Vac. Sci. Technol. A Vacuum, Surfaces, Film.*, vol. 9, no. 3, p. 1757, May 1991.

[190] G. L. Kellogg, “Temperature dependence of surface self-diffusion on Pt(001),” *Surf. Sci.*, vol. 246, no. 1–3, pp. 31–36, Apr. 1991.

[191] S. C. Wang and G. Ehrlich, “Imaging and diffusion of individual iridium adatoms on Ir(111),” *Surf. Sci.*, vol. 224, no. 1–3, pp. L997–L1003, Dec. 1989.

[192] F. Vurpillot, J. Houard, A. Vella, and B. Deconihout, “Thermal response of a field emitter subjected to ultra-fast laser illumination,” *J. Phys. D. Appl. Phys.*, vol. 42, no. 12, p. 125502, Jun. 2009.

[193] B. Gault, M. P. Moody, F. De Geuser, A. La Fontaine, L. T. Stephenson, D. Haley, and S. P. Ringer, “Spatial Resolution in Atom Probe Tomography,” *Microsc. Microanal.*, vol. 16, no. 1, pp. 99–110, Feb. 2010.

[194] I. M. Mikhailovskij, G. D. W. Smith, N. Wanderka, and T. I. Mazilova, “Non-kinkwise field evaporation and kink relaxation on stepped W(112) surface,” *Ultramicroscopy*, vol. 95, pp. 157–163, May 2003.

[195] W. A. Schmidt and N. Ernst, “On the binding strength of surface metal atoms in a high electric field—face-specific appearance energy measurements of field evaporated rhodium ions,” *Vacuum*, vol. 45, no. 2–3, pp. 255–258, Feb. 1994.

[196] A. R. Waugh, E. D. Boyes, and M. J. Southon, “Investigations of field evaporation with a field-desorption microscope,” *Surf. Sci.*, vol. 61, no. 1, pp. 109–142, Dec. 1976.

[197] E. W. Plummer, “Atomic Binding of Transition Metals on Clean Single-Crystal Tungsten

Surfaces," *J. Chem. Phys.*, vol. 49, no. 8, p. 3479, 1968.

[198] E. W. Müller, S. B. McLane, and J. A. Panitz, "Field adsorption and desorption of helium and neon," *Surf. Sci.*, vol. 17, no. 2, pp. 430–438, Oct. 1969.

[199] S. Parviainen, F. Djurabekova, S. P. Fitzgerald, A. Ruzibaev, and K. Nordlund, "Atomistic simulations of field assisted evaporation in atom probe tomography," *J. Phys. D. Appl. Phys.*, vol. 49, no. 4, p. 45302, Feb. 2016.

[200] N. Rolland, F. Vurpillot, S. Duguay, and D. Blavette, "A Meshless Algorithm to Model Field Evaporation in Atom Probe Tomography," *Microsc. Microanal.*, vol. 21, no. 6, pp. 1649–1656, Dec. 2015.

[201] F. Vurpillot, A. Bostel, E. Cadel, and D. Blavette, "The spatial resolution of 3D atom probe in the investigation of single-phase materials," *Ultramicroscopy*, vol. 84, no. 3–4, pp. 213–224, Aug. 2000.

[202] D. Niewieczerzał, C. Oleksy, and A. Szczepkowicz, "Image deformation in field ion microscopy of faceted crystals," *Ultramicroscopy*, vol. 110, no. 3, pp. 234–241, Feb. 2010.

[203] F. Vurpillot, A. Bostel, A. Menand, and D. Blavette, "Trajectories of field emitted ion in 3D atom-probe," *Eur.Phys.J*, vol. 6, 1999.

[204] A. J. W. Moore, "The simulation of FIM desorption patterns," *Philos. Mag. A*, vol. 43, no. 3, pp. 803–814, Mar. 1981.

[205] H. K. D. H. Bhadeshia, "Prevention of Hydrogen Embrittlement in Steels," *ISIJ Int.*, vol. 56, no. 1, pp. 24–36, 2016.

[206] H. S. Kitaguchi, S. Lozano-Perez, and M. P. Moody, "Quantitative analysis of carbon in cementite using pulsed laser atom probe," *Ultramicroscopy*, vol. 147, pp. 51–60, Dec. 2014.

[207] R. K. W. Marceau, P. Choi, and D. Raabe, "Understanding the detection of carbon in austenitic high-Mn steel using atom probe tomography," *Ultramicroscopy*, vol. 132, pp. 239–247, Sep. 2013.

[208] B. Gault, F. Danoix, K. Hoummada, D. Mangelinck, and H. Leitner, "Impact of directional walk on atom probe microanalysis," *Ultramicroscopy*, vol. 113, pp. 182–191, Feb. 2012.

[209] "3Depict." [Online]. Available: http://threedepict.sourceforge.net/.

[210] G. Valles, M. Panizo-Laiz, C. González, I. Martin-Bragado, R. González-Arrabal, N. Gordillo, R. Iglesias, C. L. Guerrero, J. M. Perlado, and A. Rivera, "Influence of grain boundaries on the radiation-induced defects and hydrogen in nanostructured and coarse-grained tungsten," *Acta Mater.*, vol. 122, pp. 277–286, Jan. 2017.

[211] D. R. Mason, X. Yi, M. A. Kirk, and S. L. Dudarev, "Elastic trapping of dislocation loops in cascades in ion-irradiated tungsten foils," *J. Phys. Condens. Matter*, vol. 26, no. 37, p. 375701, Sep. 2014.

[212] R. Herschitz and D. N. Seidman, “Radiation-induced precipitation in fast-neutron irradiated tungsten-rhenium alloys: An atom-probe field-ion microscope study,” *Nucl. Instruments Methods Phys. Res. Sect. B Beam Interact. with Mater. Atoms*, vol. 7–8, pp. 137–142, Mar. 1985.

[213] T. Tanno, M. Fukuda, S. Nogami, and A. Hasegawa, “Microstructure Development in Neutron Irradiated Tungsten Alloys,” *Mater. Trans.*, vol. 52, no. 7, pp. 1447–1451, 2011.

[214] W. Eckstein, J. Lhszxi, and J. László, “Sputtering of tungsten and molybdenum,” *J. Nucl. Mater.*, vol. 183, no. 1–2, pp. 19–24, Jul. 1991.

[215] G. Wehner, “Influence of the Angle of Incidence on Sputtering Yields,” *J. Appl. Phys.*, vol. 30, no. 11, p. 1762, 1959.